

DYNAMICS OF RISING BUBBLES AND STRESS MEASUREMENTS THROUGH  
BIREFRINGENCE IN VISCOELASTIC LIQUIDS

by

Pınar Eribol

B.S., Chemical Engineering, Yeditepe University, 2012

M.S., Chemical Engineering Boğaziçi University, 2014

Submitted to the Institute for Graduate Studies in  
Science and Engineering in partial fulfillment of  
the requirements for the degree of  
Doctor of Philosophy

Graduate Program in Chemical Engineering  
Boğaziçi University

2021

## ACKNOWLEDGEMENTS

I would like to acknowledge my indebtedness and render my warmest thanks to my supervisor, Assoc. Professor Kerem Uğuz, who made this work possible. His guidance and expert advice have been invaluable throughout all stages of the work. On the day, we decided to work together, he promised me that he will always be there for me in this journey. 8 years later today, I can not think of a day that i felt lonely.

I would also wish to express my gratitude to Professor Ramazan Yıldırım for his valuable suggestions which have contributed greatly to the improvement of the study. Even tough he was not my supervisor nor working in my field, I could always go to him for the most practical ideas and a different perspective to my work. The thesis has also benefited from comments and suggestions made by Professor Kunt Atalık during the study. His expertise on the subject has made this work more valuable.

Additionally, I would like to thank my committee members Professor Metin Muradoğlu and Professor Ali Koşar for their interest in my work.

I also want to thank Professor Naci İnci who opened his laboratory to start this work at the beginning. Later, his consultancy made it possible to build an optical setup at the Microfluidics Laboratory of Boğaziçi University. I would also like to extend my gratitude to Professor Amitav Sanyal who let me work in the Center for Life Sciences and Technologies for the rheological measurement parts of this work.

I am extremely grateful to my coworker Arda İnanç from the Physics Department, Boğaziçi University who taught me everything I know about optics today. It was a pleasure to work with him.

I gratefully acknowledge the help and the effort that I received from Gizem Akay at Anton Paar, Istanbul who taught me the crucial things about rheometers, and also

personally did some of the rheological measurements at Anton Paar when we had technical difficulties. I very much appreciate the support of our Boğaziçi alumnus Utkan Akcan from SNF Floerger, Turkey who provided the polymers. I also want to thank Alper Keskin from SNF Floerger whose technical expertise on the preparation of the polymer solutions changed the results of this work in the positive direction. I also acknowledge the help of our department stuffs Yakup Bal, Dilek Kirkoç, Belgin Balkan, Şükrü Ordu, Murat Düzgünoğlu and Melike Gürbüz.

Seymen İlke Kaykanat has been everything for me since I met her. I can not describe what a wonderful labmate/friend/family/teacher/co-author she was to me. The words can not describe my indebtedness for her. She was always there for me day and night last 4 years. I also want to thank her family who were always kind to me. I am deeply grateful to meet my other labmate Sercan Altundemir who taught how to stay calm in this madness. He started as my student and became my go-to person every time I needed a brilliant idea. I should not forget to mention about my ex-labmate Canberk Ozan. Even tough he left our lab years ago, he has never stopped being one of us and always been there for me until today. I should also add our undergraduates Sima Yıldız Doğan, Alperen Abacı and Hira Demirkol to this list. It was a pleasure to work with them. It is rarely this easy to have peace in a lab. Thus, I feel extremely lucky to share the lab with these people. Our Dunkin sessions will be extremely missed.

I would also like to express my appreciation to Özge Selçuk and Uğurcan Tozar. They made these challenging years easy with their friendships. I have dearly missed Uğurcan and his unlimited tea and coffee supply this year. Even tough he did not show it explicitly, I knew how much he cared for our friendship. I can not thank Özge Selçuk enough who has always supported me, pushed me and reminded me what I wanted for my future during our long talks. She was never afraid of scolding me for my own good. I also need to give my thanks to Merve Yüce. She has always cheered my mood without even trying. When I forgot, her endless passion towards science even after many failed attempts reminded me why I loved this work and had to keep working. I thank my long time friends Ece Büdeyri and Merve Yücesan. Neslihan Erdoğan helped

so much during my studies and was always one call away. I would like to thank Mark without whom this thesis wouldn't exist today, for changing my life. I don't know where I would be or what I would be doing today if I did not meet him.

I thank my aunt and uncle, Sevilay and Erol Özyurt who always believed in me and were there at tough days of my life. My cousins/sisters İrem and Pelin Özyurt, I know it was not easy for them to act like enjoying fluid mechanics. I thank entire Çetin, Eribol and Yücel families for their support.

I would also like to say a heartfelt thank to my grandparents, Nadire and Hasbi Çetin. My grandpa was my biggest fan of my (boring) research papers. I wish I could also share this work with my late great-uncle physics Professor Mustafa Çetin who also did his PhD on a very similar subject almost 45 years ago.

Nobody has been more important to me in the pursuit of this project than my brother and my parents. Their love and guidance have always been with me whatever I pursued. My mom was the person who encouraged me to apply Boğaziçi and start my journey when I think I could not get in. I guess that we both came a long way since the day she was teaching me how to read 25 years ago. Some dads do not even know what their kids study, but my father was the only technician to help me build the columns. Every morning he drove me to the university and discussed this project despite the fact that the fluid mechanics was his biggest fear 40 years ago. I know our life was extremely difficult past 20 years but my parents have always prioritized my education so I could reach this point. Finally, I want to thank my brother who made me who I am. I did this PhD and everything for both of us.

I acknowledge the financial support of TUBITAK 118M601 for this dissertation.

## ABSTRACT

# DYNAMICS OF RISING BUBBLES AND STRESS MEASUREMENTS THROUGH BIREFRINGENCE IN VISCOELASTIC LIQUIDS

Bubble dynamics in a viscoelastic liquid are studied to check the existence of a discontinuity in the terminal velocity that occurs at some critical bubble volume and cusp formation at the bubble tail and their relation with the stress around the bubble, which is measured through flow birefringence. A wide range of bubble volumes, 5-2000 mm<sup>3</sup> in 0.10-0.40 wt% polyacrylamide (PAAM) solutions is employed. The terminal velocity decreases with PAAM concentration and increases with bubble volume but plateaus. The plateau velocity is independent of PAAM concentration. No discontinuity in the terminal velocity is observed, which is supported by the bubble shape parameters of which circularity, the minor axis, and eccentricities are found to be concentration-dependent. Increasing the bubble volume changes the shape from spherical to prolate, teardrop with a cusp and cap-shapes. The critical bubble volume for the cusp formation is independent of the PAAM concentration. With the addition of 100 ppm surfactant SDS leads less distortion of the bubbles and cusp formation at smaller volumes. Large bubbles and dilute solutions cause bubbles wobbling. Increasing the PAAM and the surfactant concentrations shows an increase in the lateral direction motion. The retardance and the stretching angle around the bubble are measured for PAAM and hydroxypropyl cellulose (HPC) solution. For small bubbles, the stress is proportional to the concentration; whereas for large ones, bubble shapes become important for the stress. No significant effect of the temperature gradient on the bubble dynamics is observed. Weak convection patterns are seen through Schlieren method.

## ÖZET

# VİSKOELASTİK SIVILARDA YÜKSELEN KABARCIKLARIN DİNAMİKLERİ VE ÇİFTKIRILIM YÖNTEMİ İLE GERİLİM ÖLÇÜMLERİ

Bir viskoelastik sıvıdaki kabarcık dinamiği, bazı kritik kabarcık hacminde meydana gelen terminal hızdaki süreksizliğin varlığı ve kabarcık kuyruğundaki sivri uç oluşumu ve bunların, kabarcık etrafındaki gerilimle ilişkisi, akış çift kırılım yöntemi ile incelenmiştir. Ağırlıkça %0.10-0.40 poliakrilamid (PAAM) solüsyonları içinde çok geniş hacim aralığında, 5-2000 mm<sup>3</sup>, kabarcıklar kullanılmıştır. Terminal hız, PAAM konsantrasyonu ile azalmakta ve kabarcık hacmi ile artıp, plato yapmaktadır. Plato hızı, PAAM konsantrasyonundan bağımsızdır. Terminal hızda süreksizlik gözlemlenmemektedir ve bu şekil parametreleriyle desteklenmektedir; kabarcık daireselliği, küçük ekseni ve eksantrikliklerinin konsantrasyona bağlı olduğu bulunmuştur. Kabarcık hacminin arttırılması, şekli küreselden ovale, sivri uçlu gözyaşı damlasına ve kasket şekillerine değiştirir. Sivri uç oluşumu için kritik kabarcık hacmi, PAAM konsantrasyonundan bağımsızdır. 100 ppm sürfaktan, SDS ilavesi, küçük hacimlerde kabarcıkların daha az bozulmasına ve sivri uç oluşumuna yol açar. Büyük kabarcıklar ve seyreltik çözeltiler kabarcıkların yalpalayarak yükselmesine neden olmaktadır. Polimer ve yüzey aktif madde konsantrasyonlarının artması, yanıl yön hareketinde bir artışa yol açmaktadır. PAAM ve hidrokisipropil selüloz (HPC) çözeltileri içinde kabarcık etrafındaki retardasyon ve esneme açısı ölçülmüştür. Küçük kabarcıklar için gerilim konsantrasyonla orantılıdır; büyükler için ise kabarcık şekilleri önem kazanır. Sıcaklık gradyanının kabarcık dinamiği üzerinde önemli bir etkisi gözlenmemiştir. Schlieren yöntemi ile zayıf konveksiyon desenleri görülmüştür.

## TABLE OF CONTENTS

ACKNOWLEDGEMENTS . . . . .	iii
ABSTRACT . . . . .	vi
ÖZET . . . . .	vii
LIST OF FIGURES . . . . .	xi
LIST OF TABLES . . . . .	xxiii
LIST OF SYMBOLS . . . . .	xxv
LIST OF ACRONYMS/ABBREVIATIONS . . . . .	xxvii
1. INTRODUCTION . . . . .	1
2. LITERATURE SURVEY . . . . .	4
2.1. Non-Newtonian Liquids and Rheology . . . . .	4
2.1.1. Non-Newtonian Rheology Models . . . . .	6
2.1.1.1. Power-Law Model . . . . .	6
2.1.1.2. Carreau-Yasuda Model . . . . .	7
2.1.2. Viscoelasticity . . . . .	8
2.2. Bubble Dynamics in Viscoelastic Liquids . . . . .	9
2.2.1. Effect of the Injection Period on the Bubble Rise . . . . .	17
2.2.2. Effect of Surfactant on the Bubble Rise . . . . .	18
2.2.3. The Bubble Trajectory . . . . .	19
2.3. The Birefringence Method for the Bubble Rise Dynamics . . . . .	20
3. Materials and Their Rheological Characterization . . . . .	22
3.1. Materials . . . . .	22
3.1.1. Poly-acrylamide (PAAM) . . . . .	22
3.1.2. Hydroxypropylcellulose (HPC) . . . . .	24
3.1.3. Glycerol . . . . .	25
3.1.4. Sodium dodecyl sulfate (SDS) . . . . .	26
3.2. Rheological Characterization . . . . .	27
3.2.1. Rheological Characterization Tests . . . . .	28
3.2.1.1. Flow Curve test . . . . .	28

3.2.1.2.	Amplitude Sweep Analysis . . . . .	29
3.2.1.3.	Temperature Sweep Test . . . . .	29
3.2.2.	Rheology Results of 85 wt% Glycerol . . . . .	29
3.2.3.	Rheology Results of PAAM and PAAM+HPC Solutions . . . . .	29
4.	Experimental Setups and Methods . . . . .	37
4.1.	Experimental Setup for the Birefringence Experiments . . . . .	38
4.1.1.	Optical Experimental Setup . . . . .	38
4.1.2.	Adjusting the Light Distribution . . . . .	40
4.1.3.	The Procedure for the Birefringence Experiments . . . . .	41
4.2.	Experimental Setup for the Bubble Dynamics . . . . .	42
4.3.	Experimental Setup for the Schlieren Method . . . . .	44
4.4.	Experimental Setup for Non-Isothermal Experiments . . . . .	46
4.5.	Surface Tension Measurement . . . . .	47
5.	EXPERIMENTALLY MEASURED PARAMETERS . . . . .	50
5.1.	Measured Parameters for the Bubble Dynamics . . . . .	50
5.1.1.	Bubble Equivalent Diameter, Volume and Velocity . . . . .	50
5.1.1.1.	Bubble Equivalent Diameter, $d$ . . . . .	50
5.1.1.2.	Bubble Volume, $V$ . . . . .	50
5.1.1.3.	Bubble Velocity, $u$ . . . . .	51
5.1.2.	Bubble Shape Parameters . . . . .	52
5.1.2.1.	The Ratio of $a/b$ . . . . .	52
5.1.2.2.	Extent . . . . .	52
5.1.2.3.	Solidity . . . . .	53
5.1.2.4.	Circularity . . . . .	53
5.1.2.5.	Eccentricity - 1, $E1$ . . . . .	54
5.1.2.6.	Eccentricity - 2, $E2$ . . . . .	54
5.1.3.	Dimensionless Numbers . . . . .	54
5.2.	Measured Parameters for the Birefringence . . . . .	56
6.	IMAGE PROCESSING AND ANALYZING TECHNIQUES . . . . .	59
6.1.	Intensity Calibration . . . . .	59
6.2.	Image Analysis . . . . .	62

6.2.1.	Image Analysis for Bubble Dynamics . . . . .	62
6.2.2.	Image Analysis for Birefringence Measurements . . . . .	64
7.	RESULTS AND DISCUSSION . . . . .	66
7.1.	Isothermal Experiments . . . . .	66
7.1.1.	Control Experiments with Glycerol . . . . .	66
7.1.2.	Bubble Dynamics for Different PAAM concentrations . . . . .	67
7.1.3.	Effect of the Injection Period . . . . .	85
7.1.4.	Effect of the of Surfactant on Bubble Dynamics . . . . .	86
7.1.5.	The Bubble Trajectory . . . . .	99
7.1.6.	Unsteady-state Bubble Dynamics . . . . .	102
7.2.	Birefringence Measurements and Bubble Dynamics for Different PAAM Concentrations with 0.40 wt% HPC . . . . .	108
7.2.1.	Bubble Dynamics for Different PAAM Concentrations with 0.40 wt% HPC . . . . .	108
7.2.2.	Stress Measurement Through Birefringence . . . . .	123
7.3.	Non-Isothermal Experiments . . . . .	135
8.	CONCLUSIONS AND RECOMMENDATIONS . . . . .	139
8.1.	Conclusions . . . . .	139
8.2.	Recommendations . . . . .	143
	REFERENCES . . . . .	145
	APPENDIX A: UNCERTAINTY ANALYSES . . . . .	157
A.1.	Uncertainty Analysis for the Length . . . . .	157
A.2.	Uncertainty Analysis for the Velocity . . . . .	158
A.3.	Uncertainty Analysis for the Volume . . . . .	160
	APPENDIX B: PERMISSIONS FOR THE REPRINTED FIGURES FROM THE LITERATURE . . . . .	162

## LIST OF FIGURES

Figure 2.1.	Two plates model for the viscosity. . . . .	4
Figure 2.2.	Time-independent fluids. . . . .	5
Figure 2.3.	Flow curves for shear-thinning fluids. . . . .	6
Figure 2.4.	The representative behaviour of the viscosity of shear thinning fluids. . . . .	8
Figure 2.5.	The representation of the flow field and the negative-wake (zone 3) around a bubble rising in a viscoelastic and shear-thinning solution (reprinted with permission from [17]). . . . .	11
Figure 2.6.	A bubble with a cusp at its tip (a) rising in a mixture of PAAM-glycerol; the perpendicular view of same the bubble (b) (reprinted with permission from [13]). . . . .	12
Figure 2.7.	The improved flow field and the negative-wake around a bubble rising in a viscoelastic and shear-thinning solution (reprinted with permission from [22]). . . . .	17
Figure 3.1.	The molecular structure of PAAM. . . . .	22
Figure 3.2.	The blade marine impeller used for the preparation of the PAAM solutions (a) and the vortex created using the impeller (b). . . . .	24
Figure 3.3.	The molecular structure of HPC. . . . .	25
Figure 3.4.	The molecular structure of glycerol. . . . .	26

Figure 3.5.	The molecular structure of SDS. . . . .	27
Figure 3.6.	The MCR302 Anton Paar reometer at the Life Sciences Laboratory at Boğaziçi University. . . . .	27
Figure 3.7.	Schematic representation of the cone-plate rheometer. . . . .	28
Figure 3.8.	The flow curve of 85 wt% glycerol. . . . .	30
Figure 3.9.	Shear stress, $\tau$ vs. shear rate, $\dot{\gamma}$ for different concentrations of PAAM solutions. . . . .	31
Figure 3.10.	Shear stress, $\tau$ vs. shear rate, $\dot{\gamma}$ for different concentrations of PAAM + 0.40 wt% HPC solutions. . . . .	31
Figure 3.11.	Viscosity, $\eta$ vs. shear rate, $\dot{\gamma}$ for different concentrations of % PAAM solutions. . . . .	32
Figure 3.12.	Viscosity, $\eta$ vs. shear rate, $\dot{\gamma}$ for different concentrations of PAAM + 0.40 wt% HPC solutions. . . . .	33
Figure 3.13.	Storage, $G'$ and loss, $G''$ modulus vs. shear strain, $\gamma$ for different concentrations of PAAM solutions. . . . .	34
Figure 3.14.	Storage, $G'$ and loss, $G''$ modulus vs. shear strain, $\gamma$ for different concentrations of PAAM + 0.40 wt% HPC solutions. . . . .	34
Figure 3.15.	The effect of the temperature on the viscosity for different concen- trations of PAAM solutions. . . . .	35
Figure 4.1.	The view of liquid column (a) and the plumbing system (b). . . . .	37

Figure 4.2.	Optical setup. (1) Optical table, (2) Optical rail system, (3) Laser, (4-5) Kinematic frames and mirrors, (6) Plano-concave lens, (7) Plano-convex lens, (9) Liquid column, (8-10) Polarizers, (11) Camera, (12) Illuminator. . . . .	39
Figure 4.3.	The Z-Fold configuration for the alignment of the laser light. . . .	39
Figure 4.4.	NearTEM <sub>00</sub> Beam from the literature [79] and this study. . . . .	41
Figure 4.5.	The dark image (a) obtained at the beginning of the birefringence experiment and the birefringence image as the bubble passes(b). . .	42
Figure 4.6.	The image series obtained from a birefringence experiment. . . . .	43
Figure 4.7.	The sketch of the bubble dynamics experimental setup. (3) laser, (9) liquid column, (11) birefringence camera, (12) light source, (13) high-speed camera. . . . .	44
Figure 4.8.	The scheme of the v-type Schlieren method. . . . .	45
Figure 4.9.	The double view of Schlieren image of the single lighter plume. . . .	46
Figure 4.10.	The scheme of the liquid column designed for the non-isothermal experiments. . . . .	47
Figure 4.11.	The sketch of the Du Nouy ring method experimental setup [85]. . . .	48
Figure 4.12.	The process of Du Nouy ring method. . . . .	48
Figure 5.1.	The bubble profile used to determine the volume with the truncated cone method (reprinted with permission from [37]). . . . .	51

Figure 5.2.	The bubble shape parameter: the a/b ratio a), extent b) and solidity c). . . . .	53
Figure 5.3.	The polarization of light as it passes through a birefringent medium.	57
Figure 6.1.	Sample calibration photos for the 1/200 sec exposure time where each frame represents the photo of the laser light taken with increasing filter. . . . .	60
Figure 6.2.	The calibration graph for the 1/200 sec exposure time. . . . .	61
Figure 6.3.	Sample photo with overexposure (a) and the histogram analysis of the circled area (b). . . . .	62
Figure 6.4.	Sample photo when the overexposure is removed (a) and the histogram analysis of the circled area. . . . .	62
Figure 6.5.	The image of a bubble obtained in the birefringence experiment (a), the background image (b), the image of the bubble where the background is removed(c) and the 8-bit grayscale version of this image (d). . . . .	65
Figure 7.1.	The average terminal velocity of a bubble rising in 85 wt% glycerol as a function of bubble equivalent diameter. . . . .	66
Figure 7.2.	The average terminal velocity of a bubble rising in 85 vol% glycerol solution as a function of bubble equivalent diameter. Comparison with the literature [95,96]. . . . .	67
Figure 7.3.	The bubble volume as a function of time for 0.10 wt% PAAM solution.	68

Figure 7.4.	The average terminal velocity as a function of the bubble volume for different concentrations of PAAM solution. . . . .	69
Figure 7.5.	Shape parameter, extent as a function of the bubble volume for different concentrations of PAAM solution. . . . .	71
Figure 7.6.	Shape parameter, solidity as a function of the bubble volume for different concentrations of PAAM solution. . . . .	75
Figure 7.7.	Shape parameter, circularity as a function of the bubble volume for different concentrations of PAAM solution. . . . .	76
Figure 7.8.	Shape parameter, minor axis, $a$ as a function of the bubble volume for different concentrations of PAAM solution. . . . .	77
Figure 7.9.	Shape parameter, $b$ parameter as a function of the bubble volume for different concentrations of PAAM solution. . . . .	77
Figure 7.10.	Shape parameter, ratio of the minor axis to the major axis, $a/b$ as a function of the bubble volume for different concentrations of PAAM solution. . . . .	78
Figure 7.11.	Shape parameter, eccentricity-1, $E1$ , as a function the bubble volume for different concentrations of PAAM solution. . . . .	79
Figure 7.12.	Shape parameter, eccentricity-2, $E2$ , as a function of the bubble volume for different concentrations of PAAM solution. . . . .	80
Figure 7.13.	Shape parameter, $\beta$ as a function of the bubble volume for different concentrations of PAAM solution. . . . .	80

Figure 7.14. The bubbles where the cusp is seen for the first time at $\beta \approx 0.59$ for different PAAM concentrations. . . . .	81
Figure 7.15. $Bo$ versus $Re$ for different concentrations of PAAM solution. . . .	82
Figure 7.16. $Ca$ versus $Re$ for different concentrations of PAAM solution. . . .	83
Figure 7.17. $We$ versus $Re$ for different concentrations of PAAM solution. . . .	84
Figure 7.18. $C_D$ versus $Re$ for different concentrations of PAAM solution. . . .	85
Figure 7.19. The average terminal velocity as a function of the bubble volume for 0.25 wt% PAAM solution with different surfactant concentrations. . . .	87
Figure 7.20. Shape parameter, extent as a function of the bubble volume for 0.25 wt% PAAM solution with different surfactant concentrations. . . .	90
Figure 7.21. Shape parameter, solidity as a function of the bubble volume for 0.25 wt% PAAM solution with different surfactant concentrations. . . .	91
Figure 7.22. Shape parameter, circularity as a function of the bubble volume for 0.25 wt% PAAM solution with different surfactant concentrations. . . .	92
Figure 7.23. Shape parameter, minor axis, $a$ as a function of the bubble volume for 0.25 wt% PAAM solution with different surfactant concentrations. . . .	93
Figure 7.24. Shape parameter, $b$ as a function of the bubble volume for 0.25 wt% PAAM solution with different surfactant concentrations. . . .	93

Figure 7.25. Shape parameter, the ratio of minor axis, $a$ over $b$ as a function of the bubble volume for 0.25 wt% PAAM solution with different surfactant concentrations. . . . .	94
Figure 7.26. Shape parameter, eccentricity, $E1$ as a function of the bubble volume for 0.25 wt% PAAM solution with different surfactant concentrations. . . . .	95
Figure 7.27. Shape parameter, eccentricity, $E2$ as a function of the bubble volume for 0.25 wt% PAAM solution with different surfactant concentrations. . . . .	95
Figure 7.28. Shape parameter, $\beta$ as a function of the bubble volume for 0.25 wt% PAAM solution with different surfactant concentrations. . . . .	96
Figure 7.29. $Bo$ versus $Re$ for different concentrations of surfactant in PAAM solution. . . . .	97
Figure 7.30. $Ca$ versus $Re$ for different concentrations of surfactant in PAAM solution. . . . .	98
Figure 7.31. $We$ versus $Re$ for different concentrations of surfactant in PAAM solution. . . . .	98
Figure 7.32. Drag coefficient, $C_D$ versus $Re$ for different concentrations of surfactant in PAAM solution. . . . .	99
Figure 7.33. The trajectory of bubbles with different volumes in 0.25 wt% PAAM solution. . . . .	100

Figure 7.34.	The trajectory of bubbles with different volumes in 0.40 wt% PAAM solution. . . . .	101
Figure 7.35.	The trajectory of bubbles with different volumes in 0.25 wt% PAAM with 100 ppm SDS solution. . . . .	101
Figure 7.36.	The evolution of the bubble volume as a function of tube length/equivalent diameter for 0.25 wt% PAAM. . . . .	102
Figure 7.37.	The evolution of the bubble volume as a function of tube length/equivalent diameter for 0.40 wt% PAAM. . . . .	103
Figure 7.38.	The evolution of the bubble volume as a function of tube length/equivalent diameter for 0.25 wt% PAAM with 100 ppm SDS. . . . .	103
Figure 7.39.	The evolution of the bubble velocity as a function of tube length/equivalent diameter for 0.25 wt% PAAM. . . . .	105
Figure 7.40.	The evolution of the bubble velocity as a function of tube length/equivalent diameter for 0.40 wt% PAAM. . . . .	105
Figure 7.41.	The evolution of the bubble velocity as a function of tube length/equivalent diameter for 0.25 wt% PAAM with 100 ppm SDS. . . . .	106
Figure 7.42.	The evolution of the shape parameter, $a$ as a function of tube length/equivalent diameter for 0.25 wt% PAAM. . . . .	106
Figure 7.43.	The evolution of the shape parameter, $a$ as a function of tube length/equivalent diameter for 0.40 wt% PAAM. . . . .	107

- Figure 7.44. The evolution of the shape parameter,  $a$  as a function of tube length/equivalent diameter for 0.25 wt% PAAM with 100 ppm SDS. 107
- Figure 7.45. The average terminal velocity as a function of the bubble volume for different concentrations of PAAM with 0.40 wt% HPC solution. 109
- Figure 7.46. Shape parameter, extent as a function of the bubble volume for different concentrations of PAAM with 0.40 wt% HPC solution. . 116
- Figure 7.47. Shape parameter, solidity as a function of the bubble volume for different concentrations of PAAM with 0.40 wt% HPC solution. . 116
- Figure 7.48. Shape parameter, circularity as a function of the bubble volume for different concentrations of PAAM with 0.40 wt% HPC solution. . 117
- Figure 7.49. Shape parameter, minor axis,  $a$  as a function of the bubble volume for different concentrations of PAAM with 0.40 wt% HPC solution. 118
- Figure 7.50. Shape parameter,  $b$  as a function of the bubble volume for different concentrations of PAAM with 0.40 wt% HPC solution. . . . . 118
- Figure 7.51. Shape parameter, the ratio of the minor axis to  $b$ ,  $a/b$  as a function of the bubble volume for different concentrations of PAAM with 0.40 wt% HPC solution. . . . . 119
- Figure 7.52. Shape parameter, eccentricity-1,  $E1$  as a function of the bubble volume for different concentrations of PAAM with 0.40 wt% HPC solution. . . . . 119

Figure 7.53. Shape parameter, eccentricity-2, $E2$ as a function of the bubble volume for different concentrations of PAAM with 0.40 wt% HPC solution. . . . .	120
Figure 7.54. Shape parameter, $\beta$ as a function of the bubble volume for different concentrations of PAAM with 0.40 wt% HPC solution. . . . .	121
Figure 7.55. $Bo$ versus $Re$ for different concentrations of PAAM with 0.40 wt% HPC. . . . .	122
Figure 7.56. $Ca$ versus $Re$ for different concentrations of PAAM with 0.40 wt% HPC. . . . .	122
Figure 7.57. $We$ versus $Re$ for different concentrations of PAAM with 0.40 wt% HPC $Bo$ against $Re$ for different concentrations of PAAM solution. . . . .	123
Figure 7.58. $C_D$ versus $Re$ for different concentrations of PAAM with 0.40 wt% HPC. . . . .	124
Figure 7.59. The retardance, $\delta$ measurement for different PAAM concentrations for a bubble volume range of 140-238 mm <sup>3</sup> . . . . .	126
Figure 7.60. The stretching angle, $\chi$ measurement for different PAAM concentrations for a bubble volume range of 140-238 mm <sup>3</sup> . . . . .	127
Figure 7.61. Shape parameter, solidity as a function the bubble volume for the bubbles studied in the stress measurement. . . . .	128
Figure 7.62. The retardance, $\delta$ measurement for different PAAM concentrations for a bubble volume range of 360-600 mm <sup>3</sup> . . . . .	130

Figure 7.63.	The stretching angle, $\chi$ measurement for different PAAM concentrations for a bubble volume range of 360-600 mm <sup>3</sup> . . . . .	131
Figure 7.64.	Shape parameter, minor axis, a as a function the bubble volume for the bubbles studied in the stress measurement. . . . .	132
Figure 7.65.	Shape parameter, the ratio of the minor axis to b, a/b as a function the bubble volume for the bubbles studied in the stress measurement.	132
Figure 7.66.	The retardance, $\delta$ measurement for different PAAM concentrations for a bubble volume range of 750-1285 mm <sup>3</sup> . . . . .	133
Figure 7.67.	The stretching angle, $\chi$ measurement for different PAAM concentrations for a bubble volume range of 750-1285 mm <sup>3</sup> . . . . .	134
Figure 7.68.	The average terminal velocity as a function of the bubble volume for 0.18 wt% PAAM solution: isothermal (maroon) and 15 °C temperature gradient (pink). . . . .	136
Figure 7.69.	Shape parameter, circularity as a function of the bubble volume for 0.18 wt% PAAM solution: isothermal (maroon) and 15 °C temperature gradient (pink). . . . .	136
Figure 7.70.	The average terminal velocity as a function of the bubble volume for 0.40 wt% PAAM solution: isothermal (black) and 15°C temperature gradient (purple). . . . .	137
Figure 7.71.	Shape parameter, circularity as a function of the bubble volume for 0.40 wt% PAAM solution: isothermal (black) and 15°C temperature gradient (purple). . . . .	137

Figure 7.72. The temperature gradient observed at the tails of a small and a big bubble. . . . .	138
---	-----

## LIST OF TABLES

Table 3.1.	The physical properties of polyacrylamide [72]. . . . .	23
Table 3.2.	The physical properties of glycerol. . . . .	26
Table 3.3.	The properties of the rheometer probes used for the rheological analysis. . . . .	28
Table 3.4.	The rheological parameters for power-law model. . . . .	36
Table 3.5.	The rheological parameters for Carreau-Yasuda model. . . . .	36
Table 4.1.	The results of the Du Nouy Ring's method at 25 °C. . . . .	49
Table 7.1.	The discontinuity in the bubble terminal velocity: literature that used PAAM. . . . .	70
Table 7.2.	Parameters and dimensionless numbers for 0.25 wt% PAAM solution. . . . .	72
Table 7.3.	Parameters and dimensionless numbers for 0.40 wt% PAAM solution part (part 1/2). . . . .	73
Table 7.4.	Tested injection periods for different PAAM . . . . .	86
Table 7.5.	Parameters and dimensionless numbers for 0.25 wt% PAAM solution with 10 ppm SDS. . . . .	88

Table 7.6.	Parameters and dimensionless numbers for 0.25 wt% PAAM solution with 100 ppm SDS. . . . .	89
Table 7.7.	Parameters and dimensionless numbers for 0.10 wt% PAAM + 0.4 wt% HPC (part 1/2). . . . .	110
Table 7.8.	Parameters and dimensionless numbers for 0.18 wt% PAAM + 0.4 wt% HPC (part 1/2). . . . .	112
Table 7.9.	Parameters and dimensionless numbers for 0.25 wt% PAAM + 0.4 wt% HPC (part 1/2). . . . .	114

## LIST OF SYMBOLS

$a$	Viscosity constant of Carreau-Yasuda model
$A$	Cross section area of the bubble
$Ar$	Archimedes number
$Bo$	Bond number
$Ca$	Capillary number
$C_D$	Drag coefficient
$d$	Equivalent diameter
$dc$	Distance between cone and plate
$De$	Deborah number
$E1$	Eccentricity-1
$E2$	Eccentricity-2
$Eo$	Eötvös number
$F$	Force acts along the edge of the length
$g$	Gravitational acceleration
$G'$	Storage modulus
$G''$	Loss modulus
$Ga$	Gallilei number
$H$	Optical length
$h$	Height of the truncated cone
$I$	Intensity of light
$I_0$	Intensity of the incident light beam
$K$	Consistency index
$\ell$	Length of the edge
$Mo$	Morton number
$n$	Power-law index
$r$	Radius of the lower section of the bubble
$R$	Radius of the upper section of the bubble
$r_c$	Cone radius of the rheometer

$r_r$	Ring radius
$Re$	Reynolds number
$u_B$	Terminal velocity
$V$	Bubble volume
$V_i$	Volume of $i^{\text{th}}$ cone
$We$	Weber number
$\beta$	Empirical shape parameter
$\gamma$	Shear strain
$\dot{\gamma}$	Shear rate
$\delta$	Retardance
$\eta$	Viscosity
$\eta_0$	Zero shear rate viscosity
$\eta_a$	Apparent viscosity
$\eta_\infty$	Viscosity as the shear strain rate goes to infinity
$\theta$	Angle between cone and plate
$\lambda$	Relaxation time
$\lambda_i$	Wavelength of the incident light
$\Pi$	Correlation parameter
$\rho$	Density
$\rho_\ell$	Density of the Liquid
$\rho_g$	Density of the gas bubble
$\sigma$	Surface tension
$\tau$	Shear stress
$\chi$	Stretching angle of the polymer

**LIST OF ACRONYMS/ABBREVIATIONS**

CMC	Carboxymethylcellulose
FPS	Frame per second
HPC	Hydroxypropyl cellulose
LVE	Linear viscoelastic region
PAAM	Polyacrylamide
PIV	Particle imaging velocimetry
SDS	Sodium dodecyl sulfate

## 1. INTRODUCTION

For hundreds of years, multi-phase flows have been a topic of interest due to its wide application areas such as chemical, petrochemical, food, nuclear processes etc. Some of the important applications can be gas and oil pipelines, nuclear reactor, ink-jet printing and chemical reactors etc [1–3]. In this study, we are interested in the two-phase flow studies; in particular bubbles rising in viscoelastic liquids.

An important part of the literature deals with the gas bubbles in a Newtonian medium. While most gases and substances exhibit Newtonian behaviour, there has been a growing interest in recent years to understand the characteristics of the two-phase flows employing non-Newtonian liquids as they are found both in nature (gums, honey, biological fluids such as blood, mucus and synovial fluids) and in industrial processes (high molecular weight polymers, emulsions, plastics and some kind of dispersions). Due to the complex nature of the non-Newtonian liquids, the study of bubble motion in non-Newtonian liquids has been a challenging subject. There exists different types of non-Newtonian liquids such as Bingham plastics, Bingham pseudoplastics, shear-thinning and shear-thickening; and only shear-thinning liquids are employed in this study. Additionally, the viscoelasticity is also studied [4–6].

Bubbles are different than the rigid particles due to their mobile surfaces and their surface deformability. The bubble shape is deformed depending on the stress on it during its motion. Bubbles can exhibit different types of shapes such as spherical, prolate teardrop, oblate cusped-like and spherical cap [7]. Their motion in the non-Newtonian solutions is also different from the bubble motion in Newtonian solutions. In the literature, it is shown that it is difficult to predict the bubble velocity and shape while rising in a shear-thinning and viscoelastic liquid. Some studies reported a sudden increase in the bubble velocity up 10 fold, in polyacrylamide (PAAM) solutions [8–11]; while a jump was not reported in some other polymer solutions [7, 8, 12, 13]. The reasons attributed to the presence of the velocity jump are the cusp formed at the tip

of the bubble and the downwards velocity field, i.e., the negative-wake at the tip of this cusp [13]. The volume where the jump occurs is called the critical volume. The jump is observed at the transition from the Stokes to the Hadamard-Rybczynski regime for some studies [9]. However, there are studies where a jump is not observed even though they report the cusp-like shape and the negative-wake [11, 13–20]. The dimensionless numbers such as Reynolds,  $Re$ , Bond,  $Bo$ , capillary,  $Ca$  and Morton,  $Mo$  are used to understand the system and find the critical bubble volume where the system shows a different behaviour. The bubble shape is also an important parameter as the jump is always observed at the cusp-like shape. The bubble deformation is used to classify the bubbles according to their shapes. Particle imaging velocimetry (PIV) is a technique that is preferred to visualize the velocity field [15–17, 21, 22]. Also the birefringence, an optical method, is used to visualize the stress around the rising bubble [17–20]. The reader is referred to Clift *et al.* (1978) and Chhabra (2006) for a detailed study that considers the behaviour of particles, drops and bubbles in non-Newtonian liquids [1, 7].

It can be seen that there are various unanswered questions in bubbles rising in non-Newtonian fluid systems. Even though, the previous studies had several hypotheses, there is no certain answer why some of the studies observed the jump and the others did not. In this work, the aim is to find answers to these questions or evidences to understand the bubble dynamics better.

Based on the literature, it is hypothesized that there can be a critical bubble volume where the bubble shape, the average terminal velocity of the bubble, the polymer concentration and the stress around the rising bubble are directly correlated with each other. This study aims to show how the introduced parameters change in a system for a broad range of bubble volume, surfactant and polymer concentrations. It is expected that the findings of this study will contribute to the literature by showing which parameters are important and needed to be studied to understand the behaviour of bubble in terms of shape, velocity and stress, while rising in viscoelastic liquids.

For this purpose, the dynamics of a bubble rising in viscoelastic and shear-

thinning PAAM solutions with different concentrations are studied using multiple deformation parameters and dimensionless numbers. To illuminate this uncharted area, we examined the stress around the bubble as it rises using the birefringence method. In particular, no study, to our knowledge, has considered to quantify the stress to search if there is a relationship between the stress and the bubble dynamics using the birefringence method. Moreover, the effect of the surfactant on the bubble dynamics is studied. Finally, the bubble dynamics is examined in the presence of a temperature gradient.

A literature survey is presented in Section 2. In Section 3, the information about the materials and the rheological characterizations of the solutions are given. The experimental setups and the methods used in the experiments are presented in Section 4. The parameters that are measured during the experiments are introduced in Section 5. Image processing and the techniques used to analyze the experiments are studied in Section 6. In Section 7, the results are presented and discussed. Conclusions and recommendations are given in Section 8. Uncertainty analyses are presented in Appendix A for the experimental measurements and the calculations. Finally, the permissions for the figures taken from the literature are given in Appendix B.

## 2. LITERATURE SURVEY

In this section, a literature survey on the dynamics of a rising bubble is presented. In Section 2.1, non-Newtonian liquids and the rheological properties are introduced, and the constitutive equations used in this study are given. The dynamics of a bubble rising in viscoelastic solutions are studied in Section 2.2 in detail. This Section also includes the studies related to the injection period, the use of surfactant, the bubble trajectory and the birefringence method.

### 2.1. Non-Newtonian Liquids and Rheology

It is known from the two-plate model that when one of the plates is sheared such that it moves at constant speed  $u$  (see Figure 2.1), then there is a relationship between the applied shear stress,  $\tau$  and the shear rate,  $\dot{\gamma}$ , as

$$\eta_a = \frac{\tau}{\dot{\gamma}} \quad (2.1)$$

where  $\eta_a$  is the apparent viscosity.

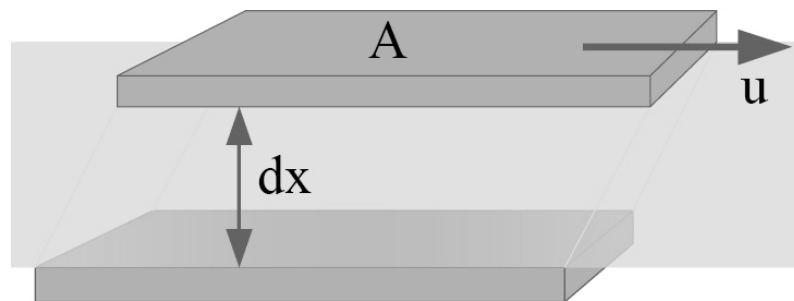


Figure 2.1. Two plates model for the viscosity.

For Newtonian fluids, the viscosity is independent of the shear rate, and is shown as  $\eta$ . For non-Newtonian fluids, the fluid viscosity changes with shear rate. Although simple gases and liquids show Newtonian behaviour, the behavior of complex systems such as emulsions, suspensions, solutions containing long molecules or fluids with high molecular weight is more complex [23].

Non-Newtonian fluids are classified as time-dependent, e.g., thixotropic and rheopectic and time-independent, e.g., Bingham plastic, Bingham pseudoplastic, dilatant, pseudoplastic, shown in Figure 2.2 [4–6, 24].

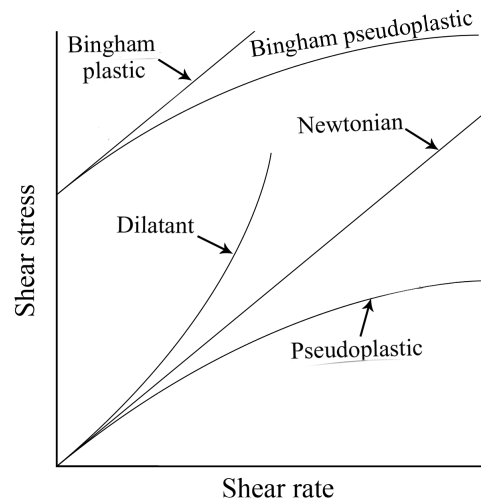


Figure 2.2. Time-independent fluids.

In this study, we are only interested in pseudoplastic (shear-thinning) fluids. The viscosity of this type of fluid decreases with shear rate (Figure 2.3). Most non-Newtonian fluids are in this class and include polymer solutions or melts, greases, starch suspensions, biological fluids, detergents, dispersion media of some drugs and dyes [25, 26]. The reader is referred to [25] for more detail about other types of non-Newtonian fluids.

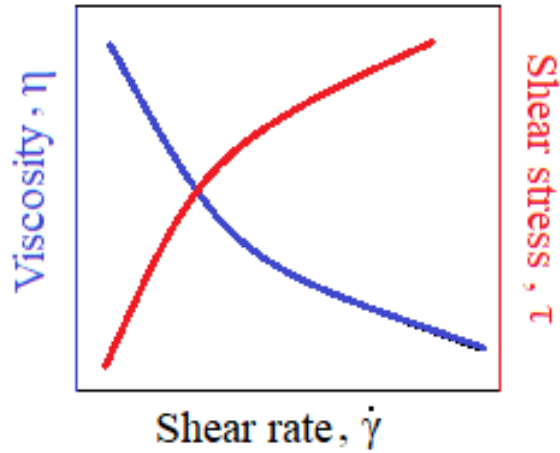


Figure 2.3. Flow curves for shear-thinning fluids.

### 2.1.1. Non-Newtonian Rheology Models

The power-law, Carreau-Yasuda, Herschel-Bulkley, Cross and Casson models are the most widely used rheological models. In this dissertation, only the power-law and the Carreau-Yasuda models are employed; therefore, only these two models are presented here.

2.1.1.1. Power-Law Model. The power-law model is widely used to characterize semi-solid materials. In addition to being a well-known and useful model, the power law model is very important as it is applicable in the  $10^1 - 10^4 \text{ s}^{-1}$  shear rate range where many commercial rheometers operate. The disadvantage of the power-law model is that materials exhibiting shear-thinning and shear-thickening behaviors cannot be identified at low and high shear rates [24, 27, 28].

The power-law model is a two-parameter model where The flow consistency index,  $K$  ( $\text{Pa}\cdot\text{s}^n$ ) is the shear stress at  $1 \text{ s}^{-1}$  shear rate, is given as follows:

$$\eta_a = K\dot{\gamma}^{n-1}. \quad (2.2)$$

The power term  $n$ , which is the flow behaviour index, is unitless. In order for the experimental data to be compatible with this model,  $K > 0$  and  $0 < n < 1$  for the shear-thinning fluids. For the special case of the Newtonian fluids where  $n$  is equal to 1, the consistency index  $K$  is equal to the viscosity of the fluid. The fluid exhibits shear-thickening behaviour when  $n$  is greater than 1.

When the logarithms of both sides of Eq. 2.2 are taken, the following equation is obtained,

$$\log(\eta_a) = \log(K) + (n - 1)\log(\dot{\gamma}) \quad (2.3)$$

where  $K$  and  $n$  parameters are determined from the intercept and the slope of  $\log\eta_a$  vs.  $\log\dot{\gamma}$  plot.

Shear-thinning fluids that are interest of this study can be described through the power-law model; but exhibit Newtonian behavior at extreme shear rates. Therefore, the viscosity versus the shear rate graph can be divided into three regions:

- (i) low shear rates: the viscosity is constant at,  $\eta_0$ .
- (ii) medium shear rates: the viscosity changes with the shear rate where the power-law model is applied.
- (iii) high shear rates: the viscosity is constant at its infinity value,  $\eta_\infty$ .

The described behaviour including the region where the power-law model is applied, can be seen in Figure 2.4. The Carreau-Yasuda model can cover the entire forementioned behaviour and is explained in Section 2.1.1.2.

2.1.1.2. Carreau-Yasuda Model. It is a model that represents the polymer flow behavior in a wider range of shear rate than the power-law model. Unlike the power-law model, it is a model in which the  $\eta_0$  and  $\eta_\infty$  parts can also be represented (Figure 2.4).

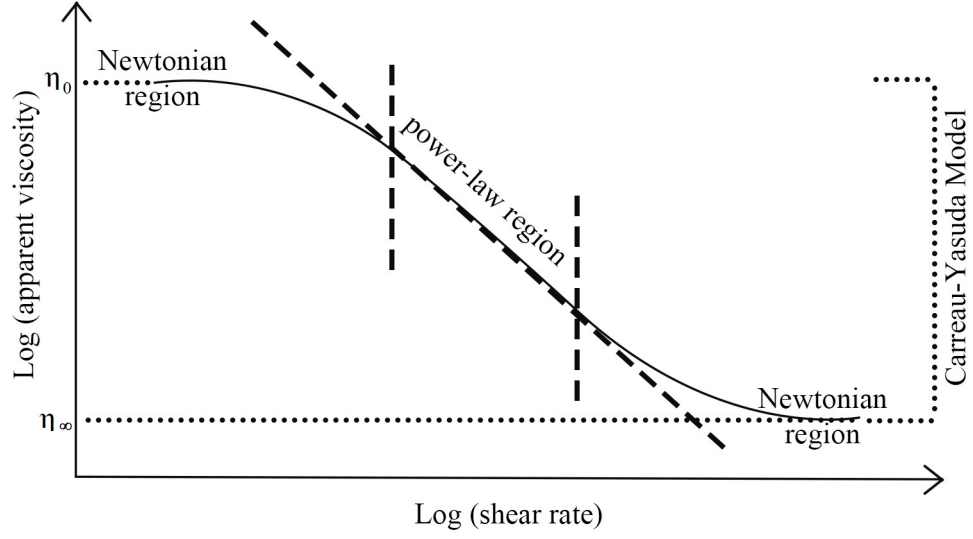


Figure 2.4. The representative behaviour of the viscosity of shear thinning fluids.

The Carreau-Yasuda model is given as follows,

$$\eta_a = \eta_\infty + (\eta_0 - \eta_\infty)(1 + (\lambda\dot{\gamma})^a)^{\frac{n-1}{a}} \quad (2.4)$$

where,  $\lambda$  is the relaxation time and used to determine the transition point from the zero shear rate zone to the shear-thinning behavior. The constant,  $a$  determines the shape of the transition between the constant viscosity region and the power-law region. If  $a$  is smaller than 1, the transition zone becomes longer. If  $a$  is greater than 1, the transition will be instantaneous. Here,  $n$  represents the flow behaviour index again. The Carreau-Yasuda model is very flexible as it is controlled by five different parameters ( $\eta_0$ ,  $\eta_\infty$ ,  $\lambda$ ,  $a$  and  $n$ ). Therefore, it is the most widely used shear viscosity model [4, 25, 28, 29].

### 2.1.2. Viscoelasticity

In this study, we are particularly interested in viscoelastic fluids. Viscoelasticity gives information about the elastic behavior of viscoelastic solids and the flow behavior of liquids. In order to understand the viscoelasticity better, it is necessary to know

what the elastic and viscous behavior is. When an external force is applied to an object, the substance changes its shape and when this force is removed, the object can return to its original state. This behavior is called as the elastic behavior. If an external force is applied to the object and the object shows delayed deformation, it exhibits viscous behavior. The difference between the delayed strain and the stress is called the phase angle. Viscoelastic behavior depends on the relationship between the elasticity and the viscosity of the material with respect to this phase angle. The stress/strain ratio obtained in rheological studies gives the modulus of the material. While examining the elastic structure of the material, the storage,  $G'$  modulus is taken into account, while the loss,  $G''$  modulus is taken into account to examine the viscous structure of the material. Viscoelasticity is studied in detail through the experimental rheological characterization in Section 3.2.

## 2.2. Bubble Dynamics in Viscoelastic Liquids

The shape and the velocity of a rising bubble depend on its size and the physical properties of the liquid, e.g., the viscosity, the density and the surface tension. The liquid-gas two phase flow is often employed in many industrial sectors, including energy generation, chemical, food, biochemical, and waste water disposal [2]. Due to the complex rheological properties of the non-Newtonian fluids such as shear-thinning, viscoelasticity, etc., the dynamics of free-rising bubbles in non-Newtonian fluids are very complex.

One of the earliest studies about the bubble motion in non-Newtonian fluids is presented by Astarita and Apuzzo (1965) [8]. They experimentally studied the terminal velocities of bubbles rising in different non-Newtonian fluids (Carbopol, carboxymethylcellulose (CMC), ET497 and J-100), which differ by viscosity and elasticity. They reported a discontinuity upto 6 folds at the bubble rise velocity at a specific bubble volume for highly elastic solutions (ET497 and J-100). This discontinuity was called a jump where the velocity value increases abruptly above a critical volume. In this work, the jump was attributed to the viscoelasticity. Later, Leal *et al.* (1971)

experimentally and theoretically investigated the discontinuity using PAAM solutions (Separan AP30) [9]. Their hypothesis was that a change in interfacial conditions due to the no-slip boundary condition to free shear caused a 5-10 fold of discontinuity at the velocity. They tested this hypothesis by comparing the terminal rise velocities of bubbles and glass spheres with the same radius. They observed no jump at the velocity of the glass sphere; but a jump in the velocity of bubble. Therefore, it was believed that the discontinuity was caused by the transition from the Stokes to Hadamard regime [9]. Acharya *et al.* (1977) also observed the discontinuity for CMC and PAAM solutions and linked the reason for this to the mobile surface of the bubbles [10] and the polymer molecules acting like a surfactant on the bubble surface. However, they also added the size of the jump was less than the previous studies [8,9]. They reported that the inertial stresses had an effect on the bubble deformation where the fluid properties of the solutions, i.e. the viscoelasticity and the surface tension are kept constant; and the elastic properties was turning bubbles into prolate and oblate shape for low and high Reynolds number,  $Re$  (the ratio of inertial forces to viscous forces), respectively. In line with the study of Astarita and Apuzzo (1965) [8], Dekee and Chhabra (1986) confirmed the absence of the discontinuity for CMC solutions [12]; and the small size of the jump observed by Acharya *et al.* (1977) can be explained by the low elasticity of CMC solutions [10]. However, Dekee *et al.* (1986, 1988) [12,14] did not observe the discontinuity for the PAAM solution (Separan AP30) and had a discrepancy with Leal *et al.* (1971) [9].

Hassager (1979) did not report any discontinuity at velocity using laser Doppler anemometry for the PAAM-glycerol mixtures but showed the presence of the velocity directed downwards at the tip of the air bubble and having a tip similar to the knife edge also known as *cusp* [13]. Hassager (1979) called this downwards velocity *negative-wake* (zone 3 in Figure 2.5) and showed that bubbles had cusp (shown from two different angles in Figure 2.6), i.e. the sharp pointy tip at the tail above a critical bubble volume in the presence of the negative-wake. They observed that the tip was becoming weaker then evolving into a rounded shape as the bubble volume decreases. Coutanceau and Hajjam (1982) also studied the effects of the viscoelasticity and the shear-thinning

property on the bubble dynamics in different viscoelastic solutions [11]. They made a comparison between viscoelastic (PAAM Separan AP30, polyox and CMC) and Newtonian solutions with the same density and the viscosity. They concluded that the elasticity of a solution was the reason for the formation of the negative-wake; therefore, the increase in the bubble velocity and the cusp formation. They also showed that the velocity was reaching to a limit with increasing elasticity. However, a limit did not exist with the increasing shear-thinning effect [11]. Using the same polymer solutions with [13] and [11], Dekee *et al.* (1988) investigated the transition of the bubble shape as a function of the bubble volume and the polymer concentration in detail; and obtained four different bubble shapes, i.e. spherical, prolate, teardrop, oblate cusped and spherical cap with increasing volume [14].

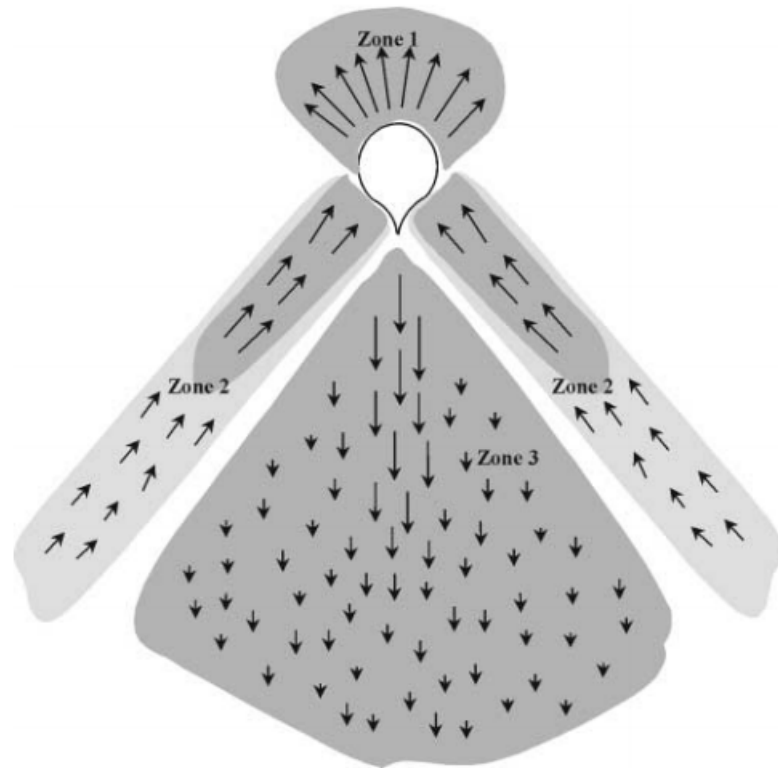


Figure 2.5. The representation of the flow field and the negative-wake (zone 3) around a bubble rising in a viscoelastic and shear-thinning solution (reprinted with permission from [17]).

In later works, the study of the bubble shape and the negative-wake became more important to understand and explain the bubble rise velocity in viscoelastic and shear-thinning liquids due to the disagreement in the literature. The presence of the discontinuity at the bubble velocity was attributed to the viscoelasticity of the solutions. The negative-wake, hence, the cusp, were also explained through the viscoelasticity. However, there were also cases where there was a cusp formation but no discontinuity in viscoelastic solutions.. For example, Dekee *et al.* (1988) clearly showed the cusp formation for a rising bubble while reporting no discontinuity at the velocity [14]. Therefore, it is necessary to inform the reader about this uncertainty and the conflict at this point. The conflict has continued in the literature until today, and in this section we are providing the results of the related studies while discussing their evidences and explanations.

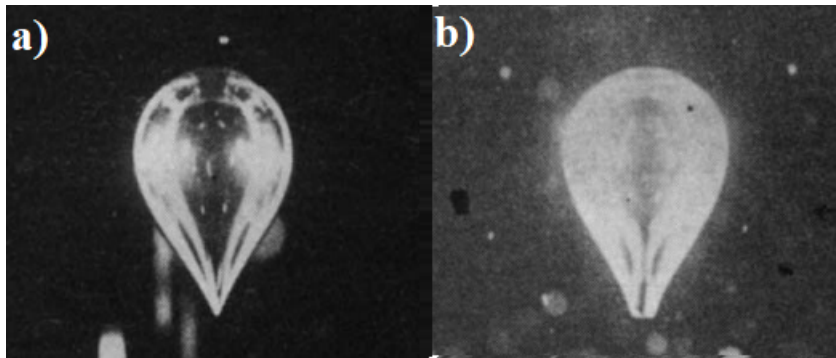


Figure 2.6. A bubble with a cusp at its tip (a) rising in a mixture of PAAM-glycerol; the perpendicular view of same the bubble (b) (reprinted with permission from [13]).

Along with the previous works, Miyahara and Yamanaka (1993) reported no discontinuity for CMC solutions and showed that for the spherical bubbles at low  $Re$ , the experimental drag coefficient,  $C_D$  is in an agreement with the Hadamard-Rybczynski type of drag coefficient,  $C_D$ . The experimental  $C_D$  deviates from the Hadamard-Rybczynski region as a cusp forms at higher  $Re$  [30]. Dewsbury *et al.* (1999) compared the rise of solid spheres to the rising bubble in CMC solution [31], and showed that the solid particles with the same volume and shape (bubble cap) as the bubbles, shared the same  $C_D$  curve for  $Re > 135$ . However, the bubbles fitted the Stokes model

$C_D$  for  $Re < 5$  where the solid particles did not. The findings of Margaritis *et al.* (1999) about  $C_D$  for  $Re < 1$  in viscoelastic and shear-thinning polysaccharide solutions are also in an agreement with Miyahara and Yamanaka (1993) [30]. They showed that  $C_D$  reaches a value of 0.95 with increasing  $Re$ ; and the terminal rise velocity does not show any discontinuity while reaching a plateau for the increasing bubble volume. Same observations were done by Amirnia *et al.* (2013) for CMC and xanthan gum solutions [32]. The validity of the Hadamard-Rybczynski type  $C_D$  was also proved for other viscoelastic and shear-thinning solutions such as xanthan gum solution [33]. Apart from these works, Zhang *et al.* (2008) developed an empirical  $C_D$  formula [34] and demonstrated that viscoelastic and shear-thinning solutions behave different than the solutions that show only shear-thinning behavior. Therefore, they proposed a modified  $Re$  that includes the elongation time,  $\lambda$  to calculate  $C_D$  for the accelerating bubble motion [34]. Wenyuan *et al.* (2010) also developed an empirical correlation for  $C_D$  that is a function of  $Re$ , Archimedes number,  $Ar$  (the ratio of the gravitational forces to the viscous forces) and Eötvös number,  $Eo$  (the gravitational forces compared to the surface tension forces) [35]. This type of  $C_D$  is different than the previously mentioned ones by including the bubble shape parameter, i.e. the aspect ratio. The  $C_D$  proposed by Wenyuan *et al.* (2010) was found to be in a good agreement with the  $C_D$  formulas developed by Dewsbury *et al.* (1999) and Zhang *et al.* (2008) [31, 34].

Wenyuan *et al.* (2010) indicated that for a given  $Re$  and  $Eo$ , the bubble shape changes for different type of polymers for a given [35]. Similar to the work of Wenyuan *et al.* (2010) [35], Li *et al.* (2012) developed an empirical  $C_D$ . However, they included the flow behaviour index,  $n$  of power-law model instead of  $\lambda$ . The proposed  $C_D$  covers a wider range of  $Re$  (0.05–300). They also provided a shape diagram to show the transition of the bubble shapes. The literature has been in an agreement that the rising bubble obtains a spherical shape due to the surface tension forces at very low  $Re$ . But a transition occurs in the shape depending upon the bubble volume and the physical properties of the surrounding phase. An early work by Grace (1973) proposed a phase diagram, *Grace-map* in terms of  $Re$ ,  $Eo$  and Morton number,  $Mo$  where one can successfully predict the shape of the bubble rising in non-Newtonian liquids [1, 36]. The

Grace-map has been used widely [35, 37]. One of the recent studies who also used the Grace-map, Xu *et al.* (2019) proposed two new shape parameters to characterize the shape of the rising bubble for xanthan gum and PAAM solutions [37]. They quantified the cusp formation through one of the proposed parameters.

Another important dimensionless number to study bubble dynamics is capillary number,  $Ca$ , which shows the ratio of the viscous to the surface tension forces. For polyox solutions, Liu *et al.* (1995) showed that the cusp formation and discontinuity occur up to 10 fold when the  $Ca$  is around unity, 1 [38]. They believed that the discontinuity was due to the cusp formation near the critical  $Ca$  value. However, when Wagner *et al.* (2000) did simulations for a similar system, they did not observe any jump due to the cusp formation [39]. Besides, Rodrigue *et al.* (1998) also did not observe any jump for low concentrations of PAAM (Separan AP273) solutions when  $Ca$  was around 1 [40] in the presence of a cusp. However, for higher, the critical  $Ca$  is around 1.

Soto *et al.* (2006) showed that the shear rates where they observed the discontinuities for different concentrations of the HASE solutions, corresponded to the appearance of normal stresses in the rheology analysis [41]. This is the first study that mentions about a critical shear rate value. They proposed that the cause of the discontinuity is the balance between elastic and surface tension forces. Pillapakam and Singh (2006) also considered the elastic and the surface tension forces. They indicated that the elastic forces being much larger than the surface tension forces causes the cusp formation [42]. However, unlike Soto *et al.* (2006) [41], they did not report any discontinuity [42]. Soto *et al.* (2006) also found out that the critical volume depends on the polymer concentration and decreases with it. Whilst this result aligned with a prior research of Herrera *et al.* (2003) [15], it had a conflict with Rodrigue and Dekee (1999) [43] as they said the critical volume is independent of the concentration. Pilz and Brenn (2007) considered both of these forces and experimentally obtained a universal correlation parameter to predict the presence/absence of the discontinuity [44]. This parameter,  $\Pi$  was a function of  $\lambda$ , the gravitational acceleration,  $g$ , the density

of the liquid,  $\rho$  and the surface tension,  $\sigma$ ; and defined as  $\lambda(g^3\rho)^{1/4}$ . The discontinuity is observed for different polymeric solutions, when  $\Pi$  was higher than 9.8938. No discontinuity is observed at low polymer concentrations and a cusp at the tip of the bubble does not ensure the presence of the discontinuity [44]. This universal correlation parameter,  $\Pi$  can be the most definite criteria to predict the behaviour of the bubble rise velocity. Hassan *et al.* (2010) investigated the effects of the viscous, inertia and surface tension forces on a bubble rising in xanthan gum solution through  $Re$  and Weber number,  $We$  (the ratio of the inertial to the surface tension forces for curved surfaces) [45]. Surface tension forces were dominant for small bubbles whereas both of inertia and surface tensions were effective for medium range of bubble volume. However, the inertia is dominant for larger bubbles. Viscous forces had a small effect for  $5 < Re < 200$  [45].

There are also some numerical work with various constitutive equations, considering bubble dynamics in viscoelastic liquids. Pillapakam and Singh (2001) used finite-element method (DNS) to show that bubbles have cusps after some critical values of  $Ca$  and Deborah number,  $De$  (represents the fluidity) [42]. The stability analysis of You *et al.* (2009) were in an agreement with Pillapakam and Singh (2001) as they also indicated the presence of a critical bubble volume and  $Ca$  for a specific  $De$  to form a cusp-like shape [46]. These studies support the findings of Wagner *et al.* (2000) and Malaga and Rallisonn (2007) who employed Lattice Boltzman and FENE models, respectively; and did not detect any discontinuity [39, 47]. In a later work, Lind and Phillips (2010) employed the boundary element method [48]. They imposed the irrotational flow assumption to prevent the negative-wake formation at the bubble's cusp-like tail. The results showed no discontinuity at rise velocity. Thus, Lind and Phillips (2010) deducted that the cusp shape is solely not enough, and a negative-wake is a prerequisite for the discontinuity [48].

Tripathi *et al.* (2015) executed unsteady simulations for a bubble rising in a Herschel-Bulkley liquid where they showed that the bubble did not reach the steady state for weak-surface tension cases [49]. The numerical simulations of Premlata *et al.*

(2017) showed that as the shear-thinning property of the liquid increases, the bubble's shape deforms less and the rise velocity increases in the low  $Eo$  and Gallilei number,  $Ga$  (the ratio of gravitational to the viscous forces) regime [50]. In a very recent work, Yuan *et al.* (2020) employed rheoInterFoam solver that is developed for viscoelastic fluids and the solver employs the finite volume method [51]. They confirmed the findings of Premlata *et al.* (2017) about the low  $Eo$  and  $Ga$  regime.

In the literature, the particle image velocimetry (PIV) method was employed to examine the flow field around a rising bubble. Funfschilling and Li (2001, 2006) did not report any discontinuity for both CMC and PAAM (AN 913 SH and AN 934 SH) solutions while proving the presence of the cusp and the negative-wake (see Figure 2.5) using the PIV method [17, 21]. In a later work, Böhm *et al.* (2016) improved the flow field around the bubble using PIV [22] by showing that there actually exists 5 different flow zones (Figure 2.7) around a cusp-like shaped bubble instead of 3 zones (Figure 2.5) reported by Funfschilling *et al.* (2006) [17, 22]. The findings of Li *et al.* (2012) was in an agreement with Funfschilling *et al.* (2006) [21] for CMC solutions while showing that the viscosity distribution around the rising bubble using PIV. A high and low viscosity regions were observed for the center of the negative-wake and around it, respectively.

On the other hand, Herrera-Velarde *et al.* (2003) who also used the PIV method, showed that the discontinuity occurred when the negative-wake forms in the PAAM solutions (PAAM Separan AP30) [15]. They also added that the critical bubble volume where the jump occurs, decreased while the magnitude of the jump increases with the increasing polymer concentration. Similarly, Kemiha *et al.* (2006) employed PIV for PAAM solutions. They experimentally proved that the cause of the negative-wake was not due to the interface deformation by comparing a solid particle and a bubble [16]. As mentioned earlier, Dewsbury *et al.* (1999) also employed both solid and deformable subjects. Even though, the rigid sphere and the bubble showed a discrepancy at  $C_D$  for low  $Re$  [31, 52], Kemiha *et al.* (2006) demonstrated the existence of a negative-wake for both, rigid and deformable surfaces [16].

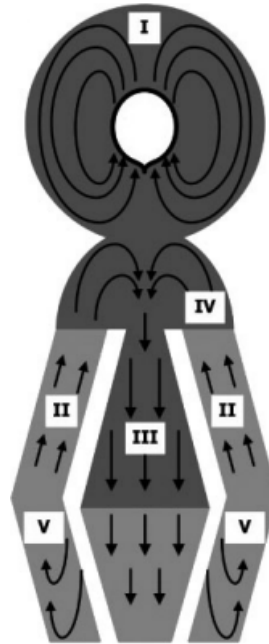


Figure 2.7. The improved flow field and the negative-wake around a bubble rising in a viscoelastic and shear-thinning solution (reprinted with permission from [22]).

Even though it did not employ a shear-thinning liquid as the rest of literature given in this section, it is worth discussing the finding of Vélez-Cordero *et al.* (2012) here [53]. This study employed a Boger-type fluid that is an elastic liquid with a constant viscosity and independent of the shear rate. The purpose was to study the bubble rise velocity where only elastic forces were effective. A discontinuity was obtained at the bubble velocity; however, no negative-wake was observed. This result is particularly interesting as it shows that a negative-wake does not necessarily exist in the presence of a discontinuity [53]. They also mentioned that this critical bubble volume is not observed at  $Ca = 1$  unlike Liu *et al.* (1995) and Rodrigue *et al.* (1998) [38,40].

### 2.2.1. Effect of the Injection Period on the Bubble Rise

An important parameter that has an effect on the bubble rise velocity is the bubble injection period. In an early study, Carreau *et al.* (1974) proved the effect of the period on the bubbles rising in CMC and PAAM solutions. Later, Dekee and

Chhabra (1986) [12] stated that they did not observe any significant effect on the velocity and the bubble shape; and they attributed the dependency on the period reported by Carreau *et al.* (1974) to the orientations of the molecular chains of ionic polymers with high molecular weight [54]. Li *et al.* (1997a, 1997b, 1998) believed that the accumulated residual stress left behind a bubble needs to be considered due to its effect on the drag. Their observations showed that accumulated stress causes an increase in the rise velocity [55–57]. Li *et al.* (2004) showed that the injection period for a constant bubble volume becomes more important as the polymer concentration increases [19]. They reported a period upto 12 s is necessary.

In a later work, Funfschilling and Li (2006) compared the injection period for glycerol (Newtonian), CMC (similar viscosity with glycerol, slight shear-thinning) and PAAM (high viscosity and highly shear-thinning) [21]. Glycerol and CMC required an injection period higher than 0.3 s. However, 60 s of injection period is required for the PAAM solution. A lower injection period causes an increase in the bubble velocity for the PAAM solution as the bubble is affected by the wake of the previous bubble. It seems like the bubble shape does not change with the injection period for the CMC solution. However, a critical bubble volume exists for the PAAM solution where the injection period starts showing its influence [21]. Some other works preferred an injection period of 300 s [15, 41, 58].

### **2.2.2. Effect of Surfactant on the Bubble Rise**

The bubble motion is also affected by the impurities that can be found on the surface of the bubbles. Small concentrations of surfactants can drastically alter the behaviour of a bubble. Clift *et al.* (1978) showed that the no-slip surface exists in the presence of the surfactant. The bubble rise velocity decreases with the addition of the surfactant into the solution due to the Marangoni effect where the surfactant concentration is not uniform along the surface of the bubble [59]. Surfactant changes the surface tension and the tangential shear stress occurs on the bubble surface. The presence of the surfactant in the medium also changes lateral movement of the bubble.

The bubble velocity decreases as the surfactant concentration increases [43,58,60] until the  $C_D$  value reaches the  $C_D$  of a rigid sphere. Karamanev (1994) stated that the bubble acts like a rigid sphere if the bubble surface is contaminated enough with the surfactant [61,62]. Cuenot *et al.* numerically showed that for a spherical bubble, the bubble velocity decreases, therefore  $C_D$  increases for  $Re < 100$  [63]. Tzounakos *et al.* (2004) experimentally showed that the surface mobility does not have any influence on the bubble shape in the presence of the surfactant whereas the rise velocity is strongly depended on the surfactant concentration [60]. However, Li *et al.* (2018) also added that the rise velocity becomes independent of the surfactant concentration after a critical bubble volume [62]. It is observed that  $C_D$  behavior changes from Stokes to Hadamard-Rybczynski regime for a given  $Re$  range. [60].

Nalajala *et al.* (2014) simulated the bubble rise and the drag forces in a power-law liquid using ANSYS Fluent [64]. Their results proved the existence of a recirculating wake at the tip of the bubble above a critical  $Re$  and surfactant concentration. The wake grows with increasing shear-thinning property. They showed that the  $C_D$  increases as the liquid becomes more shear-thinning below a critical  $Re$  [64]. In a very recent work, Ahmed *et al.* (2020) studied the effect of soluble surfactant and the viscoelasticity on the bubbly flow where they employed FENE-P viscoelastic model and the front-track method [65]. They showed that when the surfactant concentration was high enough, the bubbles travel to the core region of the channel in the lateral direction. Marangoni stresses are cancelled out by the viscoelastic stresses. A bubble-wall layer forms due to the combination elastic, inertial and Marangoni forces [65].

### 2.2.3. The Bubble Trajectory

When a bubble rises in a liquid, it tends to have an axi-asymmetric trajectory such as zigzag or spiral, depending on the physical characteristics of the liquid. Hassan *et al.* (2008) showed that the large bubbles move spirally in xanthan gum solution while the smaller bubbles exhibit less horizontal move and do a zigzag motion at low  $Re$  and  $We$ . [33,45]. It is found that the spiral movement of a large bubble is bigger

for the bubbles rising in massecuites [45], a shear-thinning sugar solution with crystal suspension, than a solution without crystals [33].

Hassan *et al.* (2010) hypothesized that the zigzag motion is due to an instability caused by the vorticity created by the wake of the bubble [45]. Böhm *et al.*(2014) showed that the ellipsoidal shaped bubbles followed a rectilinear path in xanthan gum solution [66]. Kumar *et al.* (2015) tested both shear-thinning and shear-thickening solutions [67]. They found that the bubble path does not depend on the shear-thinning or thickening property and is rectilinear [67]. Later, Xu *et al.* (2017) proved that the bubble trajectory depends on the bubble shape deformation in CMC solutions [37]. The rise of the bubble stabilizes as the polymer concentration increases. The oscillation of the bubble increases with the nozzle diameter [37].

### 2.3. The Birefringence Method for the Bubble Rise Dynamics

Some materials show anisotropic properties. The elongated shape of the molecules causes the anisotropic behavior of the liquid crystals. Some of the liquid crystals are in a cholesteric phase where the molecules are directionally oriented and stacked in a helical pattern [68]. These materials exhibit a property called birefringence, which is observed only in the presence of stress. Its magnitude of the refractive indices at each point in the material is directly related to the state of the stress at that point.

When a ray of light passes through a birefringent material, it becomes polarized, splits into two components (ordinary and extraordinary beams), and gets resolved along with the two principal stress directions. Each of these components experiences different refractive indices. The difference in the refractive indices leads to a relative phase difference between the two-component waves, which is usually called phase retardation. The magnitude of the relative retardation is given by the stress-optical law [69] which is explained in Section 5.2 in detail.

As mentioned before, PIV method can be used to visualize the flow field. As

an alternative, the birefringence can be employed to visualize what occurs around a rising bubble. The stress around the bubble can be quantified through the retardance and the stretching angle of the polymer through the birefringence method. In multiple works, Frank and his colleagues showed the stress distribution around the bubble rising in PAAM mixed with hydroxypropylcellulose (HPC) solution using the birefringence method [17–20]. HPC was added into the PAAM solution to add birefringence property to the solution. They did not quantify the stress. They visually showed the butterfly-shaped stress distribution and the negative-wake around the bubble. They also did not report any discontinuity at the rise velocity for HPC added PAAM (AN 905 SH and AN 913 SH) solutions. Oba *et al.* developed polarization imaging method; and studied the birefringence and extinction angle distributions [70]. They showed their work is applicable to image the non-uniform flow in wormlike micellar solutions [70]. In a recent work, Iwata *et al.* (2019) showed the retardance around the bubble using the birefringence for CTAB/NaSal solutions where they reported a velocity discontinuity at very small bubble volumes [71].

### 3. Materials and Their Rheological Characterization

#### 3.1. Materials

##### 3.1.1. Poly-acrylamide (PAAM)

The non-Newtonian solution is prepared with polyacrylamide (PAAM) AN SH and manufactured by SNF Floerger Turkey. The molecular formula of PAAM can be seen in Figure 3.1. Polyacrylamides are water-soluble polymers. They are widely used in drinking water production, wastewater treatment, mining enterprises, petroleum production, agriculture, textile, and cosmetic industries.

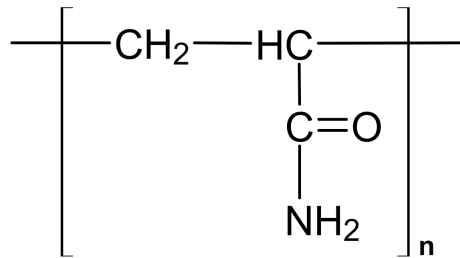


Figure 3.1. The molecular structure of PAAM.

Polyacrylamide is a high molecular weight polymer. The physical properties of PAAM can be seen from Table 3.1. Polyacrylamide is insoluble in any organic solvent except some acids (acetic, lactic), some hydroxy compounds (ethylene glycol, glycerol), some nitrogen compounds (formamide) and molten urea, and dissolves in a wide range of concentrations in water.

The viscosity of aqueous solutions increases with increasing molecular weight and decreases with increasing temperature. Viscosity in aqueous solutions of nonionic polyacrylamide is relatively unaffected by the electrolyte, and the hydrogen ion concentration [73, 74]

Table 3.1. The physical properties of polyacrylamide [72].

Appearance	White powder
Ionic character	Anionic
Charge density	Medium
Molecular weight (kg/kmol)	High (18E6-23E6)
Dissolution time in DI water @ 5 g/l @ 25°C (minutes)	60
Storage temperature (°C)	0-35
Shelf life (months)	24

PAAM has a high solubility in water, however, it dissolves very slowly. While preparing the solution, PAAM should be added to the water, not vice versa. In cold water, dissolving PAAM is more difficult than in warm water. To dissolve PAAM in cold water, more time and agitation will be required.

During this research, it was found that the preparation of the PAAM solution is highly challenging. Even though PAAM is highly soluble in water, our trials showed that the usual mixing procedures do not work for the PAAM solution. Also, the information given in the literature about the preparation procedure is very limited. Below, one can find the procedure developed based on our observations and experience.

- (i) Distilled water is warmed until (32°C). If the temperature is too low, the dissolution rate is affected where the high temperature can cause deterioration in the polymer's structure.
- (ii) A mechanical mixer with blade marine impeller (Figure 3.2a) is chosen for proper shear. A different type of impeller with low shear can result in poor mixing, where an impeller with high shear can damage the polymer molecules.
- (iii) A vortex (Figure 3.2b) is created in the middle of the distilled water using the impeller at 1500 rpm speed.
- (iv) PAAM that is in powder form is slowly added in the middle of the created vortex. This step requires extra care as adding the polymer fast can cause the powder to

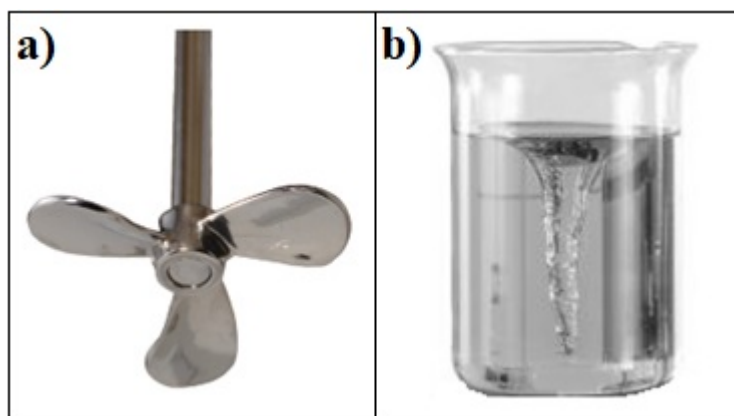


Figure 3.2. The blade marine impeller used for the preparation of the PAAM solutions (a) and the vortex created using the impeller (b).

swell and cohere to produce a mass. Once this mass is formed, the water will not be able to penetrate inside of it, and there will be lumps of polymer inside the solution.

- (v) When all of the powder is added into the vortex, the speed of the mix is reduced.
- (vi) The solution is mixed for only 60 minutes.
- (vii) The solution is transfer into a container with high surface area, and left there for 24 hours to remove the bubbles trapped inside the solution.
- (viii) The solution is stored at room temperature in a closed container, and kept away from the direct sunlight.
- (ix) Overall, it is possible to say that the rate of PAAM dissolution has a strong relationship with the amount used, the stirring speed, and the temperature.

### 3.1.2. Hydroxypropylcellulose (HPC)

Hydroxypropyl cellulose (HPC) is a derivation of cellulose that is highly soluble in water and organic compounds. Its molecular formula is given in Figure 3.3. HPC used in this work was purchased from Sigma Aldrich (CAS Number: 9004-64-2).

HPC is a liquid crystalline liquid that is in the cholesteric phase and highly bire-

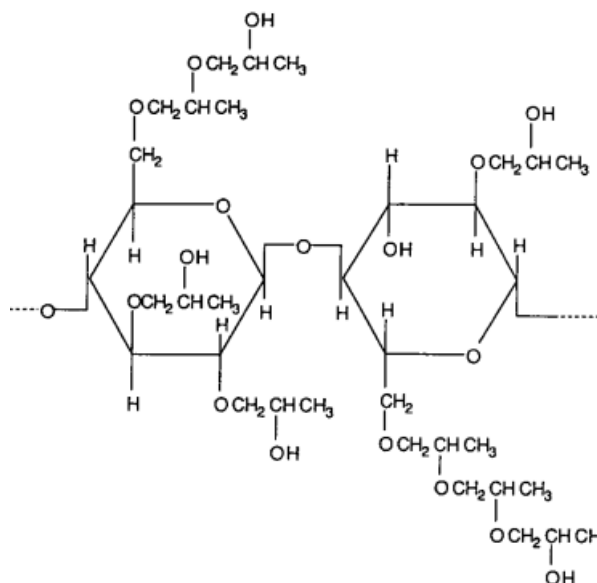


Figure 3.3. The molecular structure of HPC.

fringent. In this work, HPC is added to the PAAM solution to make the solution birefringent. HPC solution is a shear-thinning fluid, showing viscoelastic behavior. Anisotropic solutions are strongly viscoelastic. The relationship between the birefringence and the flow shows that the flow birefringence increases with HPC concentration, with a significant increase as the liquid-crystalline phase is formed [75].

### 3.1.3. Glycerol

Glycerol is a highly viscous, hygroscopic substance that contains three hydroxyl groups in its structure, dissolving completely in water. It is a biochemical compound in terms of origin. The molecular formula of glycerol is  $C_3H_8O_3$  and its IUPAC name is propane-1,2,3-triol where the molecular structure is given in Figure 3.4 [76]. In this study, glycerol is purchased from Isolab and is 85 % by weight. The calculation of the physical properties of 85 wt % of glycerol is based on the study of Cheng (2008) [77], and these values are tabulated in Table 3.2.

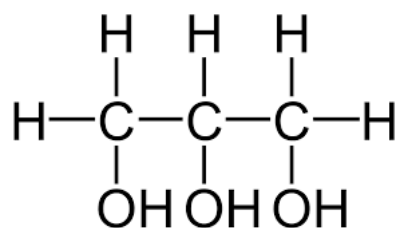


Figure 3.4. The molecular structure of glycerol.

Table 3.2. The physical properties of glycerol.

Appearance	Clear
Form	Liquid
Molecular weight (g/mol)	92.09
Fraction of glycerol by mass	0.85
Density (kg/m <sup>3</sup> )	1218.4
Dynamic viscosity (Pa.s)	0.08 5

#### 3.1.4. Sodium dodecyl sulfate (SDS)

Sodium dodecyl sulfate (SDS) is an organic compound with surfactant properties. SDS, an organic salt, is classified in the group of organosulfate compounds. The molecular formula of SDS is  $C_{12}H_{26}O_4SNa$  and its structure is given in Figure 3.5. It was purchased from Isolab and has CAS number of 151-21-3.

SDS is an anionic surfactant with a polar head sulfate group and apolar tail consisting of a 12 carbon alkyl chain. This tail gives the necessary amphiphilic properties.

Surfactants are adsorbed at the interfaces as a result of these structural units. Surfactant adsorption generally alters the surface or interfacial properties of the system. SDS molecule carries a negative charge in its active part; therefore it is called anionic.

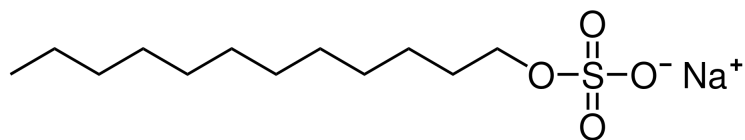


Figure 3.5. The molecular structure of SDS.

### 3.2. Rheological Characterization

In this study, the rheological measurements were carried out using Anton-Paar MCR302 rotational rheometer at the Life Sciences laboratory of Bogazici University (Figure 3.6) and MCR92 at Anton Paar, Turkey. RheoCompass software of Anton Paar is employed during the measurements.

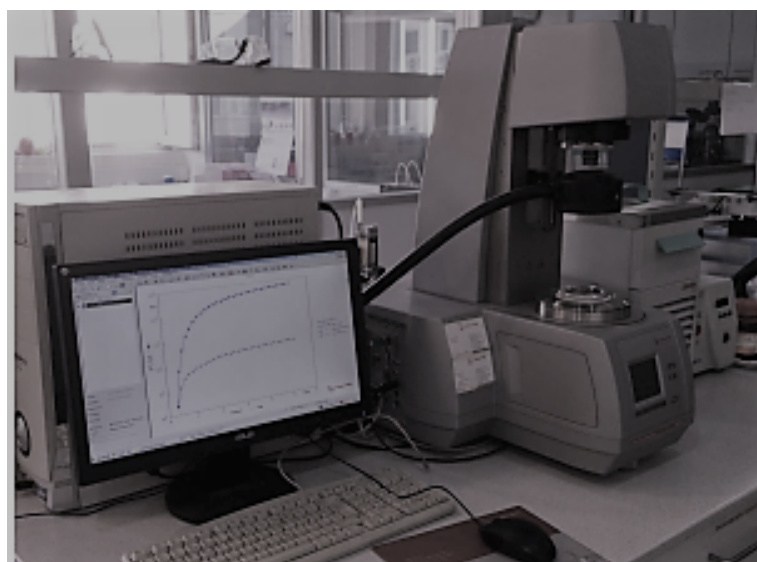


Figure 3.6. The MCR302 Anton Paar reometer at the Life Sciences Laboratory at Boğaziçi University.

Cone-plate probes (Measuring Cone CP25-2 and CP50-2) are used where the distance between the cone and the plate was 0.103 mm, and the diameter was 25 mm (CP25-2) and 50 mm (CP50-2). In Figure 3.7, the schematic representation of the cone and plate rheometer is demonstrated. In this figure,  $r_c$  is the cone radius

where  $\theta$  and  $dc$  are the angle and the distance between cone and plate, respectively. In the measurements, the lower plate is fixed, and the upper cone can rotate at fixed or variable frequency values with a variable rotation number, fixed rotation number, or certain deflection angle amplitude for oscillating tests depending on the test type.

Table 3.3. The properties of the rheometer probes used for the rheological analysis.

Probe name	Probe type	Angle ( $^{\circ}$ )	Diameter (mm)
CP 25 - 2	Cone - plate	2	25
CP 50 - 2	Cone - plate	2	50

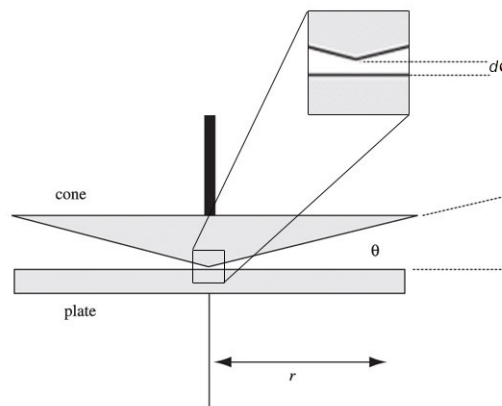


Figure 3.7. Schematic representation of the cone-plate rheometer.

During the measurements, it is ensured that the sample temperature is kept constant everywhere by using a heating top cap. In addition, the excess solution overflowing from the measurement environment is removed in order not to cause measurement errors. Before starting the measurement, the normal force value affecting the measuring element is expected to be as close as to zero.

### 3.2.1. Rheological Characterization Tests

3.2.1.1. Flow Curve test. During this test, the change in viscosity depending on the shear rate or shear stress was observed. Flow curves are usually tested over a narrow

band of shear rate. Accordingly, solutions have been analyzed at 25°C over a shear rate range of 1-100 s<sup>-1</sup>.

**3.2.1.2. Amplitude Sweep Analysis.** This test was performed to determine the viscoelastic properties of the solutions. The amplitude sweep analysis determined linear viscoelastic regions of the solutions, and the analyzes were carried out in this region. Graphs of G' (elastic) and G'' (viscous) values against strain (%) are drawn.

**3.2.1.3. Temperature Sweep Test.** To be able to observe the effect of the temperature on the viscosity of the solutions, the temperature sweep test was used. For the samples, the temperature sweep test was performed at 0.01% strain within the linear viscoelastic region determined in the amplitude sweep test, at a constant frequency of 1 Hz and increasing with a speed of 5°C/min in the range of 20°C - 50°C.

### **3.2.2. Rheology Results of 85 wt% Glycerol**

Glycerol is a Newtonian liquid and its rheology analysis for glycerol is given in the Figure 3.8. Although glycerol was purchased readily, no rheology analysis was available. Rheology analysis shows that shear stress and shear rate were directly proportional (Figure 3.8 - blue line). Although the viscosity of glycerol appears to increase with the shear rate, on careful inspection it can be seen that the change is in the order of 10E-3 (Figure 3.8 - orange line). Therefore, the viscosity of glycerol is determined to be constant with increasing shear rate, 0.085 Pa.s at 25°C as in [78].

### **3.2.3. Rheology Results of PAAM and PAAM+HPC Solutions**

In this study, since the isothermal experiments were performed at 25°C, all of the rheological analyzes of the solutions were also performed at 25°C. Unless otherwise stated, all of results presented below are valid only for 25°C.

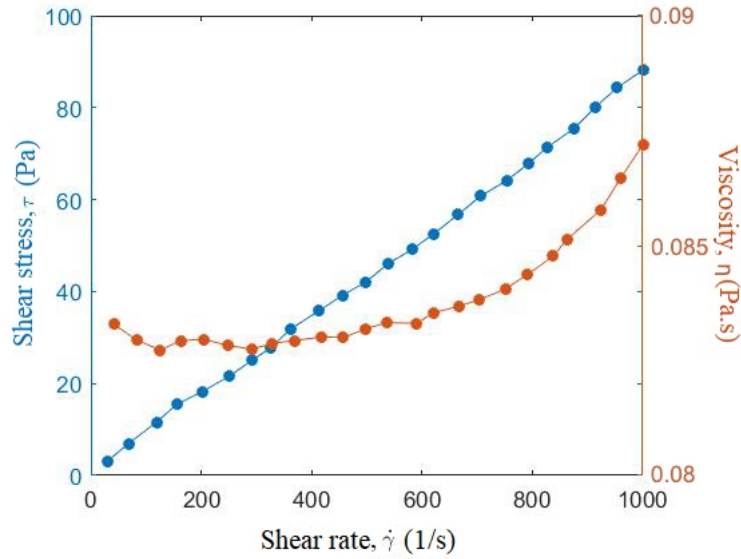


Figure 3.8. The flow curve of 85 wt% glycerol.

The rheological analysis of solutions containing only PAAM and PAAM+HPC are investigated. The concentrations used in the experiments that contained only PAAM were 0.10, 0.18, 0.25 and 0.40 wt%. The HPC concentration to be added in the birefringence experiments was tested with 3 different concentrations, i.e. 0.10, 0.20 and 0.40 wt% HPC. Birefringence was not observed enough in the trial experiments with 0.10 and 0.20 wt% HPC. For this reason, the HPC concentration was increased up to 0.40 wt%. From our previous experiments, it was known that the birefringence was observed well with 0.5 wt% concentration of HPC. However, it was known that the higher the HPC concentration is, the higher the entire solution's viscosity is. As the overall viscosity increases, it becomes more difficult to perform the experiment due to the small bubbles trapped in the solution. Therefore, it is decided to keep the HPC concentration constant at 0.4 wt% while changing the PAAM concentration as 0.10, 0.18 and 0.25 wt%

As stated in the first test, the flow curve test, the relationship between viscosity of the solutions was examined depending on the shear rate; also the relation between shear stress and shear rate was studied. For all of the solutions it was found that shear stress increases with increasing shear rate (Figure 3.9 and Figure 3.10) .

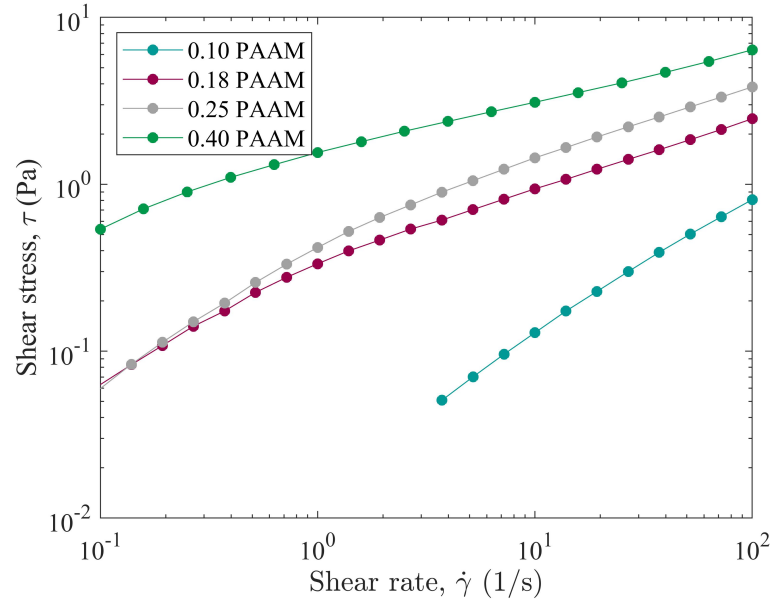


Figure 3.9. Shear stress,  $\tau$  vs. shear rate,  $\dot{\gamma}$  for different concentrations of PAAM solutions.

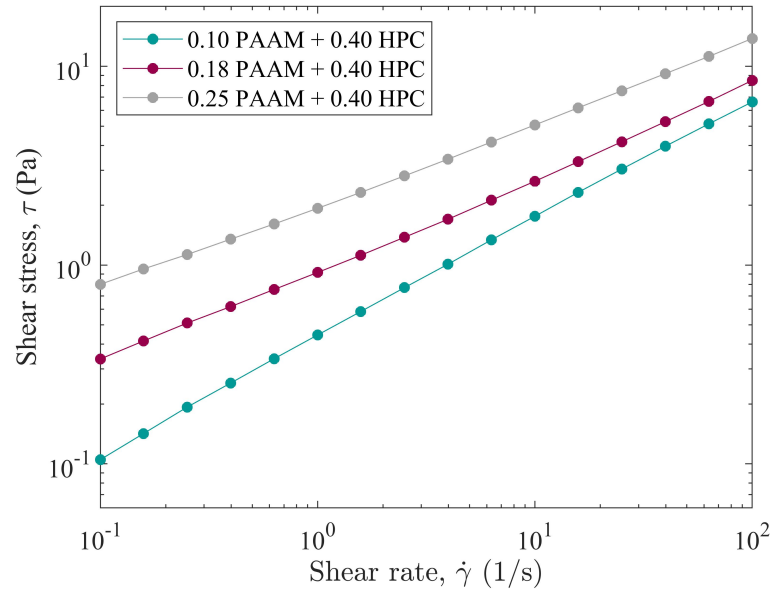


Figure 3.10. Shear stress,  $\tau$  vs. shear rate,  $\dot{\gamma}$  for different concentrations of PAAM + 0.40 wt% HPC solutions.

The solution with the highest concentration has the highest shear stress at a constant shear rate. Furthermore, the viscosity decreases with increasing shear rate (Figure 3.11 and Figure 3.12). At a constant shear rate, the solution with the highest concentration has the highest viscosity, i.e., 0.40 wt% PAAM in Figure 3.11 and 0.25 wt% PAAM + HPC in Figure 3.12.

The rheological analyses also shows that HPC had a significant effect on the viscosity. For example, the viscosity of 0.25 wt% PAAM solution is around 450 mPa.s at  $1 \text{ s}^{-1}$  shear where as it is around 2500 mPa.s for PAAM + HPC solution at the same shear rate. The flow curve test results show that all of the solutions are non-Newtonian and shear-thinning.

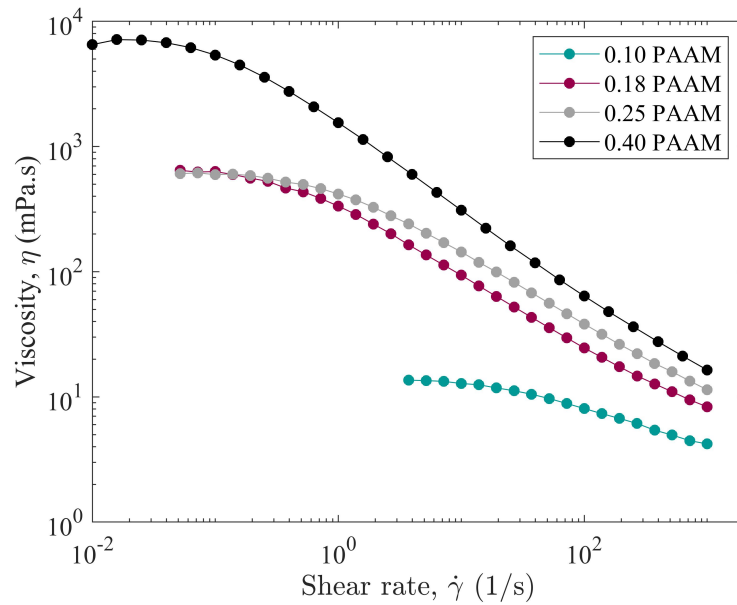


Figure 3.11. Viscosity,  $\eta$  vs. shear rate,  $\dot{\gamma}$  for different concentrations of % PAAM solutions.

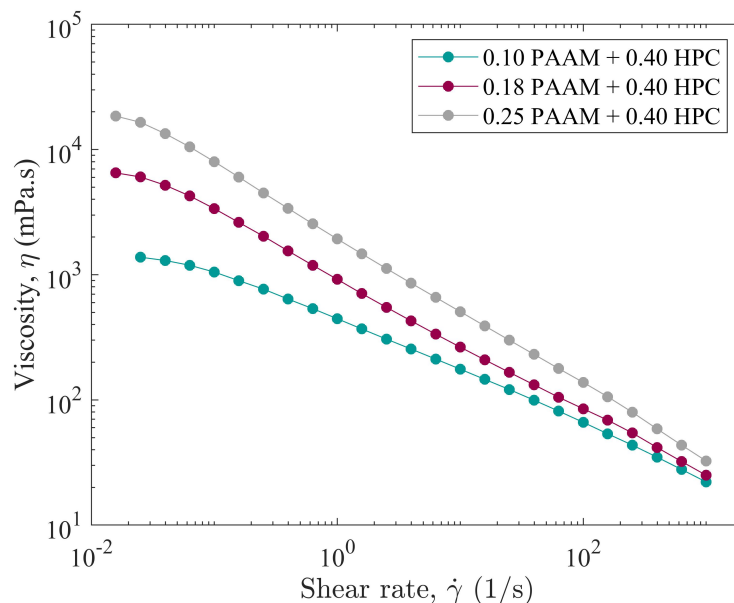


Figure 3.12. Viscosity,  $\eta$  vs. shear rate,  $\dot{\gamma}$  for different concentrations of PAAM + 0.40 wt% HPC solutions.

Amplitude sweep test was applied to the solutions to obtain information about their viscoelasticity. During an amplitude sweep test, the amplitude of the shear stress is changed while the frequency is kept constant. For the analysis, the storage modulus  $G'$  and the loss modulus  $G''$  are plotted against the shear strain (Figures 3.13) and 3.14). The ratio of the two moduli ( $G'$  and  $G''$ ) gives information about the characteristic of the sample. First, the linear viscoelastic (LVE) region is found for all solutions. The LVE region shows the test region where the tests can be done without destroying the structure of the solution. All of the solutions show a constant plateau regime in the LVE region. When this region is investigated, it is seen that the storage modulus,  $G'$  is larger than the loss modulus,  $G''$ . Therefore, it can be said that the solutions have gel-like structure. It is observed that there occurs a cross-over between storage and loss moduli. This transition shows where the solution starts behaving more like fluid than like gel. Again it is found that the addition of HPC into PAAM solution changes the structure of solution in terms of viscoelasticity.

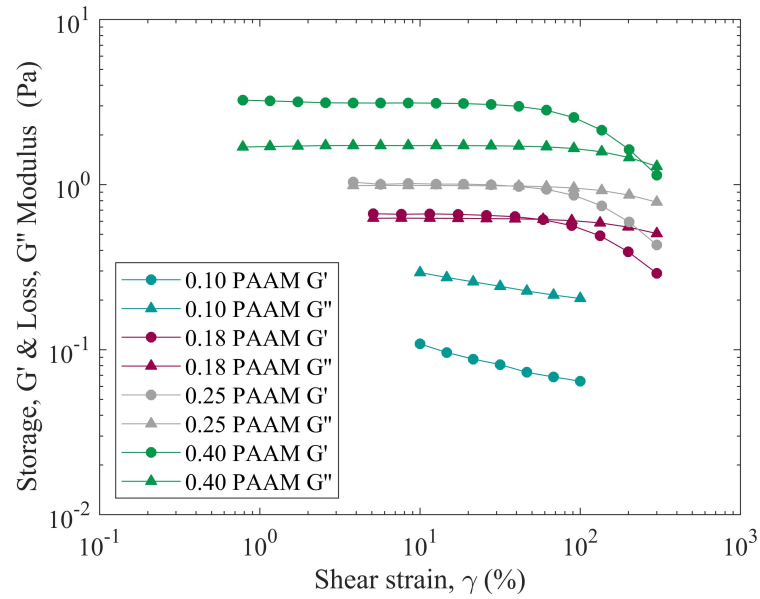


Figure 3.13. Storage,  $G'$  and loss,  $G''$  modulus vs. shear strain,  $\gamma$  for different concentrations of PAAM solutions.

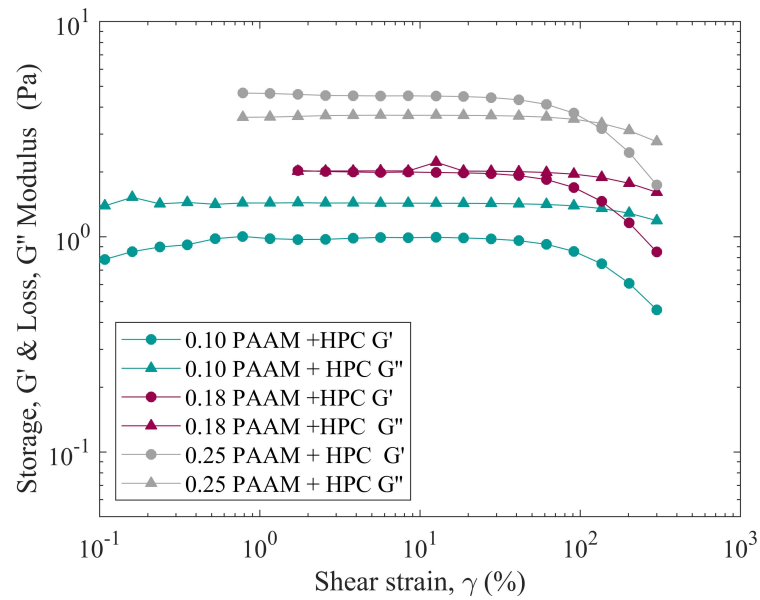


Figure 3.14. Storage,  $G'$  and loss,  $G''$  modulus vs. shear strain,  $\gamma$  for different concentrations of PAAM + 0.40 wt% HPC solutions.

The temperature-dependent variation of the apparent viscosity values was determined by applying the temperature sweep test. This test was carried out at a shear rate of  $50 \text{ s}^{-1}$  as it is calculated as the average shear rate for our experiments. Temperature sweep test was carried out by providing a  $5^\circ\text{C}$  temperature increase per minute from  $20^\circ\text{C}$  to  $50^\circ\text{C}$ . The results show that the viscosity decreases as the temperature increases (Figure 3.15). It can be said that the average viscosity drop is around 25% for the solutions.

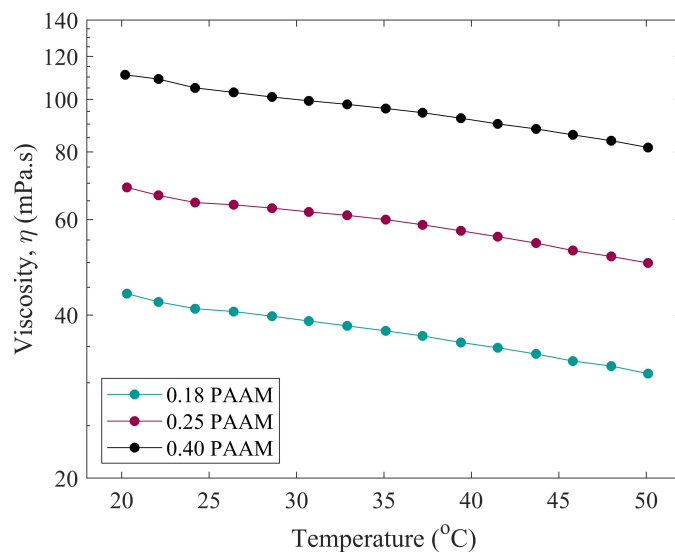


Figure 3.15. The effect of the temperature on the viscosity for different concentrations of PAAM solutions.

Finally, two different rheological models are applied, i.e. the power-law and the Carreau-Yasuda models, and tabulated in Table 3.4 and 3.5, respectively. Viscosity index,  $n$ , of the power-law equation given in Eq. 2.2 indicates how easily a fluid will deform under shear stress. In the Carreau-Yasuda model (Eq. 2.4),  $\eta_\infty$  is the value taken by viscosity as the shear strain rate goes to infinity.  $\lambda$  is called relaxation time and is the inverse of the value of the shear strain at which the viscosity begins to decrease.  $\eta_0$  is the zero viscosity value and is the value of viscosity when the shear strain rate is close to zero.  $\lambda$  and  $a$  are the relaxation time and Yasuda exponent, respectively. These rheology parameters are used in the calculation of the dimensionless numbers.

Table 3.4. The rheological parameters for power-law model.

<b>Solutions</b>	<b>n</b>	<b>K</b> (Pa.s)	<b>R<sup>2</sup></b>
0.10 wt% PAAM	0.73	0.03	0.99
0.18 wt% PAAM	0.46	0.31	0.99
0.25 wt% PAAM	0.44	0.51	0.99
0.40 wt% PAAM	0.34	1.45	0.99
0.10 wt% PAAM + 0.4 wt% HPC	0.57	0.46	0.99
0.18 wt% PAAM + 0.4 wt% HPC	0.48	0.93	0.99
0.25 wt% PAAM + 0.4 wt% HPC	0.41	1.97	0.99

Table 3.5. The rheological parameters for Carreau-Yasuda model.

<b>Solutions</b>	<b><math>\eta_0</math></b> (mPa.s)	<b><math>\eta_\infty</math></b> (mPa.s)	<b><math>\lambda</math></b> (s)	<b>n</b>	<b>a</b>	<b>R<sup>2</sup></b>
0.10 wt% PAAM	14	2.0	0.1	0.52	1.1	0.99
0.18 wt% PAAM	679	3.3	2.4	0.36	1.2	0.99
0.25 wt% PAAM	834	3.7	3.0	0.39	1.1	0.99
0.40 wt% PAAM	7105	5.0	8.4	0.29	1.5	0.99
0.10 wt% PAAM + 0.4 wt% HPC	2552	0.1	34.3	0.55	0.5	0.99
0.18 wt% PAAM + 0.4 wt% HPC	6595	4.4	36.8	0.46	2.8	0.99
0.25 wt% PAAM + 0.4 wt% HPC	18829	0.1	45.2	0.41	4.9	0.99

## 4. Experimental Setups and Methods

The liquid column is made of glass. The glass plates (0.50 cm thickness) are glued together with the aquarium silicone (Sista). Later, a transparent liquid rubber (Leak Fix Spray Rubber Transparent) is applied to the glued areas. At least four layers of spray liquid rubber application are required. The places that will not be covered are carefully masked with paper tape. After one hour of application, the liquid rubber is hardened, and the liquid column becomes leakproof. The liquid rubber can withstand temperatures between  $-40\text{ }^{\circ}\text{C}$  and  $+90\text{ }^{\circ}\text{C}$ . This temperature range is much wider than the temperatures employed in non-isothermal experiments. The liquid column dimensions are 12 cm x 12 cm x 50 cm (Figure 4.1a).

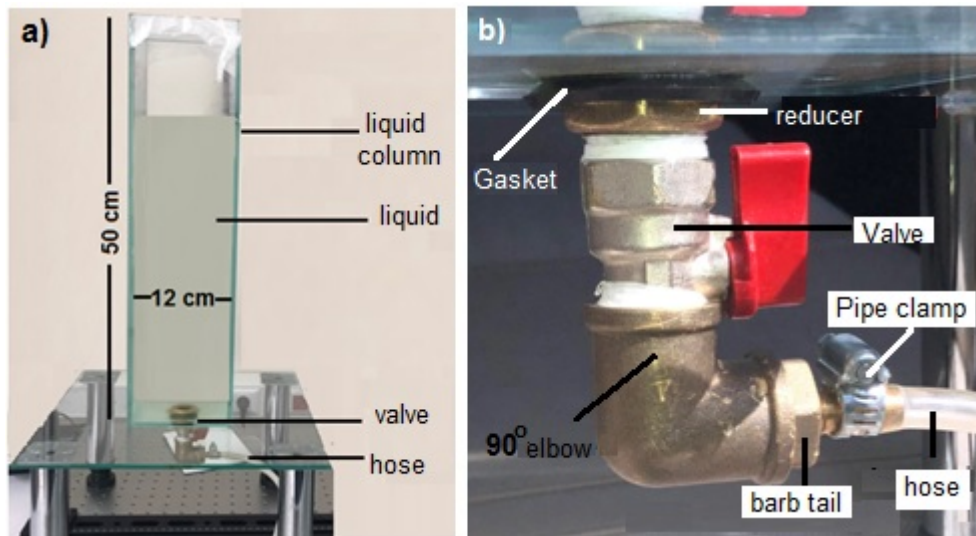


Figure 4.1. The view of liquid column (a) and the plumbing system (b).

Under the liquid column, there are a plumbing system (Kale Armatür) and hose (Evcı Plastik) (Figure 4.1b) and a syringe with a volume of 60 ml (SET Plastic Syringe) connected to this hose. At the beginning of the experiment, the syringe is filled with air. During the experiment, a bubble is obtained by manually pushing air from the syringe. Although this method is not fully controlled, bubble size with a wide range of volumes can be obtained. A syringe, directly connected to the liquid column is used

in another liquid column to obtain bubbles with smaller sizes. With the needle (21G) coming out of this syringe, bubbles are sent into the liquid directly.

#### 4.1. Experimental Setup for the Birefringence Experiments

This section deals with the optical setup to analyze the bubble dynamics, i.e., the shape, the speed and also the birefringence experimental setup.

##### 4.1.1. Optical Experimental Setup

The experimental setup is shown in Figure 4.2. In order to ensure a stable and easy optical alignment, two interlocking rails (Thorlabs – XT66SD-750) are mounted on the optical table (B6090AX), and the optical materials are mounted on these rails. In order to align the laser (CNI Lasers – MLL-III-637-100mW) light on the rail, kinematic frames numbered 4 and 5, with mirrors inside (Thorlabs – PF10-03-P01 inside KM100), are used as "Z-Fold" configuration as shown in Figure 4.3.

First of all, the target (Thorlabs – LMR1AP) is placed on the rail with the help of the optical post (Thorlabs – TR300-M), the post holder (Thorlabs – PH150-M), the rail carrier (Thorlabs – XT66P2-M) and the lens mount (LMR1) at the height level where the birefringence around the bubbles will be measured. After fixing it at 35 cm height from the optical table, the target is slid on the rail and brought to the closest position to the laser. Here, by manipulating the two knobs of the kinematic frame numbered 4, it is ensured that the laser coincided with the target. Later, the target is shifted to the farthest position from the laser on the rail, and this time, the laser is brought to the target with the help of the knobs of the kinematic frame numbered 5. The target is brought close to the laser again, and this process continues until the laser does not deviate from the target when the target is at either end of the rail. Thus, the alignment of the laser beam on the optical table and the rails is achieved.



Figure 4.2. Optical setup. (1) Optical table, (2) Optical rail system, (3) Laser, (4-5) Kinematic frames and mirrors, (6) Plano-concave lens, (7) Plano-convex lens, (9) Liquid column, (8-10) Polarizers, (11) Camera, (12) Illuminator.

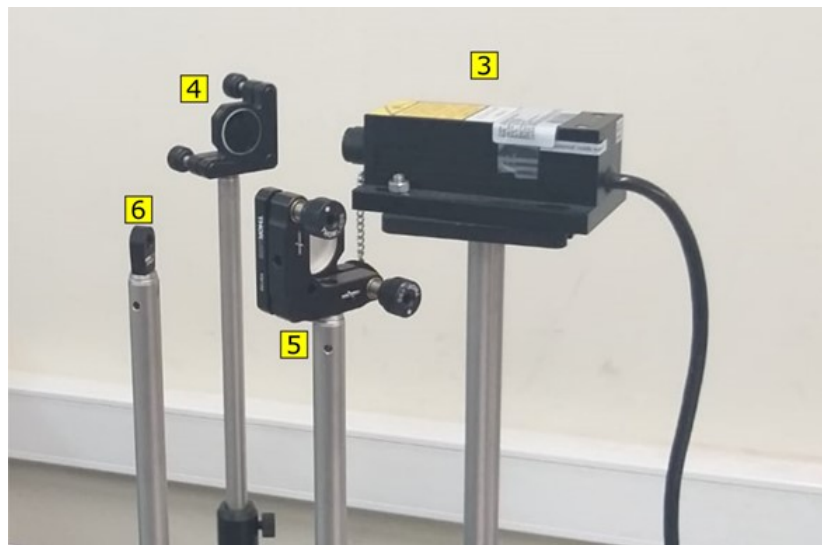


Figure 4.3. The Z-Fold configuration for the alignment of the laser light.

Two optical lenses and their frames (Thorlabs – LMR2 -M and LMR6-M) are used to bring the laser beam to the appropriate size. One of these lenses is plano-concave (Thorlabs – LC1975-A), and the other one is plano-convex (Thorlaabs – LA1380-A). In order to check the alignment of the optical lenses with the laser beam that is previously aligned with the rail system, the lenses are placed on the rail starting from the farthest end of the laser. Therefore, first of all, the plano-convex lens, number 7, is placed on the rail with the flat side of the lens facing the laser, and it is checked whether the reflected laser light was symmetrical, smooth, and in line with the incoming laser light. If these conditions are not met, the alignment of the lens is completed by changing the angle and the height of the lens. The same procedure is applied to the plano-concave, number 6 lens that is positioned closer to the laser on the rail. However, the flat side of this lens is positioned so that it faces the plano-convex lens, number 7, instead of facing the direction of the laser beam. In this way, the laser beam is aligned according to the column criteria and in a collimated manner.

Finally, polarizers (polarizer and analyzer with 2 in diameter, Thorlabs – LPVISE 200-A) are installed in high precision rotating frames (Thorlabs – PRM2-M) with polarization directions perpendicular to each other. The liquid column is placed on the rail system in between the polarizers after the lenses as shown in Figure 4.2. In order to perform birefringence analysis, the camera (Nikon D7200) is placed at the end of the optical assembly using a tripod stabilizer, after the polarizer number 10.

#### 4.1.2. Adjusting the Light Distribution

The transverse mode of the laser used in the experiments is Near  $TEM_{00}$ , and its M2 value is 1.135. Although lasers with this mode are more affordable than the lasers in the  $TEM_{00}$  mode, the shapes of the beam spots are more distorted and far from Gaussian. Their shape is elliptical rather than circular since one axis has more openings than the other. This one-way opening causes the shape of the beam spot in that direction and the edges of the lenses inside the laser to be cropped due to the diffraction effect. The sample image of a laser from the literature [79] and the image

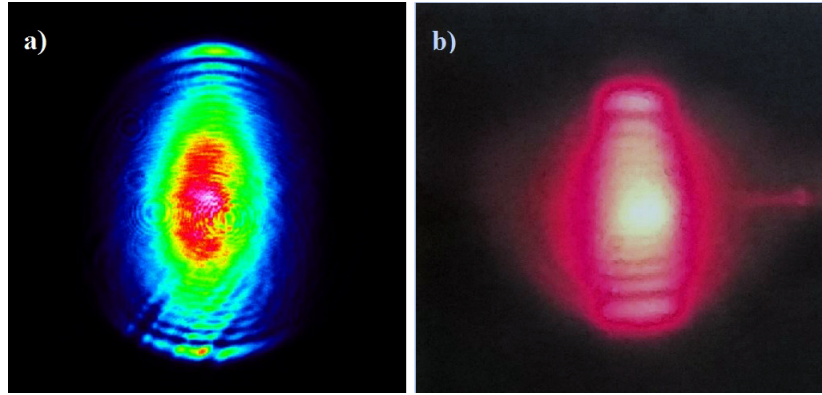


Figure 4.4. Near $\text{TEM}_{00}$  Beam from the literature [79] and this study.

of the laser used in the experiments with  $\text{TEM}_{00}$  mode are given in Figure 4.4.

This clipping in the shape of the laser beam spot is a factor that adversely affects the birefringence experiments. Magnifying the laser beam and using the medium-intensive part of the beam to get rid of this clipping is one of the methods. This problem has been solved in this study by magnifying the laser beam since magnification is also necessary for birefringence experiments. A small number of defects in the middle region were also eliminated by the laser beam being homogenized as it passes through the solution and matching the location of bubbles with the middle part of the beam for the birefringence analysis.

#### 4.1.3. The Procedure for the Birefringence Experiments

The Nikon D7200 camera is used in high resolution (1920x1080) to record the birefringence experiments. Videos are captured at 60 fps. Since the polarizer is perpendicular to the analyzer at the beginning of the experiment and no bubble passes through the liquid at that time, no optical axis difference occurs in the liquid. Therefore, the laser beam passing through the polarizer cannot pass through the analyzer (Figure 4.2) since it is parallel to the polarizer and perpendicular to the analyzer; thus, a dark image like in Figure 4.5a is obtained at the beginning of the experiment. When the bubble rises in the column and reaches the measurement area, a difference

in the optical axis occurs due to the angle change between the liquid molecules. In this way, the laser beam passing through the polarizer changes its direction while passing through the liquid, and since every component of the laser beam is no longer perpendicular to the analyzer, it succeeds in passing through the analyzer. As a result, a light formation is observed around the bubble (Figure 4.5b).

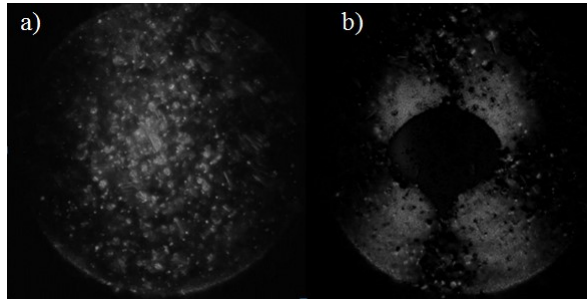


Figure 4.5. The dark image (a) obtained at the beginning of the birefringence experiment and the birefringence image as the bubble passes(b).

As it is mentioned before, the polarizer and the analyzer are perpendicular to each other throughout the entire experiment. The birefringence experiments are performed twice. However, in the second experiment, both the polarizer and the analyzer were shifted by an angle of  $45^\circ$ .

The image series obtained from a birefringence experiment can be seen in Figure 4.6. The experiment shown in Figure 4.6 was overexposed for the visual quality. Due to the overexposure, a completely dark image has not been obtained in this series of experimental images as mentioned for Figure 4.5a. A relatively darker view is obtained in Figure 4.6a. Then, in Figure 4.6b-p, the laser beam that has managed to pass through the polarizer can be seen as a result of the bubble motion.

## 4.2. Experimental Setup for the Bubble Dynamics

A high-speed camera (Optronis CamRecord CR600x2) is used in the experiments for volume-velocity analysis of the bubbles. The camera resolution is 1280 x 1024

pixels and can record a maximum of 500 fps. This camera is positioned perpendicular to the laser beam, facing the illuminator and the liquid column. The drawing of the idiomatic mechanism of bubble dynamics experiments is given in Figure 4.7. For simplicity, the optical part is not shown in detail. Single color LED continuous light (Mcoplus LE520A) is preferred for the illumination.

The light intensity of the illuminator and homogeneous the reflection of this light onto the liquid in the column are essential in terms of the boundaries of the bubbles along the column. For this reason, the light skate is covered with a diffuser. Because the light is perpendicular to the camera, the bubble boundaries become more pronounced. Bubbles with clear boundaries could be separated and analyzed easily by the volume-velocity analysis algorithm.

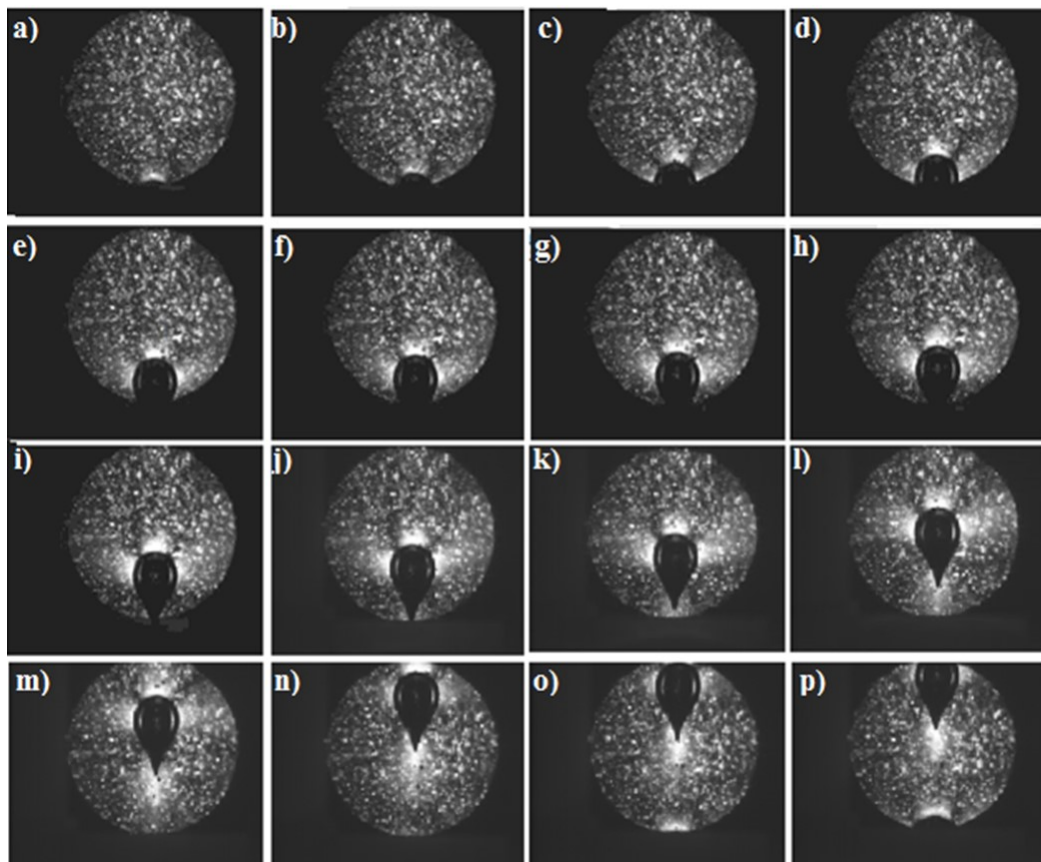


Figure 4.6. The image series obtained from a birefringence experiment.

The camera is controlled from a computer using TimeBench 2.6.30 software. The camera is operated via a trigger. In the experiments, image ROI trigger sensitivity setting is employed where the camera starts recording as the brightness of the specified area changes. Therefore, an area in the frame where the bubble will pass is chosen, and the camera triggers when the brightness changes in this area by 90%. Thanks to the multi-segment feature of the camera, a separate video is shot for each bubble, and finally, they are turned into a single video by the software. Thus, high-speed processes such as bubble movement can be recorded, and less memory is used by not recording the moments when the bubble does not pass.

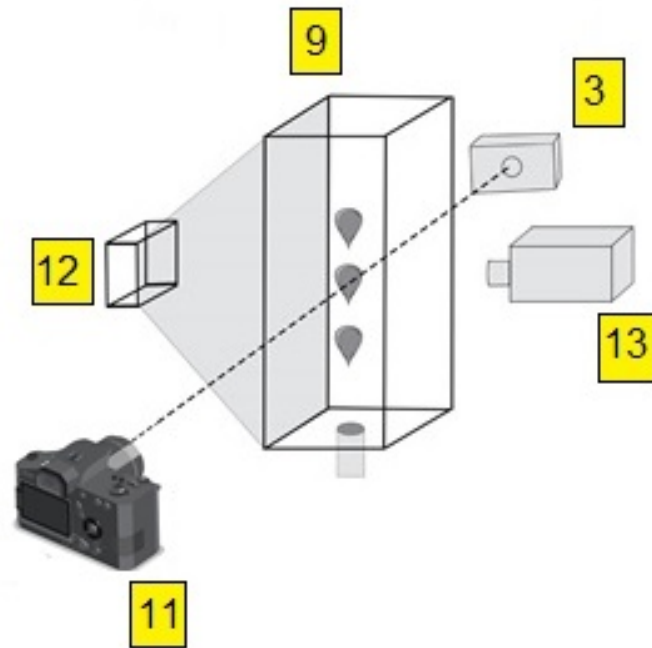


Figure 4.7. The sketch of the bubble dynamics experimental setup. (3) laser, (9) liquid column, (11) birefringence camera, (12) light source, (13) high-speed camera.

### 4.3. Experimental Setup for the Schlieren Method

The Schlieren imaging technique captures density gradients that are usually invisible in a transparent medium such as air, water, and glass. While Schlieren imaging is often used for laboratory-based in-depth studies, the technique known as shadowg-

raphy is more commonly used in field studies. When a light ray hits an environment, variations in the density gradient change the direction of the light to make it visible. There are different types of Schlieren method, such as v-, y- or z- type systems, based on the system's layout. In this study, the v-type system is used, and the system drawing is shown in Figure 4.8.

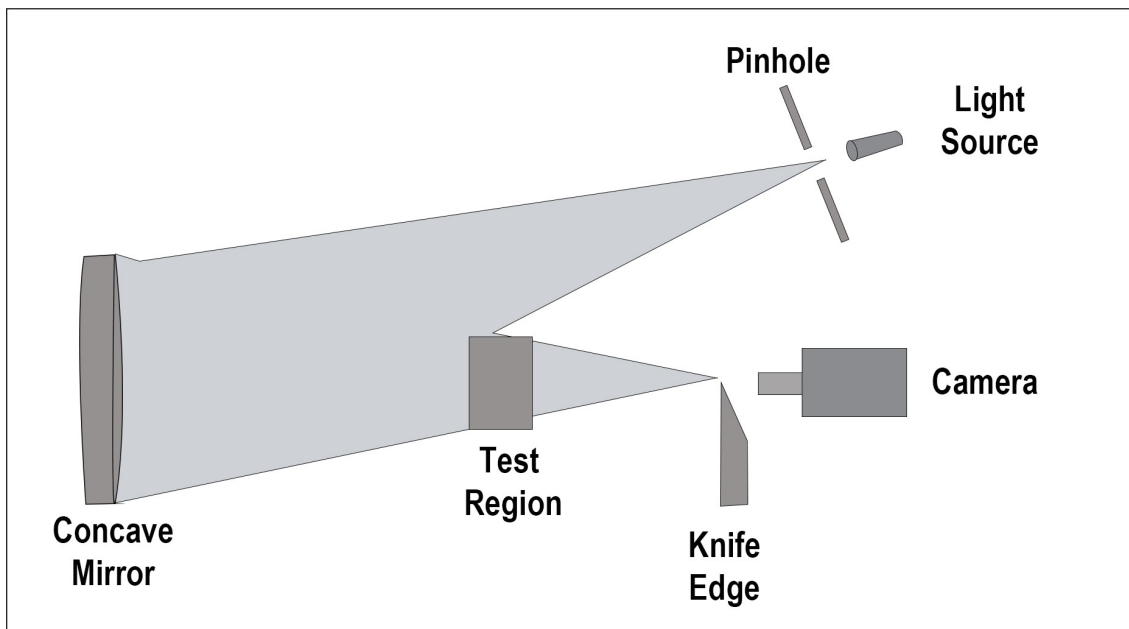


Figure 4.8. The scheme of the v-type Schlieren method.

The v-type Schlieren device employs a point light source to generate a beam of light. However, instead of the optical lenses used in other types, the v-type device employs a concave mirror to focus the light back to a single point. At that point, the razor edge cuts off the light that comes directly while allowing the refracted light to pass around the razor captured by an imaging device [80]. The light source and the razor edge are placed at twice the focal length of the concave mirror, resulting in the incoming light being reflected to the razor.

The image obtained from a demonstration of the Schlieren experiment is given in Figure 4.9. In this figure, there is a single plume of a lighter. In v-type Schlieren setups, the double imaging situation can cause problems if the focal length of the concave



Figure 4.9. The double view of Schlieren image of the single lighter plume.

mirror is short, which causes the beam light to be refracted twice. A beamsplitter cube is used to remove the double image formation. Even though, this modification worked, it caused other problems. Therefore, the double view problem is kept and it was only overcome by adjusting the distance of the camera from the mirror, increasing the double images from each other and cutting the view into two during the video analysis.

#### 4.4. Experimental Setup for Non-Isothermal Experiments

For the nonisothermal experiments, a different liquid column was designed. This column's one wall is made of aluminum and attached to a water bath where the temperature is always kept constant at  $25^{\circ}\text{C}$ . A heating plate is placed next to the opposite wall. The scheme of the designed liquid column can be seen in Figure 4.10. The temperature is monitored at different spots (shown as red dots in Figure 4.10) using thermocouples. The bubble dynamics are investigated as explained in Section 4.2.

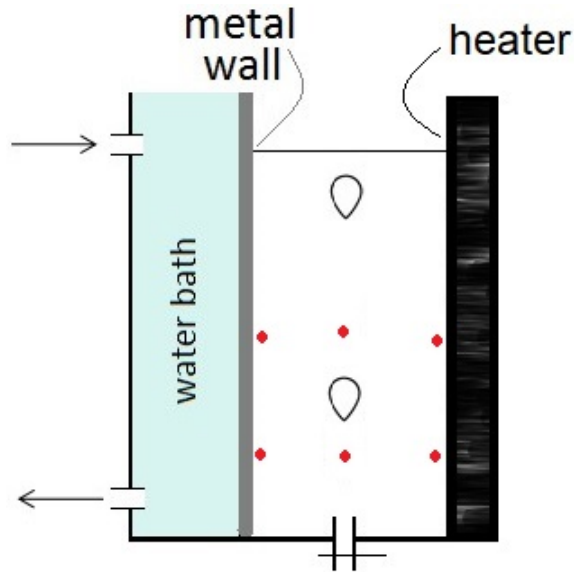


Figure 4.10. The scheme of the liquid column designed for the non-isothermal experiments.

#### 4.5. Surface Tension Measurement

Du Nuoy ring, a very common method, is used to measure the surface tension of the solutions with and without surfactants. A platinum-iridium ring is submerged in a liquid and then the liquid is drained from the beaker. The force required for the ring to pull up the meniscus of the liquid is proportional to the surface tension [81–83]. The experimental setup used for the Du Nouy method is given in Figure 4.11.

First, the ring is immersed into the solution (Figure 4.12-2), where the torsion dynamometer is set to 0. Then, the solution is drained from the bottom of the beaker. As the solution is drained, the lever arm of the torsion dynamometer is readjusted to balance the white line that is shown on the dynamometer. The value read on the torsion dynamometer is recorded when the Du Nouy ring is separated from the solution's surface (Figure 4.12-4). This value is the force,  $F$  that acts along the edge of the length,  $l$ , which is parallel to the surface to keep the film [84, 85].

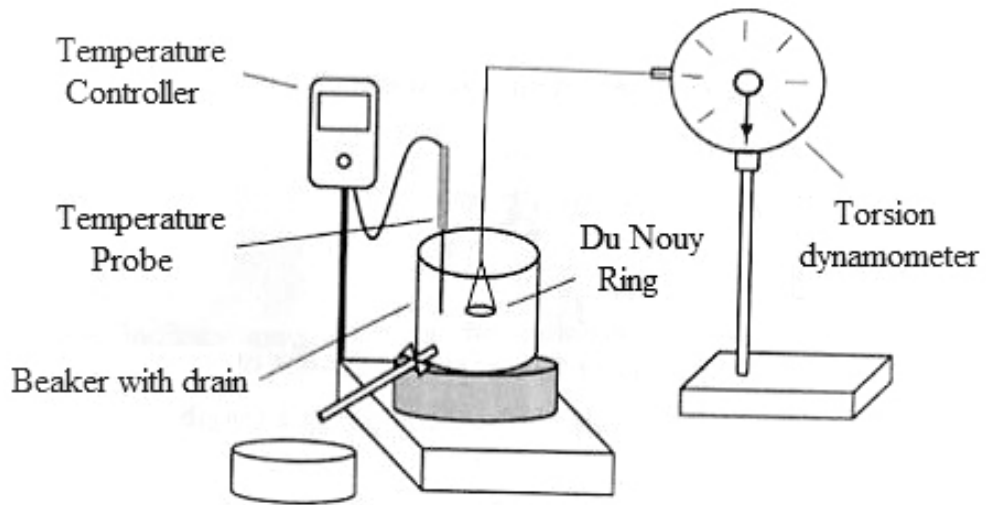


Figure 4.11. The sketch of the Du Nouy ring method experimental setup [85].

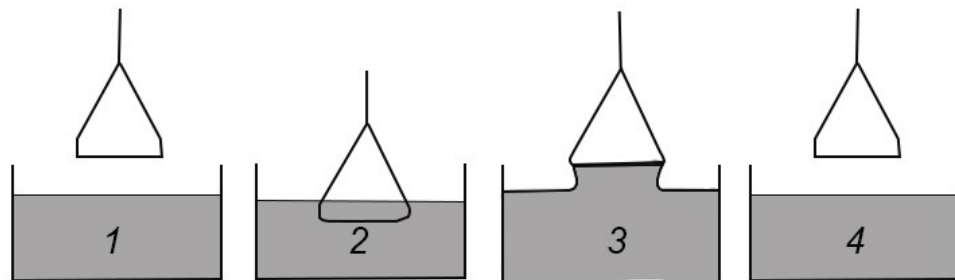


Figure 4.12. The process of Du Nouy ring method.

The surface tension,  $\gamma$  can be calculated as

$$\gamma = \frac{F}{\ell}, \quad (4.1)$$

where  $\ell$  is the length of edge and given as

$$\ell = 2 * 2 * \pi * r_r. \quad (4.2)$$

Here, the diameter of the ring,  $r_r$  used in the experiment is 19.65 mm.

It turns out that the surface tension of the 0.25 wt% PAAM solution is 74 mN/m, which is close to the value of water, 72 mN/m at 24°C [86]. The results also show that the surface tension decreases with increasing surfactant, SDS concentration. The surface tension of the solutions are given in Table 4.1.

Table 4.1. The results of the Du Nouy Ring's method at 25 °C.

<b>Solution Type</b>	<b>Surface Tension (mN/m)</b>
0.25 wt% PAAM	74.0
0.25 wt% PAAM + 10 ppm SDS	66.8
0.25 wt% PAAM % 100 ppm SDS	45.2

## 5. EXPERIMENTALLY MEASURED PARAMETERS

In this section, the measured parameters are explained in detail before presenting the results. The section includes two sub-sections for bubble dynamics and birefringence measurements.

### 5.1. Measured Parameters for the Bubble Dynamics

Here, first the bubble diameter and volume calculations are shown. Then, the bubble shape parameters are explained. Finally, the dimensionless numbers required to study and understand the bubble dynamics are presented.

#### 5.1.1. Bubble Equivalent Diameter, Volume and Velocity

5.1.1.1. Bubble Equivalent Diameter, d. In the equivalent diameter method, the recorded image of the bubble is analyzed with the edge detection algorithm that will be mentioned in Section 6.2.1. The volume ( $V$ ) of the bubble is obtained, then a diameter calculation is made for this area.

Equivalent diameter ( $d$ ) is the diameter value of this bubble if it was spherical and calculated as follows,

$$d = \sqrt[3]{\frac{6V}{\pi}}. \quad (5.1)$$

5.1.1.2. Bubble Volume,  $V$ . At first, the rotating solid method was applied to calculate the bubble volume. However, this method was time consuming and not sensitive as it was required. Therefore, the truncated cone method is adopted. The shape of the bubble is considered to be axisymmetric with respect to the major axis of the bubble profile. The bubble is divided into multiple groups of small truncated cones as shown

in Figure 5.1. The volume of each ( $i^{\text{th}}$ ) cone is calculated by the formula given below,

$$V_i = \frac{\Pi h}{3} (R^2 + r^2 + Rr) \quad (5.2)$$

where  $R$  and  $r$  are the radius of the lower and upper sections, respectively; and  $h$  is the height of the cone. These three variables can be derived directly from bubble profiles [87]. Finally, the total volume of the bubble is the sum of all the smaller cones (Figure 5.1).

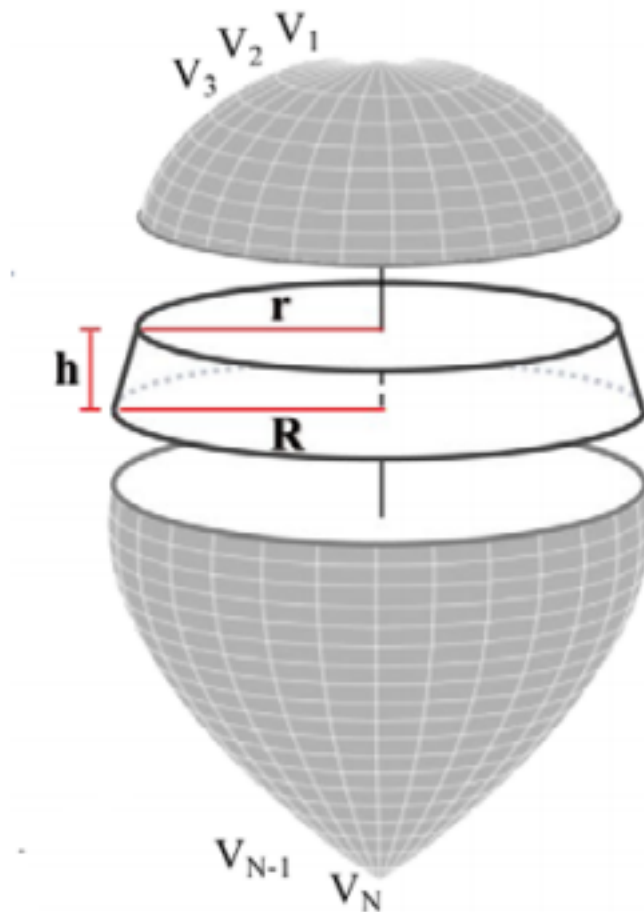


Figure 5.1. The bubble profile used to determine the volume with the truncated cone method (reprinted with permission from [37]).

5.1.1.3. Bubble Velocity,  $u$ . The change in the position of the bubble is used to calculate the bubble velocity,  $u_b$ . First, the coordinates of the center of mass are determined

for each video frame, and the difference in the center of mass coordinates,  $x_i$  between the two consecutive frames of the bubble, is recorded and divided by the time difference between the frames,  $\Delta t$ . Thus, the average bubble velocity can be obtained through the liquid column as

$$u_b = \frac{x_i - x_{i-1}}{\Delta t}. \quad (5.3)$$

The terminal bubble velocity,  $u_B$  is calculated as the average value of the velocity values,  $u_b$  above the distance where the bubble velocity seemed to reach a steady value. It was made sure that the change in the bubble velocity is less than 5% and at least 26 frames are used to calculate the average terminal bubble velocity,  $u_B$ .

### 5.1.2. Bubble Shape Parameters

5.1.2.1. The Ratio of a/b. It is the ratio of the minor axis,  $a$  to the distance,  $b$  from the center of gravity to the tip of the bubble's tail (Figure 5.2a). The principal axis is the end points of the longest line that can be drawn through the bubble. The major axis length of a bubble is the pixel distance between the major axis endpoints, which is the distance between the bubble's apex and the tip of the bubble's tail. The minor axis is the end points of the longest line that can be drawn on the bubble while remaining perpendicular to the main axis. The minor axis length of an object is the pixel distance between minor axis endpoints.

5.1.2.2. Extent. It is the ratio of the area of the bubble ( $S_5$ ) to the area of the bounding box of the bubble ( $S_1+S_2+S_3+S_4+S_5$ ) (Figure 5.2b). The bounding box of a bubble is a rectangle surrounding the bubble. The dimensions of the bounding box are the dimensions of the major and minor axes.

$$\text{Extent} = \frac{S_5}{S_1+S_2+S_3+S_4+S_5} \quad (5.4)$$

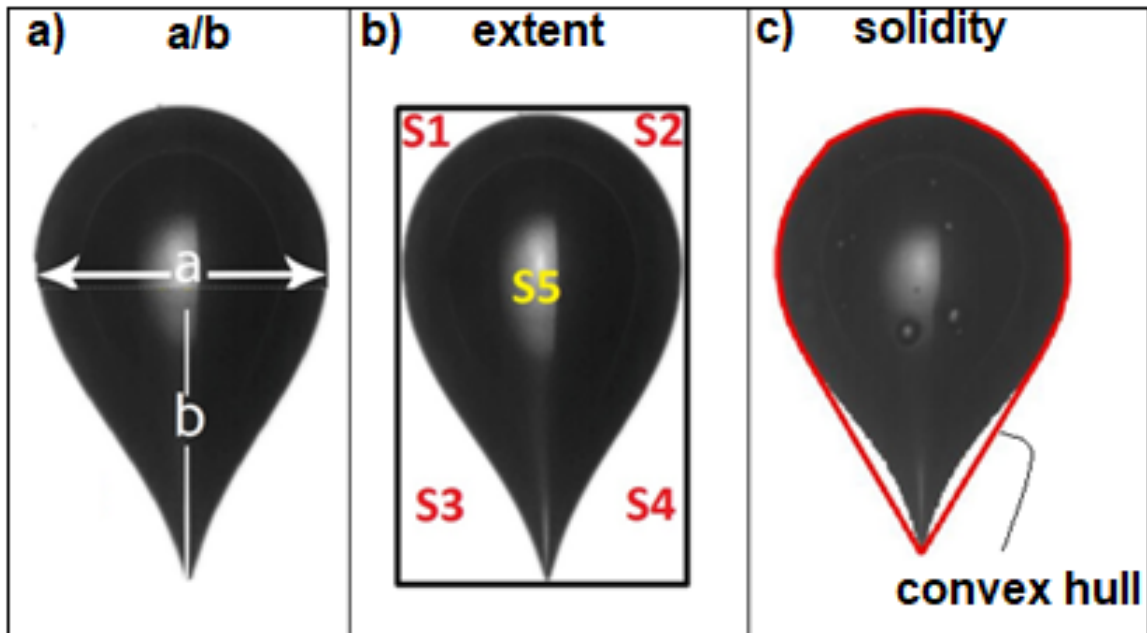


Figure 5.2. The bubble shape parameter: the  $a/b$  ratio a), extent b) and solidity c).

**5.1.2.3. Solidity.** This parameter defines whether a shape is convex or concave (Figure 5.2c). It can be found by dividing the area inside the bubble into the area surrounded by a convex body (convex hull). The convex body (convex hull) can be thought of as a rubber band stretched around the bubble seen as red line in Figure 5.2c. The solidity of a completely convex shape is 1. The more the solidity deviates from 1, the greater the degree of concavity in the structure is (Figure 5.2c).

**5.1.2.4. Circularity.** It mathematically shows the degree of resemblance to a perfect circle. A value of 1 means a perfect circle. As the roundness value deviates from 1, the shape becomes less circular.

The circularity parameter is calculated as

$$\text{Circularity} = 4\pi \frac{\text{Bubble area}}{\text{Bubble perimeter}^2}. \quad (5.5)$$

5.1.2.5. Eccentricity - 1,  $E1$ . It is the ratio of the length of a bubble's short (minor) axis to the length of its long (major) axis.

5.1.2.6. Eccentricity - 2,  $E2$ . It is defined as the ratio of equivalent diameter to the short (minor) axis.

### 5.1.3. Dimensionless Numbers

Dimensional numbers show how the system behaves and allow comparisons between different systems. The dimensionless numbers used in this study are as follows:

- (i) Reynolds number,  $Re$ : It is the ratio of the inertial forces to the viscous forces. Chhabra (1988) [7] and Lali *et al.* (1989) [88] defined the average shear rate over an entire particle as

$$\dot{\gamma} = \frac{u_B}{d} \quad (5.6)$$

where  $\dot{\gamma}$  is the shear rate,  $u_B$  the terminal velocity, and  $d$  is the equivalent diameter given in Eq. 5.1.

The apparent viscosity,  $\eta$  for power-law fluids is defined as

$$\eta = K \left( \frac{u_B}{d} \right)^{n-1}. \quad (5.7)$$

Here,  $n$  is the flow behaviour index (dimensionless) and  $K$  is flow consistency index ( $\text{Pa}\cdot\text{s}^n$ ). Finally,  $Re$  for a power-law fluid becomes,

$$Re = \frac{\rho u_B^{(2-n)} d^n}{K}. \quad (5.8)$$

- (ii) Bond number,  $Bo$ : It is a dimensionless group used for the analysis of the behavior of bubbles and drops [3]. In the literature, it is sometimes referred to as the

Eötvös number.  $Bo$  represents the ratio of the force of gravity to the force of surface tension and is shown as

$$Bo = \frac{\rho d^2 g}{\sigma} \quad (5.9)$$

where  $\sigma$  is the surface tension of the liquid and  $g$  the gravitational acceleration [3].

(iii) Capillary number,  $Ca$ : It is a number that relates the viscous forces in the system to the surface tension forces and is given as [3]

$$Ca = \frac{\eta u_B}{\sigma}. \quad (5.10)$$

(iv) Weber number,  $We$ : It is the ratio of inertial forces to surface tension forces and given as

$$We = \frac{\rho u_B^2}{\sigma}. \quad (5.11)$$

(v) Drag coefficient,  $C_D$ : It is used to measure the friction or resistance of a bubble or droplet rising in a liquid medium. There are several ways to calculate  $C_D$ . It can be calculated experimentally for a rising bubble as

$$C_D = \frac{4}{3} \frac{dg}{u_B^2} \left( \frac{\rho_\ell - \rho_g}{\rho_\ell} \right). \quad (5.12)$$

According to Hadamard-Rybczynski' law [89, 90] for  $Re < 1$  [18], the drag coefficient for deformable bubbles is

$$C_{D,2} = \frac{16}{Re}. \quad (5.13)$$

Using Hadamard-Rybczynski' law, Margaritis *et al.* (1999) empirically obtained  $C_D$  for shear-thinning fluids for  $Re < 60$  as [32, 91]

$$C_{D,3} = \frac{16}{Re} (1 + 0.173 Re^{0.657}) + \frac{0.413}{1 + 16300 Re^{-1.09}}. \quad (5.14)$$

## 5.2. Measured Parameters for the Birefringence

The polarization of the light is given in Figure 5.3. The stress-optical law is used in the retardance,  $\delta$  (phase delay) and the stretching angle,  $\chi$  calculations. The equations used for the analyzes are given below. The calculated retardance,  $\delta$  will be a depth average value for the bubble volume.

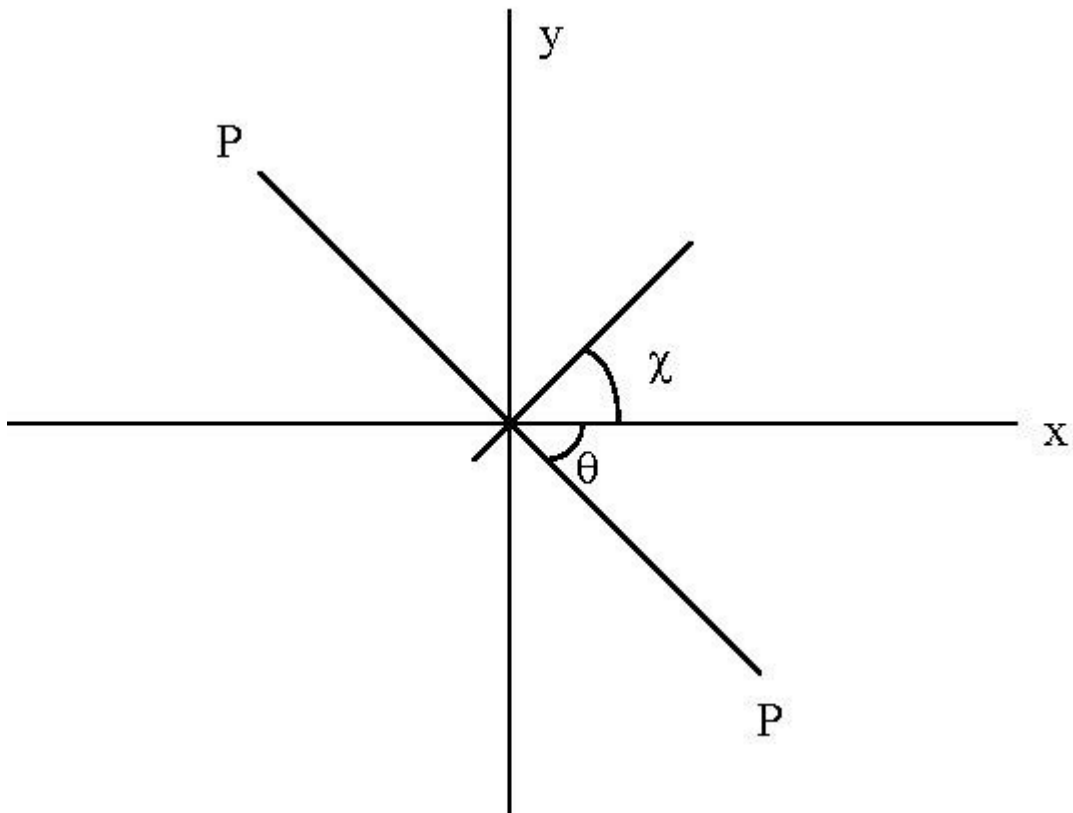


Figure 5.3. The polarization of light as it passes through a birefringent medium.

The intensity of light passing and transmitted through a birefringent medium is denoted by  $I(\theta)$  and is shown as follows, using the stress-optic law as

$$I(\theta) = I_0 \sin^2([\chi + \delta]) \left(\frac{\delta}{2}\right). \quad (5.15)$$

Here  $I_0$  indicates the intensity of the incident light beam and its calculation is shown in Section 6.1.  $I_0$  is constant throughout the experiment for a given solution concen-

tration.  $I_0$  needs to be studied and adjusted for each concentration value.

The experiments are repeated at two different angles. In the first case, the polarizer and the analyzer are perpendicular to each other. In the second case, the polarizer and the analyzer are again perpendicular to each other; however both are rotated  $45^\circ$  in the same direction compared to the first case.

When both of the experiments are performed, the bubbles with the same volume from each experiment are matched with each other where the intensity of the first case is called  $I(\theta)$  and the second one is called  $I(\theta + 45)$ .

The retardance,  $\delta$  can be calculated as

$$I(\theta) + I(\theta + 45) = I_0 \sin^2 \left( \frac{\delta}{2} \right). \quad (5.16)$$

If  $\theta = 0$  in Eq. 5.15, the equation becomes

$$\frac{I(\theta)}{I(\theta + 45)} = \tan^2(2\chi), \quad (5.17)$$

and  $\chi$  can be calculated from here.

The retardance,  $\delta$  is directly proportional to the birefringence,  $\Delta n$  as it is given in Eq. 5.18 where  $h$  and  $\lambda_i$  indicate the optical path and the wavelength of the incident light, respectively.

In this study, the optical path is the distance that light travels through the polymer solution; i.e. the column width of 12 cm.  $\lambda_i$  indicates the wavelength of the incident light, and its value for the laser used in the experimental setup is 637 nm.

The birefringence can be calculated from the following correlation as

$$\delta = \frac{2\pi h}{\lambda_i} \Delta n. \quad (5.18)$$

## 6. IMAGE PROCESSING AND ANALYZING TECHNIQUES

### 6.1. Intensity Calibration

When the birefringence experiments were performed, it has been noticed that the pixel values obtained from the birefringence photographs recorded with the camera did not reflect the actual light intensity coming to the camera sensor; and it would be wrong to use these pixel values directly in the optical stress law. Therefore, there is a need for the calibration of the intensity.

The reason for the mismatch between the intensity and the pixel value is that while converting the lossless raw data format, recorded by the camera, to non-lossless formats such as the *jpeg* extension, the camera uses *RGB* values and calculates according to a formula predetermined by the company for the camera, i.e., Nikon in this study [92]. For this reason, the actual light intensity - average pixel value calibration was performed separately for the exposure times of the camera that are used in the experiments.

For this purpose, the intensity of the laser light coming to the camera was measured with a light intensity sensor (Thorlabs/PDA55) that is placed right in front of the camera, and then the laser light was photographed with the camera. Then, using ND filters (Thorlabs/NDC-50C-4M) which are known to reduce the light intensity with a specified ratio, an average of about twenty-five photographs of the laser light, which can vary in number according to the exposure setting, were taken. As an example, sample photos with decreasing light intensity taken at 1/200 sec exposure time are shown in Figure 6.1. The photographs were processed in MATLAB, and the average pixel value was examined by selecting the same area in each frame where the laser light is visible and smooth. Thus, both the actual light intensity coming into the camera in each photo and the average pixel value of the image corresponding to that light

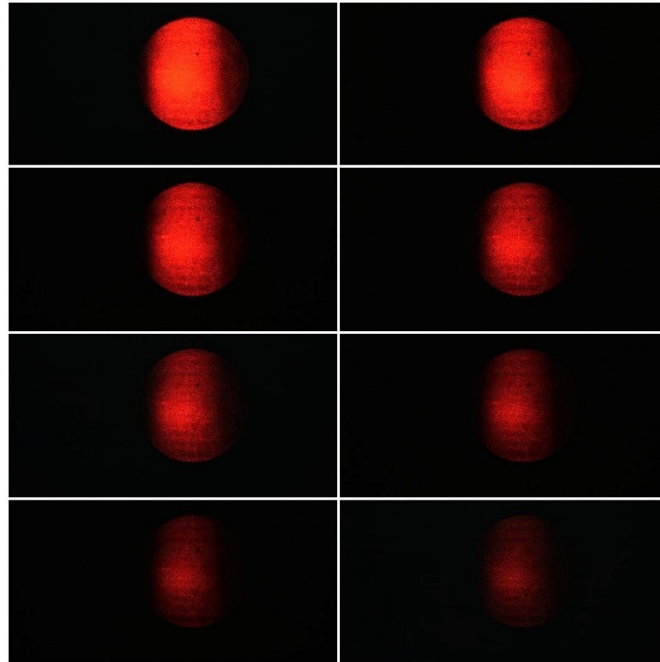


Figure 6.1. Sample calibration photos for the 1/200 sec exposure time where each frame represents the photo of the laser light taken with increasing filter.

intensity was obtained. A graph similar to that in Figure 6.2 is plotted for each of the exposure times measured using the collected data.

As seen in the literature, the relationship between the intensity versus pixel value is not linear, but a cubic polynomial [93]. For example, the response curve of selected digital cameras are shown in the literature [94]. For calibration, it is sufficient to obtain the response curve for each exposure time to be used in the birefringence experiments. After the experiment, in order to obtain the actual light intensity, this calibration curve is used. Since the density of the liquid in the column and the applied laser power may vary from experiment to experiment due to the concentration of the solution, the  $I_0$  light intensity in the formulas will also change. In order to use the correct  $I_0$  value, only the polarizer and the analyzer are removed before each experiment, and the image of the camera and the laser light are recorded. Then, the actual value of  $I_0$  is calculated using the response curve belonging to the exposure time at which this image is recorded.

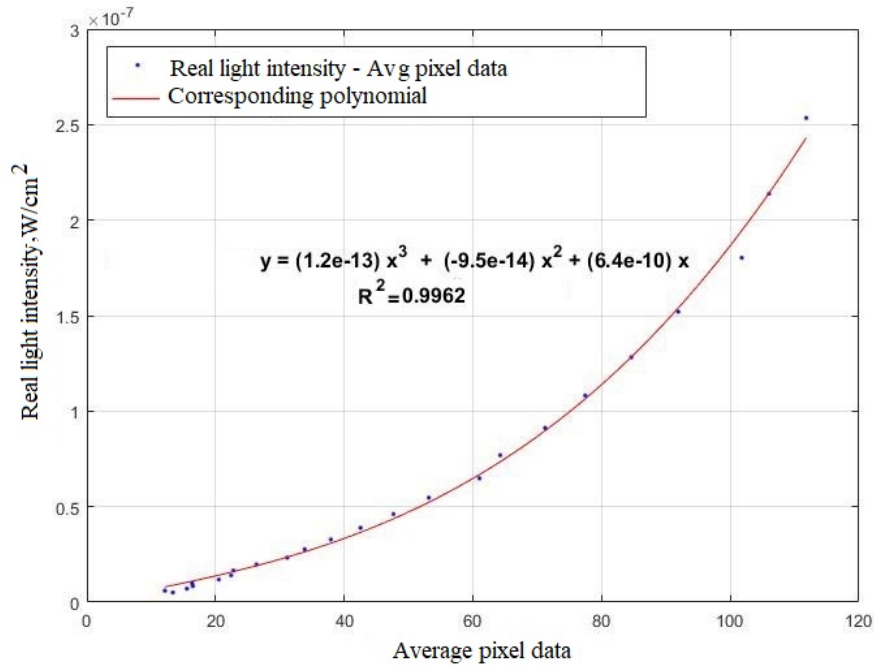


Figure 6.2. The calibration graph for the 1/200 sec exposure time.

A critical issue to be considered in terms of photographing the light intensity in the experiments is overexposure. In cases of overexposure, birefringent measurements will be inaccurate because the pixel values reach a maximum value of 255 (for 8-bit) when the camera exposure time or the laser power is high. Since the pixel values should decrease or increase according to the changing parameters of the bubble or the solution, the pixel values will not undergo any change in case of overexposure, and the analysis using these pixels will also be wrong. The presence of the overexposure is checked with the histogram feature in Image J of the photos recorded using large bubbles at the beginning of each experiment. The overexposure problem is solved by adjusting the power of the laser in case of overexposure. A sample photograph with overexposure (Figure 6.4a) and the histogram measurement of the chosen region (circled with blue on Figure 6.4b) where the birefringence is observed in this photograph are given. As can be seen from the histogram graph, there are about 1494 overexposed pixels.

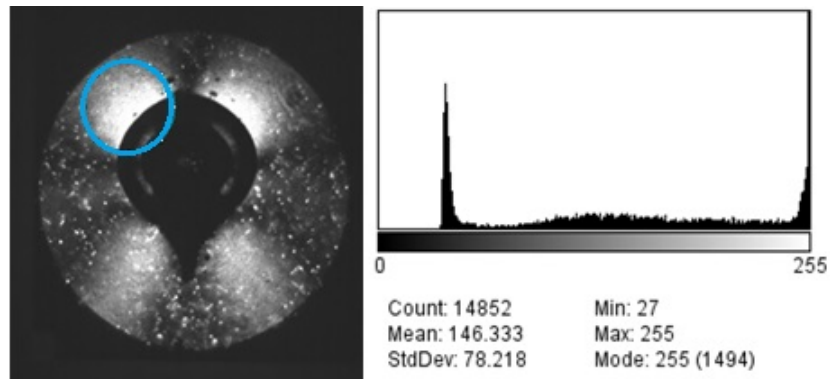


Figure 6.3. Sample photo with overexposure (a) and the histogram analysis of the circled area (b).

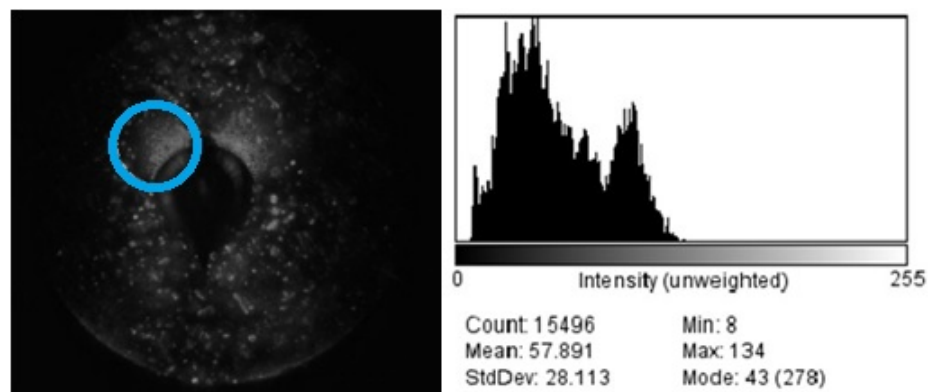


Figure 6.4. Sample photo when the overexposure is removed (a) and the histogram analysis of the circled area.

## 6.2. Image Analysis

### 6.2.1. Image Analysis for Bubble Dynamics

MATLAB library functions are used for the edge detection algorithm of the bubbles. The algorithm used for the edge detection and to measure bubble properties, i.e. volume, velocity and shape parameters, are as follows:

#### Calibration:

- Entering the fps (frame per second) information of the experiment video after running the code and using *imdistline* on the ruler image (taken for the calibration purposes at the beginning of each experiment by placing a ruler in the liquid column) in the first frame.
- Choosing the region of the bubble's movement path by cutting it with *imcrop*.
- Determining the position of the label (a label with a specific size is placed on the edge of the liquid column) to be able to remove possible vibrations by cutting with *imcrop* later in the algorithm.

#### Bubble creation:

- Running the *imbinarize* code whose *adaptive threshold* feature is selected to detect bubbles in each frame.
- Using the *imfill* function to fill in the middle of bubbles that is caused by the light shining on the bubble surface.
- Binary recovery of all bubbles in each frame.

#### Filtering:

- Using *bwareafilt* to get the bubble with the largest area in a frame.
- Using *bwareaopen* to filter the bubbles with an area below than a specified value to eliminate very small bubbles.

#### Calculation of bubble parameters:

- Obtaining bubble area with *bwarea* and calculation of the equivalent diameter.
- Determining the coordinates of the center of mass of the bubble with *regionprops*, numbering the bubble and finding other geometric properties.

- Removal of position and velocity shifts caused by possible vibrations from the parameters that is found using the label mentioned above.
- Finding bubble perimeter with *bwboundaries*.
- Finding the volume using the truncated cone volume method.
- Finding the shape parameter,  $\beta$  by adapting the parametric equation to the environment.
- Finding the convex body around the circumference with the *convhull*.
- Finding the major and minor axes and the angles of these axes with the *bwferet* function.

Finalizing:

- Matrix and vectorial recordings of all analysis results.
- Visual recording of the results with *writeVideo*.

### 6.2.2. Image Analysis for Birefringence Measurements

In order to perform birefringence analysis, the photograph of each bubble must first go through some processes. The captured video is divided into frames by a software (Free Video to JPG), and each frame of each bubble observed during the experiment is extracted as in Figure 6.5a. Besides, the initial frame of the video is extracted to be used as the background frame (Figure 6.5b). The background image is subtracted from the bubble image (Figure 6.5c). Finally, the image (Fig 6.5c) is converted to grayscale, i.e., 8 bits. ImageJ program was used for all of these processes.

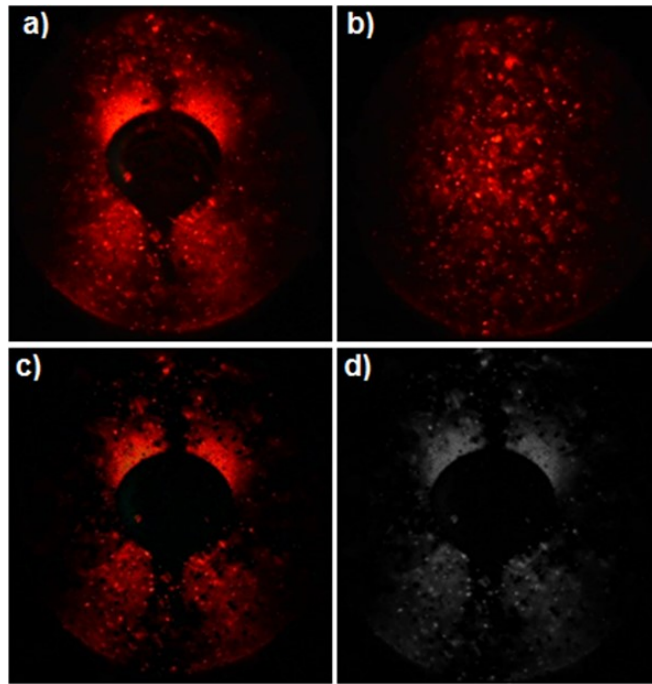


Figure 6.5. The image of a bubble obtained in the birefringence experiment (a), the background image (b), the image of the bubble where the background is removed(c) and the 8-bit grayscale version of this image (d).

The bubble images are analyzed using MATLAB. As mentioned in Section 5.2, the experiments are performed for a second time by rotating both the polarizer and the analyzer in the same direction for  $45^\circ$ . From each experiment, two intensity values are obtained. When the bubbles with the same volume are matched from both experiments i.e., the first intensity value is named as  $I(\theta)$  and the second intensity where the polarizer and analyzer are shifted by  $45^\circ$  is called  $I(\theta + 45)$ . As bubbles are assumed to be symmetrical, the measurements are performed only for the left side of the bubble. The retardance,  $\delta$  and the polymer stretching angle,  $\chi$  are calculated using the equations given in Section 5.2,  $I(\theta)$ ,  $I(\theta + 45)$  and  $I_0$  (explained in Section 6.1).

## 7. RESULTS AND DISCUSSION

### 7.1. Isothermal Experiments

#### 7.1.1. Control Experiments with Glycerol

Even though, this work is only interested in non-Newtonian solutions, the experiments are also performed with a Newtonian solution, i.e. glycerol. To test the experimental setup by comparing the results with the literature. The average terminal velocity of the bubbles are measured and drawn against the bubble equivalent diameter to study the dynamics of an air bubble rising in glycerol; and shown in Figure 7.1.

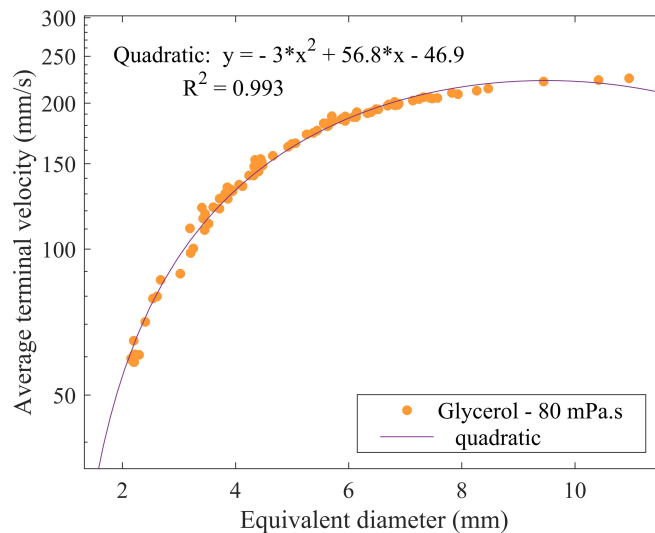


Figure 7.1. The average terminal velocity of a bubble rising in 85 wt% glycerol as a function of bubble equivalent diameter.

Iwata *et. al* (2019) [71] stated that the average terminal velocity and the bubble diameter are quadratically related for  $Re < 1$  which is the Stokes region. The  $Re$  for the data in Figure 7.1 is between 2 and 40. It was found that the average terminal velocity is quadratically proportional to the equivalent diameter for this study as well.

To compare our results with the literature [95,96], first the viscosity of glycerol is measured and reported in Section 3.2.2. The comparison is given in Figure 7.2. The results are close to each other and matching in terms of behaviour. Specifically, it can be seen that the results are closer to each other with increasing bubble equivalent diameter.

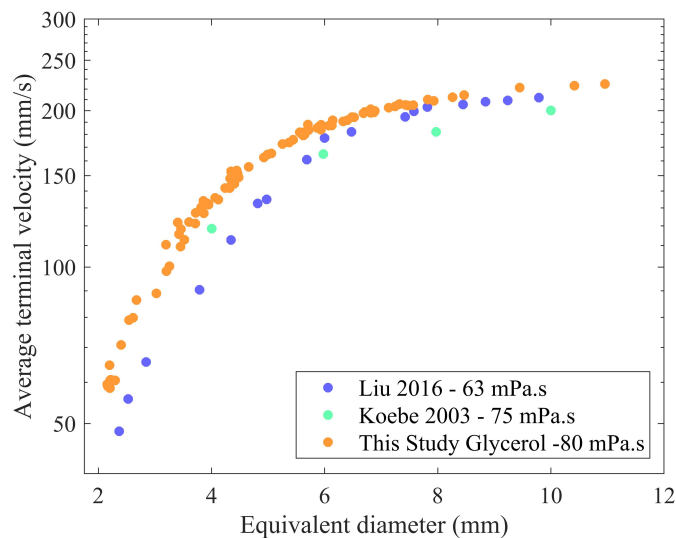


Figure 7.2. The average terminal velocity of a bubble rising in 85 vol% glycerol solution as a function of bubble equivalent diameter. Comparison with the literature [95,96].

### 7.1.2. Bubble Dynamics for Different PAAM concentrations

To study the effect of the concentration on the bubble dynamics, four different concentrations, i.e., 0.10, 0.18, 0.25 and 0.40 wt%, are employed. At this point, it is necessary to add that the legends of 0.10 wt% PAAM, 0.18 wt% PAAM, 0.25 wt% PAAM and 0.40 wt% PAAM are labeled as 0.10 PAAM, 0.18 PAAM, 0.25 PAAM, 0.40 PAAM, respectively to prevent the crowding in the graphs.

For 0.10 wt% PAAM solution, bubbles larger than  $100 \text{ mm}^3$  showed a 3D motion, which is captured as the volume is investigated as a function of time, i.e., the column length (Figure 7.3). Bubbles larger than  $100 \text{ mm}^3$  showed wobbling and hence these

bubbles are not considered in the steady-state results. Consequently, for the 0.10 wt% PAAM solution, the terminal velocity results (Figure 7.4) include bubble volumes up to  $100 \text{ mm}^3$ .

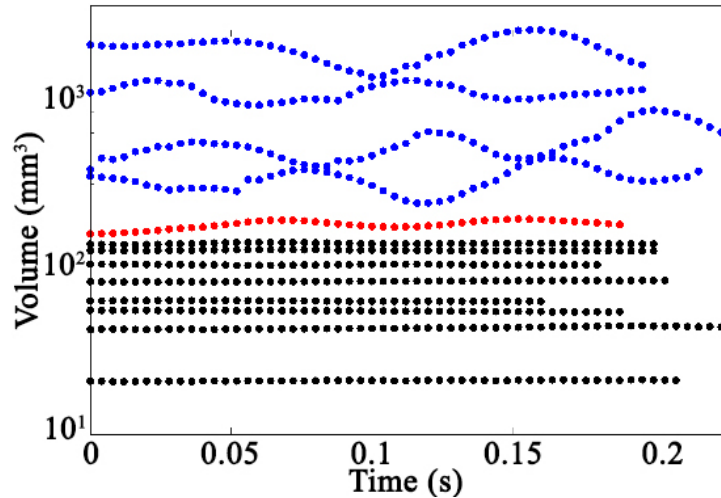


Figure 7.3. The bubble volume as a function of time for 0.10 wt% PAAM solution.

In Figure 7.4, the average bubble terminal velocity is drawn against the bubble volume for 0.10, 0.18, 0.25 and 0.40 wt% concentrations. It is observed that for a given polymer concentration, the bubble terminal velocity increases as the bubble volume increases. Until  $300 \text{ mm}^3$ , the polymer concentration has an effect on the average terminal velocity. The results show that, the average terminal velocity of a bubble increases and makes a plateau around  $250 \text{ mm/s}$  for all concentrations. Bubble terminal velocity reaching a plateau is an expected behaviour regardless of the polymer type or concentration and matches with the literature [30].

It is found that the terminal velocities for 0.18 and 0.25 wt% PAAM are very close to each other and they even coincide with each other for bubble volumes larger than  $20 \text{ mm}^3$ . This result is expected as the viscosity of both solutions are very close to each other for the shear rate of interest ( $50 \text{ s}^{-1}$  in order of magnitude, Figure 3.11), including the zero shear rate viscosity,  $\eta_0$ . The results also show that 0.10 wt% solution has the highest average bubble terminal velocity for the limited bubble volume range.

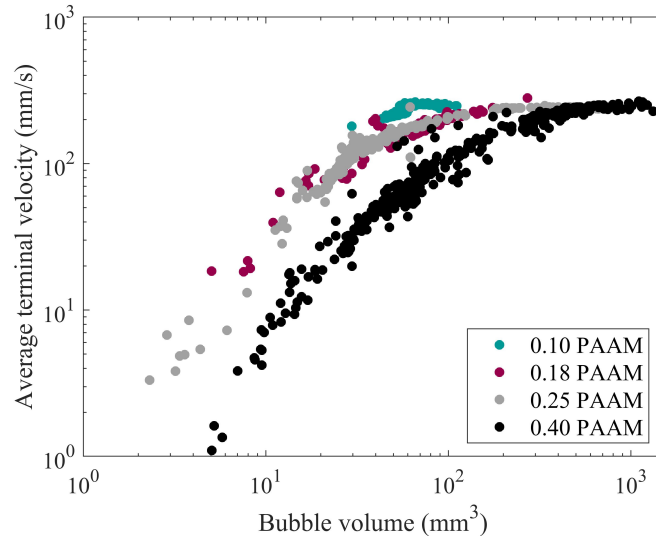


Figure 7.4. The average terminal velocity as a function of the bubble volume for different concentrations of PAAM solution.

Finally, no evidence is found regarding the discontinuity in the bubble terminal velocity. There is no consensus in the literature on the presence of discontinuity for the bubble terminal velocity at a critical volume (Table 7.1). The results clearly indicate that experiments performed with PAAM of certain brands, e.g. Floerger (also used in this dissertation), Sigma-Aldrich and Sinopharm, show no discontinuity. However, a discontinuity in the velocity is detected for Separan AP-30, Praestol and P2540 brands of PAAM. Therefore, one might say that the discontinuity is directly related with the manufacturing of the polymer.

Besides the velocity, we are also interested in bubble shapes. The parameters and their definitions are given in Section 5.1.2. The images, the bubble dynamics parameters and the dimensionless numbers of the bubbles are tabulated in Table 7.2 for 0.25 wt% PAAM solution and Table 7.3 for 0.40 wt% PAAM solution. In these tables,  $V$ ,  $d$ ,  $u_B$ ,  $a$ ,  $b$ ,  $C$ ,  $Ext$ ,  $Sol$ ,  $E-1$ ,  $E-1$ ,  $E-2$  are volume ( $\text{mm}^3$ ), equivalent diameter (mm), the minor axis (mm), the distance from center of gravity to the tail (mm), circularity, extent, solidity, eccentricity 1 and 2, respectively.

Table 7.1. The discontinuity in the bubble terminal velocity: literature that used PAAM.

Study	PAAM polymer concentration, type and brand	Discontinuity
[18]	0.25, 0.50 and 0.75 wt % AN 913 SH -Floerger	No
[20]	0.25, 0.50 and 0.75 wt % AN 913 SH - Floerger	No
[16]	0.5 and 1.0 wt % AN 905 SH - Floerger	No
[35]	0.6, 0.8 and 1.0 wt% AR - Sinopharm	No
[37]	0.10, 0.25, 0.50 1.00 and 1.25 wt % Sigma Aldrich	No
[15]	0.15, 0.20 and 0.25 wt % Separan-AP30	Yes
[14]	0.5, 1.0 and 1.5 wt% - Separan AP3	Yes
[97]	0.5, 1.0 and 1.5 wt% - Separan AP30	Yes
[58]	0.075, 0.1, 0.15, 0.2 and 0.25 wt % - Separan AP-273	Yes
[40]	0.05, 0.10, 0.15, 0.20 and 0.25 wt % - Separan AP-273	Yes
[40]	0.5 and 1 wt % Separan AP- 230	Yes
[44]	0.1, 0.3, 0.8, 1 and 0.05 wt % Praestol 2500	Yes
[44]	0.1, 0.3, 0.8, 1 and 0.05 wt % - P2450	Yes

The first shape parameter investigated here is the extent of the bubble. The extent is defined as the ratio of the bubble's area to the area of the bubble's bounding box as defined in Eq. 5.4 and shown in Figure 5.2b. This parameter is used to obtain information about how the area of a bubble changes and to observe if the concavity of a bubble can be tracked. The results show that the extent decreases with increasing concentration for a given bubble volume (see the bubble volume with  $\sim 300 \text{ mm}^3$ , extent decreases from 0.74 to 0.70 in Tables 7.2 and 7.3, respectively).

The results show that the extent decreases until  $\sim 25 \text{ mm}^3$  which means that the bubble's area decreases compared to its bounding box. This can be explained by the bubbles turning from spherical to the prolate shape at this volume range (Table 7.2 and 7.3). As the bubble turns into a teardrop shape, the extent decreases. As soon as, the bubble shape starts growing in the horizontal direction, i.e., when it finally reaches the cap shape, the extent starts to increase. This increase is more significant for the 0.25 wt% concentration compared to the 0.40 wt% concentration due its shape not

reaching cap shape. For 0.18 wt% PAAM concentration, there is not enough data to observe the changes described above.

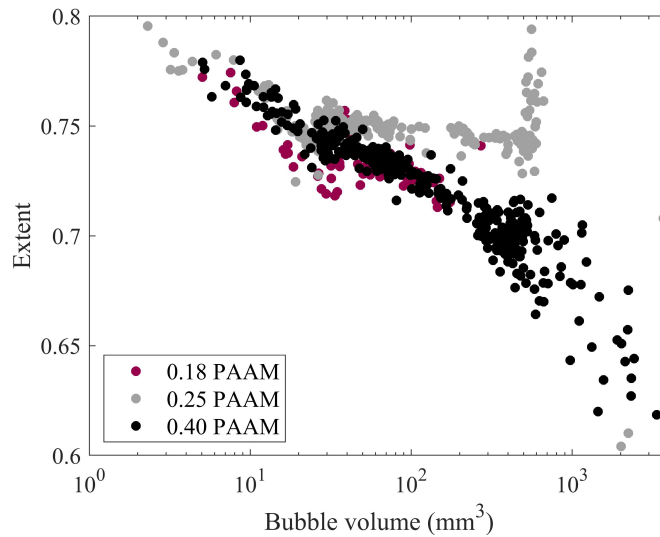


Figure 7.5. Shape parameter, extent as a function of the bubble volume for different concentrations of PAAM solution.

Next, the solidity of the bubbles is investigated. The solidity shows how concave a bubble is. A value of 1 for the solidity means that the bubble has a convex shape. It can be seen from Figure 7.6 that the solidity is independent of the polymer concentration. The solidity, first increases, then around 200 mm<sup>3</sup> bubble volume, it starts decreasing. It is predicted that as the cusp at the bubble tail becomes more pronounced at this volume range, the bubble becomes more concave (see Table 7.2 and 7.3).

The third parameter is the circularity of the bubble. If the circularity is 1, it means that the shape is perfectly circular. First of all, it is necessary to state that the circularity is drawn for bubble volumes larger than 25 mm<sup>3</sup>. The circularity measurement could not be performed for the bubbles that are smaller than 25 mm<sup>3</sup> since the code could not measure the circularity parameter correctly. When a bubble is very small, the edge of the bubble is not clear enough to detect due to the low resolution.

Table 7.2. Parameters and dimensionless numbers for 0.25 wt% PAAM solution.

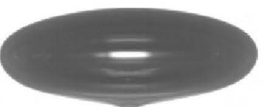
Bubble	V	d	$U_B$	a/b	a	b	C	Ext	Sol	E-1	E-2	$\beta$	$\dot{\gamma}$	Re	Bo	We	Ca	$C_D$
	4	2	5	1.9	2.07	1.11	-	0.78	0.984	0.94	0.98	0.65	2.66	0.04	0.55	8.E-04	0.1	914
	12	3	37	1.7	2.80	1.64	-	0.77	0.987	0.88	1.01	0.63	13.14	0.87	1.07	5.E-02	0.4	27
	51	5	163	1.9	4.53	2.41	0.99	0.75	0.989	0.94	1.01	0.57	35.50	10.74	2.79	2.E+00	1.8	2
	100	6	207	1.6	5.20	3.17	0.99	0.75	0.990	0.82	1.11	-	35.89	17.24	4.41	3.E+00	2.3	2
	305	8	242	1.0	5.46	5.38	0.83	0.74	0.988	0.51	1.53	-	28.94	25.91	9.25	7.E+00	2.7	2
	490	10	231	-	-	-	0.69	0.73	0.985	0.41	1.77	-	23.63	25.93	12.69	7.E+00	2.6	2
	663	11	236	-	-	-	0.61	0.76	-	0.32	2.11	-	21.84	28.05	15.52	8.E+00	2.7	3
 *	2012	16	264	-	-	-	-	-	-	-	-	-	-	-	-	-	-	-

Table 7.3. Parameters and dimensionless numbers for 0.40 wt% PAAM solution (part 1/2).

Bubble	V	d	$U_B$	a/b	a	b	C	Ext	Sol	E-1	E-2	$\beta$	$\dot{\gamma}$	Re	Bo	We	Ca	$C_D$
	5	2	2	1.8	2.17	1.18	-	0.78	0.984	0.93	0.99	0.73	0.75	0.00	0.61	8.E-05	0.2	10699
	12	3	11	1.7	2.80	1.67	-	0.76	0.986	0.87	1.01	0.62	3.92	0.06	1.07	5.E-03	1.1	299
	50	5	70	1.6	4.52	2.81	1.00	0.74	0.990	0.85	1.02	0.56	15.19	1.37	2.79	3.E-01	6.7	12
	106	6	78	1.5	5.75	3.77	0.98	0.73	0.991	0.82	1.02	0.53	13.25	1.79	4.56	5.E-01	7.5	13
	301	8	196	-	-	-	0.96	0.70	0.990	-	1.02	0.48	23.55	9.37	9.17	4.E+00	18.8	3

Table 7.3. Parameters and dimensionless numbers for 0.40 wt% PAAM solution (part 2/2).

Bubble	V	d	$U_B$	a/b	a	b	C	Ext	Sol	E-1	E-2	$\beta$	$\dot{\gamma}$	Re	Bo	We	Ca	$C_D$
	496	10	239	-	-	-	0.94	0.70	0.985	-	1.12	-	24.33	13.81	12.79	8.E+00	23.0	2
	661	11	251	-	-	-	0.92	0.68	0.980	-	1.09	-	23.19	15.43	15.49	9.E+00	24.1	2
 *	2027	16	252	-	-	-	-	-	-	-	-	-	-	-	-	-	-	-

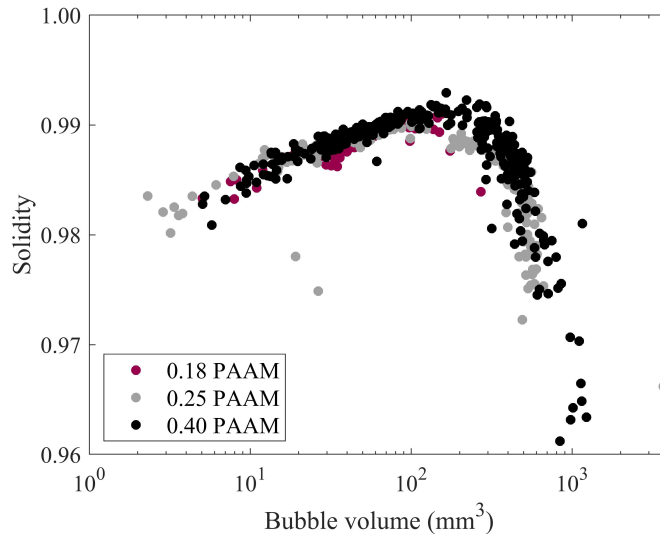


Figure 7.6. Shape parameter, solidity as a function of the bubble volume for different concentrations of PAAM solution.

The circularity is almost 1 for 25 mm<sup>3</sup> for all concentrations. At this stage the bubbles are changing from the spherical to the slightly prolate shape. Then, it starts to decrease slowly until a volume of 100 mm<sup>3</sup>. From 25 to 100 mm<sup>3</sup>, the circularity of the bubble in 0.40 wt% PAAM solution is less than the circularity observed in other concentrations. Around 100 mm<sup>3</sup>, the circularity abruptly decreases for the bubbles of 0.18 and 0.25 wt% PAAM concentrations. It is clear from Table 7.2 that the shape suddenly starts growing in the horizontal axis and deviates from the circularity. However, the circularity of the bubble in 0.40 wt% concentration is still close to 1 until 300 mm<sup>3</sup> and then it deviates significantly but less steeply than the circularity observed for 0.18 and 0.25 wt% solutions. The circularity change of 300 to 500 mm<sup>3</sup> bubble volume for the 0.40 wt% PAAM solution can be seen in Table 7.3.

The next shape parameters are  $a$ ,  $b$  and their ratio,  $a/b$ . As explained in Section 7.10,  $a$  is the minor axis and the smallest distance of the bubble and  $b$  is the distance between the center of gravity to the tip of the bubble. Figure 7.8 shows that  $a$  does not depend on the concentration until  $\sim 100$  mm<sup>3</sup>. For larger bubble volumes,  $a$  is constant for 0.18 and 0.25 wt% concentrations where it keeps increasing for the 0.40

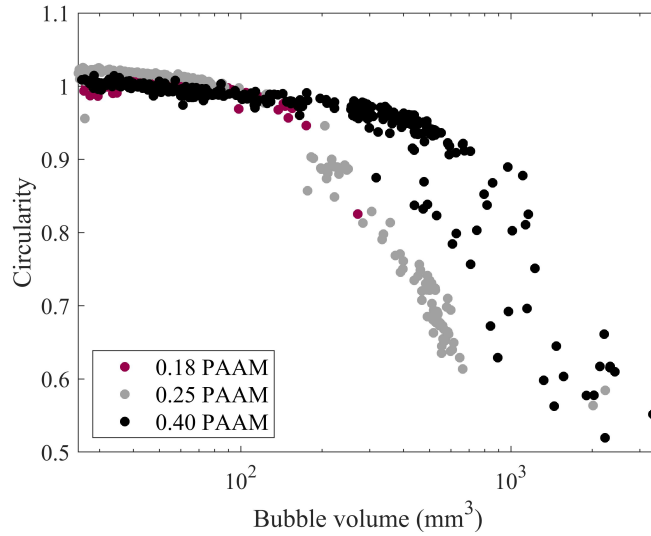


Figure 7.7. Shape parameter, circularity as a function of the bubble volume for different concentrations of PAAM solution.

wt% concentration until  $\sim 1000 \text{ mm}^3$ . It should be noted that as the parameter  $a$  is defined as the minimum distance value for a bubble, when the bubble starts growing horizontally, at some point the definitions of  $a$  and  $b$  are switched (see Figure 5.2, which change for wide bubbles). This switch is seen at around  $100 \text{ mm}^3$  bubbles for 0.18 and 0.25 wt% PAAM solutions, and at around  $500 \text{ mm}^3$  bubbles for 0.40 wt% PAAM solution (see Table 7.3).

The major axis,  $b$  increases constantly for all concentrations as seen in Figure 7.9. At these critical values mentioned in the previous paragraph,  $b$  becomes the longest of bubble volumes distance in the horizontal direction. In parallel with these results, the  $a/b$  value, as shown in Figure 7.10, it first decreases at different rates for different concentrations as the bubble turns from spherical to prolate and from prolate to teardrop shape, then increases as  $a$  starts growing much faster in the horizontal direction. Finally, after the aforementioned critical values,  $a/b$  starts decreasing.

The eccentricity-1,  $E1$ , defines the ratio of the length of a bubble's short (minor) axis to the length of its long (major) axis. This parameter shows how elliptical a

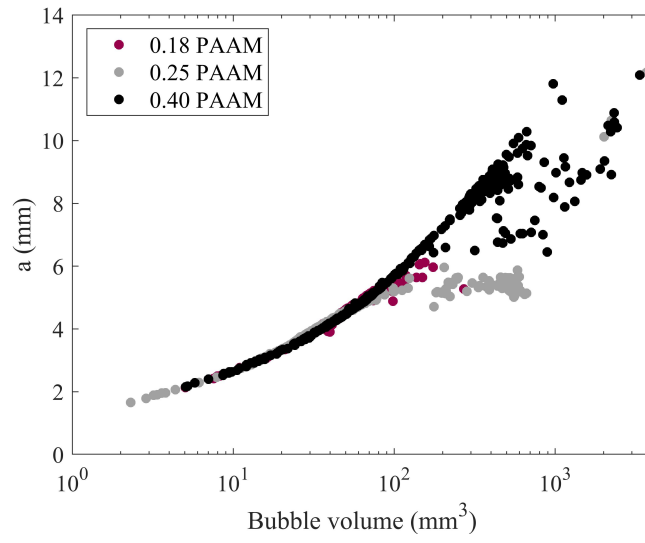


Figure 7.8. Shape parameter, minor axis,  $a$  as a function of the bubble volume for different concentrations of PAAM solution.

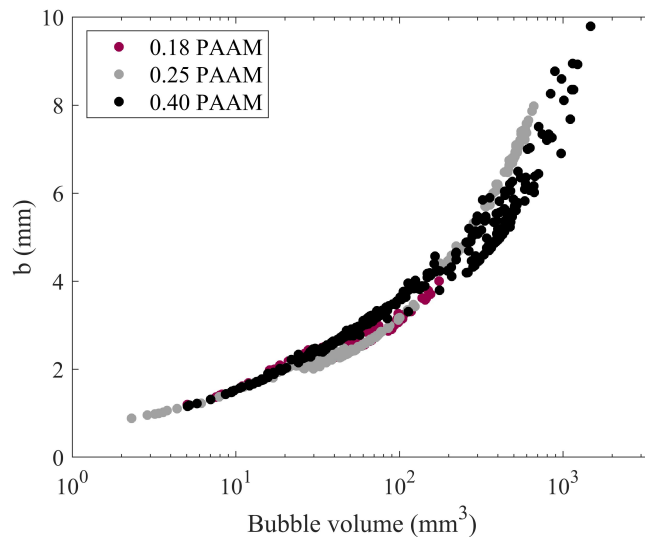


Figure 7.9. Shape parameter,  $b$  parameter as a function of the bubble volume for different concentrations of PAAM solution.

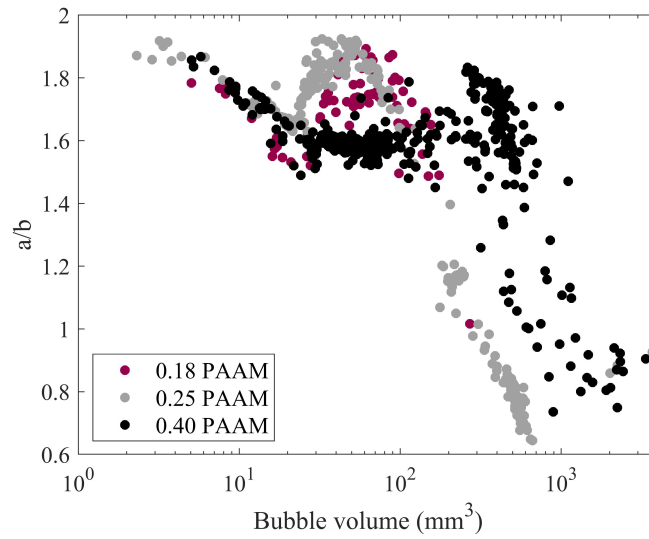


Figure 7.10. Shape parameter, ratio of the minor axis to the major axis,  $a/b$  as a function of the bubble volume for different concentrations of PAAM solution.

bubble is. For this parameter, the same pattern is observed with  $a/b$  as their definitions are similar to each other. However, sometimes  $a/b$  sometimes  $E1$  is preferred in the literature. Hence, here both are presented. It is observed that the eccentricity of the bubble decreases as the major axis increases. For example, the bubble becomes less eccentric as the volume changes from 5 to 80  $\text{mm}^3$  for the 0.40 wt% concentration. Then it starts to increase due to the horizontal expansion of the bubble and finally decreases around 400-500  $\text{mm}^3$  due to the definition of major and minor axis (Figure 7.11). Also, one can say from Figure 7.11 that the bubble with a volume of  $\sim 300$   $\text{mm}^3$  is more eccentric for 0.25 wt% than 0.40 wt%. Bubbles of both 0.25 wt% and 0.40 wt% concentrations become significantly eccentric after 80  $\text{mm}^3$  and 400  $\text{mm}^3$ , respectively (see Table 7.3). Finally, the difference in the eccentricity becomes negligible at very high volumes where the bubbles of both concentrations have a cap shape.

The next parameter is the eccentricity-2,  $E2$ , and is defined as the ratio of the equivalent diameter to the minor axis. It should be reminded that the minor axis is in the horizontal direction for the small volumes, and then it shifts to the vertical direction since the bubbles grow much faster horizontally.  $E2$  being close to 1 shows

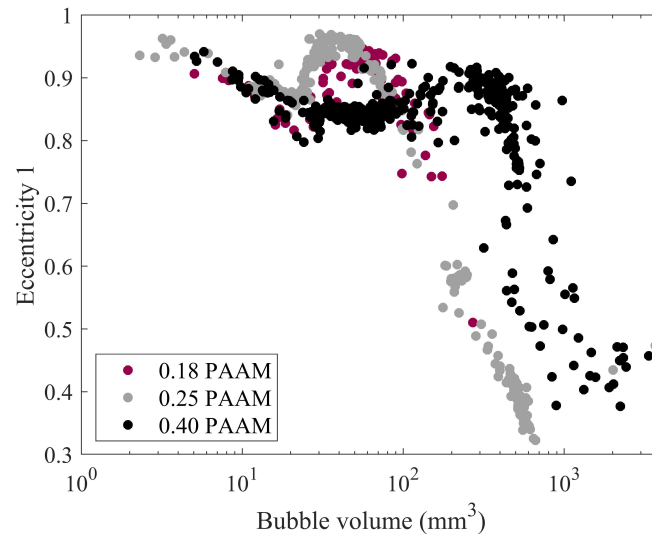


Figure 7.11. Shape parameter, eccentricity-1,  $E1$ , as a function the bubble volume for different concentrations of PAAM solution.

that the bubble has a circular shape. Unlike the previous parameters, the equivalent diameter is obtained through the volume. It can be seen from Figure 7.12 that  $E2$  is independent of the PAAM concentration until  $\sim 80 \text{ mm}^3$  bubble volume.  $E2$  is constant at around 1, i.e., bubbles with almost circular shape, until some volume. Then, there is deviation from the circularity, i.e., the eccentricity increases. This increase happens at lower bubble volumes in solutions with lower concentrations. The  $E2$  for bubbles of volumes around  $500\text{-}600 \text{ mm}^3$  in  $0.25 \text{ wt}\%$  PAAM concentration is almost double the  $E2$  for bubbles in  $0.40 \text{ wt}\%$  PAAM solution. Thus, it can be concluded that the bubbles are axysymmetrical.

The next parameter is  $\beta$ , which is defined by Xu *et al.* (2019) [37] to determine the bubble volume at which a cusp is formed at the tail of the bubbles rising in the PAAM and xanthan gum solutions (Figure 7.13).  $\beta$  is an empirical parameter and applied to one side of the bubble only as the bubbles are assumed to be axisymmetric. If  $\beta$  is less than 0.60 for a bubble, then it should have a cusp according to Xu *et al.* (2019) [37]. This empirical correlation is applied to this system and the results are given for a determination coefficient,  $R^2$  of 0.9. The results are presented in Figure

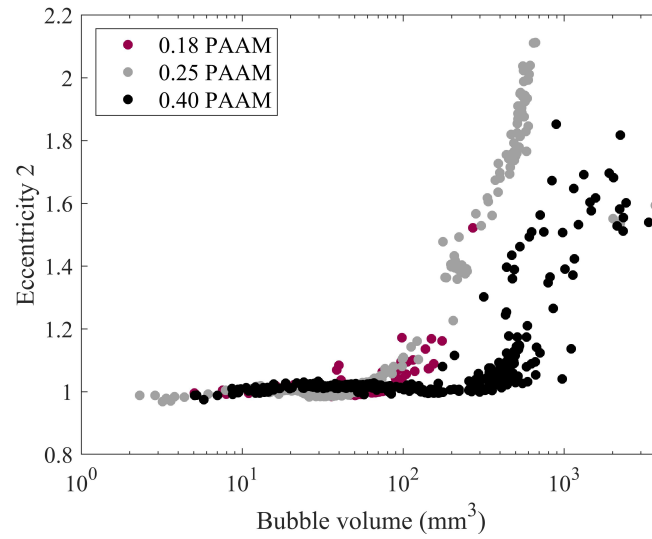


Figure 7.12. Shape parameter, eccentricity-2,  $E2$ , as a function of the bubble volume for different concentrations of PAAM solution.

7.13 where the red line shows  $\beta=0.6$ .

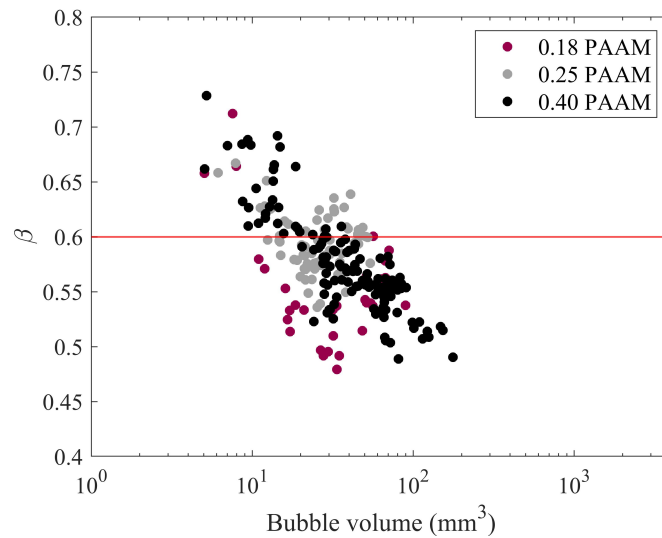


Figure 7.13. Shape parameter,  $\beta$  as a function of the bubble volume for different concentrations of PAAM solution.

The results show that  $\beta$  can be determined from the fits for a bubble volume range of 10-200 mm<sup>3</sup>. The results are more representative and in accordance with

visual observations of the cusp for the 0.40 wt% concentration. The graphs shows that a bubble that has a volume larger than  $\sim 25 \text{ mm}^3$  should have a cusp for all concentrations. For this purpose, a bubble volume range of 15-30  $\text{mm}^3$  is specifically studied. The findings are in a good match with the study of Xu *et al.* (2019) as the first bubbles with a cusp are observed at 26  $\text{mm}^3$ , 24  $\text{mm}^3$  and 24  $\text{mm}^3$  for 0.18 wt%, 0.25 wt%, 0.40 wt% PAAM concentration studies, respectively (see Figure 7.14). Xu *et al.* (2019) detected the cusp formation ( $\beta < 0.6$ ) for the xanthan gum solutions, but not for the PAAM concentrations of 0.10, 0.25, 0.50, 1.00 and 1.25 wt%.

As mentioned earlier at the beginning of this section while discussing the discontinuity detection for different PAAM polymers, it is seen that similar results are obtained for the same types and brands of the polymer. Here, we report a cusp formation for the same bubble volume range for the 0.25 wt% PAAM (Sigma Aldrich) solution in this study where Xu *et al.* (2019) did not observe any. Here, we also conclude that the cusp formation volume is concentration independent.

Concentration (wt%)	0.18	0.25	0.40
Volume ( $\text{mm}^3$ )	26	24	24
			

Figure 7.14. The bubbles where the cusp is seen for the first time at  $\beta \approx 0.59$  for different PAAM concentrations.

Finally, for the bubble dynamics of the PAAM solutions, dimensionless numbers are calculated. The definitions of the dimensionless numbers are given in Section 5.1.3. First, the Bond number,  $Bo$ , is presented versus the Reynolds number,  $Re$ , in Figure 7.15.  $Bo$  represents the ratio of the gravitational forces over the surface tension forces, and  $Re$  is the ratio of the inertial forces to the viscous forces.  $Bo$  is constant for small

$Re$  and it is less than 1. Then,  $Bo$  increases suddenly at different values of  $Re$  for each concentration.

At first,  $Re$  increases due to the increase in the equivalent diameter,  $d$  and the terminal velocity,  $u_B$ . In the mean time,  $Bo$  increases only with  $d$ . For a larger bubble volume,  $u_B$  becomes constant as shown in Figure 7.4 and the only contribution to  $Re$  comes from  $d$  which includes the viscosity behaviour index,  $n$  ( $n < 1$  for shear-thinning liquids) as its power. While the increase in  $Re$  slows down due to this,  $Bo$  increases proportional to the square of  $d$  which results in an abrupt increase. Thus, the effect of the surface tension decreases and the bubble shape deviates from the spherical to the cap shape (see Tables 7.2 and 7.3). Also, each concentration shows a sudden increase in  $Bo$  at different  $Re$  since the polymer concentration changes the rheological properties,  $n$  and  $K$ .

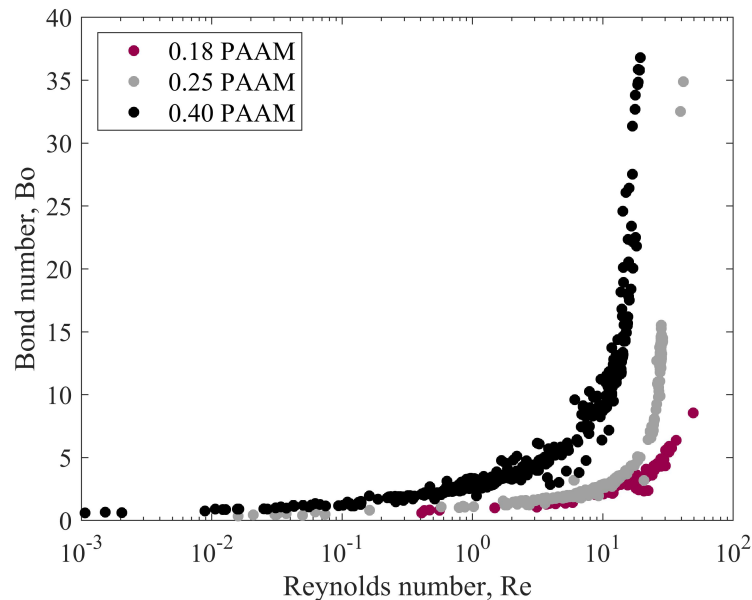


Figure 7.15.  $Bo$  versus  $Re$  for different concentrations of PAAM solution.

The next dimensionless number is the Capillary number,  $Ca$ , that is the ratio of the viscous forces to the surface tension forces in the system (see Figure 7.16). The behaviour is similar to what is observed in  $Re$  vs.  $Bo$  in Figure 7.15. For a given  $Re$ ,

$Ca$  of 0.40 wt% concentration is much higher than the other concentrations due to the high viscosity of 0.40 wt% solution.

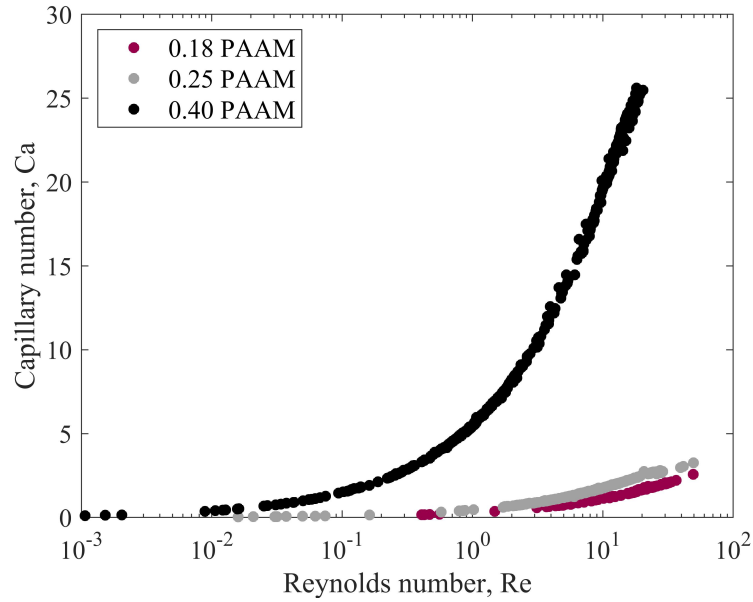


Figure 7.16.  $Ca$  versus  $Re$  for different concentrations of PAAM solution.

Next, Weber number,  $We$ , which represents the ratio of the inertial forces to the surface tension forces is plotted in Figure 7.17. For a given equivalent diameter, the inertial forces are greater than the surface tension forces. The increase in  $We$  is smaller than the increase in  $Bo$ . The effect of the polymer concentration shows its effect on  $We$  at small  $d$ . As  $d$  increases,  $u_B$  reaches the plateau value for all concentrations and the only contribution to  $We$  comes from  $d$ .

Finally, the drag coefficient,  $C_D$ , is calculated according to Eq. 5.12 as plotted in Figure 7.18.  $C_{D,2}$  and  $C_{D,3}$  show the drag coefficient for Hadamard-Rybczynski regime and are valid for  $Re < 1$  and  $Re < 60$ , respectively; and it is applicable for deformable surfaces. It is observed that  $C_D$  is slightly higher than  $C_{D,2}$  at different  $Re$  regions for each concentration. Figure 7.18 shows that the bubbles act like solid spheres at  $Re \approx 0.001 - 0.002$  for 0.40 wt%, at  $Re \approx 0.02 - 0.2$  for 0.25 wt% and at  $Re \approx 0.3 - 1.0$  for 0.18 wt% (see the first bubble of Tables 7.2 and 7.3). For these regions, the bubbles are

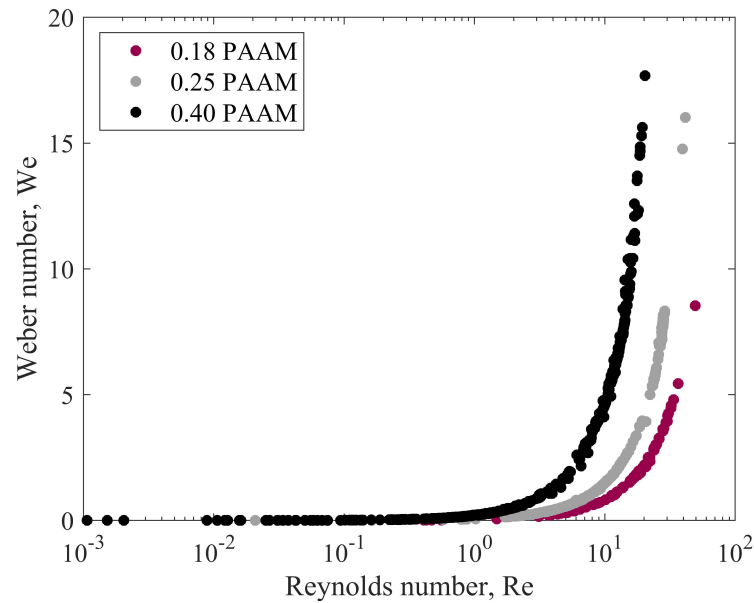


Figure 7.17.  $We$  versus  $Re$  for different concentrations of PAAM solution.

deviate from Hadamard-Rybczynski regime, to the  $C_D$  of Stokes' law which is  $24/Re$  and not shown on the plot. A transition from Stokes to Hadamard-Rybczynski regime occurs where these given  $Re$  regions end.

For larger volumes, the bubbles start fitting Hadamard-Rybczynski regime after the given  $Re$  regions for each concentration. For  $Re=1$ , the results fit  $C_{D,3}$  regime until  $Re=60$  which is in a good correlation with the definition of  $C_{D,3}$  [32, 91].

In the literature, it is reported that the discontinuity at the bubble velocity is observed at the transition from the Stokes to the Hadamard-Rybczynski regime [9]. It was also reported that the cusp starts forming at this transition [30]. However, as stated before, there is no discontinuity in the bubble velocity at a critical volume for this system. Additionally, the cusp formation does not occur at these transitions for any of the polymer concentrations. As stated previously, the cusp forms around  $25 \text{ mm}^3$ , and the  $Re$  value is much higher for these bubble volumes.

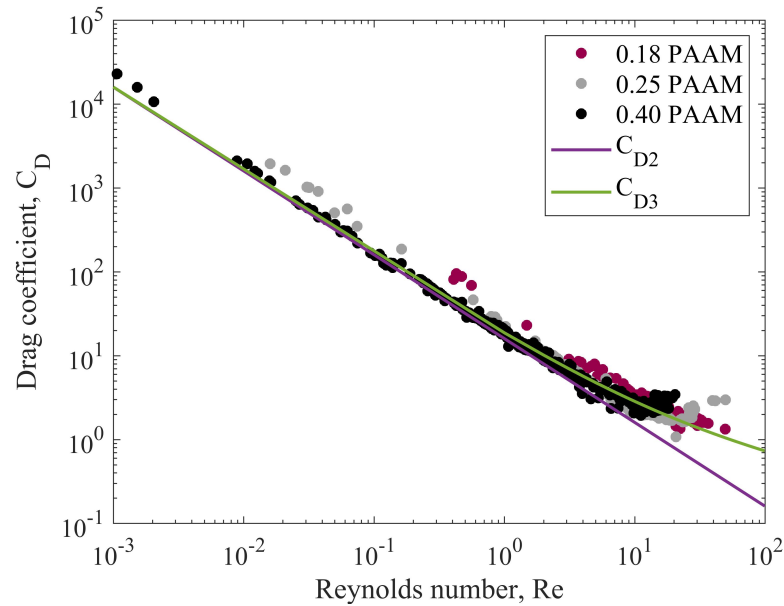


Figure 7.18.  $C_D$  versus  $Re$  for different concentrations of PAAM solution.

### 7.1.3. Effect of the Injection Period

The injection period is a crucial part of the bubble dynamic studies as it is proved to affect the results considerably. The injection period depends on the physical properties of the polymer used and also the bubble size.

To determine the injection period that does not affect the results, an experiment was designed specifically for this purpose. It is made sure that only a single bubble rises throughout the column. The tested injection periods for a bubble volume of 2000 mm<sup>3</sup> are tabulated in Table 7.4

The results show that there exists a critical injection period for each concentration. The injection periods of 15, 33 and 57 s were determined to be safe for 0.10, 0.25 and 0.40 wt% concentrations, respectively. The increase in the injection period with the increasing polymer concentration is in an agreement with literature [19]. Below these injection periods, it is determined that the terminal bubble velocity,  $u_B$  increases and reaches a plateau value for the entire bubble volume range. The results also shows

Table 7.4. Tested injection periods for different PAAM

	<b>0.10 wt%</b>	<b>0.25 wt%</b>	<b>0.40 wt%</b>
<b>Period (s)</b>	0.5	4.5	11
	5	9	25
	15	20	32
	-	33	57

that the bubble shapes are also affected with decreasing injection period. The bubble shapes elongate in the vertical direction. The increase in the bubble terminal velocity and the elongated bubble shape were also confirmed by Funfschilling and Li (2006) for 0.5 wt% PAAM (913 SH, SNF Floerger) solution [21]. In the light of this investigation, the bubble injection period is set to 60 s for a bubble volume range of  $\sim 10 - 2000 \text{ mm}^3$  in this study for all PAAM concentrations.

#### 7.1.4. Effect of the of Surfactant on Bubble Dynamics

Surfactants have an extremely important role in the dynamics of the bubbles as they alter the surface tension forces. For this purpose, the polymer, PAAM concentration is kept constant at 0.25 wt% and different concentrations of SDS (a water soluble surfactant) are added. The surface tension of 0.25 wt% PAAM solution is 74 mN/m as shown in Section 4.5. The surface tension is lowered to 66.8 and 45.2 mN/m for 10 and 100 ppm of SDS, respectively. 10 ppm of SDS is shown not to have any significant effect on bubble dynamics.

First of all, the average bubble terminal velocity,  $u_B$  is studied and shown in Figure 7.19. The results show that 10 ppm SDS slightly affects the terminal velocity until  $\sim 50 \text{ mm}^3$ . When we look at the effect of 100 ppm, it can be seen that the terminal velocity significantly decreases for a given bubble volume. However its effect diminishes around  $\sim 250 \text{ mm}^3$  and the bubble terminal velocity for all concentrations reaches a

plateau value at  $\sim 250 \text{ mm}^3$ . The decrease in the bubble velocity with the addition of the surfactant is expected [1] and can be explained by the Marangoni effects. Tables 7.5 and 7.6 show the bubble images and respective bubble dynamics data of 0.25 wt% PAAM solution with 10 ppm and 100 ppm, respectively. In these tables,  $V$ ,  $d$ ,  $u_B$ ,  $a$ ,  $b$ ,  $C$ ,  $\text{Ext}$ ,  $\text{Sol}$ ,  $E-1$ ,  $E-1$ ,  $E-2$  are volume ( $\text{mm}^3$ ), equivalent diameter (mm), the minor axis (mm), the distance from center of gravity to the tail (mm), circularity, extent, solidity, eccentricity 1 and 2, respectively.

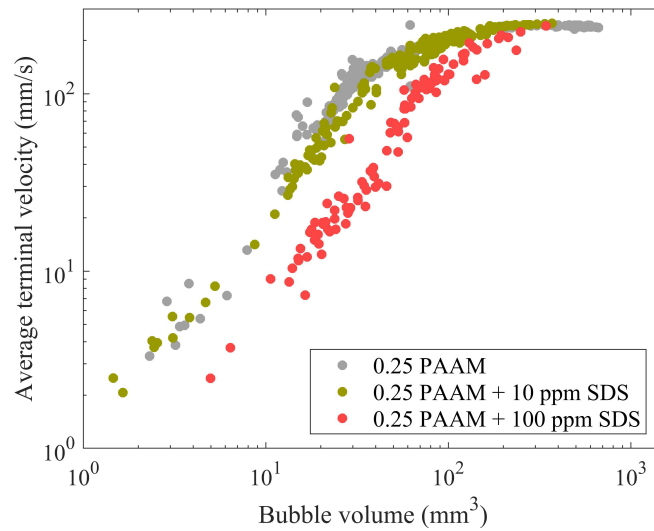


Figure 7.19. The average terminal velocity as a function of the bubble volume for 0.25 wt% PAAM solution with different surfactant concentrations.

Extent results of the bubbles are given in Figure 7.20. The surfactant concentration does not have any effect on the extent for bubble volumes up to  $30 \text{ mm}^3$  and the ratio of the bubble area to its bounding box decreases similarly. In this regime, the bubbles have a prolate shape and evolve into the teardrop shape. The bubble area decreases compared to the bounding box. The bubbles start expanding in the horizontal direction for the PAAM solution around  $\sim 30 \text{ mm}^3$ . However, the extent value decreases for the PAAM solutions with the surfactant in it. It means that the bubbles are not growing horizontally as much as the bubbles do in clean liquids, without surfactant. Solutions with 10 ppm SDS show that the decrease in the extent slows down after  $\sim 50 \text{ mm}^3$ .

Table 7.5. Parameters and dimensionless numbers for 0.25 wt% PAAM solution with 10 ppm SDS.

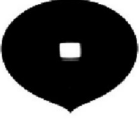
Bubble	V	d	$U_B$	a/b	a	b	C	Ext	Sol	E-1	E-2	$\beta$	$\dot{\gamma}$	Re	Bo	We	Ca	$C_D$
	4	2	5	1.9	1.96	1.05	-	0.79	0.984	0.94	0.99	0.69	2.82	0.04	0.55	9.E-04	0.1	847
	20	3	44	1.6	3.33	2.07	-	0.74	0.987	0.85	1.01	0.56	13.01	1.22	1.67	1.E-01	0.5	23
	49	5	160	1.8	4.55	2.48	-	0.74	0.989	0.95	1.00	0.60	35.19	10.39	3.04	2.E+00	2.0	2
	104	6	218	1.6	5.27	3.25	0.97	0.72	0.987	0.81	1.11	0.23	37.43	18.77	4.99	4.E+00	2.7	2
	190	7	239	1.4	5.76	4.25	0.91	0.71	0.982	0.68	1.24	0.43	33.54	23.70	7.47	6.E+00	3.0	2

Table 7.6. Parameters and dimensionless numbers for 0.25 wt% PAAM solution with 100 ppm SDS.

Bubble	V	d	$U_B$	a/b	a	b	C	Ext	Sol	E-1	E-2	$\beta$	$\dot{\gamma}$	Re	Bo	We	Ca	$C_D$
	5	2	2	1.9	2.18	1.17	-	0.76	0.981	0.94	0.97	0.65	1.17	0.01	0.97	3.E-04	0.0	4479
	18	3	17	1.7	3.18	1.92	-	0.76	0.987	0.85	1.02	0.62	5.30	0.28	2.28	2.E-02	0.3	144
	53	5	47	1.3	4.48	3.42	0.93	0.70	0.987	0.73	1.04	0.43	10.07	1.56	4.72	2.E-01	0.9	28
	100	6	129	1.4	5.68	4.19	0.92	0.68	0.981	0.77	1.01	0.28	22.40	8.25	7.19	2.E+00	2.4	5
	195	7	214	1.8	6.94	3.93	0.91	0.67	0.974	0.88	1.04	0.33	29.68	19.95	11.24	7.E+00	3.9	2

Table 7.5 shows that the bubble expands horizontally around this volume whereas this is not observed for a bubble in the presence of 100 ppm SDS and consequently, the bubbles have elongated shape. For the larger bubbles, the extent parameter keeps decreasing for 100 ppm since the bubbles are still vertically elongated whereas for the solution without surfactant, the extent increases due to the cap formation.

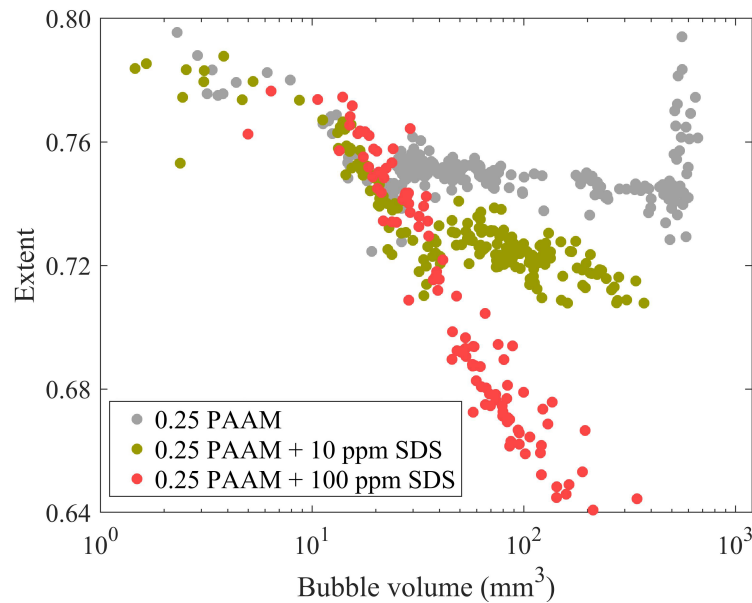


Figure 7.20. Shape parameter, extent as a function of the bubble volume for 0.25 wt% PAAM solution with different surfactant concentrations.

The next parameter is the effect of the solidity and the results are given in Figure 7.21. In Section 7.1.2, it was shown that the solidity is independent of the polymer concentration in the absence of the surfactant. The solidity increases for all of the solutions and becomes closer to 1, i.e., the bubble reaches a convex shape. This can be explained by the bubbles turning from a spherical to a prolate shape. However, the solidity changes with the addition of the surfactant for a given volume after  $\sim 100$   $\text{mm}^3$  bubble volume. The decrease is significant for both 10 and 100 ppm surfactant concentrations. Therefore, the concavity increases for a bubble volume with increasing surfactant concentration. When Tables 7.2, 7.5 and 7.6 are checked simultaneously for a bubble volume of around  $100 \text{ mm}^3$ , one can see that the concavity increases at the lower half of the bubble as the surfactant concentration increases. As the surfactant

concentration increases at the rear of the bubbles (tail), the surface tension forces are weakened and the bubbles stretch out vertically.

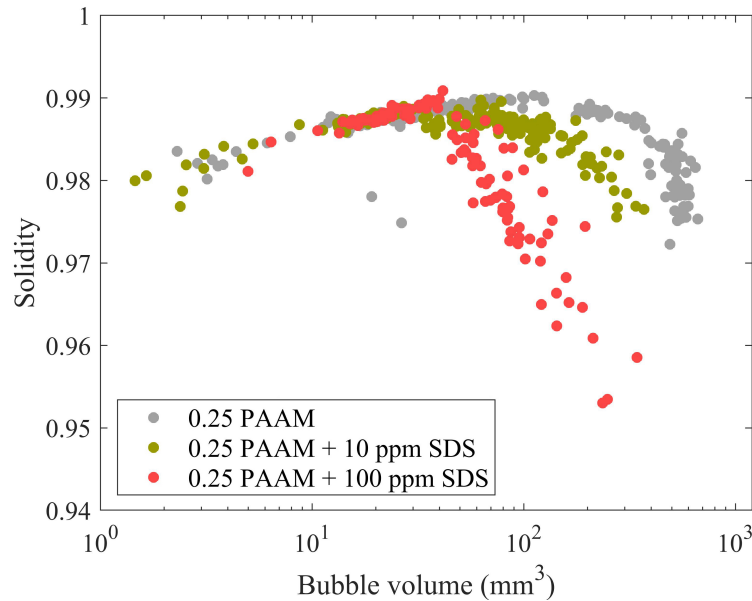


Figure 7.21. Shape parameter, solidity as a function of the bubble volume for 0.25 wt% PAAM solution with different surfactant concentrations.

The effect of the surfactant concentration on the circularity of the bubble is given in Figure 7.22. The circularity decreases quickly for the PAAM solution with 100 ppm surfactant whereas the decrease is slower for the other concentrations. Similar to the concavity, the elongation caused by the weakened surface tension forces makes the bubble deviate from its circular shape. However, the circularity curves cross each other around  $\sim 200 \text{ mm}^3$ . After this point, the bubble grows in the horizontal direction and deviates from the circularity for the solution that has no surfactant.

Next,  $a$ ,  $b$  and  $a/b$  parameters are presented in Figures 7.23, 7.24 and 7.25, respectively. The results show that the surfactant does not have any effect on the minor axis,  $a$ . The change for the 0.25 wt% PAAM solution without the surfactant after  $\sim 200 \text{ mm}^3$  is caused by the change of the axes and explained earlier in Section 7.1.2. Figure 7.24 shows that the surfactant does not have any effect on  $b$  for spherical and prolate bubbles, i.e., bubbles of small volumes. However, the increase in the  $b$

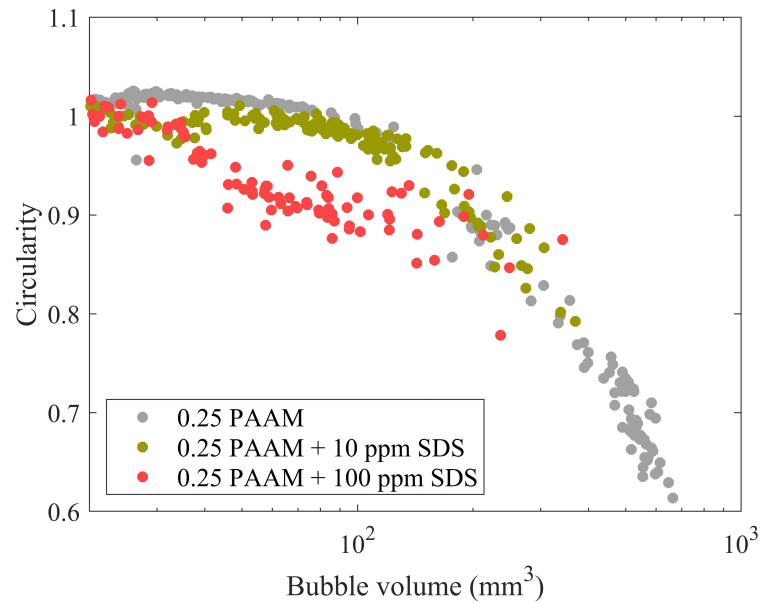


Figure 7.22. Shape parameter, circularity as a function of the bubble volume for 0.25 wt% PAAM solution with different surfactant concentrations.

is much faster for the 100 ppm concentration compared to the other solutions. As explained in this section for the earlier parameters, the tail of the bubbles elongates. Therefore, the distance between the center of mass and the tip of the bubble increases. The  $a/b$  clearly shows that the bubbles also start growing horizontally (after  $\sim 50 \text{ mm}^3$ ). This change can be observed from Table 7.6 for the bubbles with the volumes of 53 and  $100 \text{ mm}^3$ . This behaviour is also similar to the effect of increasing PAAM concentration on  $a/b$ .

When the eccentricity-1, E1 is studied, it is observed from Figure 7.26 that the surfactant does not affect this parameter until  $\sim 20 \text{ mm}^3$ . However, the tail elongates and becomes less eccentric with increasing bubble volume in the presence of 100 ppm surfactant.

The observations for the eccentricity-2, E2 (Figure 7.27), are similar to the ones presented for PAAM solutions in the absence of the surfactant. 10 ppm surfactant does not have any effect, and the eccentricity remains around 1 for the 100 ppm surfactant

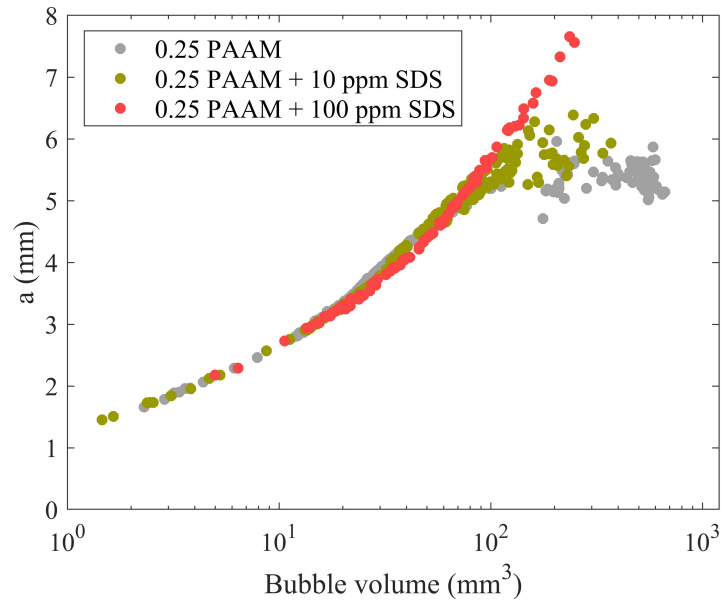


Figure 7.23. Shape parameter, minor axis,  $a$  as a function of the bubble volume for 0.25 wt% PAAM solution with different surfactant concentrations.

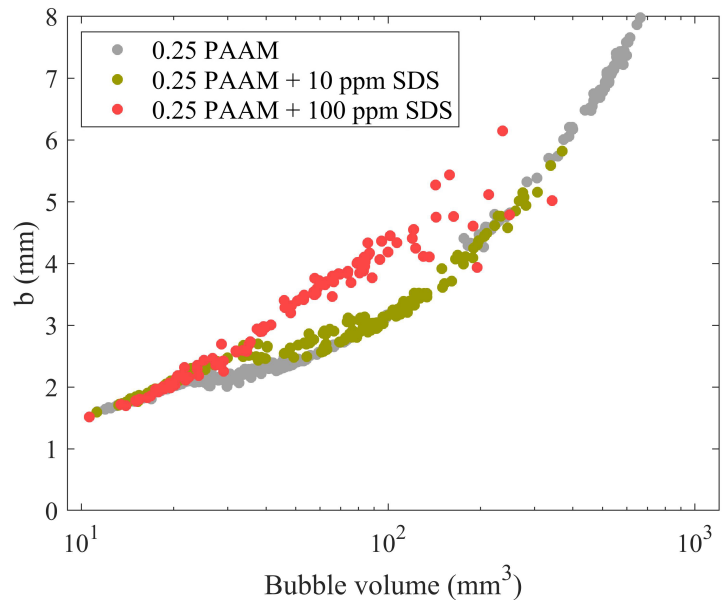


Figure 7.24. Shape parameter,  $b$  as a function of the bubble volume for 0.25 wt% PAAM solution with different surfactant concentrations.

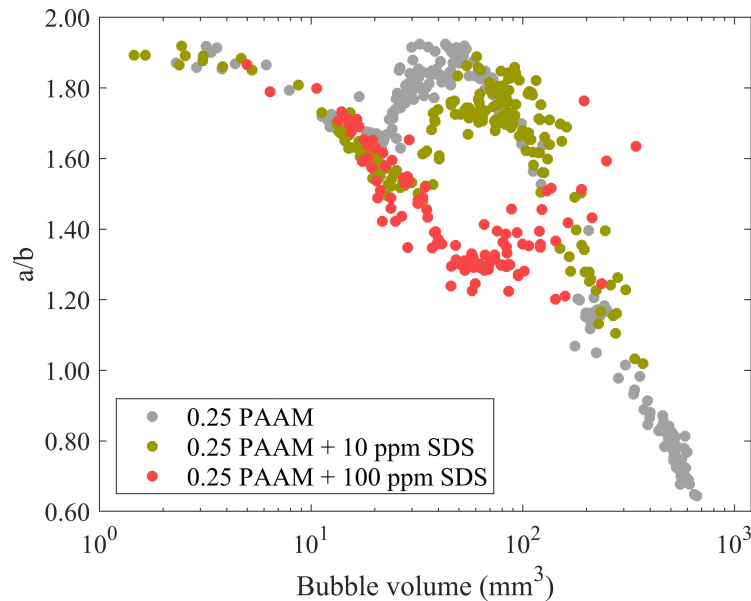


Figure 7.25. Shape parameter, the ratio of minor axis,  $a$  over  $b$  as a function of the bubble volume for 0.25 wt% PAAM solution with different surfactant concentrations.

concentration while others are increasing. It can be seen from Tables 7.5 and 7.6 that the bubble ( $195 \text{ mm}^3$ ) is more circular for a solution with 100 ppm SDS than the bubble ( $190 \text{ mm}^3$ ) in a solution with 10 ppm SDS.

Lastly,  $\beta$  is studied to understand the effect of the surfactant on the cusp formation and is shown in Figure 7.28. It is reported in Section 7.1.2 that the cusp formation occurs around  $25 \text{ mm}^3$  for 0.25 wt% in the absence of the surfactant. The cusp formation starts at a slightly lower volume once the surfactant is added. The cusp becomes more pronounced with the increase of the surfactant which can also be observed from the bubble images from Table 7.5 ( $49 \text{ mm}^3$ ) and Table 7.6 ( $53 \text{ mm}^3$ ). This observation is in a good agreement with the work of Li *et al.* (2011) who reported that cusps become more pronounced as the surfactant concentration increases for different concentrations of PAAM solutions with Triton X-100 as the surfactant [97]. Previously, we concluded that the cusp formation is concentration independent whereas it is highly dependent on the surfactant concentration.

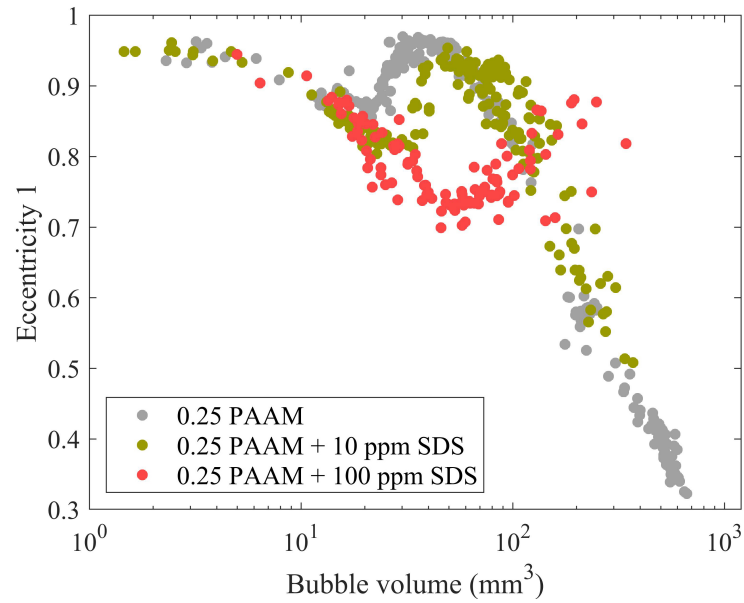


Figure 7.26. Shape parameter, eccentricity, E1 as a function of the bubble volume for 0.25 wt% PAAM solution with different surfactant concentrations.

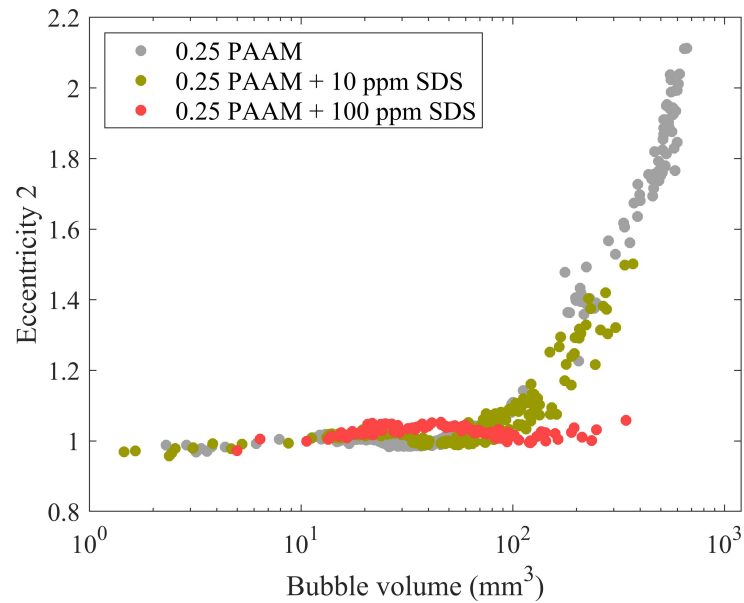


Figure 7.27. Shape parameter, eccentricity, E2 as a function of the bubble volume for 0.25 wt% PAAM solution with different surfactant concentrations.

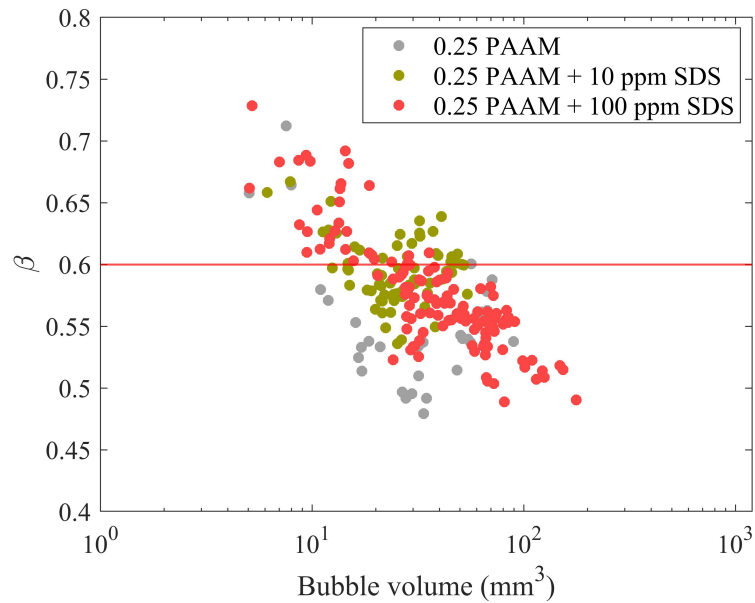


Figure 7.28. Shape parameter,  $\beta$  as a function of the bubble volume for 0.25 wt% PAAM solution with different surfactant concentrations.

First dimensionless number studied is the Bond number,  $Bo$  for different concentrations of the surfactant. The results are given in Figure 7.29 and show that 10 ppm of surfactant has almost no effect on the system. However, 100 ppm surfactant SDS significantly increases  $Bo$  for a given  $Re$ , except at high  $Re$ . Since the surfactant decreases the surface tension, the increase in  $Bo$  is expected. One should remember that for a given  $Re$ , bubbles may have different volumes as the terminal velocity decreases with the surfactant concentration. For example, it can be seen from Tables 7.5 and 7.6 that 195  $\text{mm}^3$  bubble rising in a solution with 100 ppm SDS has a higher  $Bo$  (11.24) than the 190  $\text{mm}^3$  bubble in a solution with 10 ppm SDS (7.47). Therefore, the change detected in Figure 7.29 is actually the effect of the surfactant on the terminal velocity observed in  $Re$ .

Next, the capillary number,  $Ca$  is presented in Figure 7.30. For a given  $Re$ ,  $Ca$  is higher with the surfactant for a certain range of  $Re$ . For a given bubble diameter, the changes that come from the terminal velocity and the surface tension will compete in  $Ca$  (Eq. 5.10). Once, Tables 7.5 and 7.6 are studied together, it is found that

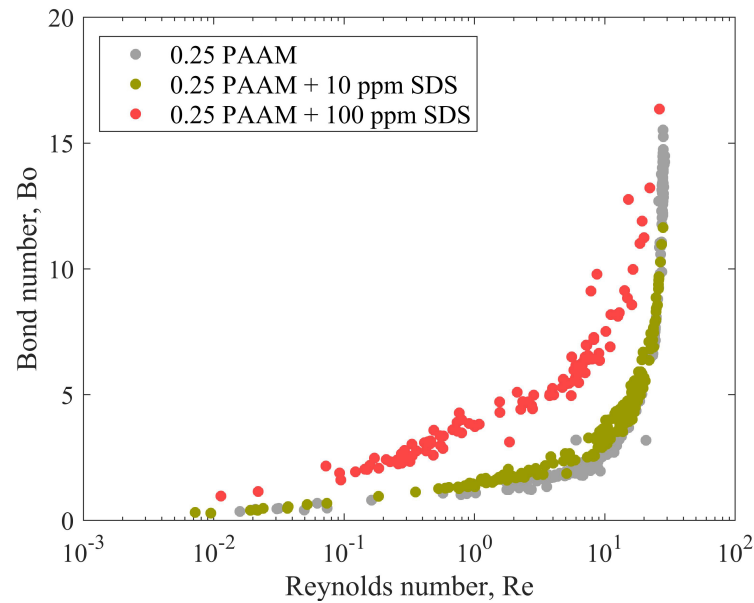


Figure 7.29.  $Bo$  versus  $Re$  for different concentrations of surfactant in PAAM solution.

for the small bubbles the terminal velocity is dominating, but as the bubble diameter increases, the contribution of surface tension is more pronounced.

The next dimensionless number is the Weber number,  $We$  (Figure 7.31). Similar to  $Ca$ , the terminal velocity and the surface tension compete for a given bubble diameter as the surfactant concentration changes (Eq. 5.11). However,  $We$  is proportional to the square of the terminal velocity. As the bubble diameter increases, the effect of the surfactant on the terminal velocity diminishes. For small bubble volumes, without surfactant  $We$  is large since the velocity is high which contributes to  $We$  more than the surface tension.

Lastly,  $C_D$  is studied to examine the effect of the surface tension on the drag. It is found that  $C_D$  increases and does not fit Hadamard–Rybczynski regime for  $Re < 1$  ( $C_{D,2}$ ). When the surfactant is added into the solution, it accumulates on the bubble surface which causes bubble act like a solid sphere. The increase in the  $C_D$  with the addition of the surfactant is also observed in the literature and explained by the

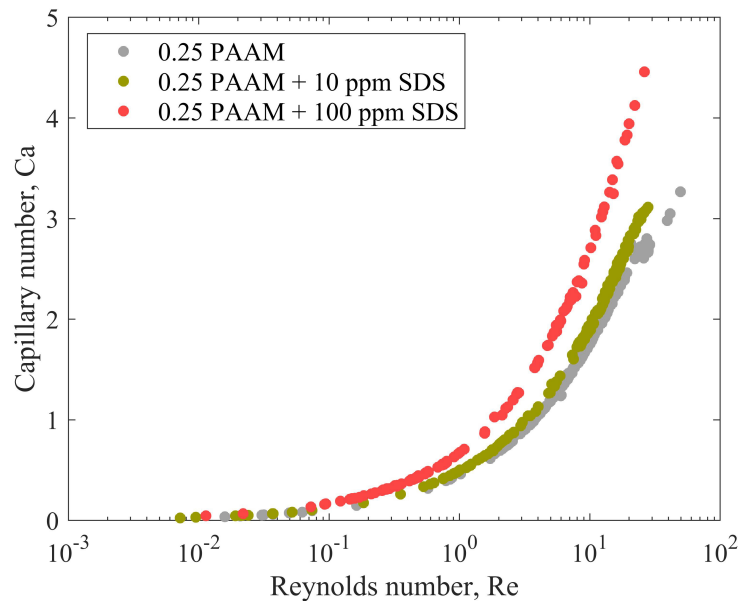


Figure 7.30.  $Ca$  versus  $Re$  for different concentrations of surfactant in PAAM solution.

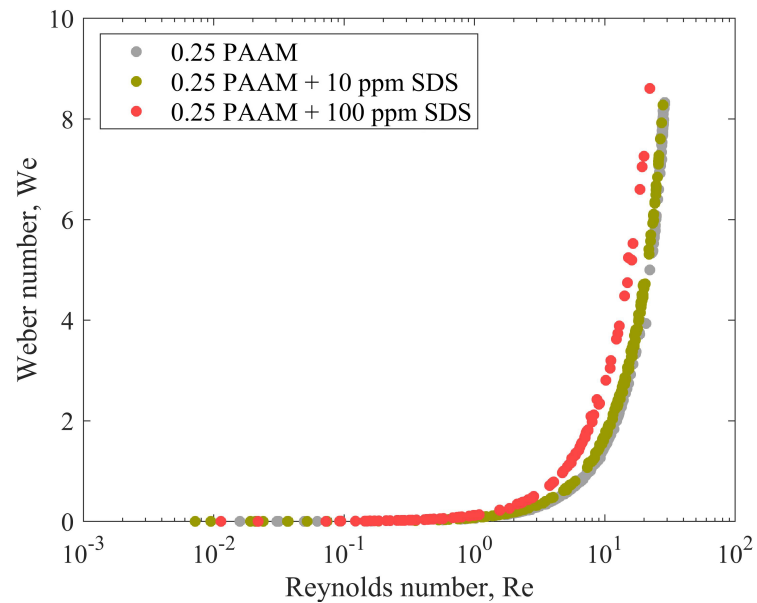


Figure 7.31.  $We$  versus  $Re$  for different concentrations of surfactant in PAAM solution.

decrease in the bubble terminal velocity [63,97]. Therefore,  $C_D$  increases, and it starts deviating from the Hadamard–Rybczynski towards the Stokes’ regime for small bubble volumes. The results show that  $C_D$  fits the Hadamard–Rybczynski regime for  $Re < 60$ ,  $C_{D,3}$  which means the accumulation on the bubble surface is not too high to deviate  $C_D$  from the Hadamard–Rybczynski regime.

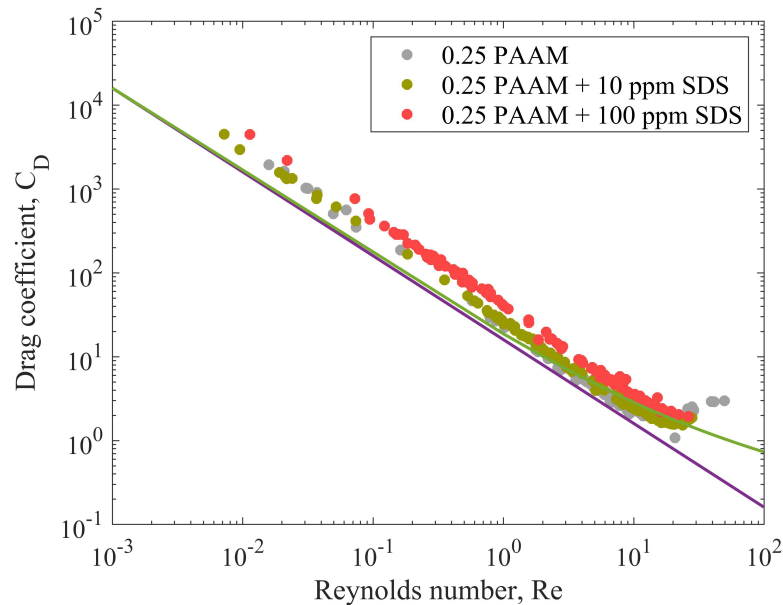


Figure 7.32. Drag coefficient,  $C_D$  versus  $Re$  for different concentrations of surfactant in PAAM solution.

### 7.1.5. The Bubble Trajectory

When a bubble rises in a liquid column, it tends to have an axi-symmetric trajectory such as zigzag or spiral, depending on the physical characteristics and the bubble volume of the liquid. Therefore, we also studied the trajectory of the rising bubble. In this section, 3 different solutions are studied, namely 0.25 wt% PAAM, 0.40 wt% PAAM and 0.25 wt% PAAM with 100 ppm SDS solutions. A bubble volume range of 20 to 2000 mm<sup>3</sup> is presented here. The x-axis shows the horizontal deviation of the bubble in mm where the y-axis represents the tube length/equivalent diameter.

Here, it should be reminded that the bubble terminal velocity is lowered when

the surfactant is added into the system. In this kind of a system, the small bubbles (20 and 50  $\text{mm}^3$ ) are recorded for a fixed number of frames. Therefore, the bubbles for this system are recorded for a limited time due to the low terminal velocity.

Figures 7.33, 7.34 and 7.35 show the trajectory results for bubbles in 0.25 wt% PAAM, 0.40 wt% 40 PAAM and 0.25 wt% PAAM with 100 ppm SDS solutions, respectively. The results show that the bubbles first deviate to the right most of the time which can be due to an experimental bias. Later, it seems like the bubbles turn to the core of the column. As the polymer and the surfactant concentrations increase, the path instability and the bubble oscillation increase and the bubble do a lateral motion, which is in agreement with the literature [65, 98, 99].

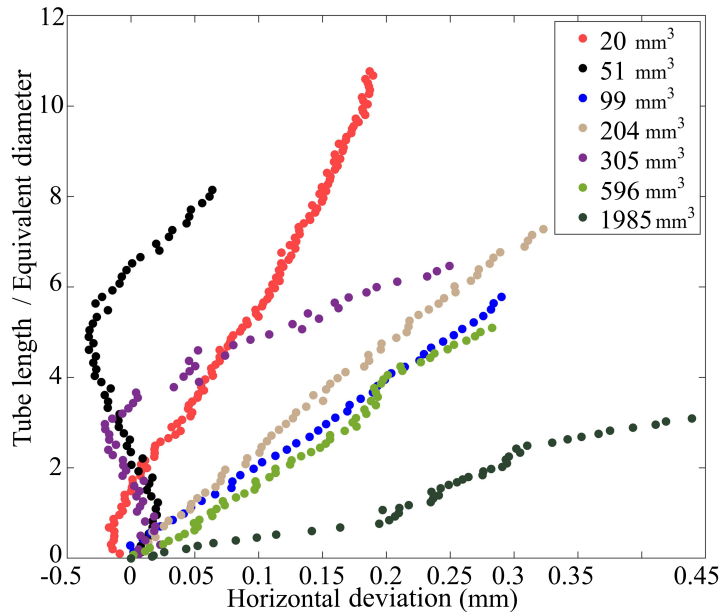


Figure 7.33. The trajectory of bubbles with different volumes in 0.25 wt% PAAM solution.

It should be noted that the deviation grows in the x-direction as the bubble volume increases. However, it reaches a maximum of 0.45 mm where the equivalent diameter of the biggest bubble represented here is 7 mm for 2000  $\text{mm}^3$ . Also, a bubble can be recorded for a maximum of 6 cm after leaving the inlet completely in the vertical direction.

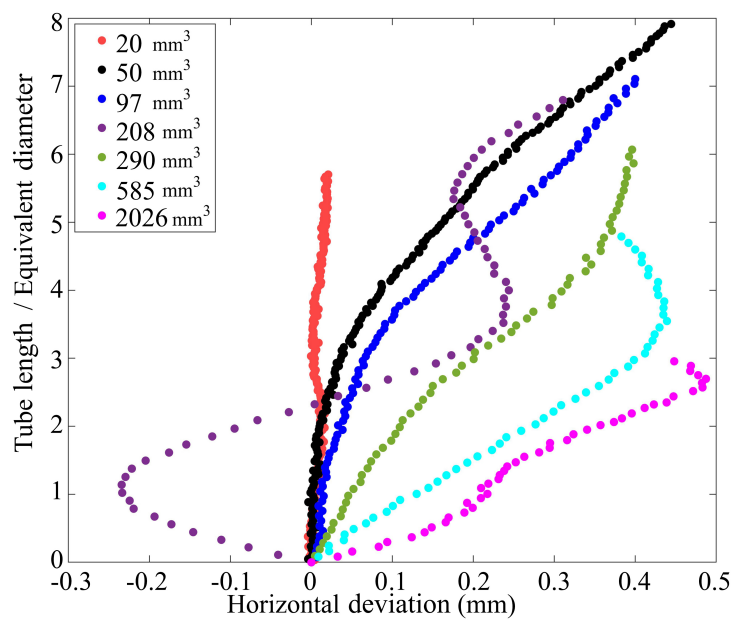


Figure 7.34. The trajectory of bubbles with different volumes in 0.40 wt% PAAM solution.

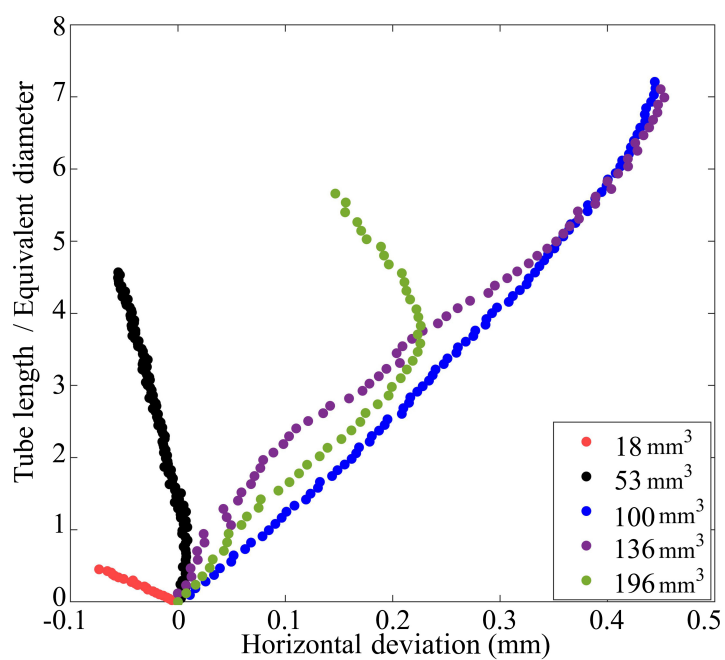


Figure 7.35. The trajectory of bubbles with different volumes in 0.25 wt% PAAM with 100 ppm SDS solution.

### 7.1.6. Unsteady-state Bubble Dynamics

In this section, the evolutions of the bubbles' volumes, shapes and velocities while rising through the liquid are given. The unsteady results are presented as a function of the tube length (the vertical distance travelled by the bubble)/equivalent diameter. Here the bubble volume, the bubble velocity and an example shape parameter are given for 0.25 wt% PAAM, 0.40 wt% PAAM and 0.25 PAAM with 100 ppm SDS solutions.

In Figure 7.36, the evolution of the bubble volume for 0.25 wt% PAAM solution. The results show that the bubble volume reaches steady state except the highest bubble volume, 1985 mm<sup>3</sup>. When a similar bubble volume range is studied for 0.40 wt% PAAM solution (Figure 7.37), a similar observation is done. However, the oscillation in the largest bubble volume (2026 mm<sup>3</sup>) decreases as the polymer concentration increases. A smaller range of bubble volume is studied for 0.25 wt% in the presence of 100 ppm SDS, given in Figure 7.38. Hence, no such unsteady behavior is observed.

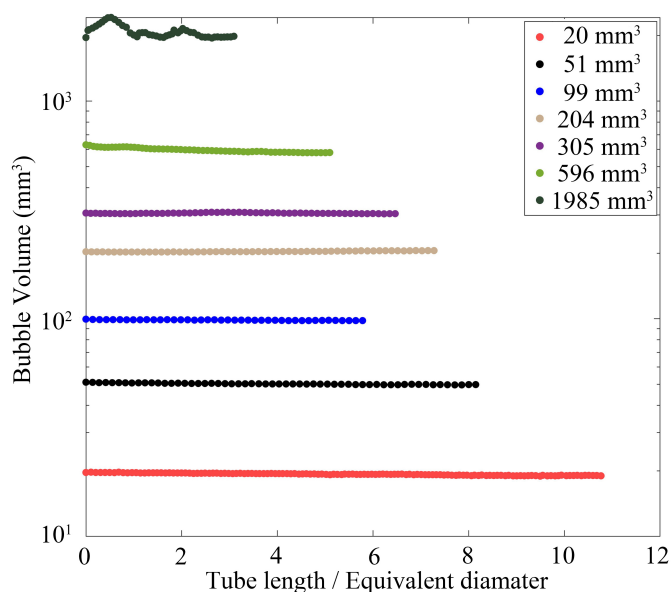


Figure 7.36. The evolution of the bubble volume as a function of tube length/equivalent diameter for 0.25 wt% PAAM.

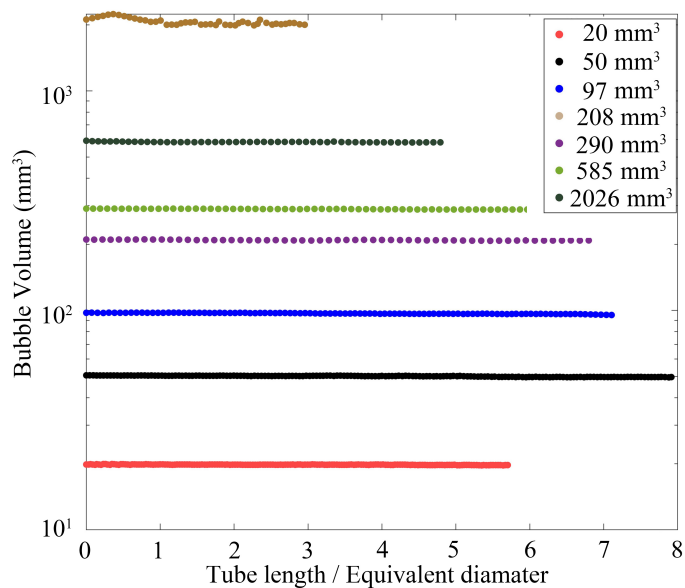


Figure 7.37. The evolution of the bubble volume as a function of tube length/equivalent diameter for 0.40 wt% PAAM.

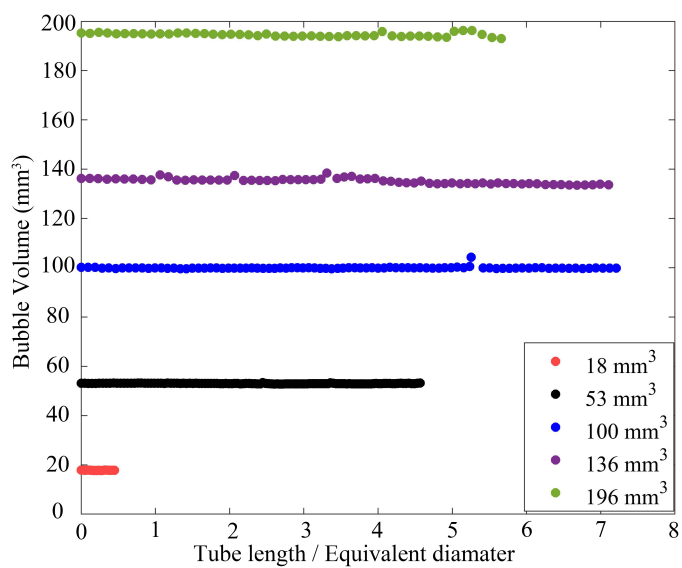


Figure 7.38. The evolution of the bubble volume as a function of tube length/equivalent diameter for 0.25 wt% PAAM with 100 ppm SDS.

The next parameter studied is the bubble velocity and given in Figures 7.39, 7.40 and 7.41 for three different concentrations. Similarly, an ongoing oscillation occurs for  $1985 \text{ mm}^3$  in Figure 7.39 due to the wobbling of the bubble. Therefore, this size of bubble should not be considered in steady-state analysis. Especially, when SDS is added, the oscillation amplitude is larger. When Figures 7.40 and 7.41 are studied, it is seen that it takes longer time for the velocity to reach the steady-state compared to the volume.

Finally, the shape parameter, minor axis,  $a$ , is chosen as an example and presented in Figures 7.42, 7.43 and 7.44 for 0.25 wt% PAAM, 0.40 wt% PAAM and 0.25 wt PAAM with SDS solutions, respectively. It is observed that there occurs small changes at the beginning of the motion, then the bubbles reach a steady-state value for the rest of the distance travelled. Again,  $1985 \text{ mm}^3$  in Figure 7.42 and  $2026 \text{ mm}^3$  in Figure 7.43 show oscillations for the recorded distance. The rest of the bubbles presented in Figures 7.42, 7.43 and 7.44 reach a steady-state value quickly. The largest bubbles of both Tables 7.2 and 7.3 show oscillation and marked with a sign, \*; and their bubble dynamics results are not given. Also, the step changes (for example  $50 \text{ mm}^3$  in Figure 7.43) are observed due the replacement of  $a$  with the shape parameter,  $b$  as the bubble expands horizontally.

The results show that it is necessary to do an unsteady-state pre-analysis to determine the safe bubble volume range to present steady results for the chosen solution and the distance recorded. For an unsteady-state analysis, it is important to observe the motion of a bubble for a long distance (tube length).

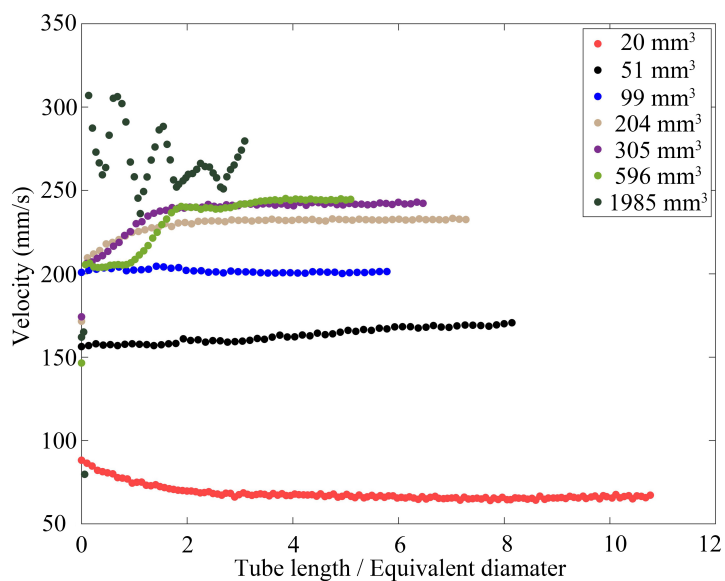


Figure 7.39. The evolution of the bubble velocity as a function of tube length/equivalent diameter for 0.25 wt% PAAM.

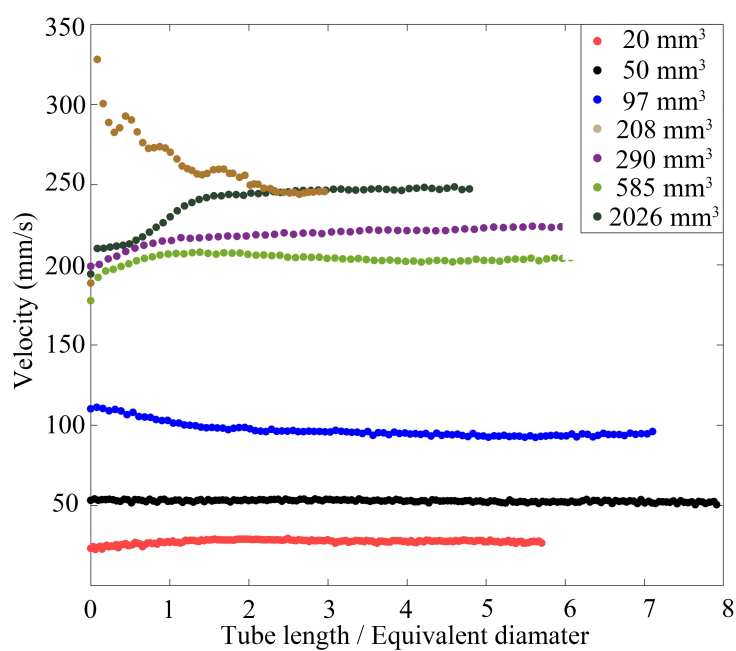


Figure 7.40. The evolution of the bubble velocity as a function of tube length/equivalent diameter for 0.40 wt% PAAM.

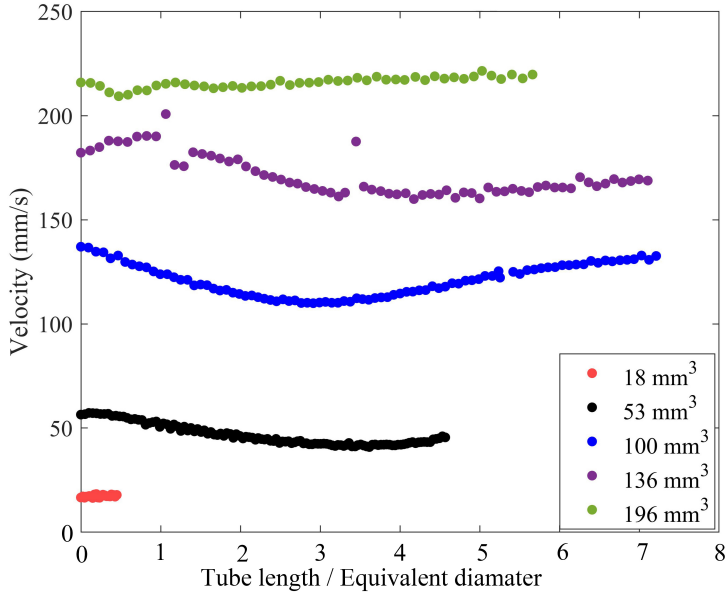


Figure 7.41. The evolution of the bubble velocity as a function of tube length/equivalent diameter for 0.25 wt% PAAM with 100 ppm SDS.

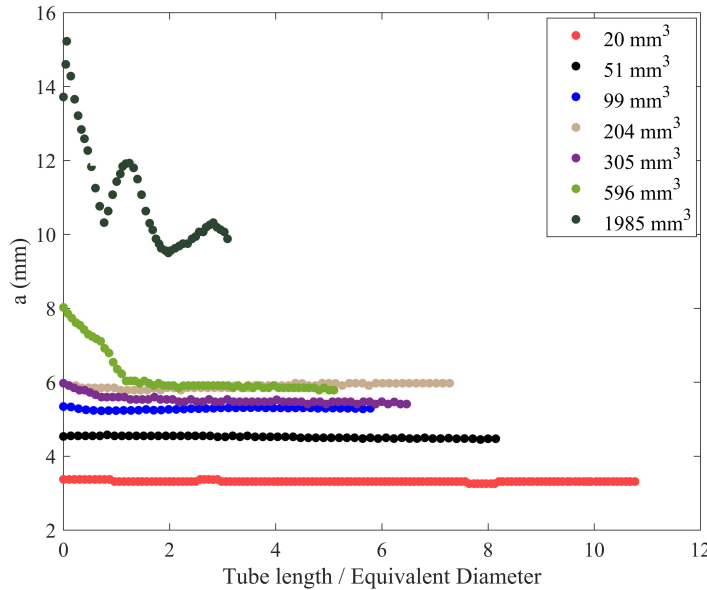


Figure 7.42. The evolution of the shape parameter, a as a function of tube length/equivalent diameter for 0.25 wt% PAAM.

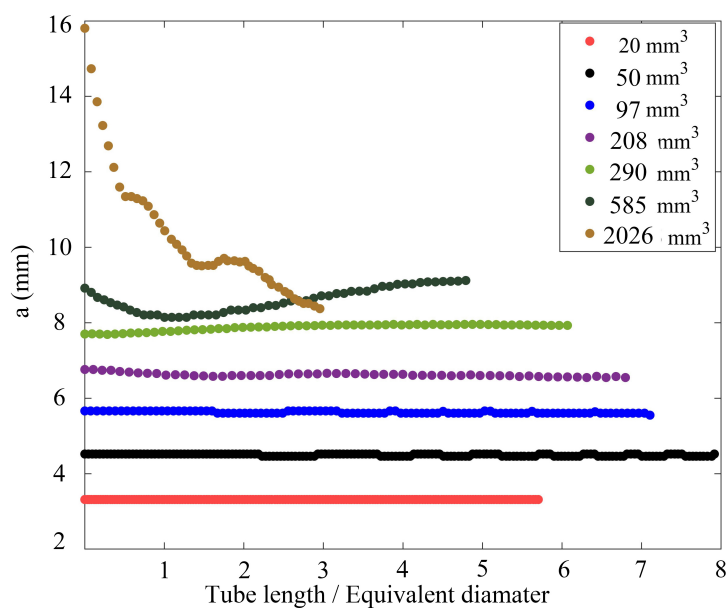


Figure 7.43. The evolution of the shape parameter,  $a$  as a function of tube length/equivalent diameter for 0.40 wt% PAAM.

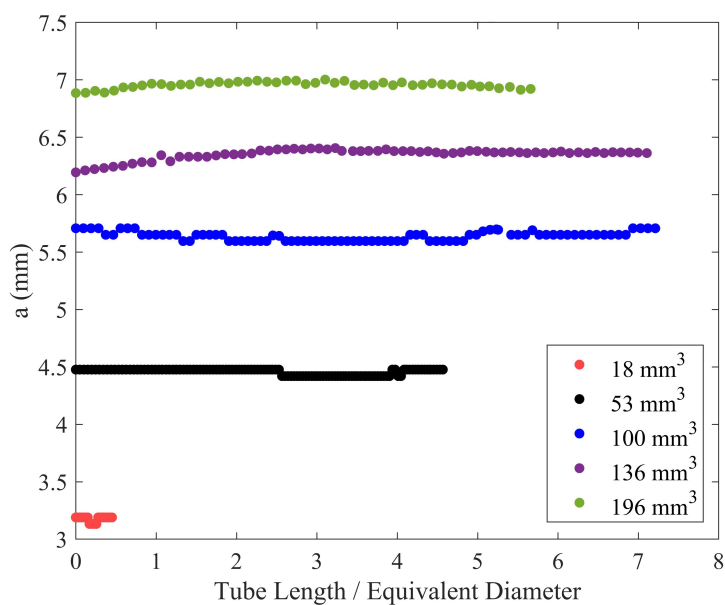


Figure 7.44. The evolution of the shape parameter,  $a$  as a function of tube length/equivalent diameter for 0.25 wt% PAAM with 100 ppm SDS.

## 7.2. Birefringence Measurements and Bubble Dynamics for Different PAAM Concentrations with 0.40 wt% HPC

### 7.2.1. Bubble Dynamics for Different PAAM Concentrations with 0.40 wt% HPC

The stress measurement around the rising bubble could not be obtained in polyacrylamide (PAAM) solutions as PAAM is not birefringent enough. Hence, hydroxypropyl cellulose (HPC) is added. In this section, HPC concentration is kept constant at 0.40 wt%. Therefore, the legends of the graphs do not include the concentration information to avoid crowded legends.

When the bubble dynamics of the PAAM solutions are studied, it is observed that bubbles in 0.10 wt% PAAM showed a 3D motion. However, when HPC is added to the same solution, bubbles exhibit axysymmetric motion. It should be noted that when 0.40 wt% HPC is added to the 0.40 wt% PAAM solution, the solution becomes extremely viscous and is not employed in this study.

First, the average bubble terminal velocity is presented in Figure 7.45. The bubble volume range is between 20 and 3500 mm<sup>3</sup> for 0.10 and 0.18 wt% PAAM solutions, whereas the range starts from 100 mm<sup>3</sup> for 0.25 wt%. Similar to the only PAAM solutions, there is no sign of velocity jump at some critical bubble volume. Similarly, in all solutions, the terminal velocity versus the bubble volume reaches a plateau value. The average bubble terminal velocity in a HPC added solution is lower than that in only PAAM solution.

The first shape parameter is the extent which shows the ratio of the area of the bubble to the area of its bounding box. It can be seen from Figure 7.46 that until 150 mm<sup>3</sup>, this parameter is concentration independent. However, the decrease in the extent value slows down for 0.10 wt% PAAM solution where the decrease is much faster for the other solutions. Consequently, the extent for bubbles larger than 150 mm<sup>3</sup> in a

0.10 wt% PAAM solution, is smaller than for bubbles in other solutions. The bubble becomes more concave as the polymer concentration increases which can also be seen from Tables 7.7, 7.8 and 7.9. Also, a bubble with a volume of around  $100 \text{ mm}^3$  in a HPC added 0.25 wt% PAAM solution, is more concave. One can attribute this change to the increase in the viscoelasticity of the solution.

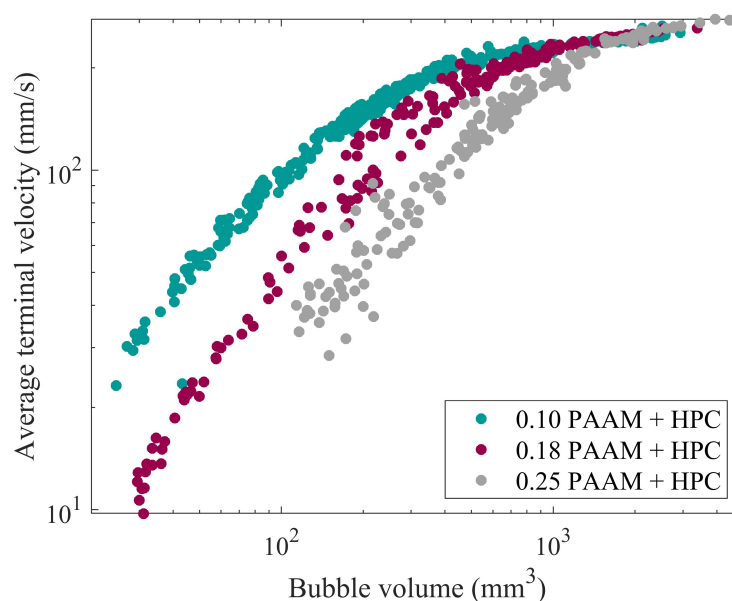


Figure 7.45. The average terminal velocity as a function of the bubble volume for different concentrations of PAAM with 0.40 wt% HPC solution.

Next, the shape parameter, solidity is studied in Figure 7.47. The solidity directly measures the concavity of a bubble. Previously, it was reported that this parameter is independent of the polymer concentration (Figure 7.6) but is significantly affected by the addition of the surfactant into the solution. Figure 7.47 shows that the solidity is again concentration independent. The rapid decrease in the solidity (increase in the concavity) is clear in Table 7.7 as the volume increases from  $748$  to  $1000 \text{ mm}^3$ .

When there is no HPC in the PAAM solution (Figure 7.7), the circularity is constant around 1 until  $150 \text{ mm}^3$  bubble volume. However, once HPC is added, the circularity decreases starting from a bubble volume of  $70 \text{ mm}^3$  (Figure 7.48). The bubbles of the lowest PAAM concentration are close to the circular shape. Table

Table 7.7. Parameters and dimensionless numbers for 0.10 wt% PAAM + 0.4 wt% HPC (part 1/2).

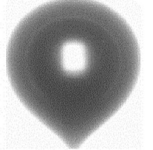
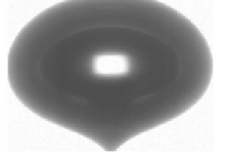
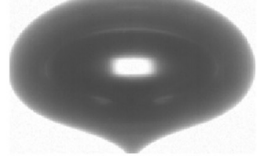
Bubble	V	d	$U_B$	a/b	a	b	C	Ext	Sol	E-1	E-2	$\beta$	$\dot{\gamma}$	Re	Bo	We	Ca	$C_D$
	31	4	34	1.6	3.85	2.34	-	0.75	0.986	0.86	1.01	-	8.62	0.72	2.01	6.E-02	1.2	45
	104	6	99	1.6	5.81	3.69	0.97	0.72	0.989	0.85	1.00	-	16.92	4.21	4.51	8.E-01	3.4	8
	197	7	141	1.6	7.22	4.47	0.96	0.71	0.990	0.89	1.00	-	19.49	7.90	6.91	2.E+00	4.9	5
	498	10	217	1.5	8.46	5.70	0.93	0.71	0.984	0.74	1.16	-	22.02	17.44	12.82	6.E+00	7.5	3
	748	11	226	1.3	8.92	6.83	0.88	0.70	0.977	0.65	1.26	-	20.03	19.97	16.81	8.E+00	7.8	3

Table 7.7. Parameters and dimensionless numbers for 0.10 wt% PAAM + 0.4 wt% HPC (part 2/2).

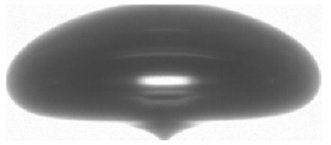
Bubble	V	d	$U_B$	a/b	a	b	C	Ext	Sol	E-1	E-2	$\beta$	$\dot{\gamma}$	Re	Bo	We	Ca	$C_D$
	1004	12	235	1.1	8.68	8.01	0.81	0.70	0.967	0.54	1.43	-	18.90	22.37	20.46	9.E+00	8.1	3
	1523	14	237	0.8	8.48	9.99	0.64	0.69	0.934	0.43	1.68	-	16.63	24.62	27.01	1.E+01	8.2	3
	2007	16	243	0.8	8.70	11.28	0.61	0.68	0.930	0.39	1.80	-	15.52	26.81	32.47	1.E+01	8.4	3

Table 7.8. Parameters and dimensionless numbers for 0.18 wt% PAAM + 0.4 wt% HPC (part 1/2).

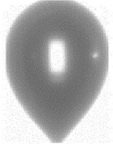
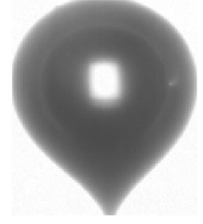
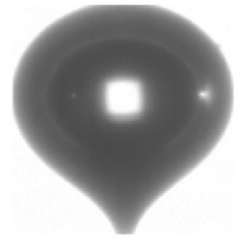
Bubble	V	d	$U_B$	a/b	a	b	C	Ext	Sol	E-1	E-2	$\beta$	$\dot{\gamma}$	Re	Bo	We	Ca	$C_D$
	30	4	11	1.6	3.77	2.39	-	0.75	0.986	0.82	1.02	-	2.76	0.08	1.97	6.E-03	0.9	445
	106	6	51	1.3	5.57	4.25	0.93	0.71	0.989	0.72	1.06	-	8.75	1.01	4.58	2.E-01	4.6	29
	207	7	94	1.4	7.08	5.23	0.93	0.70	0.989	0.75	1.04	-	12.84	2.83	7.14	9.E-01	8.4	11
	496	10	177	1.4	9.66	6.67	0.91	0.67	0.979	0.82	1.02	-	17.98	8.47	12.79	4.E+00	15.7	4
	751	11	202	1.5	11.01	7.19	0.91	0.67	0.972	0.87	1.02	-	17.88	11.07	16.85	6.E+00	18.0	4

Table 7.8. Parameters and dimensionless numbers for 0.18 wt% PAAM + 0.4 wt% HPC (part 2/2).

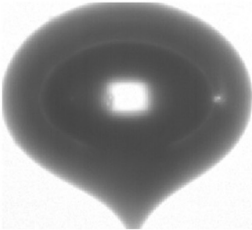
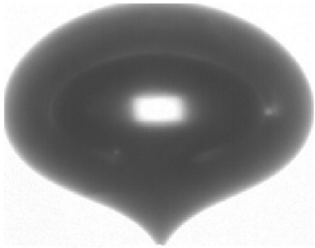
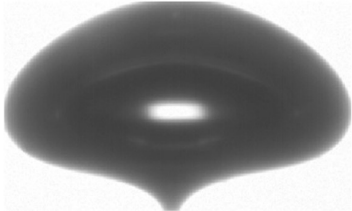
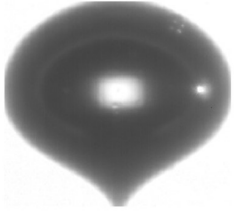
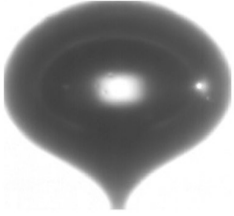
Bubble	V	d	$U_B$	a/b	a	b	C	Ext	Sol	E-1	E-2	$\beta$	$\dot{\gamma}$	Re	Bo	We	Ca	$C_D$
	981	12	224	1.7	11.47	6.83	0.91	0.67	0.971	0.84	1.07	-	18.16	13.55	20.14	8.E+00	20.0	3
	1495	14	244	-	-	-	0.89	0.66	0.963	-	1.11	-	17.18	16.49	26.69	1.E+01	21.7	3
	2065	16	249	-	-	-	0.80	0.66	0.952	-	1.32	-	15.78	17.97	33.09	1.E+01	22.2	3

Table 7.9. Parameters and dimensionless numbers for 0.25 wt% PAAM + 0.4 wt% HPC (part 1/2).

Bubble	V	d	$U_B$	a/b	a	b	C	Ext	Sol	E-1	E-2	$\beta$	$\dot{\gamma}$	Re	Bo	We	Ca	$C_D$
	116	6	33	1.3	5.64	4.43	0.91	0.72	0.982	0.69	1.07	-	5.51	0.28	4.86	9.E-02	8.5	71
	206	7	53	1.2	6.84	5.50	0.91	0.71	0.989	0.69	1.07	-	7.19	0.62	7.12	3.E-01	13.4	35
	505	10	119	1.2	9.42	8.09	0.85	0.66	0.979	0.67	1.05	-	12.02	2.56	12.95	2.E+00	30.2	9
	750	11	159	1.3	11.11	8.56	0.85	0.66	0.974	0.75	1.01	-	14.15	4.32	16.84	4.E+00	40.6	6

Table 7.9. Parameters and dimensionless numbers for 0.25 wt% PAAM + 0.4 wt% HPC (part 2/2).

Bubble	V	d	$U_B$	a/b	a	b	C	Ext	Sol	E-1	E-2	$\beta$	$\dot{\gamma}$	Re	Bo	We	Ca	$C_D$
	998	12	189	1.4	12.30	9.04	0.85	0.66	0.966	0.79	1.01	-	15.27	5.90	20.38	6.E+00	48.2	5
	1548	14	244	1.7	13.19	7.97	0.92	0.68	0.978	0.83	1.09	-	16.99	9.37	27.30	1.E+01	62.1	3
	2016	16	249	-	-	-	0.86	0.65	0.951	-	1.06	-	15.89	10.04	32.57	1.E+01	63.4	3

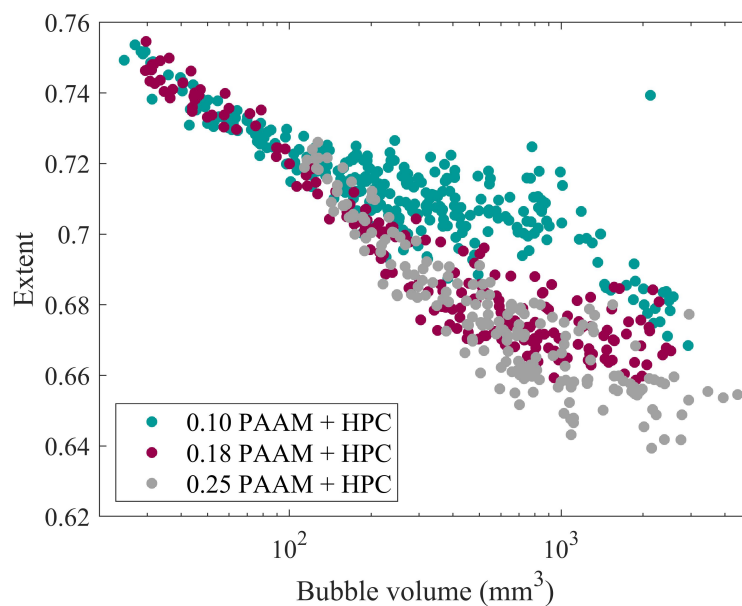


Figure 7.46. Shape parameter, extent as a function of the bubble volume for different concentrations of PAAM with 0.40 wt% HPC solution.

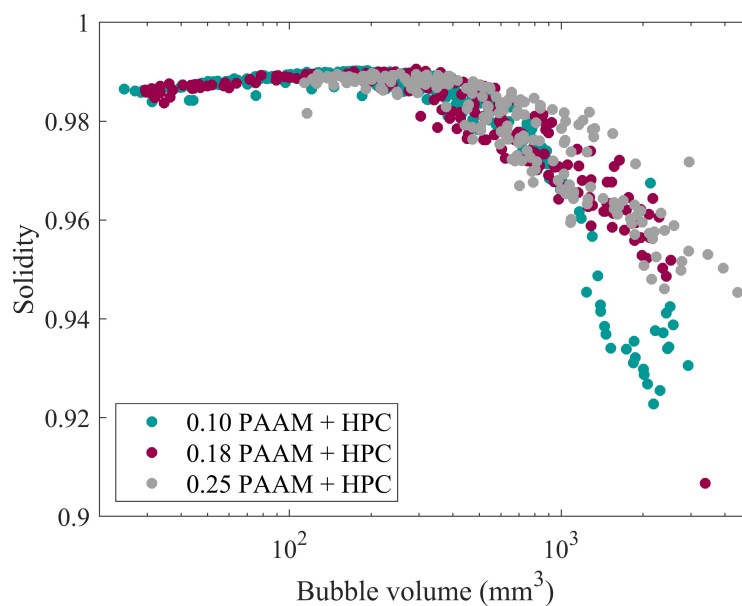


Figure 7.47. Shape parameter, solidity as a function of the bubble volume for different concentrations of PAAM with 0.40 wt% HPC solution.

7.7 shows that the bubbles of 10 wt% PAAM solution rapidly extend horizontally after reaching a critical volume, which is 550 mm<sup>3</sup>. Tables 7.8 and 7.9 show that the bubbles are first elongated vertically until the critical volume, then they start expanding horizontally and become closer to a circular shape until very high bubble volumes (> 1000 mm<sup>3</sup>). This oscillation in the circularity is not observed for the PAAM solutions in the absence of HPC nor when a surfactant is added.

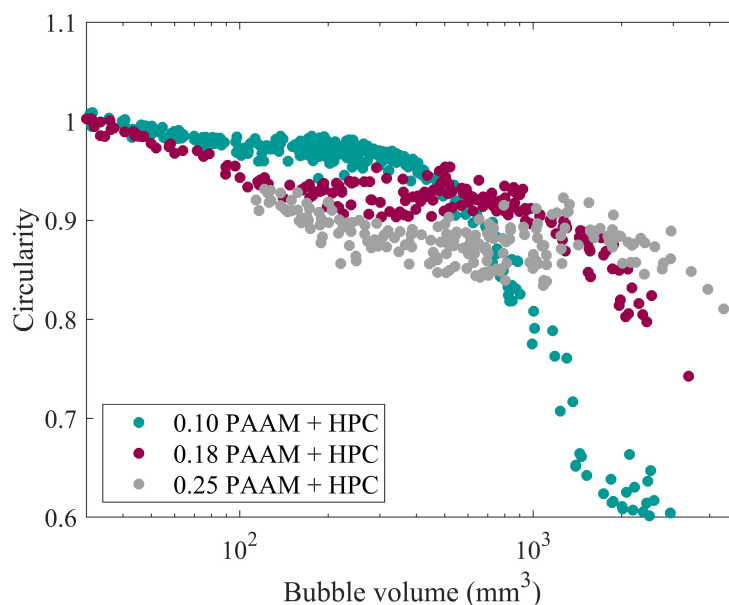


Figure 7.48. Shape parameter, circularity as a function of the bubble volume for different concentrations of PAAM with 0.40 wt% HPC solution.

Next,  $a$ ,  $b$  and  $a/b$  shape parameters are investigated in Figures 7.49, 7.50 and 7.51. It is mentioned in Sections 7.1.2 and 7.1.4 that as the bubble sizes grow horizontally,  $a$  and  $b$  are swapped. Figure 7.49 shows that the  $a$  is independent of the polymer concentration until a bubble volume of around 1000 mm<sup>3</sup>. Afterwards,  $a$  and  $b$  are swapped for bubbles in 0.10 and 0.18 wt% PAAM. A similar behaviour is observed for  $b$  (Figure 7.50). When the plot of  $a/b$  is analyzed in Figure 7.51, one can say that bubbles grow vertically first, then horizontally. Similar observations can be done for the eccentricity-1,  $E1$  (Figure 7.52) as for  $a/b$  parameter. The bubbles show a horizontally expanding eccentric (elliptic) shape for volumes higher than 100, 200 and 325 mm<sup>3</sup> rising in 0.10, 0.18 and 0.25 wt% PAAM solutions with HPC, respectively.

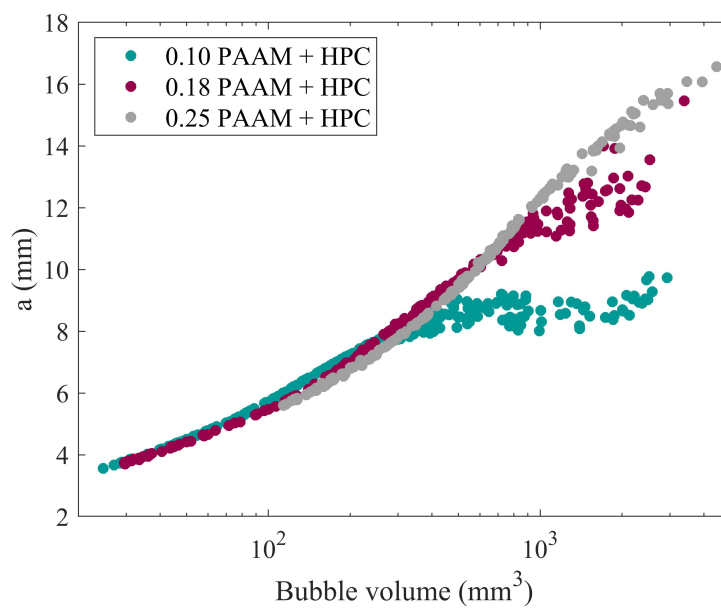


Figure 7.49. Shape parameter, minor axis,  $a$  as a function of the bubble volume for different concentrations of PAAM with 0.40 wt% HPC solution.

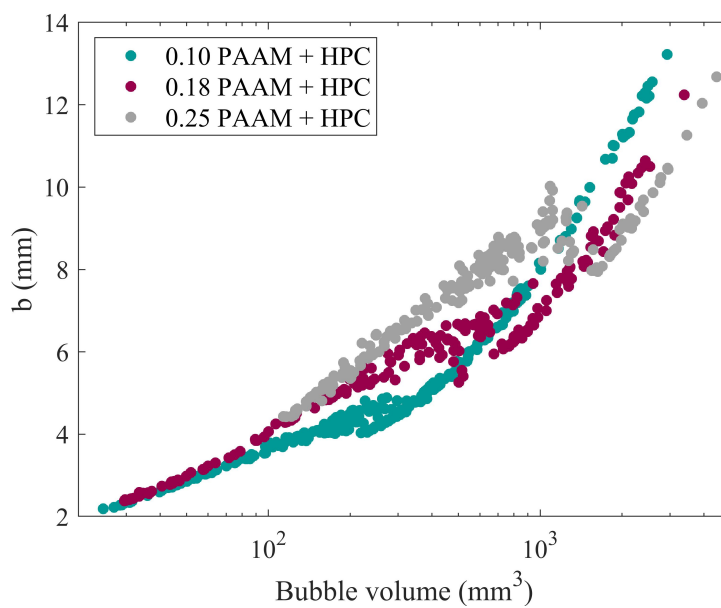


Figure 7.50. Shape parameter,  $b$  as a function of the bubble volume for different concentrations of PAAM with 0.40 wt% HPC solution.

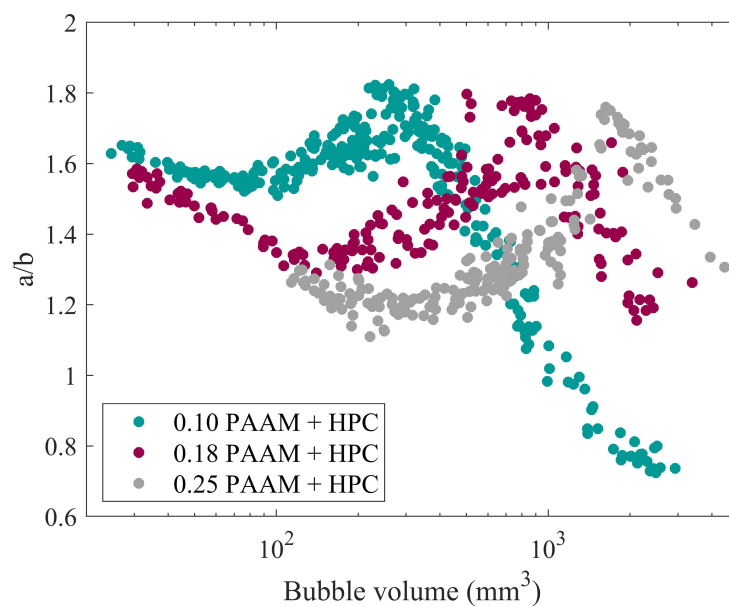


Figure 7.51. Shape parameter, the ratio of the minor axis to b,  $a/b$  as a function of the bubble volume for different concentrations of PAAM with 0.40 wt% HPC solution.

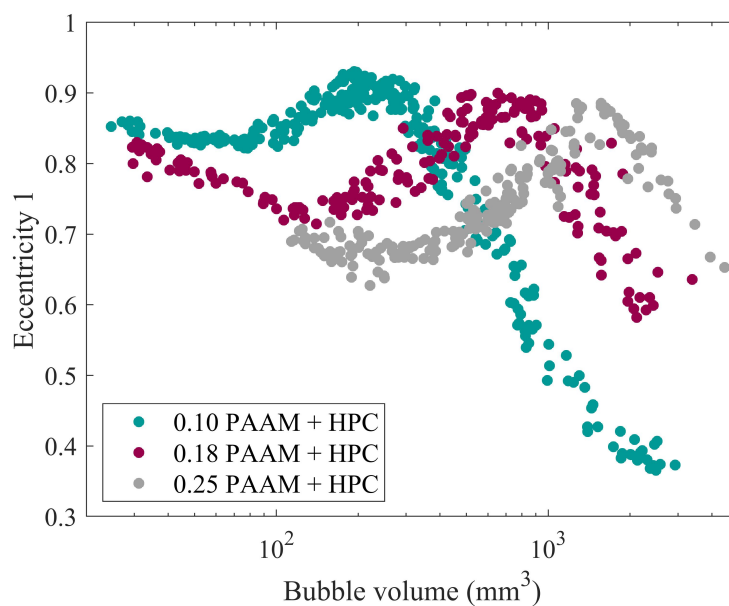


Figure 7.52. Shape parameter, eccentricity-1,  $E1$  as a function of the bubble volume for different concentrations of PAAM with 0.40 wt% HPC solution.

The shape parameter, eccentricity-2 informs about the circularity. Figure 7.53 shows that as the concentration of the polymer increases the bubble deviates more from the circular shape and become more elliptic. Tables 7.7, 7.8 and 7.9 also show largest bubbles in the 0.10 wt% PAAM solution are more elliptic. These observations with the circularity shape parameter results verify that the bubbles are axysymmetric.

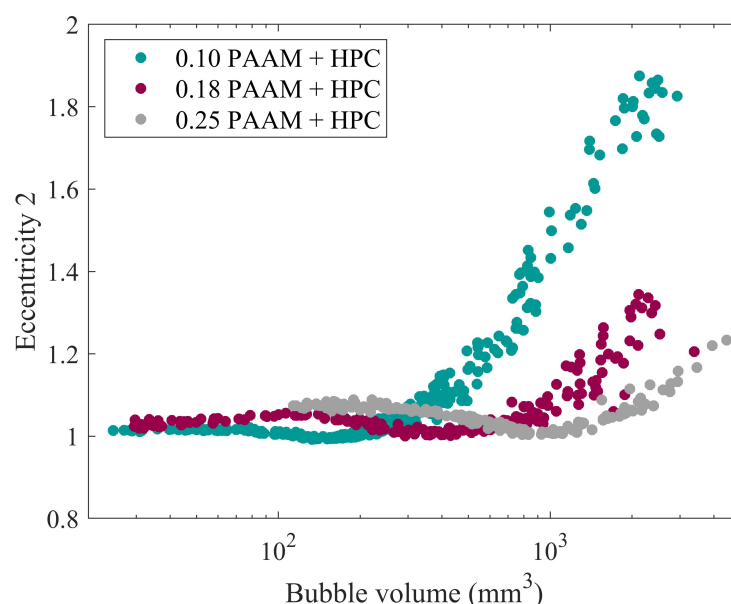


Figure 7.53. Shape parameter, eccentricity-2, E2 as a function of the bubble volume for different concentrations of PAAM with 0.40 wt% HPC solution.

The last shape parameter for this section is  $\beta$  which shows the presence of a cusp at the tip of the bubble. In Sections 7.1.2 and 7.1.4, it is shown that this parameter works well for a certain bubble volume range and predicts the critical bubble volume successfully. The shape parameter,  $\beta$  results are presented in Figure 7.54. It is found that the  $\beta$  value is below 0.6 which indicates that a cusp should be formed for the entire bubble volume range. However, the determination coefficient,  $R^2$  is highly below 0.9. Therefore, one can say that this parameter does not work when HPC is added into the PAAM solutions. The bubble shapes can be seen from Tables 7.7, 7.8 and 7.9 where there is a cusp formation. One should remember that this parameter is obtained empirically for only PAAM solutions [37]. Adding 0.40 wt% HPC, which may be responsible for this incompatibility, changes the rheological properties.

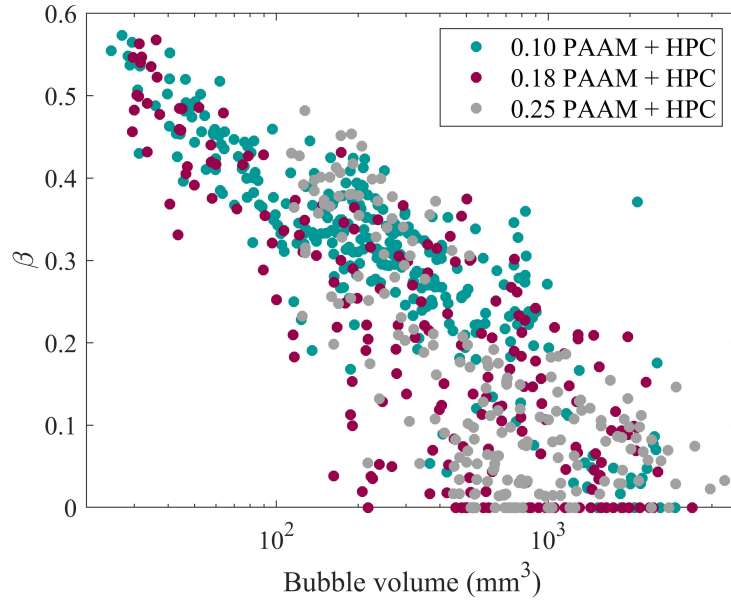


Figure 7.54. Shape parameter,  $\beta$  as a function of the bubble volume for different concentrations of PAAM with 0.40 wt% HPC solution.

The first dimensionless number studied in this section is the  $Bo$  number and given in Figure 7.55. For a constant PAAM concentration, when the rheological properties of the solutions are compared (Table 3.4), it can be seen that the flow consistency index,  $K$  increases highly with the addition of HPC. Also, for a given bubble diameter, the terminal velocity decreases. Both of these changes cause a decrease in  $Re$  for a given bubble diameter. For a given bubble volume,  $Bo$  is constant ( $Bo \approx 13$  for  $490 \text{ mm}^3$  in Table 7.2 and  $505 \text{ mm}^3$  in Table 7.9). Therefore, we can say that this plot is shifted to the left when HPC is added into the PAAM solution at constant concentration.

Next,  $Ca$  is studied in Figure 7.56. The behaviour is similar to that without HPC as presented in Figure 7.16. The terminal velocity of the bubbles decrease and the viscosity of the solution increases as HPC is added. The contribution of the viscosity is dominant; therefore,  $Ca$  increases.

The behavior of the Weber,  $We$ , versus  $Re$  (Figure 7.57) is similar to what is obtained without HPC (Figure 7.17).  $We$  becomes smaller when HPC is added into

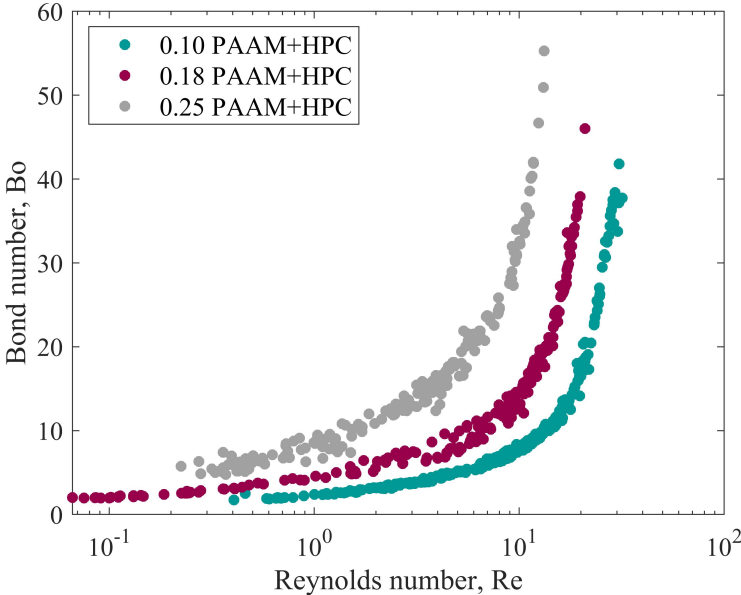


Figure 7.55.  $Bo$  versus  $Re$  for different concentrations of PAAM with 0.40 wt% HPC.

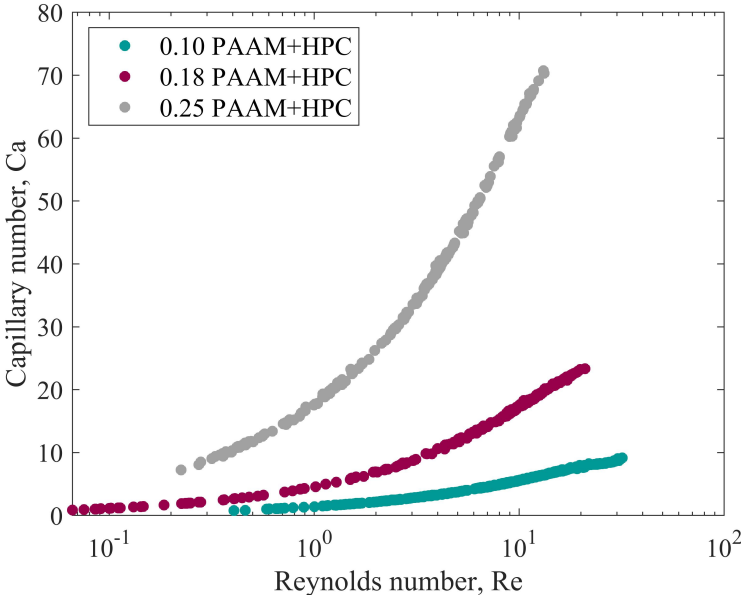


Figure 7.56.  $Ca$  versus  $Re$  for different concentrations of PAAM with 0.40 wt% HPC.

the solution for the 0.25 wt% PAAM. Hence, the inertial forces decrease when HPC is added. However, when the bubble size increases ( $V \approx 2000 \text{ mm}^3$ ),  $We$  stays constant with the HPC addition. Since the bubble terminal velocity reaches the same plateau value, its effect diminishes and both solutions have the same  $We$ .

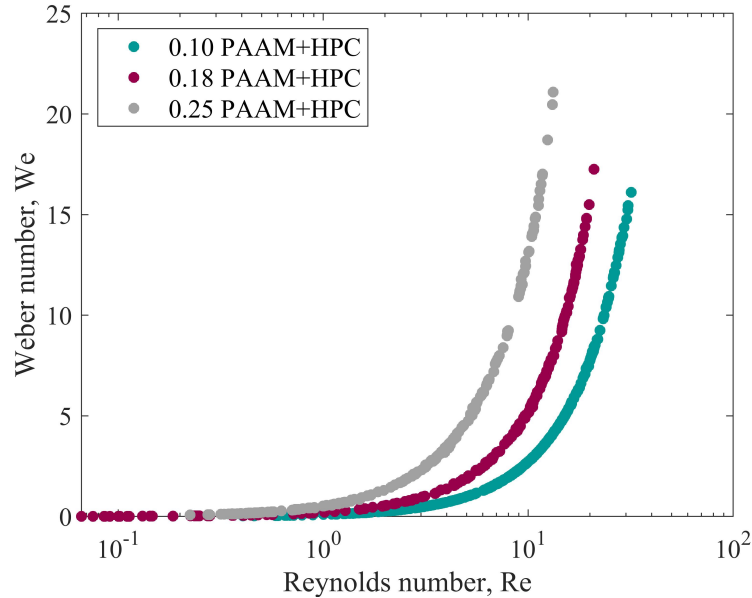


Figure 7.57.  $We$  versus  $Re$  for different concentrations of PAAM with 0.40 wt% HPC Bo against  $Re$  for different concentrations of PAAM solution.

Finally,  $C_D$  is presented in Figure 7.58. In the presence of HPC, only 0.25 wt% PAAM is close to the Hadamard-Rybczynski regime for  $Re < 1$ , and it fits  $C_{D,3}$  for  $Re > 1$ . However, the other solutions do not fit these regimes. The increase in the  $C_D$  can be attributed to the surface of the bubble becoming more rigid in the presence of HPC.

### 7.2.2. Stress Measurement Through Birefringence

In this section, the results of the stress measurement around a rising bubble will be presented and discussed. The details about the method, the experimental setup and how the stress is quantified are given in Sections 2.3, 4.1 and 5.2, respectively.

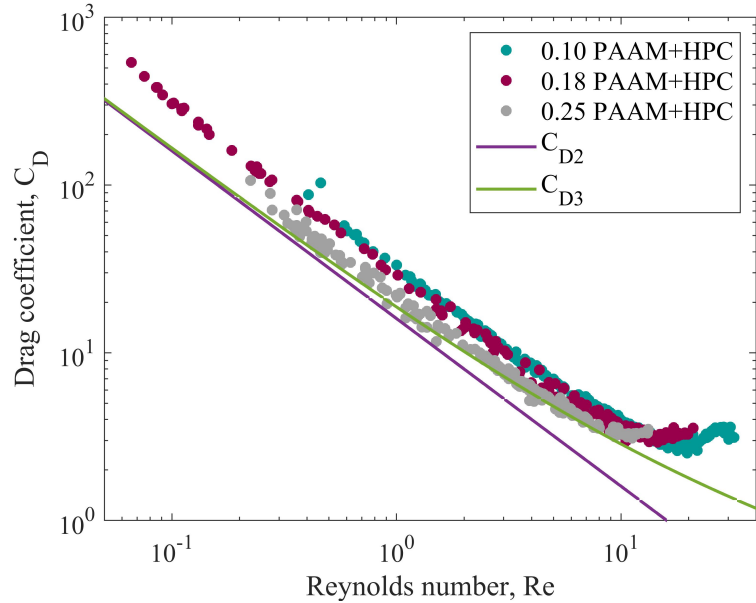


Figure 7.58.  $C_D$  versus  $Re$  for different concentrations of PAAM with 0.40 wt% HPC.

In the literature, for some work the presence of the discontinuity is attributed to the formation of a negative wake at the trailing tip of the bubble, or to the cusp formation. On the other hand, some work argue that the discontinuity in the velocity and the cusp formation are not related.

In the previous section (Section 7.2.1), we report that there is no discontinuity at the velocity for the polymer, the concentration and the bubble volume range investigated. Therefore, in this section, the focus is on the stress around the bubble and to explain the relationship between the stress and any of the above quantities, i.e., the cusp formation and the velocity discontinuity, if there is any.

The results are given in terms of the retardance,  $\delta$  and the stretching angle,  $\chi$ . Birefringence,  $\Delta n$  is directly proportional to the retardance with a constant (see Eqn. 5.18). Therefore, it is not given here separately. Both  $\delta$  and  $\chi$  are given for a bubble volume range of 140-1285 mm<sup>3</sup> at three different PAAM concentrations (0.10, 0.18 and 0.25 wt%) in the presence of a constant HPC concentration of 0.40 wt% are presented.

The retardance measurements are presented in Figures 7.59, 7.62 and 7.66 for increasing bubble volume where each column represents a polymer concentration increasing from left to right. Same representation is valid for the stretching angle measurements in Figures 7.60, 7.63 and 7.67. The intensity scales are given on the right side of each row.

The measurements are performed only for the left half of the bubbles as they are assumed axisymmetric. In the previous section, this assumption was proved by analyzing the circularity and eccentricity-2, E2 results together. As the light is deemed due to the polarizers, the recording is not of high resolution. All the cutting of the bubbles into half is automated; however, some are not very clear due to low resolution and the difficulty in edge detection.

When Figure 7.59 is analyzed, the retardance intensity is not high for the given bubble volume range. However, it can still be noticed that the retardance increases from low to high concentration and for a constant polymer concentration, a slight increase can be seen with the growing bubble size. Figure 7.60 also shows a similar pattern, i.e., the polymer stretches more with increasing polymer concentration and the bubble volume. At this bubble volume range, the bubbles have prolate shape and are convex (Figure 7.61). Also, bubbles rising in 10 wt% PAAM solution has the highest average terminal velocity while having the lowest retardance around it (Figure 7.2.2).

As the bubble volume increases, a significant change immediately appears in both  $\delta$  and  $\chi$  as given in Figures 7.62 and 7.63, respectively. It is observed that the stress occurs on top of the bubble due to the squeezing and also around the lower half of the bubbles. The stretching angle,  $\chi$  clearly shows the effect of the increase in the bubble volume for a given bubble concentration in Figure 7.63.

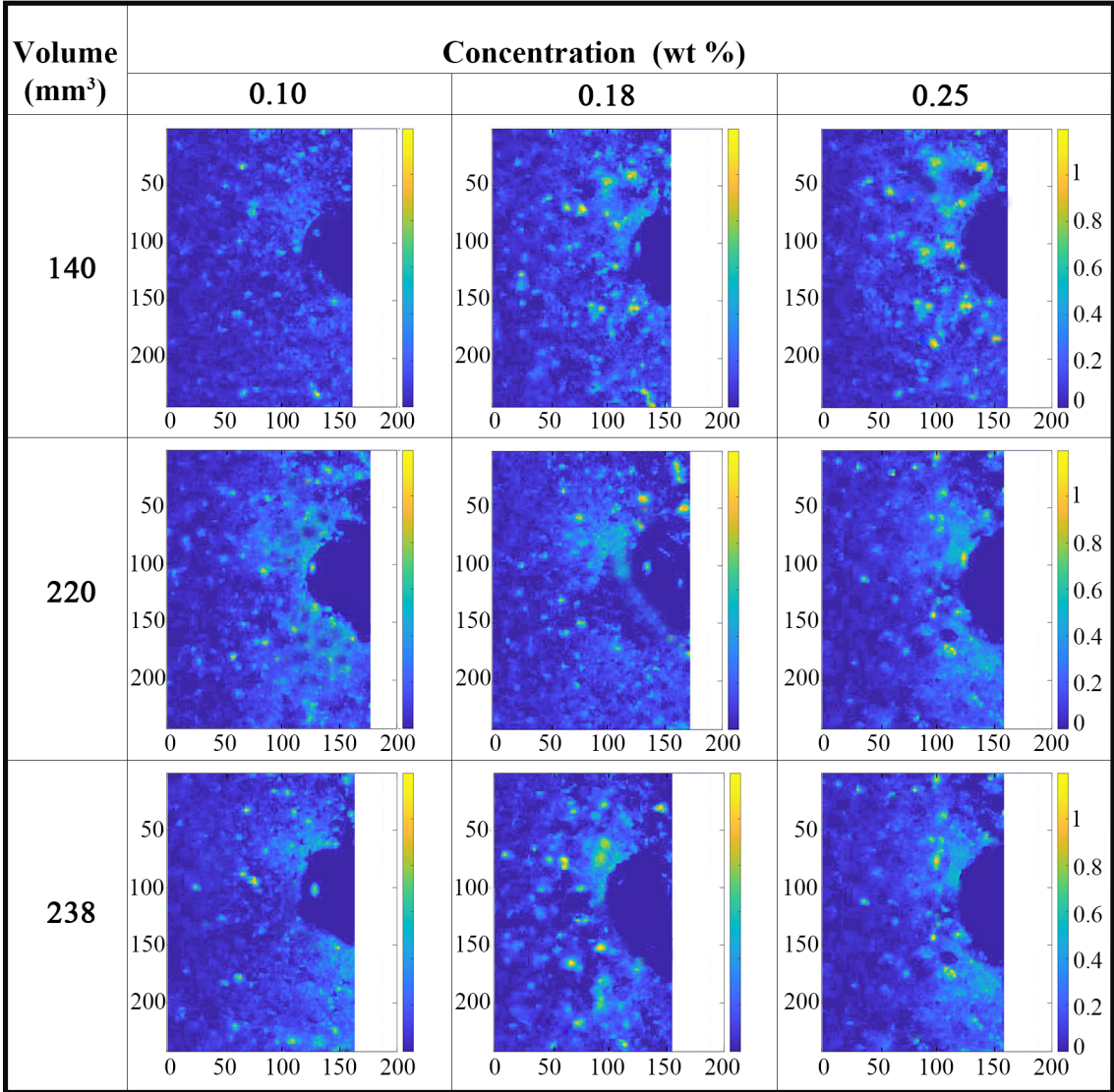


Figure 7.59. The retardance,  $\delta$  measurement for different PAAM concentrations for a bubble volume range of 140-238 mm<sup>3</sup>.

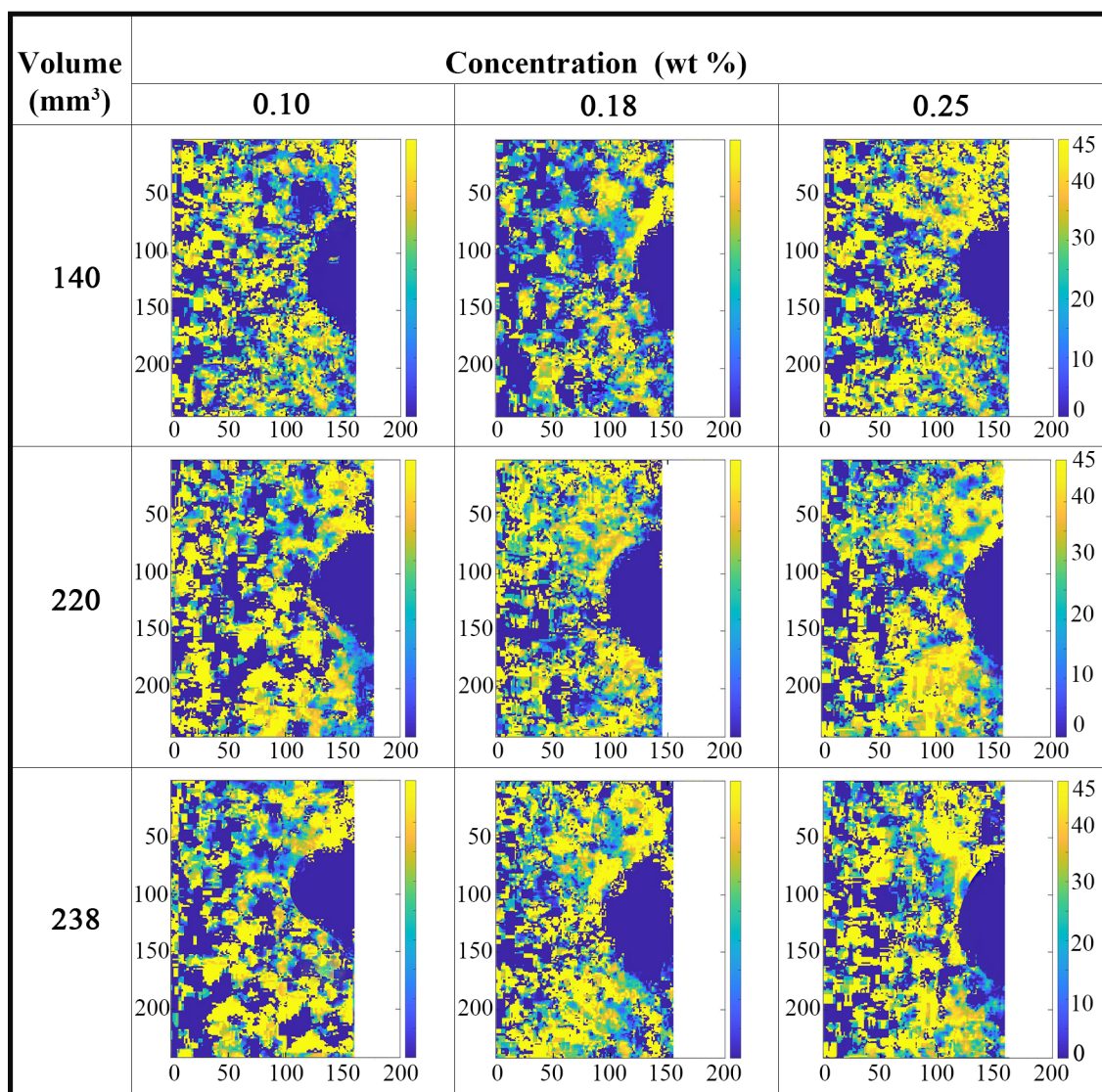


Figure 7.60. The stretching angle,  $\chi$  measurement for different PAAM concentrations for a bubble volume range of 140-238 mm<sup>3</sup>.

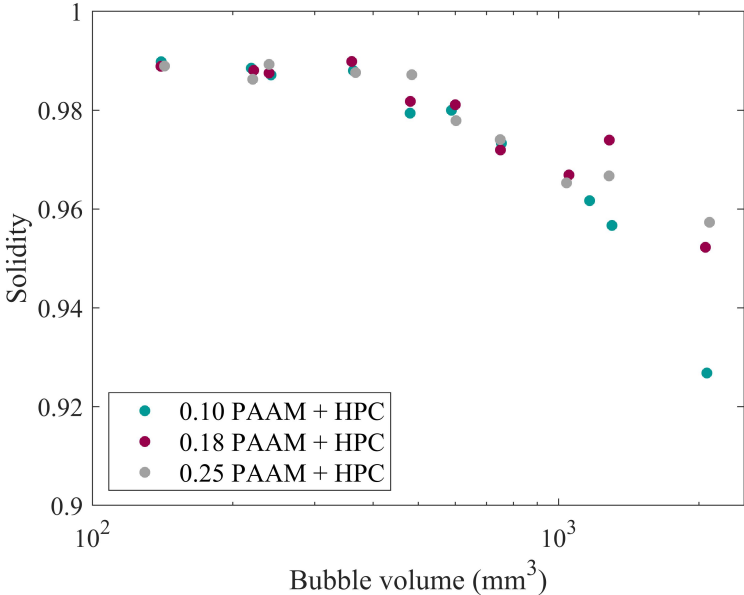
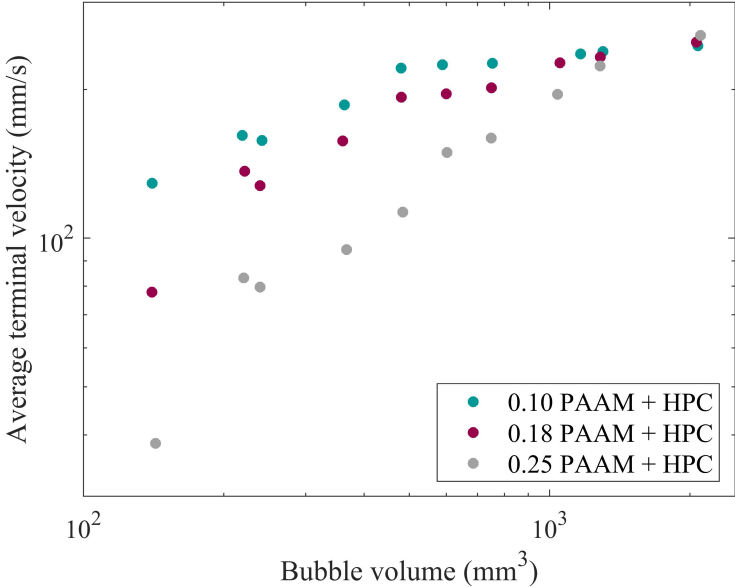


Figure 7.61. Shape parameter, solidity as a function the bubble volume for the bubbles studied in the stress measurement.



In smaller volumes (Figure 7.59), it is observed that the retardance,  $\delta$  is significantly less for low concentration solutions. However, when a larger volume range (360 to 600 mm<sup>3</sup>) is considered in Figure 7.62. it is observed that the  $\delta$  abruptly increases for the lowest polymer concentration. Figure 7.2.2 shows that the terminal velocities of large bubbles in all concentrations are very close to each other. However, a significant difference in  $\delta$  exists at the tail.

The effect of the bubble shape through bubble parameters is investigated on the retardance,  $\delta$ . Figure 7.61 shows that the bubbles have similar concavity for all concentrations until 1000 mm<sup>3</sup> bubble volume. When the shape parameters,  $a$  and  $a/b$  are studied in Figures 7.64 and 7.65, it is seen that the minor axis,  $a$  is replaced with the shape parameter  $b$  as the bubble is highly expanded horizontally, especially for high concentrations. Thus, the sudden increase in the retardance can be linked to the change in the bubble shape. Figure 7.63 shows that the stretching angle,  $\chi$  is dissipated to a wider region as the PAAM concentration increases. The change in the bubble shape for a constant volume can be connected to the dissipation of the intensity.

When the bubble volume range increases to 750-1285 mm<sup>3</sup>, it is observed that the retardance,  $\delta$  (Figure 7.66) significantly increases on the top of the bubble. It is also noticed that the stretching angle,  $\chi$  (Figure 7.67) increases at the trailing tip of the bubbles. The increase in both  $\delta$  and stretching angle,  $\chi$  intensities may be reflecting the negative wake and the cusp formation.

It can be concluded from the birefringence experiment that the stress around a rising bubble is directly in a relationship with the bubble shape. As the bubble volume increases, this relationship becomes more prominent. Even though, we could not characterize the cusp formation with the empirical shape parameter,  $\beta$  due to the addition of HPC, the bubbles showed a cusp formation (see Tables 7.7, 7.8 and 7.9). We proved that the cusp formation and the stress occurring at the tip of the bubble are not prerequisites for the the discontinuity at the bubble terminal velocity.

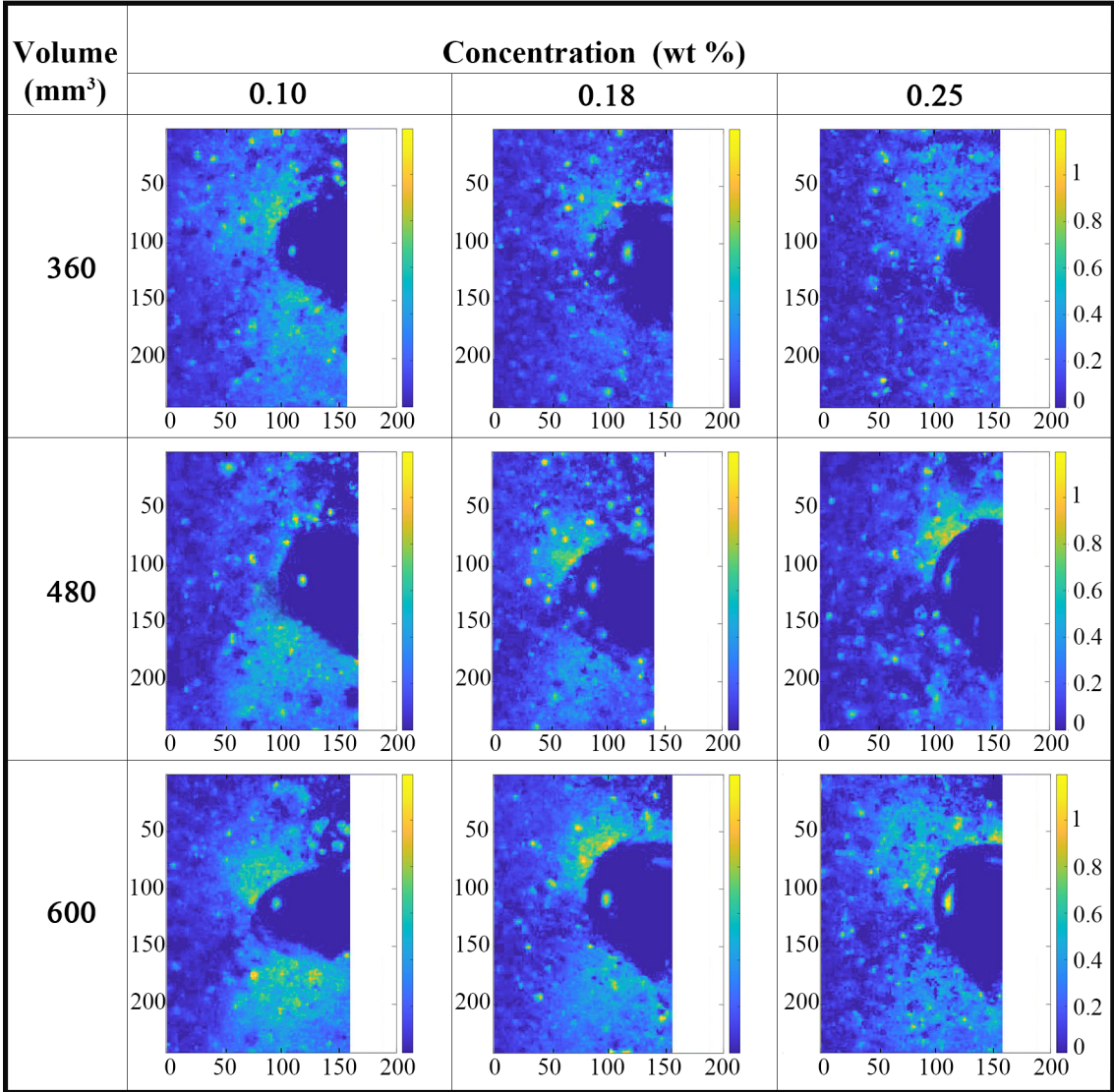


Figure 7.62. The retardance,  $\delta$  measurement for different PAAM concentrations for a bubble volume range of 360-600 mm<sup>3</sup>.

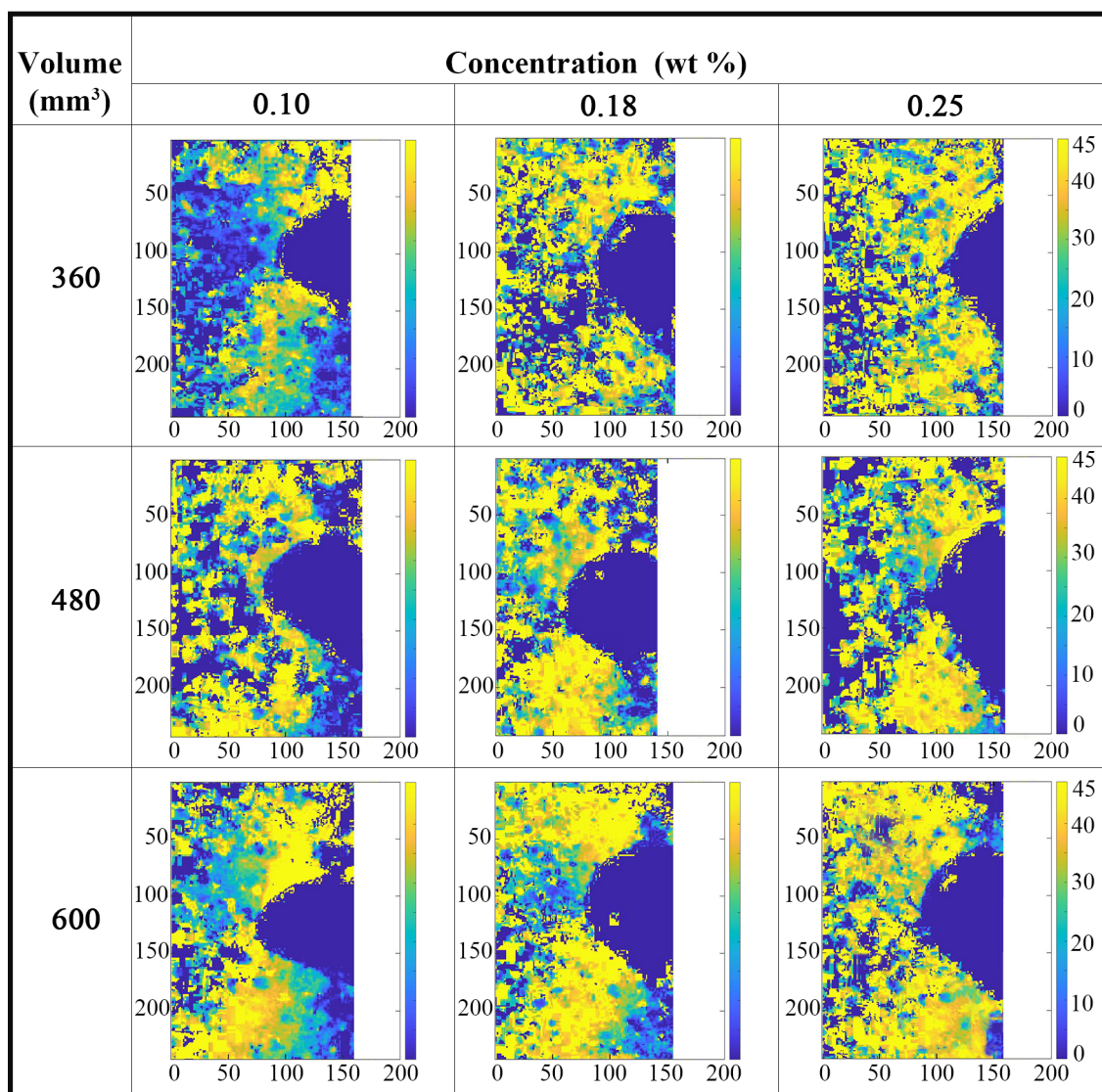


Figure 7.63. The stretching angle,  $\chi$  measurement for different PAAM concentrations for a bubble volume range of 360-600 mm<sup>3</sup>.

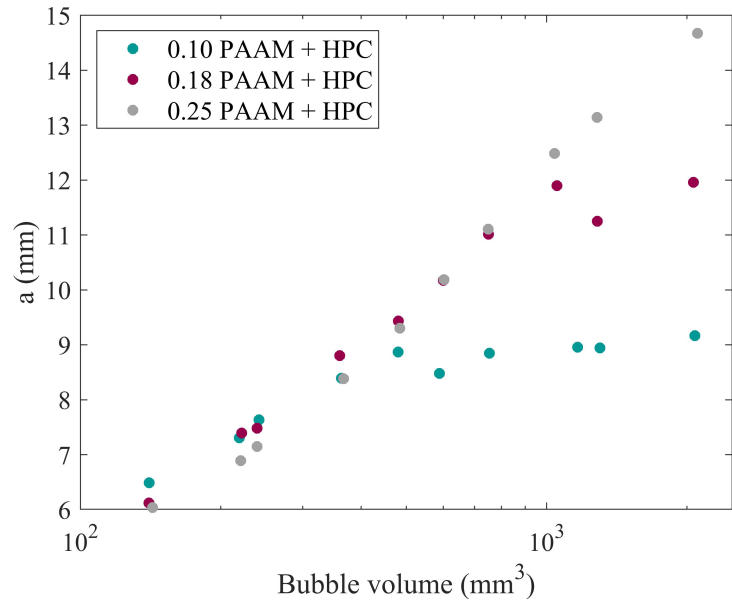


Figure 7.64. Shape parameter, minor axis,  $a$  as a function the bubble volume for the bubbles studied in the stress measurement.

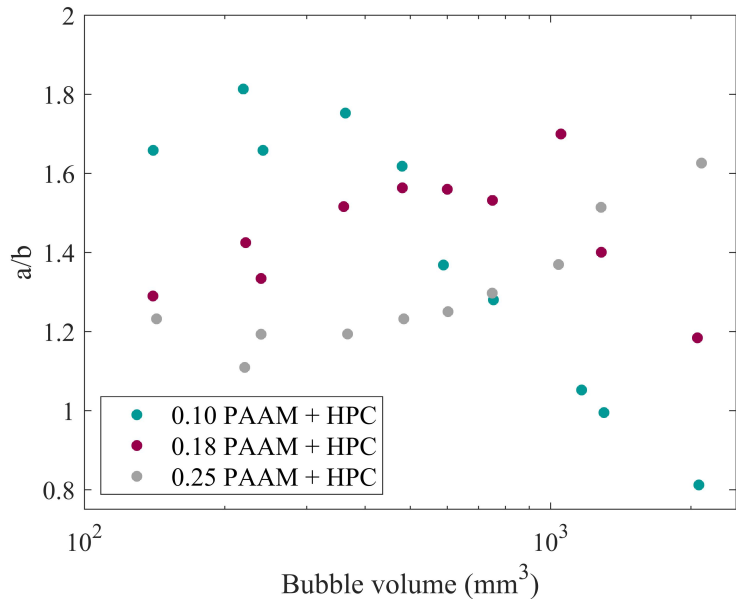


Figure 7.65. Shape parameter, the ratio of the minor axis to  $b$ ,  $a/b$  as a function the bubble volume for the bubbles studied in the stress measurement.

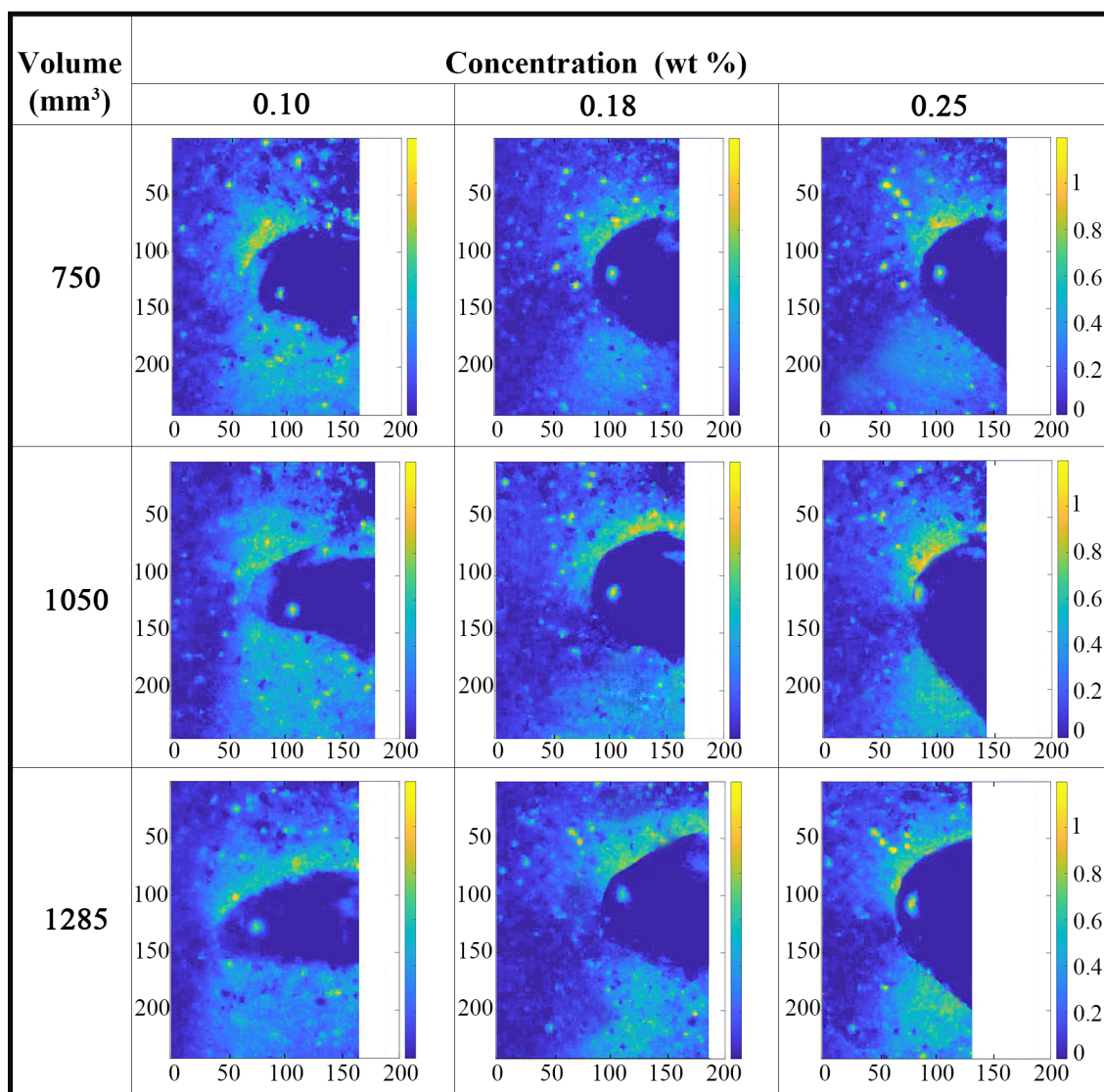


Figure 7.66. The retardance,  $\delta$  measurement for different PAAM concentrations for a bubble volume range of 750-1285 mm<sup>3</sup>.

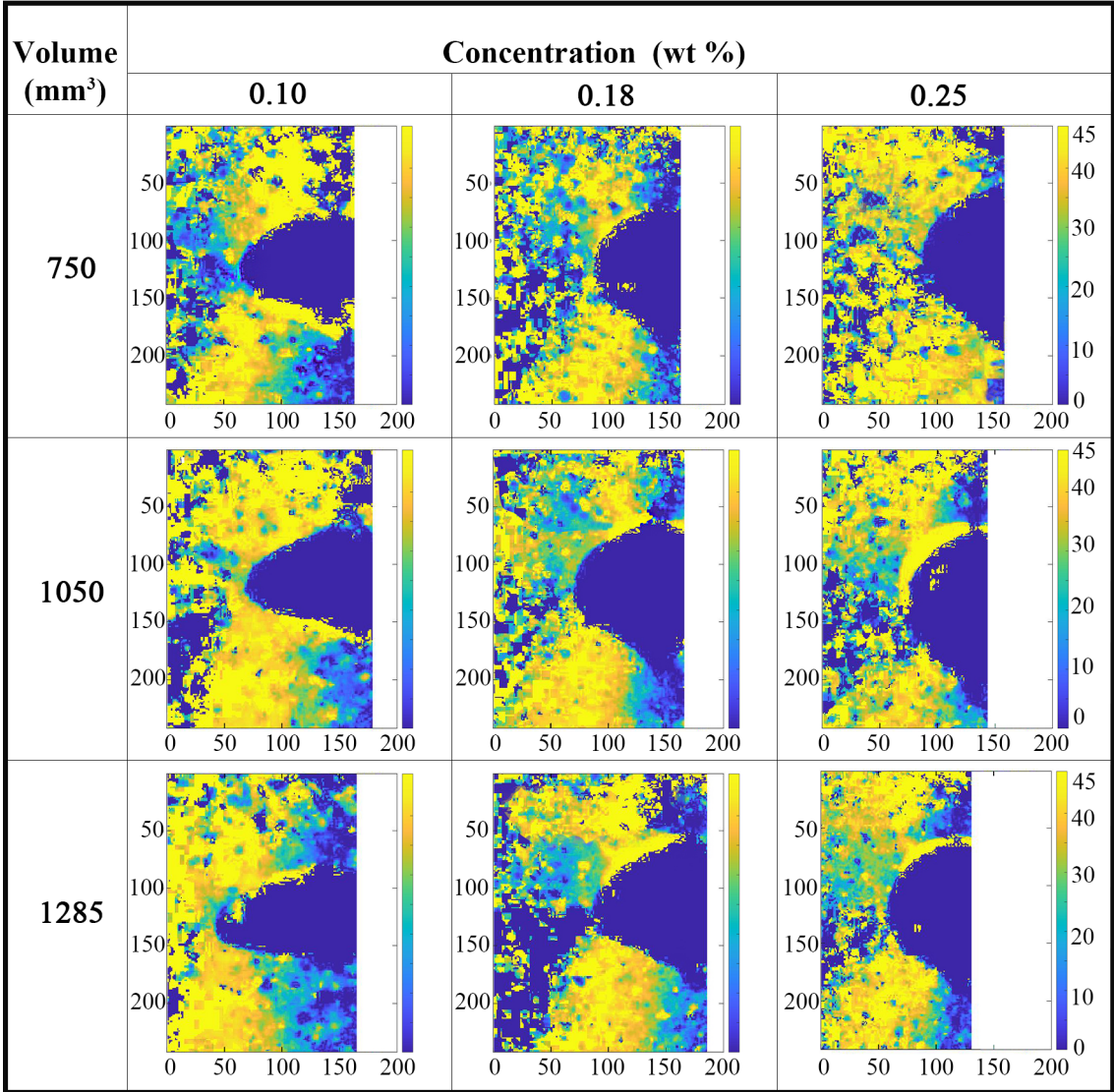


Figure 7.67. The stretching angle,  $\chi$  measurement for different PAAM concentrations for a bubble volume range of 750-1285 mm<sup>3</sup>.

### 7.3. Non-Isothermal Experiments

In Section 7.1, the bubble dynamics is presented for an isothermal system. In this section, the bubbles rising PAAM solution is studied in the presence of a temperature gradient applied in the horizontal direction.

The experimental setup for this system is explained in Section 4.4. A temperature gradient is formed by applying heat from one wall whereas the other wall is kept constant at 25°C using a water bath. Temperature gradients of 25-40°C and 25-50°C are created and the experiments are performed when the system reaches the steady-state. 0.18, 0.25 and 0.40 wt% PAAM solutions are tested.

Even though no measurable effect is observed in any of the solutions in terms of bubble terminal velocity and bubble shape, the average terminal velocity and circularity results are presented for 0.18 wt% (Figures 7.68, 7.69) and 0.40 wt% (Figures 7.70, 7.71) PAAM solutions.

A temperature gradient is observed through Schlieren method, especially on the tail of a bubble rising in the solution, as presented in Figure 7.72. Apparently this gradient is not enough to cause an observable effect on the bubble dynamics. If a larger temperature gradient is applied, there is a risk of polymer degradation. So, one method may be to apply the temperature gradient along the vertical direction.

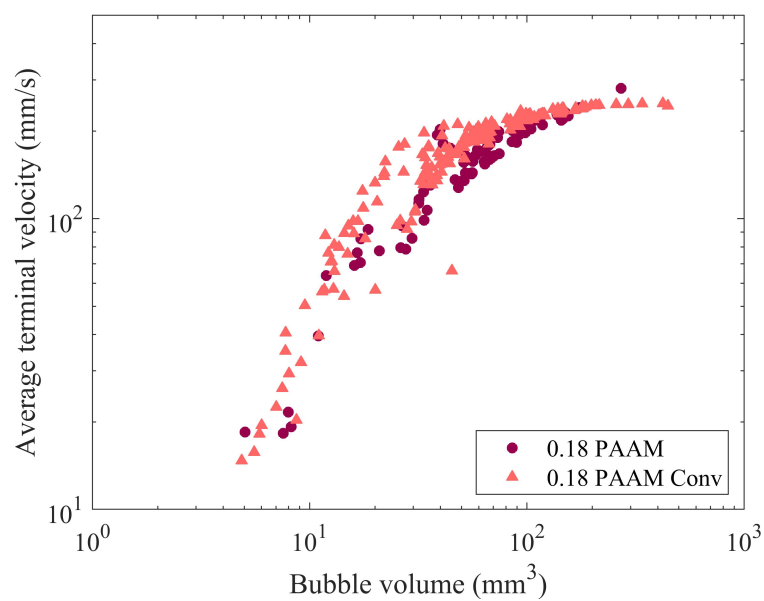


Figure 7.68. The average terminal velocity as a function of the bubble volume for 0.18 wt% PAAM solution: isothermal (maroon) and 15 °C temperature gradient (pink).

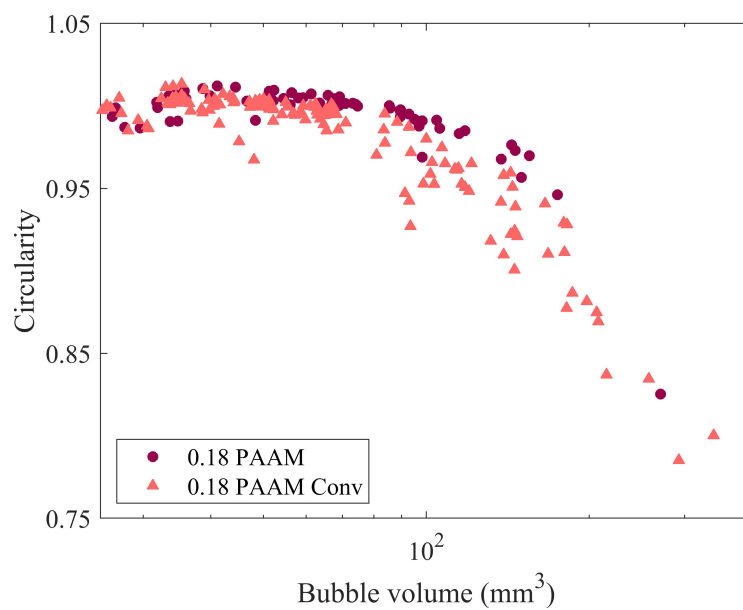


Figure 7.69. Shape parameter, circularity as a function of the bubble volume for 0.18 wt% PAAM solution: isothermal (maroon) and 15 °C temperature gradient (pink).

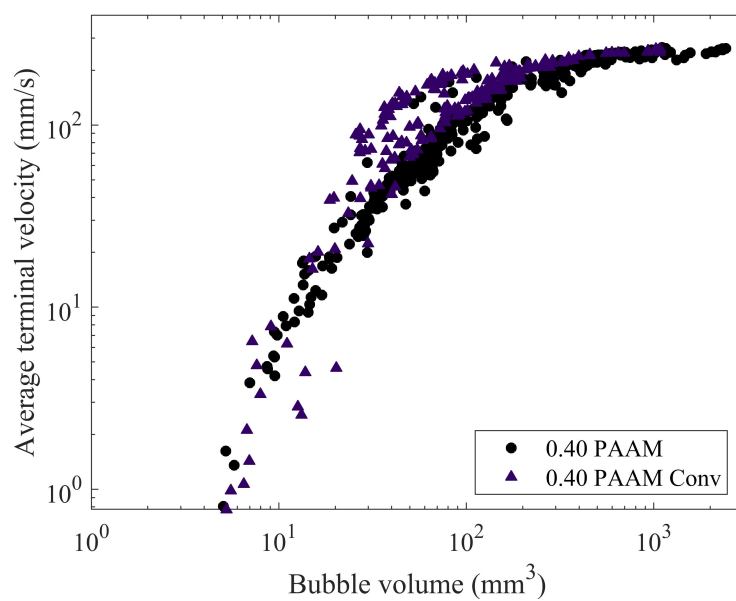


Figure 7.70. The average terminal velocity as a function of the bubble volume for 0.40 wt% PAAM solution: isothermal (black) and 15°C temperature gradient (purple).

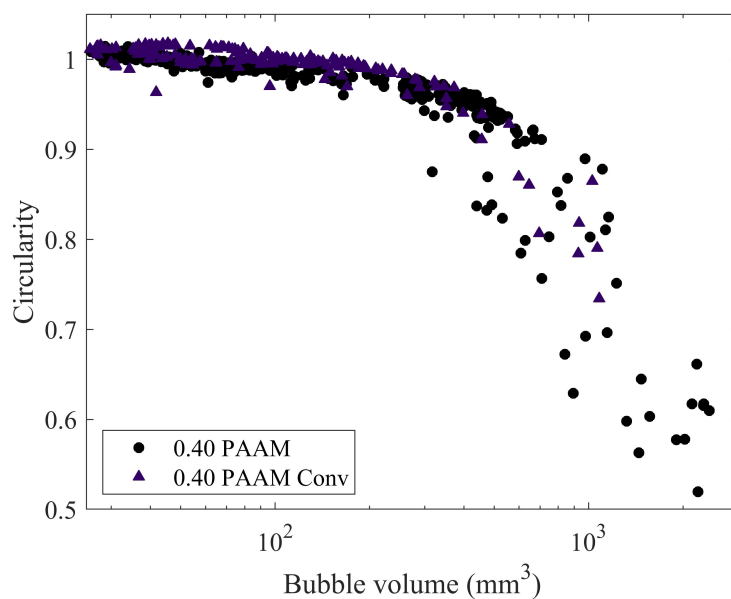


Figure 7.71. Shape parameter, circularity as a function of the bubble volume for 0.40 wt% PAAM solution: isothermal (black) and 15°C temperature gradient (purple).

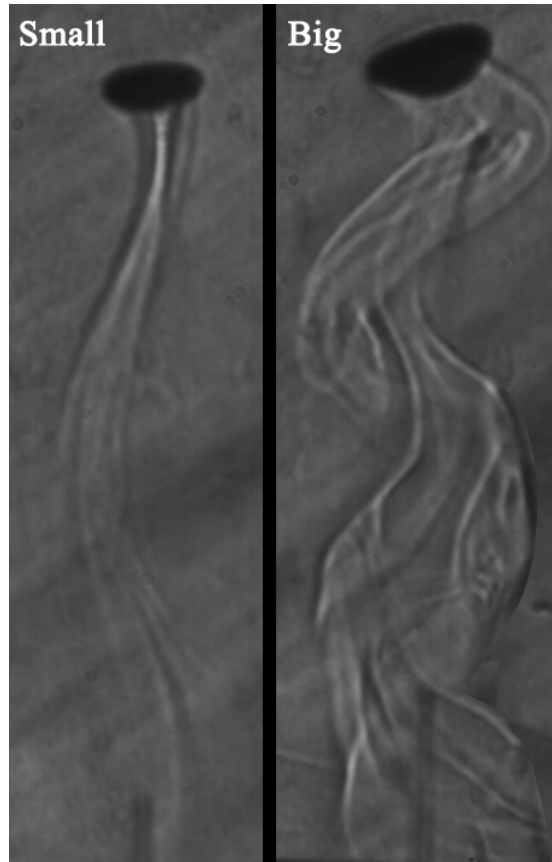


Figure 7.72. The temperature gradient observed at the tails of a small and a big bubble.

## 8. CONCLUSIONS AND RECOMMENDATIONS

In this chapter, the dissertation is concluded by summarizing the most important and relevant results of the study and recommendations are provided for future studies.

### 8.1. Conclusions

In this dissertation, the dynamics of a bubble rising in a viscoelastic liquid is studied. In the literature, there are various unanswered questions regarding especially a jump in the steady bubble velocity that occurs at a critical bubble volume. Some studies attribute the discontinuity to the negative wake and the cusp formation at the tail of the bubble; whereas others claim that there is no relationship amongst these parameters. Therefore, a study is designed to answer these questions or find evidences to understand the behavior of a rising bubble in a large bubble volume range.

The bubble dynamics is studied using different concentrations of PAAM solutions, which show both viscoelastic and shear-thinning rheology. For different PAAM concentrations, it is observed that the terminal velocity reaches a plateau with increasing bubble volume in accordance with the literature. We did not obtain any evidences of the presence of a discontinuity at the bubble terminal velocity for the studied bubble volume range and polymer concentrations. The detailed literature survey regarding the PAAM types and brands shows that the discontinuity is directly related to the manufacturing of the polymer. In the literature, there is no experiment with the PAAM used in this study (AN 934 SH by SNF Floerger) showed a discontinuity in the bubble velocity.

Bubble shapes observed with increasing bubble volume are spherical, prolate, teardrop with a cusp, and cap-shape. Shape parameters included in this study are extent, solidity, circularity, minor axis,  $a$ , the distance between the center of gravity and tip of the bubble tail,  $b$ , the  $a/b$  ratio, eccentricity-1, eccentricity -2, and the em-

pirical shape parameter,  $\beta$ . The results show that the solidity and  $b$  are concentration-independent parameters. Solidity showed how a bubble reaches a more concave shape with increasing bubble volume. Additionally, extent shows the change of bubble shape from prolate to teardrop. Circularity,  $a$ , and eccentricities show the effect of the polymer concentration on the bubble shape. A bubble loses its circularity, becomes wider horizontally, and more elliptic after a critical bubble volume for low polymer concentration. The empirical cusp parameter,  $\beta$  developed for PAAM solutions is successfully used to determine the critical bubble volume for the cusp formation. In this dissertation, the results show that the critical bubble volume is independent of the polymer concentration. In the literature, it was claimed that the cusp formation causes a discontinuity. Here, we show that there is no discontinuity in the bubble velocity in the presence of a cusp.

The dimensionless numbers,  $Re$ ,  $Bo$ ,  $Ca$ ,  $We$ , and  $C_D$  are analyzed to understand the forces acting on the system for a broad range of bubble volume and different polymer concentrations. For smaller bubble volumes, the concentration is important for  $Re$  and  $We$  due to its effect on the bubble velocity. As the bubble volume increases for a given PAAM concentration, gravitational forces become dominant for  $Bo$ , and the effect of the surface tension decreases which causes a change in the bubble shape from spherical to cap-shape. For low concentrations and  $Re < 1$ , the spherical-shaped bubbles act like a solid sphere and deviate from  $C_D$  of Hadamard Rybczynski which is for deformable surfaces. For higher  $Re$ , larger bubble volumes fit Hadamard Rybczynski regardless of the polymer concentration. Even though a transition occurs from Stokes to Hadamard Rybczynski, there is no velocity discontinuity at a critical bubble volume, as suggested by some work in the literature.

Since the surface tension forces play an important role in the bubble dynamics as seen from  $Bo$  versus  $Re$  in the PAAM studies, the effect of the surfactant is studied for 0, 10 and 100 ppm concentrations. 10 and 40% decrease occurred in the surface tension for 10 and 100 ppm SDS concentrations, respectively. The study shows that 10 ppm is effective only for the extent and the solidity parameters and has a negligible

effect on the velocity and the other shape parameters. As the surfactant concentration increases, the bubbles slow down. However, the average terminal velocity reaches the same plateau value regardless of the surfactant concentration. The bubble expands less in the horizontal direction and elongates more in the vertical direction in the presence of the surfactant. Overall, the bubbles are less distorted in the presence of the surfactant. There exist critical volumes for the surfactant to affect the concavity and the circularity of bubbles. It is shown that the cusp formation occurs for smaller bubble volumes when a surfactant is added into the system and is highly dependent on the surfactant concentration whereas the polymer concentration did not have any effect.

The effect of the surfactant concentration on  $Re$  and  $Ca$  diminishes due to the plateau regime as the bubble volume increases. However, its effect becomes more prominent for  $Bo$ . It is also found that even for small surfactant concentration, drag increases and deviates from Hadamard Rybczynski regime. This is explained by the accumulation of the surfactant on the bubble surface where Hadamard Rybczynski applies to deformable surfaces only. It fits Hadamard Rybczynski equation for higher  $Re$ .

For the PAAM studies, the effect of the injection period is studied to determine a safe period that does not affect the results and found that the required injection period increases as the polymer concentration increases; and 60 s is chosen as the injection period for the experiments which is in a good agreement with the literature.

In this study, the bubble velocity and shape parameters are mostly presented at steady-state. However, the unsteady analysis of the bubbles is also important to determine whether steady-state is reached. It is shown that the bubbles do a wobbling motion as the polymer concentration decreases. Also for a given polymer concentration, wobbling occurs above a critical volume. The bubble trajectory is studied and it is found that the bubbles most of the time move towards the right side of the column which is believed to be experimentally biased. The increase in the polymer and surfactant

concentration increases the path instability and the oscillation of the rising bubble. However, the lateral movement of the bubble is found to be very small.

Finally, the stress field around the bubble as it rises in the viscoelastic liquid is studied. The stress-optic law, i.e., the flow birefringence method is used and the retardance of the light beam occurs in the presence of the stress. HPC is added into the PAAM solution to give the birefringent property. In the literature, some work hypothesized that the negative-wake (downwards flow) and the cusp are pre-requisites for the discontinuity at the bubble velocity, and some reported they are not related. Here, it is shown that a discontinuity did not exist even though a negative-wake and cusp start forming. A negative-wake is observed at a critical bubble volume, which is much higher than the critical discontinuity volumes reported in the literature. For smaller bubble volumes, the polymer concentration has a significant effect on retardance. However, it is found that the bubble shape becomes important for stress as the bubble volume increases. Therefore, the stress around a rising bubble is directly related to the bubble shape.

At last, the bubble dynamics is studied in the presence of a temperature gradient. Even though a temperature gradient is successfully achieved, no significant change is observed in the bubble dynamics. Schlieren method showed that the convection was not clearly visible.

In the beginning of this study, it is hypothesized that there could be a critical bubble volume where the bubble's shape and the average terminal velocity, the polymer concentration and the stress around the rising bubble are correlated. It is successfully shown which shape parameters and dimensionless numbers are important for different cases such as the cusp formation or stress around the bubble for a wide bubble volume range, and various polymer or the surfactant concentrations. It is proven that the shape parameters are as important as the polymer concentration for the stress formation around the rising bubble above a critical bubble volume. This study also emphasizes the importance of the rheology in the bubble dynamics in non-Newtonian liquids. The

uncertainty in the literature concerning the discontinuity in the terminal velocity of the bubble at a critical volume, the cusp formation, the stress around the bubble and the negative wake can be enlightened if only the bubble dynamics studies are integrated with the rheological properties of the liquids, especially the viscoelasticity.

## 8.2. Recommendations

The present work contributes to the bubble dynamics in viscoelastic liquids by studying multiple parameters. This field is still full of unknowns and requires more controlled and focus work to have a better understanding of the bubble motion.

When our findings are combined with a detailed literature survey, it is found that there is likely to be a relationship between the discontinuity and PAAM used; and the studies are suffering from a lack of information and a detailed rheology analysis. Since polymers can differ from one batch to another and cover a broad range of molecular weight, it is suggested to employ custom design polymers with known rheological properties. This would help to contribute to the literature by minimizing the unknowns related to the polymer and giving specific and reproducible results that can be used to compare and improve.

In the bubble dynamics, the experiments are performed for a broad range of bubble volumes which creates difficulty for the analysis since the light, camera, and recording settings are sensitive. Therefore, the study should be divided into smaller sections of the bubble volume to get more accurate results. Besides, the field of view of the camera needs to be increased without sacrificing the resolution for the unsteady-state and the trajectory studies. On the other hand, with this big number of data, principle component analysis may give a correlation between different shape parameters.

Similar arguments are also valid for surfactant experiments. Additionally, wider range of concentration and surfactant type could be employed.

The injection system for the bubbles needs to be improved and automatized as it mostly depends on the experimentalist in the current system and the syringe pump can create a limited volume range. Considering the discontinuities reported in the literature occur at very small volumes, the effect of the experimentalist should be removed.

The edge detection consists of an important part of the birefringence study. Another camera is used to measure the bubble volume, then the recordings of two videos are matched later which can cause errors. Even though the birefringence results are highly promising, it would benefit from a high-speed camera with high resolution, and the entire analysis can be automated. Also, during the experiments, the birefringence method is found to be promising to study the bubble breakage and coalescence; and the wall-effect. Thus, the study can be extended to a new direction.

Finally, a detailed understanding is required for the non-isothermal experiments before designing a new experimental setup. The results clearly show that the current system is not appropriate to understand the effect of the temperature gradient. Our studies with the Schlieren method showed that the study of the effect of the temperature gradient in the vertical direction is promising. Applying the birefringence method to the non-isothermal study would also be interesting.

## REFERENCES

1. Clift, R., J. Grace and M. Weber, *Bubbles, Drops, and Particles*, Dover Publications Inc., Mineola, NY, USA, 1978.
2. Lohse, D. and W. H. M. Zijm, “Bubble Puzzles”, *Physics Today*, Vol. 56, No. 2, pp. 36–41, 2003.
3. Chhabra, R. P., *Bubbles, Drops, and Particles in Non-Newtonian Fluids*, CRC Press, Boca Raton, FL, USA, 2006.
4. Barnes, H. A., J. F. Hutton and K. Walters, *An Introduction to Rheology*, Vol. 3, Elsevier, Amsterdam, NL, 1989.
5. Huilgol, R. R. and N. Phan-Thien, *Fluid Mechanics of Viscoelasticity: General Principles, Constitutive Modelling, Analytical and Numerical Techniques*, Elsevier, Amsterdam, NL, 1997.
6. Phan-Thien, N. and N. Mai-Duy, *Understanding Viscoelasticity: an Introduction to Rheology*, Springer, New York City, NY, USA, 2017.
7. Chhabra, R., “Hydrodynamics of Bubbles and Drops in Rheologically Complex Liquids”, *Encyclopedia of Fluid Mechanics*, Vol. 7, pp. 253–286, 1988.
8. Astarita, G. and G. Apuzzo, “Motion of Gas Bubbles in Non-Newtonian Liquids”, *AIChE Journal*, Vol. 11, No. 5, pp. 815–820, 1965.
9. Leal, L., J. Skoog and A. Acrivos, “On the Motion of Gas Bubbles in a Viscoelastic Liquid”, *The Canadian Journal of Chemical Engineering*, Vol. 49, No. 5, pp. 569–575, 1971.
10. Acharya, A., R. Mashelkar and J. Ulbrecht, “Mechanics of Bubble Motion and

- Deformation in Non-Newtonian Media”, *Chemical Engineering Science*, Vol. 32, No. 8, pp. 863–872, 1977.
11. Coutanceau, M. and M. Hajjam, “Viscoelastic Effect on the Behaviour of an Air Bubble Rising Axially in a Tube”, *Applied Scientific Research*, Vol. 38, No. 1, pp. 199–207, 1982.
  12. Dekee, D., P. Carreau and J. Mordarski, “Bubble Velocity and Coalescence in Viscoelastic Liquids”, *Chemical Engineering Science*, Vol. 41, No. 9, pp. 2273–2283, 1986.
  13. Hassager, O., “Negative Wake Behind Bubbles in Non-Newtonian Liquids”, *Nature*, Vol. 279, No. 5712, pp. 402–403, 1979.
  14. De Kee, D. and R. Chhabra, “A Photographic Study of Shapes of Bubbles and Coalescence in Non-Newtonian Polymer Solutions”, *Rheologica Acta*, Vol. 27, No. 6, pp. 656–660, 1988.
  15. Herrera-Velarde, J., R. Zenit, D. Chehata and B. Mena, “The Flow of Non-Newtonian Fluids around Bubbles and Its Connection to the Jump Discontinuity”, *Journal of Non-Newtonian Fluid Mechanics*, Vol. 111, No. 2-3, pp. 199–209, 2003.
  16. Kemiha, M., X. Frank, S. Poncin and H. Z. Li, “Origin of the Negative Wake Behind a Bubble Rising in Non-Newtonian Fluids”, *Chemical Engineering Science*, Vol. 61, No. 12, pp. 4041–4047, 2006.
  17. Funfschilling, D. and H. Z. Li, “Flow of Non-Newtonian Fluids around Bubbles: PIV Measurements and Birefringence Visualisation”, *Chemical Engineering Science*, Vol. 56, No. 3, pp. 1137–1141, 2001.
  18. Frank, X., H. Z. Li, D. Funfschilling, F. Burdin and Y. Ma, “Bubble Motion in Non-Newtonian Fluids and Suspensions”, *The Canadian Journal of Chemical Engineering*, Vol. 81, No. 3-4, pp. 483–490, 2003.

19. Li, H. Z., X. Frank, D. Funfschilling and P. Diard, “Bubbles’ Rising Dynamics in Polymeric Solutions”, *Physics Letters A*, Vol. 325, No. 1, pp. 43–50, 2004.
20. Frank, X. and H. Z. Li, “Complex Flow around a Bubble Rising in a Non-Newtonian Fluid”, *Physical Review E*, Vol. 71, No. 3, p. 036309, 2005.
21. Funfschilling, D. and H. Li, “Effects of the Injection Period on the Rise Velocity and Shape of a Bubble in a Non-Newtonian Fluid”, *Chemical Engineering Research and Design*, Vol. 84, No. 10, pp. 875–883, 2006.
22. Böhm, L., M. Brehmer and M. Kraume, “Comparison of the Single Bubble Ascent in a Newtonian and a Non-Newtonian Liquid: a Phenomenological PIV Study”, *Chemie Ingenieur Technik*, Vol. 88, No. 1-2, pp. 93–106, 2016.
23. Ibarz, A. and G. V. Barbosa-Cánovas, *Unit Operations in Food Engineering*, CRC Press, Boca Raton, FL, USA, 2002.
24. Rao, M. A., *Rheology of Fluid and Semisolid Foods: Principles and Applications*, Springer US, NY, USA, 2010.
25. Chhabra, R. P. and J. F. Richardson, *Non-Newtonian Flow and Applied Rheology: Engineering Applications*, Butterworth Heinemann, Oxford, UK, 2011.
26. Irgens, F., *Rheology and Non-Newtonian Fluids*, Vol. 190, Springer, Cham, Swiss, 2014.
27. Barnes, H. A., *A Handbook of Elementary Rheology*, Vol. 1, University of Wales, Institute of Non-Newtonian Fluid Mechanics Aberystwyth, Wales, UK, 2000.
28. Macosko, C. W., *Rheology Principles: Measurements and Applications*, VCH Publishers, Weinheim, DE, 1994.
29. Malkin, A. Y. and A. I. Isayev, *Rheology: Concepts, Methods, and Applications*,

ChemTec Publishing, Ontario, CA, 2017.

30. Miyahara, T. and S. Yamanaka, “Mechanics of Motion and Deformation of a Single Bubble Rising Through Quiescent Highly Viscous Newtonian and Non-Newtonian Media”, *Journal of Chemical Engineering of Japan*, Vol. 26, No. 3, pp. 297–302, 1993.
31. Dewsbury, K., D. Karamanev and A. Margaritis, “Hydrodynamic Characteristics of Free Rise of Light Solid Particles and Gas Bubbles in Non-Newtonian Liquids”, *Chemical Engineering Science*, Vol. 54, No. 21, pp. 4825–4830, 1999.
32. Amirnia, S., J. R. de Bruyn, M. A. Bergougnou and A. Margaritis, “Continuous Rise Velocity of Air Bubbles in Non-Newtonian Biopolymer Solutions”, *Chemical Engineering Science*, Vol. 94, pp. 60–68, 2013.
33. Hassan, N., M. M. K. Khan, M. Rasul and D. W. Rackemann, “An Experimental Investigation of Bubble Rise Characteristics in a Crystal Suspended Non-Newtonian Fluid”, *AIP Conference Proceedings*, Vol. 1027, pp. 743–745, American Institute of Physics, 2008.
34. Zhang, L., C. Yang and Z.-S. Mao, “An Empirical Correlation of Drag Coefficient for a Single Bubble Rising in Non-Newtonian Liquids”, *Industrial & Engineering Chemistry Research*, Vol. 47, No. 23, pp. 9767–9772, 2008.
35. Wenyuan, F., M. Youguang, J. Shaokun, Y. Ke and L. Huaizhi, “An Experimental Investigation for Bubble Rising in Non-Newtonian Fluids and Empirical Correlation of Drag Coefficient”, *Journal of Fluids Engineering*, Vol. 132, No. 2, 2010.
36. Grace, J., “Shapes and Velocities of Bubbles Rising in Infinite Liquid”, *Transactions of the Institution of Chemical Engineers*, Vol. 51, pp. 116–120, 1973.
37. Xu, F., N. Midoux, H.-Z. Li, G. Hébrard and N. Dietrich, “Characterization of Bubble Shapes in Non-Newtonian Fluids by Parametric Equations”, *Chemical En-*

*gineering & Technology*, Vol. 42, No. 11, pp. 2321–2330, 2019.

38. Liu, Y., T. Liao and D. Joseph, “A Two-Dimensional Cusp at the Trailing Edge of an Air Bubble Rising in a Viscoelastic Liquid”, *Journal of Fluid Mechanics*, Vol. 304, pp. 321–342, 1995.
39. Wagner, A., L. Giraud and C. Scott, “Simulation of a Cusped Bubble Rising in a Viscoelastic Fluid with a New Numerical Method”, *Computer Physics Communications*, Vol. 129, No. 1-3, pp. 227–232, 2000.
40. Rodrigue, D., D. De Kee and C. C. M. Fong, “Bubble Velocities: Further Developments on the Jump Discontinuity”, *Journal of Non-Newtonian Fluid Mechanics*, Vol. 79, No. 1, pp. 45–55, 1998.
41. Soto, E., C. Goujon, R. Zenit and O. Manero, “A Study of Velocity Discontinuity for Single Air Bubbles Rising in an Associative Polymer”, *Physics of Fluids*, Vol. 18, No. 12, p. 121510, 2006.
42. Pillapakam, S. B. and P. Singh, “A Level-Set Method for Computing Solutions to Viscoelastic Two-Phase Flow”, *Journal of Computational Physics*, Vol. 174, No. 2, pp. 552–578, 2001.
43. Rodrigue, D. and D. Dekee, “Bubble Velocity Jump Discontinuity in Polyacrylamide Solutions: a Photographic Study”, *Rheologica Acta*, Vol. 38, No. 2, pp. 177–182, 1999.
44. Pilz, C. and G. Brenn, “On the Critical Bubble Volume at the Rise Velocity Jump Discontinuity in Viscoelastic Liquids”, *Journal of Non-Newtonian Fluid Mechanics*, Vol. 145, No. 2-3, pp. 124–138, 2007.
45. Hassan, N., M. M. K. Khan, M. Rasul and D. W. Rackemann, “Bubble Rise Velocity and Trajectory in Xanthan Gum Crystal Suspension”, *Applied Rheology*, Vol. 20, No. 6, 2010.

46. You, R., A. Borhan and H. Haj-Hariri, “Stability Analysis of Cusped Bubbles in Viscoelastic Flows”, *Journal of Fluid Mechanics*, Vol. 621, p. 131, 2009.
47. Malaga, C. and J. Rallison, “A Rising Bubble in a Polymer Solution”, *Journal of Non-Newtonian Fluid Mechanics*, Vol. 141, No. 1, pp. 59–78, 2007.
48. Lind, S. J. and T. N. Phillips, “The Effect of Viscoelasticity on a Rising Gas Bubble”, *Journal of Non-Newtonian Fluid Mechanics*, Vol. 165, No. 15-16, pp. 852–865, 2010.
49. Tripathi, M. K., K. C. Sahu, G. Karapetsas and O. K. Matar, “Bubble Rise Dynamics in a Viscoplastic Material”, *Journal of Non-Newtonian Fluid Mechanics*, Vol. 222, pp. 217–226, 2015.
50. Premlata, A., M. K. Tripathi, B. Karri and K. C. Sahu, “Dynamics of an Air Bubble Rising in a Non-Newtonian Liquid in the Axisymmetric Regime”, *Journal of Non-Newtonian Fluid Mechanics*, Vol. 239, pp. 53–61, 2017.
51. Yuan, W., M. Zhang, B. C. Khoo and N. Phan-Thien, “Dynamics and Deformation of a Three-Dimensional Bubble Rising in Viscoelastic Fluids”, *Journal of Non-Newtonian Fluid Mechanics*, Vol. 285, p. 104408, 2020.
52. Dewsbury, K., D. Karamanev and A. Margaritis, “Dynamic Behavior of Freely Rising Buoyant Solid Spheres in Non-Newtonian Liquids”, *AIChE Journal*, Vol. 46, No. 1, pp. 46–51, 2000.
53. Vélez-Cordero, J. R., D. Sámano and R. Zenit, “Study of the Properties of Bubbly Flows in Boger-Type Fluids”, *Journal of Non-Newtonian Fluid Mechanics*, Vol. 175, pp. 1–9, 2012.
54. Carreau, P., M. Devic and M. Kapellas, “Dynamique des Bulles en Milieu ViscoéLastique”, *Rheologica Acta*, Vol. 13, No. 3, pp. 477–489, 1974.

55. Li, H. Z., Y. Mouline, L. Choplin and N. Midoux, "Rheological Simulation of in-line Bubble Interactions", *American Institute of Chemical Engineers. AIChE Journal*, Vol. 43, No. 1, p. 265, 1997a.
56. Li, H. Z., Y. Mouline, L. Choplin and N. Midoux, "Chaotic Bubble Coalescence in Non-Newtonian Fluids", *International Journal of Multiphase Flow*, Vol. 23, No. 4, pp. 713–723, 1997b.
57. Li, H., Y. Mouline, D. Funfschilling, P. Marchal, L. Choplin and N. Midoux, "Evidence for in-line Bubble Interactions in Non-Newtonian Fluids", *Chemical Engineering Science*, Vol. 53, No. 12, pp. 2219–2230, 1998.
58. Rodrigue, D., D. De Kee and C. C. M. Fong, "An Experimental Study of the Effect of Surfactants on the Free Rise Velocity of Gas Bubbles", *Journal of Non-Newtonian Fluid Mechanics*, Vol. 66, No. 2-3, pp. 213–232, 1996.
59. Leven, M. D. and J. Newman, "The Effect of Surfactant on the Terminal and Interfacial Velocities of a Bubble or Drop", *AIChE Journal*, Vol. 22, No. 4, pp. 695–701, 1976.
60. Tzounakos, A., D. G. Karamanev, A. Margaritis and M. A. Bergougnou, "Effect of the Surfactant Concentration on the Rise of Gas Bubbles in Power-Law Non-Newtonian Liquids", *Industrial & Engineering Chemistry Research*, Vol. 43, No. 18, pp. 5790–5795, 2004.
61. Karamanev, D. G., "Rise of Gas Bubbles in Quiescent Liquids", *AIChE Journal*, Vol. 40, No. 8, pp. 1418–1421, 1994.
62. Li, S. B., J. G. Fan, R. D. Li, L. Wang and J. D. Luan, "Effect of Surfactants on Hydrodynamics Characteristics of Bubble in Shear Thinning Fluids at Low Reynolds Number", *Journal of Central South University*, Vol. 25, No. 4, pp. 805–811, 2018.

63. Cuenot, B., J. Magnaudet and B. Spennato, “The Effects of Slightly Soluble Surfactants on the Flow around a Spherical Bubble”, *Journal of Fluid Mechanics*, Vol. 339, pp. 25–53, 1997.
64. Nalajala, V. S. and N. Kishore, “Drag of Contaminated Bubbles in Power-Law Fluids”, *Colloids and Surfaces A: Physicochemical and Engineering Aspects*, Vol. 443, pp. 240–248, 2014.
65. Ahmed, Z., D. Izbassarov, P. Costa, M. Muradoglu and O. Tammisola, “Turbulent Bubbly Channel Flows: Effects of Soluble Surfactant and Viscoelasticity”, *Computers & Fluids*, Vol. 212, p. 104717, 2020.
66. Böhm, L., T. Kurita, K. Kimura and M. Kraume, “Rising Behaviour of Single Bubbles in Narrow Rectangular Channels in Newtonian and Non-Newtonian Liquids”, *International Journal of Multiphase Flow*, Vol. 65, pp. 11–23, 2014.
67. Kumar, P., K. Jin and S. P. Vanka, “Bubble Rise and Deformation in a Non-Newtonian Fluid in a Square Duct”, *Computational Methods and Tools in Thermal Fluids Sciences*, pp. 1–15, 2015.
68. Bahadur, B., *Liquid Crystal-Applications and Uses-I*, World Scientific, Salem, MA, USA, 1990.
69. Muller, R. and B. Vergnes, “Validity of the Stress Optical Law and Application of Birefringence to Polymer Complex Flows”, *Rheology Series*, Vol. 5, pp. 257–284, Elsevier, 1996.
70. Oba, N. and T. Inoue, “An Apparatus for Birefringence and Extinction Angle Distributions Measurements in Cone and Plate Geometry by Polarization Imaging Method”, *Rheologica Acta*, Vol. 55, No. 9, pp. 699–708, 2016.
71. Iwata, S., T. Takahashi, T. Onuma, R. Nagumo and H. Mori, “Local Flow Around a Tiny Bubble Under a Pressure-Oscillation Field in a Viscoelastic Worm-like Mi-

- cellar Solution”, *Journal of Non-Newtonian Fluid Mechanics*, Vol. 263, pp. 24–32, 2019.
72. Aniq-Mexico, *Technical Datasheet Flopam AN 934 SH*, 2019, <https://aniq.org.mx/pqta/pdf/FLOERGER.pdf>, May 2020.
73. Snell, F. D., C. L. Hilton, L. S. Ettre and other, *Encyclopedia of Industrial Chemical Analysis*, Interscience Publishers, New York, NY, USA, 1985.
74. Considine, D. M., *Chemical and Process Technology Encyclopedia*, McGraw-Hill, New York, NY, USA, 1974.
75. Navard, P. and J. Haudin, “Rheology of Hydroxypropylcellulose Solutions”, *Journal of Polymer Science Part B: Polymer Physics*, Vol. 24, No. 1, pp. 189–201, 1986.
76. Pagliaro, M. and M. Rossi, *The Future of Glycerol*, RSC Publishing, Cambridge, UK, 2008.
77. Cheng, N.-S., “Formula for the Viscosity of a Glycerol- Water Mixture”, *Industrial & Engineering Chemistry Research*, Vol. 47, No. 9, pp. 3285–3288, 2008.
78. Wagner, M., K. Reiche, A. Blume and P. Garidel, “Viscosity Measurements of Antibody Solutions by Photon Correlation Spectroscopy: an Indirect Approach—Limitations and Applicability for High Concentration Liquid Protein Solutions”, *Pharmaceutical Development and Technology*, Vol. 18, No. 4, pp. 963–970, 2013.
79. Laserglow-Technologies, *Laser Beam Profiles*, 2017, <https://www.laserglow.com/content/Laser-Beam-Profiles>, September 2019.
80. Gopal, V., J. L. Klosowiak, R. Jaeger, T. Selimkhanov and M. J. Hartmann, “Visualizing the Invisible: the Construction of Three Low-cost Schlieren Imaging Systems for the Undergraduate Laboratory”, *European Journal of Physics*, Vol. 29,

No. 3, p. 607, 2008.

81. Du Noüy, P. L., “A New Apparatus for Measuring Surface Tension”, *The Journal of General Physiology*, Vol. 1, No. 5, p. 521, 1919.
82. Zuidema, H. and G. Waters, “Ring Method for the Determination of Interfacial Tension”, *Industrial & Engineering Chemistry Analytical Edition*, Vol. 13, No. 5, pp. 312–313, 1941.
83. Lunkenheimer, K. and K.-D. Wantke, “Determination of the Surface Tension of Surfactant Solutions Applying the Method of Lecomte du Noüy (Ring Tensiometer)”, *Colloid and Polymer Science*, Vol. 259, No. 3, pp. 354–366, 1981.
84. Atkins, P. W. and J. De Paula, *Atkins’ Physical Chemistry*, Oxford University Press, Oxford, UK, 10th edition, 2014.
85. *The Physicochemical Systems Laboratory Manual*, Bogazici University Department of Chemical Engineering, Istanbul, Turkey, 2020.
86. Pallas, N. and Y. Harrison, “An Automated Drop Shape Apparatus and the Surface Tension of Pure Water”, *Colloids and Surfaces*, Vol. 43, No. 2, pp. 169–194, 1990.
87. Grace, J., T. Wairegi and T. Nguyen, “Shapes and Velocities of Single Drops and Bubbles Moving Freely Through Immiscible Liquids”, Vol. 54, No. 3, pp. 167–173, 1976.
88. Lali, A., A. Khare, J. Joshi and K. Nigam, “Behaviour of Solid Particles in Viscous Non-Newtonian Solutions: Settling Velocity, Wall Effects and Bed Expansion in Solid-Liquid Fluidized Beds”, *Powder Technology*, Vol. 57, No. 1, pp. 39–50, 1989.
89. Hadamard, J., “Mouvement Permanent Lent D’une Sphère Liquid et Visqueuse Dans un Liquide Visqueux”, *Comptes rendus de l’Académie des Sciences*, Vol. 152, pp. 1735–1738, 1911.

90. Rybczynski, W., “Über die Fortschreitende Bewegung einer Flüssigen Kugel in einem Zahen Medium”, *Bulletin international de l’Académie des sciences de Cracovie*, Vol. 1, pp. 40–46, 1911.
91. Margaritis, A., D. W. te Bokkel and D. G. Karamanev, “Bubble Rise Velocities and Drag Coefficients in Non-Newtonian Polysaccharide Solutions”, *Biotechnology and Bioengineering*, Vol. 64, No. 3, pp. 257–266, 1999.
92. Hiscocks, P. D. and P. Eng, “Measuring Luminance with a Digital Camera”, *Syscomp Electronic Design Limited*, Vol. 686, 2011.
93. Jaloxa, *WebHDR Camera Calibration*, 2011, <http://www.jaloxa.eu/webhdr/calibrate.shtml>, October 2019.
94. Jacobs, A., “High Dynamic Range Imaging and its Application in Building Research”, *Advances in Building Energy Research*, Vol. 1, No. 1, pp. 177–202, 2007.
95. Liu, L., H. Yan, G. Zhao and J. Zhuang, “Experimental Studies on the Terminal Velocity of Air Bubbles in Water and Glycerol Aqueous Solution”, *Experimental Thermal and Fluid Science*, Vol. 78, pp. 254–265, 2016.
96. Koebe, M., D. Bothe and H.-J. Warnecke, “Direct Numerical Simulation of Air Bubbles in Water/Glycerol Mixtures: Shapes and Velocity Fields”, *Fluids Engineering Division Summer Meeting*, Vol. 36975, pp. 415–421, 2003.
97. Li, W., *Buoyancy-driven Motion of Bubbles in the Presence of Soluble Surfactants*, Master’s Thesis, University of New Hampshire, New Hampshire, USA, 2011.
98. Li, Y., T. Zhu, Y. Liu, Y. Tian and H. Wang, “Effects of Surfactant on Bubble hydrodynamic Behavior Under Flotation-related Conditions in Wastewater”, *Water Science and Technology*, Vol. 65, No. 6, pp. 1060–1066, 2012.
99. Wang, H., J. Yang, S. Lei and X. Wang, “Comparing the Effect of Biosurfactant and

Chemical Surfactant on Bubble Hydrodynamics in a Flotation Column”, *Water Science and Technology*, Vol. 68, No. 4, pp. 783–790, 2013.

## APPENDIX A: UNCERTAINTY ANALYSES

If a quantity is not determined explicitly in an experiment and is based on the variables that are obtained directly through the experiments, an uncertainty analysis is required. Uncertainty analysis offers us a methodological approach to the sensitivity of the results. With this approach, a range for possible errors is determined. In this section, the uncertainty analyses done for the length, the bubble velocity and the volume are given.

### A.1. Uncertainty Analysis for the Length

The measured pixel length of the calibration object and the uncertainty from the MATLAB's *imdistline* function is  $x = 818.6 \text{ pixel} \pm 1.4 \text{ pixel}$  ( $\Delta x = 1.4 \text{ pixel}$ ). The length and the uncertainty of the calibration object is  $y = 76.2 \pm 0.1 \text{ mm}$  ( $\Delta y = 0.1 \text{ mm}$ ). The length of a pixel,  $p$  and its uncertainty value,  $\Delta p$  in mm are calculated as

$$p = \frac{y}{x}, \quad (\text{A.1})$$

where  $\Delta p$  is

$$\Delta p = \sqrt{\left(\frac{dp}{dy}\right)^2 (\Delta y)^2 + \left(\frac{dp}{dx}\right)^2 (\Delta x)^2}. \quad (\text{A.2})$$

The uncertainty in pixel becomes

$$\Delta p = \sqrt{\frac{1}{x^2} (\Delta y)^2 + \frac{y^2}{x^4} (\Delta x)^2}. \quad (\text{A.3})$$

Thus, the pixel length with its uncertainty,  $\mathbf{p}$  becomes  $0.0931 \pm 0.0002 \text{ mm/pixel}$  using Eq. A.1-A.3.

A sample uncertainty analysis for the minor axis,  $a$  of a bubble is shown below where  $a=85$  pixel ( $\Delta a=1$  pixel). The length of  $a$  in millimeter is  $m$  and its uncertainty,  $\Delta m$  are 7.9 mm and 0.1 mm through Eq. A.4-A.6, respectively.

The length of  $a$  in millimeter is calculated as

$$m = p \times a, \quad (\text{A.4})$$

where the uncertainty becomes

$$\Delta m = \sqrt{\left(\frac{dm}{dp}\right)^2 (\Delta p)^2 + \left(\frac{dm}{da}\right)^2 (\Delta a)^2} \quad (\text{A.5})$$

and

$$\Delta m = \sqrt{a^2(\Delta p)^2 + p^2(\Delta a)^2}. \quad (\text{A.6})$$

The minor axis in millimeter with its uncertainty,  $\mathbf{m}$  becomes  $7.9 \pm 0.1$  mm

## A.2. Uncertainty Analysis for the Velocity

The uncertainty analysis is done as follows where  $u$ ,  $\Delta u$ ,  $z$  and  $t$  are the bubble velocity, the uncertainty in the bubble velocity, the path that the bubble travels and the time difference between two consecutive video frames, respectively.

The uncertainty in the velocity is

$$\Delta u = \sqrt{\left(\frac{du}{dz}\right)^2 (\Delta z)^2 + \left(\frac{du}{dt}\right)^2 (\Delta t)^2}, \quad (\text{A.7})$$

where it turns into the following in order as

$$\Delta u = \sqrt{\frac{1}{t^2}(\Delta z)^2 + \frac{z^2}{t^4}(\Delta t)^2}, \quad (\text{A.8})$$

$$\frac{\Delta u}{u} = \frac{t}{z} \sqrt{\frac{1}{t^2}(\Delta z)^2 + \frac{z^2}{t^4}(\Delta t)^2}, \quad (\text{A.9})$$

$$\frac{\Delta u}{u} = \sqrt{\left(\frac{\Delta z}{z}\right)^2 + \left(\frac{\Delta t}{t}\right)^2}. \quad (\text{A.10})$$

A sample uncertainty analysis for the bubble velocity,  $u$  is done where the pixel length of the path that the bubble's center of gravity takes between the two consecutive frames,  $z_{pixel}$  is  $15 \text{ pixel} \pm 1 \text{ pixel}$ .

The distance in millimeters of the bubble's center of gravity between two frames,  $z$  is calculated as

$$z = p \times z_{pixel}. \quad (\text{A.11})$$

The uncertainty in the distance in millimeters of the bubble's center of gravity becomes

$$\Delta z = \sqrt{\left(\frac{dz}{dp}\right)^2 (\Delta p)^2 + \left(\frac{dz}{dz_{pixel}}\right)^2 (\Delta z_{pixel})^2}, \quad (\text{A.12})$$

and

$$\Delta z = \sqrt{(z_{pixel})^2 (\Delta p)^2 + p^2 (\Delta z_{pixel})^2}. \quad (\text{A.13})$$

Thus,  $z$  and  $\Delta z$  are calculated as 1.4 mm and 0.1 mm, respectively.

Finally,  $u$  and  $\Delta u$  are determined as 140 mm/s and 10 mm/s, respectively, where  $t = 0.0100 \pm 0.0001$  s. Therefore, the uncertainty analysis for the velocity becomes  $\mathbf{u} = 140 \pm 10$  mm/s.

### A.3. Uncertainty Analysis for the Volume

The truncated-cone method is used through Eq. 5.2 to calculate the bubble volume.  $R$  and  $r$  are found by the edge detection of the bubble; and both of their uncertainties are 1 pixel ( $\Delta R=1$  pixel and  $\Delta r=1$  pixel).

Hence, the uncertainty in the truncated-cone volume,  $\Delta V_i$  is

$$\Delta V_i = \sqrt{\left(\frac{dV_i}{dr}\right)^2 (\Delta r)^2 + \left(\frac{dV_i}{dR}\right)^2 (\Delta R)^2}, \quad (\text{A.14})$$

and

$$\Delta V_i = \frac{\pi h}{3} \sqrt{(2r + R)^2 (\Delta r)^2 + (2R + r)^2 (\Delta R)^2}. \quad (\text{A.15})$$

The bubble volume,  $V$  is

$$V = \sum_{i=1}^N V_i, \quad (\text{A.16})$$

where the uncertainty in the bubble volume  $\Delta V$  is calculated as follows

$$\Delta V = \sqrt{(\Delta V_1)^2 + (\Delta V_2)^2 + (\Delta V_3)^2 + \cdots + (\Delta V_N)^2}. \quad (\text{A.17})$$

The calculated volume and the uncertainty of the volume are found in pixel<sup>3</sup> unit and the following formulas is applied to calculate the volume as

$$V_{\text{mm}^3} = p^3 \times V_{\text{pixel}^3}, \quad (\text{A.18})$$

where its uncertainty in  $\text{mm}^3$  is calculated as follows

$$\Delta V_{\text{mm}^3} = \sqrt{\left(\frac{dV_{\text{mm}^3}}{dp}\right)^2 (\Delta p)^2 + \left(\frac{dV_{\text{mm}^3}}{dV_{\text{piksel}^3}}\right)^2 (\Delta V_{\text{piksel}^3})^2}, \quad (\text{A.19})$$

and

$$\Delta V_{\text{mm}^3} = \sqrt{(3p^2 x V_{\text{piksel}^3})^2 (\Delta p)^2 + (p^3)^2 (\Delta V_{\text{piksel}^3})^2}. \quad (\text{A.20})$$

The volume and the uncertainty of a sample bubble are found as  $V_{\text{pixel}^3} = 910000 \text{ pixel}^3$  and  $\Delta V_{\text{piksel}^3} = 2200 \text{ piksel}^3$ . Finally, the bubble volume,  $\mathbf{V}$  with its uncertainty is calculated as  $\mathbf{V}_{\text{mm}^3} = 730 \text{ mm}^3 \pm 5 \text{ mm}^3$

## **APPENDIX B: PERMISSIONS FOR THE REPRINTED FIGURES FROM THE LITERATURE**

The permissions taken for the Figures 2.5, 2.6, 2.7 and 5.1 used from [13,17,22,37] are given in this section in order.

5/16/2021

RightsLink Printable License

ELSEVIER LICENSE  
TERMS AND CONDITIONS

May 16, 2021

---

This Agreement between PINAR ERİBOL ("You") and Elsevier ("Elsevier") consists of your license details and the terms and conditions provided by Elsevier and Copyright Clearance Center.

License Number	5070900885160
License date	May 16, 2021
Licensed Content Publisher	Elsevier
Licensed Content Publication	Chemical Engineering Science
Licensed Content Title	Flow of non-Newtonian fluids around bubbles: PIV measurements and birefringence visualisation
Licensed Content Author	Denis Funfschilling,Huai Z. Li
Licensed Content Date	Feb 1, 2001
Licensed Content Volume	56
Licensed Content Issue	3
Licensed Content Pages	5
Start Page	1137
End Page	1141
Type of Use	reuse in a thesis/dissertation

5/16/2021

RightsLink Printable License

Portion	figures/tables/illustrations
Number of figures/tables/illustrations	1
Format	both print and electronic
Are you the author of this Elsevier article?	No
Will you be translating?	No
Title	Dynamics of Rising Bubbles and Stress Measurements through Birefringence in Viscoelastic Liquids
Institution name	Boğaziçi University
Expected presentation date	Jun 2021
Portions	10
Requestor Location	PINAR ERİBOL BOGAZICI UNIVERSITY DEPARTMENT OF CHEMICAL ENGINEERING  ISTANBUL, BEBEK 34342 Turkey Attn: PINAR ERİBOL
Publisher Tax ID	GB 494 6272 12
Customer VAT ID	TR123456789
Total	0.00 USD
Terms and Conditions	

### INTRODUCTION

1. The publisher for this copyrighted material is Elsevier. By clicking "accept" in connection with completing this licensing transaction, you agree that the following terms and conditions apply to this transaction (along with the Billing and Payment terms and conditions established by Copyright Clearance Center, Inc. ("CCC"), at the time that you opened your Rightslink account and that are available at any time at <http://myaccount.copyright.com>).

**GENERAL TERMS**

2. Elsevier hereby grants you permission to reproduce the aforementioned material subject to the terms and conditions indicated.

3. Acknowledgement: If any part of the material to be used (for example, figures) has appeared in our publication with credit or acknowledgement to another source, permission must also be sought from that source. If such permission is not obtained then that material may not be included in your publication/copies. Suitable acknowledgement to the source must be made, either as a footnote or in a reference list at the end of your publication, as follows:

"Reprinted from Publication title, Vol /edition number, Author(s), Title of article / title of chapter, Pages No., Copyright (Year), with permission from Elsevier [OR APPLICABLE SOCIETY COPYRIGHT OWNER]." Also Lancet special credit - "Reprinted from The Lancet, Vol. number, Author(s), Title of article, Pages No., Copyright (Year), with permission from Elsevier."

4. Reproduction of this material is confined to the purpose and/or media for which permission is hereby given.

5. Altering/Modifying Material: Not Permitted. However figures and illustrations may be altered/adapted minimally to serve your work. Any other abbreviations, additions, deletions and/or any other alterations shall be made only with prior written authorization of Elsevier Ltd. (Please contact Elsevier's permissions helpdesk [here](#)). No modifications can be made to any Lancet figures/tables and they must be reproduced in full.

6. If the permission fee for the requested use of our material is waived in this instance, please be advised that your future requests for Elsevier materials may attract a fee.

7. Reservation of Rights: Publisher reserves all rights not specifically granted in the combination of (i) the license details provided by you and accepted in the course of this licensing transaction, (ii) these terms and conditions and (iii) CCC's Billing and Payment terms and conditions.

8. License Contingent Upon Payment: While you may exercise the rights licensed immediately upon issuance of the license at the end of the licensing process for the transaction, provided that you have disclosed complete and accurate details of your proposed use, no license is finally effective unless and until full payment is received from you (either by publisher or by CCC) as provided in CCC's Billing and Payment terms and conditions. If full payment is not received on a timely basis, then any license preliminarily granted shall be deemed automatically revoked and shall be void as if never granted. Further, in the event that you breach any of these terms and conditions or any of CCC's Billing and Payment terms and conditions, the license is automatically revoked and shall be void as if never granted. Use of materials as described in a revoked license, as well as any use of the materials beyond the scope of an unrevoked license, may constitute copyright infringement and publisher reserves the right to take any and all action to protect its copyright in the materials.

9. Warranties: Publisher makes no representations or warranties with respect to the licensed material.

10. Indemnity: You hereby indemnify and agree to hold harmless publisher and CCC, and their respective officers, directors, employees and agents, from and against any and all claims arising out of your use of the licensed material other than as specifically authorized pursuant to this license.

11. No Transfer of License: This license is personal to you and may not be sublicensed, assigned, or transferred by you to any other person without publisher's written permission.

5/16/2021

RightsLink Printable License

12. **No Amendment Except in Writing:** This license may not be amended except in a writing signed by both parties (or, in the case of publisher, by CCC on publisher's behalf).

13. **Objection to Contrary Terms:** Publisher hereby objects to any terms contained in any purchase order, acknowledgment, check endorsement or other writing prepared by you, which terms are inconsistent with these terms and conditions or CCC's Billing and Payment terms and conditions. These terms and conditions, together with CCC's Billing and Payment terms and conditions (which are incorporated herein), comprise the entire agreement between you and publisher (and CCC) concerning this licensing transaction. In the event of any conflict between your obligations established by these terms and conditions and those established by CCC's Billing and Payment terms and conditions, these terms and conditions shall control.

14. **Revocation:** Elsevier or Copyright Clearance Center may deny the permissions described in this License at their sole discretion, for any reason or no reason, with a full refund payable to you. Notice of such denial will be made using the contact information provided by you. Failure to receive such notice will not alter or invalidate the denial. In no event will Elsevier or Copyright Clearance Center be responsible or liable for any costs, expenses or damage incurred by you as a result of a denial of your permission request, other than a refund of the amount(s) paid by you to Elsevier and/or Copyright Clearance Center for denied permissions.

#### LIMITED LICENSE

The following terms and conditions apply only to specific license types:

15. **Translation:** This permission is granted for non-exclusive world **English** rights only unless your license was granted for translation rights. If you licensed translation rights you may only translate this content into the languages you requested. A professional translator must perform all translations and reproduce the content word for word preserving the integrity of the article.

16. **Posting licensed content on any Website:** The following terms and conditions apply as follows: Licensing material from an Elsevier journal: All content posted to the web site must maintain the copyright information line on the bottom of each image; A hyper-text must be included to the Homepage of the journal from which you are licensing at <http://www.sciencedirect.com/science/journal/xxxxx> or the Elsevier homepage for books at <http://www.elsevier.com>; Central Storage: This license does not include permission for a scanned version of the material to be stored in a central repository such as that provided by Heron/XanEdu.

Licensing material from an Elsevier book: A hyper-text link must be included to the Elsevier homepage at <http://www.elsevier.com>. All content posted to the web site must maintain the copyright information line on the bottom of each image.

**Posting licensed content on Electronic reserve:** In addition to the above the following clauses are applicable: The web site must be password-protected and made available only to bona fide students registered on a relevant course. This permission is granted for 1 year only. You may obtain a new license for future website posting.

17. **For journal authors:** the following clauses are applicable in addition to the above:

#### Preprints:

A preprint is an author's own write-up of research results and analysis, it has not been peer-reviewed, nor has it had any other value added to it by a publisher (such as formatting, copyright, technical enhancement etc.).

5/16/2021

RightsLink Printable License

Authors can share their preprints anywhere at any time. Preprints should not be added to or enhanced in any way in order to appear more like, or to substitute for, the final versions of articles however authors can update their preprints on arXiv or RePEc with their Accepted Author Manuscript (see below).

If accepted for publication, we encourage authors to link from the preprint to their formal publication via its DOI. Millions of researchers have access to the formal publications on ScienceDirect, and so links will help users to find, access, cite and use the best available version. Please note that Cell Press, The Lancet and some society-owned have different preprint policies. Information on these policies is available on the journal homepage.

**Accepted Author Manuscripts:** An accepted author manuscript is the manuscript of an article that has been accepted for publication and which typically includes author-incorporated changes suggested during submission, peer review and editor-author communications.

Authors can share their accepted author manuscript:

- immediately
  - via their non-commercial person homepage or blog
  - by updating a preprint in arXiv or RePEc with the accepted manuscript
  - via their research institute or institutional repository for internal institutional uses or as part of an invitation-only research collaboration work-group
  - directly by providing copies to their students or to research collaborators for their personal use
  - for private scholarly sharing as part of an invitation-only work group on commercial sites with which Elsevier has an agreement
- After the embargo period
  - via non-commercial hosting platforms such as their institutional repository
  - via commercial sites with which Elsevier has an agreement

In all cases accepted manuscripts should:

- link to the formal publication via its DOI
- bear a CC-BY-NC-ND license - this is easy to do
- if aggregated with other manuscripts, for example in a repository or other site, be shared in alignment with our hosting policy not be added to or enhanced in any way to appear more like, or to substitute for, the published journal article.

**Published journal article (JPA):** A published journal article (PJA) is the definitive final record of published research that appears or will appear in the journal and embodies all value-adding publishing activities including peer review co-ordination, copy-editing, formatting, (if relevant) pagination and online enrichment.

Policies for sharing publishing journal articles differ for subscription and gold open access articles:

**Subscription Articles:** If you are an author, please share a link to your article rather than the full-text. Millions of researchers have access to the formal publications on ScienceDirect, and so links will help your users to find, access, cite, and use the best available version.

Theses and dissertations which contain embedded PJAs as part of the formal submission can be posted publicly by the awarding institution with DOI links back to the formal publications on ScienceDirect.

If you are affiliated with a library that subscribes to ScienceDirect you have additional private sharing rights for others' research accessed under that agreement. This includes use for classroom teaching and internal training at the institution (including use in course packs and courseware programs), and inclusion of the article for grant funding purposes.

**Gold Open Access Articles:** May be shared according to the author-selected end-user license and should contain a [CrossMark logo](#), the end user license, and a DOI link to the formal publication on ScienceDirect.

Please refer to Elsevier's [posting policy](#) for further information.

18. **For book authors** the following clauses are applicable in addition to the above: Authors are permitted to place a brief summary of their work online only. You are not allowed to download and post the published electronic version of your chapter, nor may you scan the printed edition to create an electronic version. **Posting to a repository:** Authors are permitted to post a summary of their chapter only in their institution's repository.

19. **Thesis/Dissertation:** If your license is for use in a thesis/dissertation your thesis may be submitted to your institution in either print or electronic form. Should your thesis be published commercially, please reapply for permission. These requirements include permission for the Library and Archives of Canada to supply single copies, on demand, of the complete thesis and include permission for Proquest/UMI to supply single copies, on demand, of the complete thesis. Should your thesis be published commercially, please reapply for permission. Theses and dissertations which contain embedded PJAs as part of the formal submission can be posted publicly by the awarding institution with DOI links back to the formal publications on ScienceDirect.

### **Elsevier Open Access Terms and Conditions**

You can publish open access with Elsevier in hundreds of open access journals or in nearly 2000 established subscription journals that support open access publishing. Permitted third party re-use of these open access articles is defined by the author's choice of Creative Commons user license. See our [open access license policy](#) for more information.

#### **Terms & Conditions applicable to all Open Access articles published with Elsevier:**

Any reuse of the article must not represent the author as endorsing the adaptation of the article nor should the article be modified in such a way as to damage the author's honour or reputation. If any changes have been made, such changes must be clearly indicated.

The author(s) must be appropriately credited and we ask that you include the end user license and a DOI link to the formal publication on ScienceDirect.

If any part of the material to be used (for example, figures) has appeared in our publication with credit or acknowledgement to another source it is the responsibility of the user to ensure their reuse complies with the terms and conditions determined by the rights holder.

#### **Additional Terms & Conditions applicable to each Creative Commons user license:**

**CC BY:** The CC-BY license allows users to copy, to create extracts, abstracts and new works from the Article, to alter and revise the Article and to make commercial use of the Article (including reuse and/or resale of the Article by commercial entities), provided the user gives appropriate credit (with a link to the formal publication through the relevant DOI), provides a link to the license, indicates if changes were made and the licensor is not represented as endorsing the use made of the work. The full details of the license are available at <http://creativecommons.org/licenses/by/4.0>.

**CC BY NC SA:** The CC BY-NC-SA license allows users to copy, to create extracts, abstracts and new works from the Article, to alter and revise the Article, provided this is not done for commercial purposes, and that the user gives appropriate credit (with a link to the formal publication through the relevant DOI), provides a link to the license, indicates if changes were made and the licensor is not represented as endorsing the use made of the

5/16/2021

RightsLink Printable License

work. Further, any new works must be made available on the same conditions. The full details of the license are available at <http://creativecommons.org/licenses/by-nc-sa/4.0>.

**CC BY NC ND:** The CC BY-NC-ND license allows users to copy and distribute the Article, provided this is not done for commercial purposes and further does not permit distribution of the Article if it is changed or edited in any way, and provided the user gives appropriate credit (with a link to the formal publication through the relevant DOI), provides a link to the license, and that the licensor is not represented as endorsing the use made of the work. The full details of the license are available at <http://creativecommons.org/licenses/by-nc-nd/4.0>. Any commercial reuse of Open Access articles published with a CC BY NC SA or CC BY NC ND license requires permission from Elsevier and will be subject to a fee.

Commercial reuse includes:

- Associating advertising with the full text of the Article
- Charging fees for document delivery or access
- Article aggregation
- Systematic distribution via e-mail lists or share buttons

Posting or linking by commercial companies for use by customers of those companies.

## 20. Other Conditions:

v1.10

Questions? [customercare@copyright.com](mailto:customercare@copyright.com) or +1-855-239-3415 (toll free in the US) or +1-978-646-2777.

5/15/2021

RightsLink Printable License

SPRINGER NATURE LICENSE  
TERMS AND CONDITIONS

May 15, 2021

---

This Agreement between PINAR ERİBOL ("You") and Springer Nature ("Springer Nature") consists of your license details and the terms and conditions provided by Springer Nature and Copyright Clearance Center.

License Number	5070220886507
License date	May 15, 2021
Licensed Content Publisher	Springer Nature
Licensed Content Publication	Nature
Licensed Content Title	Negative wake behind bubbles in non-newtonian liquids
Licensed Content Author	OLE HASSAGER
Licensed Content Date	May 1, 1979
Type of Use	Thesis/Dissertation
Requestor type	academic/university or research institute
Format	print and electronic
Portion	figures/tables/illustrations
Number of figures/tables/illustrations	1
Will you be translating?	no
Circulation/distribution	30 - 99

5/15/2021

RightsLink Printable License

Author of this Springer Nature content	no
Title	Electrohydrodynamic Instability of Three-Phase Flow
Institution name	Boğaziçi University
Expected presentation date	Jun 2021
Portions	fig1
Requestor Location	PINAR ERİBOL BOGAZICI UNIVERSITY DEPARTMENT OF CHEMICAL ENGINEERING  ISTANBUL, BEBEK 34342 Turkey Attn: PINAR ERİBOL
Customer VAT ID	TR123456789
Total	0.00 USD

Terms and Conditions

### **Springer Nature Customer Service Centre GmbH Terms and Conditions**

This agreement sets out the terms and conditions of the licence (the **Licence**) between you and **Springer Nature Customer Service Centre GmbH** (the **Licensor**). By clicking 'accept' and completing the transaction for the material (**Licensed Material**), you also confirm your acceptance of these terms and conditions.

#### **1. Grant of License**

**1. 1.** The Licensor grants you a personal, non-exclusive, non-transferable, world-wide licence to reproduce the Licensed Material for the purpose specified in your order only. Licences are granted for the specific use requested in the order and for no other use, subject to the conditions below.

**1. 2.** The Licensor warrants that it has, to the best of its knowledge, the rights to license reuse of the Licensed Material. However, you should ensure that the material you are requesting is original to the Licensor and does not carry the copyright of another entity (as credited in the published version).

**1. 3.** If the credit line on any part of the material you have requested indicates that it was reprinted or adapted with permission from another source, then you should also seek permission from that source to reuse the material.

## 2. Scope of Licence

- 2. 1.** You may only use the Licensed Content in the manner and to the extent permitted by these Ts&Cs and any applicable laws.
- 2. 2.** A separate licence may be required for any additional use of the Licensed Material, e.g. where a licence has been purchased for print only use, separate permission must be obtained for electronic re-use. Similarly, a licence is only valid in the language selected and does not apply for editions in other languages unless additional translation rights have been granted separately in the licence. Any content owned by third parties are expressly excluded from the licence.
- 2. 3.** Similarly, rights for additional components such as custom editions and derivatives require additional permission and may be subject to an additional fee. Please apply to [Journalpermissions@springernature.com](mailto:Journalpermissions@springernature.com)/[bookpermissions@springernature.com](mailto:bookpermissions@springernature.com) for these rights.
- 2. 4.** Where permission has been granted **free of charge** for material in print, permission may also be granted for any electronic version of that work, provided that the material is incidental to your work as a whole and that the electronic version is essentially equivalent to, or substitutes for, the print version.
- 2. 5.** An alternative scope of licence may apply to signatories of the [STM Permissions Guidelines](#), as amended from time to time.

## 3. Duration of Licence

- 3. 1.** A licence for is valid from the date of purchase ('Licence Date') at the end of the relevant period in the below table:

Scope of Licence	Duration of Licence
Post on a website	12 months
Presentations	12 months
Books and journals	Lifetime of the edition in the language purchased

## 4. Acknowledgement

- 4. 1.** The Licensor's permission must be acknowledged next to the Licenced Material in print. In electronic form, this acknowledgement must be visible at the same time as the figures/tables/illustrations or abstract, and must be hyperlinked to the journal/book's homepage. Our required acknowledgement format is in the Appendix below.

## 5. Restrictions on use

- 5. 1.** Use of the Licensed Material may be permitted for incidental promotional use and minor editing privileges e.g. minor adaptations of single figures, changes of format, colour and/or style where the adaptation is credited as set out in Appendix 1 below. Any other changes including but not limited to, cropping, adapting, omitting material that affect the meaning, intention or moral rights of the author are strictly prohibited.

**5. 2.** You must not use any Licensed Material as part of any design or trademark.

**5. 3.** Licensed Material may be used in Open Access Publications (OAP) before publication by Springer Nature, but any Licensed Material must be removed from OAP sites prior to final publication.

## **6. Ownership of Rights**

**6. 1.** Licensed Material remains the property of either Licensor or the relevant third party and any rights not explicitly granted herein are expressly reserved.

## **7. Warranty**

IN NO EVENT SHALL LICENSOR BE LIABLE TO YOU OR ANY OTHER PARTY OR ANY OTHER PERSON OR FOR ANY SPECIAL, CONSEQUENTIAL, INCIDENTAL OR INDIRECT DAMAGES, HOWEVER CAUSED, ARISING OUT OF OR IN CONNECTION WITH THE DOWNLOADING, VIEWING OR USE OF THE MATERIALS REGARDLESS OF THE FORM OF ACTION, WHETHER FOR BREACH OF CONTRACT, BREACH OF WARRANTY, TORT, NEGLIGENCE, INFRINGEMENT OR OTHERWISE (INCLUDING, WITHOUT LIMITATION, DAMAGES BASED ON LOSS OF PROFITS, DATA, FILES, USE, BUSINESS OPPORTUNITY OR CLAIMS OF THIRD PARTIES), AND WHETHER OR NOT THE PARTY HAS BEEN ADVISED OF THE POSSIBILITY OF SUCH DAMAGES. THIS LIMITATION SHALL APPLY NOTWITHSTANDING ANY FAILURE OF ESSENTIAL PURPOSE OF ANY LIMITED REMEDY PROVIDED HEREIN.

## **8. Limitations**

**8. 1. BOOKS ONLY:** Where 'reuse in a dissertation/thesis' has been selected the following terms apply: Print rights of the final author's accepted manuscript (for clarity, NOT the published version) for up to 100 copies, electronic rights for use only on a personal website or institutional repository as defined by the Sherpa guideline ([www.sherpa.ac.uk/romeo/](http://www.sherpa.ac.uk/romeo/)).

**8. 2.** For content reuse requests that qualify for permission under the [STM Permissions Guidelines](#), which may be updated from time to time, the STM Permissions Guidelines supersede the terms and conditions contained in this licence.

## **9. Termination and Cancellation**

**9. 1.** Licences will expire after the period shown in Clause 3 (above).

**9. 2.** Licensee reserves the right to terminate the Licence in the event that payment is not received in full or if there has been a breach of this agreement by you.

## **Appendix 1 — Acknowledgements:**

5/15/2021

RightsLink Printable License

**For Journal Content:**

Reprinted by permission from [the Licensor]: [Journal Publisher (e.g. Nature/Springer/Palgrave)] [JOURNAL NAME] [REFERENCE CITATION (Article name, Author(s) Name), [COPYRIGHT] (year of publication)]

**For Advance Online Publication papers:**

Reprinted by permission from [the Licensor]: [Journal Publisher (e.g. Nature/Springer/Palgrave)] [JOURNAL NAME] [REFERENCE CITATION (Article name, Author(s) Name), [COPYRIGHT] (year of publication), advance online publication, day month year (doi: 10.1038/sj.[JOURNAL ACRONYM].)]

**For Adaptations/Translations:**

Adapted/Translated by permission from [the Licensor]: [Journal Publisher (e.g. Nature/Springer/Palgrave)] [JOURNAL NAME] [REFERENCE CITATION (Article name, Author(s) Name), [COPYRIGHT] (year of publication)]

**Note: For any republication from the British Journal of Cancer, the following credit line style applies:**

Reprinted/adapted/translated by permission from [the Licensor]: on behalf of Cancer Research UK: : [Journal Publisher (e.g. Nature/Springer/Palgrave)] [JOURNAL NAME] [REFERENCE CITATION (Article name, Author(s) Name), [COPYRIGHT] (year of publication)]

**For Advance Online Publication papers:**

Reprinted by permission from The [the Licensor]: on behalf of Cancer Research UK: [Journal Publisher (e.g. Nature/Springer/Palgrave)] [JOURNAL NAME] [REFERENCE CITATION (Article name, Author(s) Name), [COPYRIGHT] (year of publication), advance online publication, day month year (doi: 10.1038/sj.[JOURNAL ACRONYM].)]

**For Book content:**

Reprinted/adapted by permission from [the Licensor]: [Book Publisher (e.g. Palgrave Macmillan, Springer etc) [Book Title] by [Book author(s)] [COPYRIGHT] (year of publication)]

**Other Conditions:**

Version 1.3

Questions? [customercare@copyright.com](mailto:customercare@copyright.com) or +1-855-239-3415 (toll free in the US) or +1-978-646-2777.

5/16/2021

RightsLink Printable License

**JOHN WILEY AND SONS LICENSE  
TERMS AND CONDITIONS**

May 16, 2021

---

This Agreement between PINAR ERİBOL ("You") and John Wiley and Sons ("John Wiley and Sons") consists of your license details and the terms and conditions provided by John Wiley and Sons and Copyright Clearance Center.

License Number 5070891172052

License date May 16, 2021

Licensed Content  
Publisher John Wiley and SonsLicensed Content  
Publication Chemie Ingenieur Technik - CITLicensed Content  
Title Comparison of the Single Bubble Ascent in a Newtonian and a Non-Newtonian Liquid: A Phenomenological PIV StudyLicensed Content  
Author Lutz Böhm, Manuel Brehmer, Matthias KraumeLicensed Content  
Date Dec 4, 2015Licensed Content  
Volume 88Licensed Content  
Issue 1-2Licensed Content  
Pages 14

Type of use Dissertation/Thesis

Requestor type University/Academic

5/16/2021

RightsLink Printable License

Format	Print and electronic
Portion	Figure/table
Number of figures/tables	1
Will you be translating?	No
Title	Dynamics of Rising Bubbles and Stress Measurements through Birefringence in Viscoelastic Liquids
Institution name	Boğaziçi University
Expected presentation date	Jun 2021
Portions	fig 4
Requestor Location	PINAR ERİBOL BOGAZICI UNIVERSITY DEPARTMENT OF CHEMICAL ENGINEERING  ISTANBUL, BEBEK 34342 Turkey Attn: PINAR ERİBOL
Publisher Tax ID	EU826007151
Customer VAT ID	TR123456789
Total	0.00 USD

Terms and Conditions

**TERMS AND CONDITIONS**

This copyrighted material is owned by or exclusively licensed to John Wiley & Sons, Inc. or one of its group companies (each a "Wiley Company") or handled on behalf of a society with which a Wiley Company has exclusive publishing rights in relation to a particular work (collectively "WILEY"). By clicking "accept" in connection with completing this licensing

5/16/2021

RightsLink Printable License

transaction, you agree that the following terms and conditions apply to this transaction (along with the billing and payment terms and conditions established by the Copyright Clearance Center Inc., ("CCC's Billing and Payment terms and conditions"), at the time that you opened your RightsLink account (these are available at any time at <http://myaccount.copyright.com>).

### Terms and Conditions

- The materials you have requested permission to reproduce or reuse (the "Wiley Materials") are protected by copyright.
- You are hereby granted a personal, non-exclusive, non-sub licensable (on a stand-alone basis), non-transferable, worldwide, limited license to reproduce the Wiley Materials for the purpose specified in the licensing process. This license, **and any CONTENT (PDF or image file) purchased as part of your order**, is for a one-time use only and limited to any maximum distribution number specified in the license. The first instance of republication or reuse granted by this license must be completed within two years of the date of the grant of this license (although copies prepared before the end date may be distributed thereafter). The Wiley Materials shall not be used in any other manner or for any other purpose, beyond what is granted in the license. Permission is granted subject to an appropriate acknowledgement given to the author, title of the material/book/journal and the publisher. You shall also duplicate the copyright notice that appears in the Wiley publication in your use of the Wiley Material. Permission is also granted on the understanding that nowhere in the text is a previously published source acknowledged for all or part of this Wiley Material. Any third party content is expressly excluded from this permission.
- With respect to the Wiley Materials, all rights are reserved. Except as expressly granted by the terms of the license, no part of the Wiley Materials may be copied, modified, adapted (except for minor reformatting required by the new Publication), translated, reproduced, transferred or distributed, in any form or by any means, and no derivative works may be made based on the Wiley Materials without the prior permission of the respective copyright owner. **For STM Signatory Publishers clearing permission under the terms of the [STM Permissions Guidelines](#) only, the terms of the license are extended to include subsequent editions and for editions in other languages, provided such editions are for the work as a whole in situ and does not involve the separate exploitation of the permitted figures or extracts**, You may not alter, remove or suppress in any manner any copyright, trademark or other notices displayed by the Wiley Materials. You may not license, rent, sell, loan, lease, pledge, offer as security, transfer or assign the Wiley Materials on a stand-alone basis, or any of the rights granted to you hereunder to any other person.
- The Wiley Materials and all of the intellectual property rights therein shall at all times remain the exclusive property of John Wiley & Sons Inc, the Wiley Companies, or their respective licensors, and your interest therein is only that of having possession of and the right to reproduce the Wiley Materials pursuant to Section 2 herein during the continuance of this Agreement. You agree that you own no right, title or interest in or to the Wiley Materials or any of the intellectual property rights therein. You shall have no rights hereunder other than the license as provided for above in Section 2. No right, license or interest to any trademark, trade name, service mark or other branding ("Marks") of WILEY or its licensors is granted hereunder, and you agree that you shall not assert any such right, license or interest with respect thereto
- NEITHER WILEY NOR ITS LICENSORS MAKES ANY WARRANTY OR REPRESENTATION OF ANY KIND TO YOU OR ANY THIRD PARTY, EXPRESS, IMPLIED OR STATUTORY, WITH RESPECT TO THE MATERIALS OR THE ACCURACY OF ANY INFORMATION CONTAINED IN THE

5/16/2021

RightsLink Printable License

MATERIALS, INCLUDING, WITHOUT LIMITATION, ANY IMPLIED WARRANTY OF MERCHANTABILITY, ACCURACY, SATISFACTORY QUALITY, FITNESS FOR A PARTICULAR PURPOSE, USABILITY, INTEGRATION OR NON-INFRINGEMENT AND ALL SUCH WARRANTIES ARE HEREBY EXCLUDED BY WILEY AND ITS LICENSORS AND WAIVED BY YOU.

- WILEY shall have the right to terminate this Agreement immediately upon breach of this Agreement by you.
- You shall indemnify, defend and hold harmless WILEY, its Licensors and their respective directors, officers, agents and employees, from and against any actual or threatened claims, demands, causes of action or proceedings arising from any breach of this Agreement by you.
- IN NO EVENT SHALL WILEY OR ITS LICENSORS BE LIABLE TO YOU OR ANY OTHER PARTY OR ANY OTHER PERSON OR ENTITY FOR ANY SPECIAL, CONSEQUENTIAL, INCIDENTAL, INDIRECT, EXEMPLARY OR PUNITIVE DAMAGES, HOWEVER CAUSED, ARISING OUT OF OR IN CONNECTION WITH THE DOWNLOADING, PROVISIONING, VIEWING OR USE OF THE MATERIALS REGARDLESS OF THE FORM OF ACTION, WHETHER FOR BREACH OF CONTRACT, BREACH OF WARRANTY, TORT, NEGLIGENCE, INFRINGEMENT OR OTHERWISE (INCLUDING, WITHOUT LIMITATION, DAMAGES BASED ON LOSS OF PROFITS, DATA, FILES, USE, BUSINESS OPPORTUNITY OR CLAIMS OF THIRD PARTIES), AND WHETHER OR NOT THE PARTY HAS BEEN ADVISED OF THE POSSIBILITY OF SUCH DAMAGES. THIS LIMITATION SHALL APPLY NOTWITHSTANDING ANY FAILURE OF ESSENTIAL PURPOSE OF ANY LIMITED REMEDY PROVIDED HEREIN.
- Should any provision of this Agreement be held by a court of competent jurisdiction to be illegal, invalid, or unenforceable, that provision shall be deemed amended to achieve as nearly as possible the same economic effect as the original provision, and the legality, validity and enforceability of the remaining provisions of this Agreement shall not be affected or impaired thereby.
- The failure of either party to enforce any term or condition of this Agreement shall not constitute a waiver of either party's right to enforce each and every term and condition of this Agreement. No breach under this agreement shall be deemed waived or excused by either party unless such waiver or consent is in writing signed by the party granting such waiver or consent. The waiver by or consent of a party to a breach of any provision of this Agreement shall not operate or be construed as a waiver of or consent to any other or subsequent breach by such other party.
- This Agreement may not be assigned (including by operation of law or otherwise) by you without WILEY's prior written consent.
- Any fee required for this permission shall be non-refundable after thirty (30) days from receipt by the CCC.
- These terms and conditions together with CCC's Billing and Payment terms and conditions (which are incorporated herein) form the entire agreement between you and WILEY concerning this licensing transaction and (in the absence of fraud) supersedes all prior agreements and representations of the parties, oral or written. This Agreement may not be amended except in writing signed by both parties. This Agreement shall be binding upon and inure to the benefit of the parties' successors, legal representatives, and authorized assigns.

5/16/2021

RightsLink Printable License

- In the event of any conflict between your obligations established by these terms and conditions and those established by CCC's Billing and Payment terms and conditions, these terms and conditions shall prevail.
- WILEY expressly reserves all rights not specifically granted in the combination of (i) the license details provided by you and accepted in the course of this licensing transaction, (ii) these terms and conditions and (iii) CCC's Billing and Payment terms and conditions.
- This Agreement will be void if the Type of Use, Format, Circulation, or Requestor Type was misrepresented during the licensing process.
- This Agreement shall be governed by and construed in accordance with the laws of the State of New York, USA, without regards to such state's conflict of law rules. Any legal action, suit or proceeding arising out of or relating to these Terms and Conditions or the breach thereof shall be instituted in a court of competent jurisdiction in New York County in the State of New York in the United States of America and each party hereby consents and submits to the personal jurisdiction of such court, waives any objection to venue in such court and consents to service of process by registered or certified mail, return receipt requested, at the last known address of such party.

## WILEY OPEN ACCESS TERMS AND CONDITIONS

Wiley Publishes Open Access Articles in fully Open Access Journals and in Subscription journals offering Online Open. Although most of the fully Open Access journals publish open access articles under the terms of the Creative Commons Attribution (CC BY) License only, the subscription journals and a few of the Open Access Journals offer a choice of Creative Commons Licenses. The license type is clearly identified on the article.

### The Creative Commons Attribution License

The [Creative Commons Attribution License \(CC-BY\)](#) allows users to copy, distribute and transmit an article, adapt the article and make commercial use of the article. The CC-BY license permits commercial and non-

### Creative Commons Attribution Non-Commercial License

The [Creative Commons Attribution Non-Commercial \(CC-BY-NC\) License](#) permits use, distribution and reproduction in any medium, provided the original work is properly cited and is not used for commercial purposes. (see below)

### Creative Commons Attribution-Non-Commercial-NoDerivs License

The [Creative Commons Attribution Non-Commercial-NoDerivs License \(CC-BY-NC-ND\)](#) permits use, distribution and reproduction in any medium, provided the original work is properly cited, is not used for commercial purposes and no modifications or adaptations are made. (see below)

### Use by commercial "for-profit" organizations

Use of Wiley Open Access articles for commercial, promotional, or marketing purposes requires further explicit permission from Wiley and will be subject to a fee.

Further details can be found on Wiley Online Library  
<http://olabout.wiley.com/WileyCDA/Section/id-410895.html>

5/16/2021

RightsLink Printable License

**Other Terms and Conditions:**

**v1.10 Last updated September 2015**

Questions? [customercare@copyright.com](mailto:customercare@copyright.com) or +1-855-239-3415 (toll free in the US) or +1-978-646-2777.



5/9/2021

RightsLink Printable License

JOHN WILEY AND SONS LICENSE  
TERMS AND CONDITIONS

May 09, 2021

---

This Agreement between PINAR ERİBOL ("You") and John Wiley and Sons ("John Wiley and Sons") consists of your license details and the terms and conditions provided by John Wiley and Sons and Copyright Clearance Center.

License Number 5064921223528

License date May 09, 2021

Licensed Content  
Publisher John Wiley and Sons

Licensed Content  
Publication Chemical Engineering & Technology

Licensed Content Title Characterization of Bubble Shapes in Non-Newtonian Fluids by  
Parametric Equations

Licensed Content  
Author Feishi Xu, Noel Midoux, Huai-Zhi Li, et al

Licensed Content Date Aug 7, 2019

Licensed Content  
Volume 42

Licensed Content Issue 11

Licensed Content  
Pages 10

Type of use Dissertation/Thesis

Requestor type University/Academic

5/9/2021

RightsLink Printable License

Format	Print and electronic
Portion	Figure/table
Number of figures/tables	1
Will you be translating?	No
Title	Electrohydrodynamic Instability of Three-Phase Flow
Institution name	Boğaziçi University
Expected presentation date	Jun 2021
Portions	figure 4
Requestor Location	PINAR ERİBOL BOGAZICI UNIVERSITY DEPARTMENT OF CHEMICAL ENGINEERING ISTANBUL, BEBEK 34342 Turkey Attn: PINAR ERİBOL
Publisher Tax ID	EU826007151
Customer VAT ID	TR123456789
Total	0.00 USD

Terms and Conditions

**TERMS AND CONDITIONS**

This copyrighted material is owned by or exclusively licensed to John Wiley & Sons, Inc. or one of its group companies (each a "Wiley Company") or handled on behalf of a society with which a Wiley Company has exclusive publishing rights in relation to a particular work (collectively "WILEY"). By clicking "accept" in connection with completing this licensing transaction, you agree that the following terms and conditions apply to this transaction (along with the billing and payment terms and conditions established by the Copyright Clearance Center Inc., ("CCC's Billing and Payment terms and conditions"), at the time that

5/9/2021

RightsLink Printable License

you opened your RightsLink account (these are available at any time at <http://myaccount.copyright.com>).

### Terms and Conditions

- The materials you have requested permission to reproduce or reuse (the "Wiley Materials") are protected by copyright.
- You are hereby granted a personal, non-exclusive, non-sub licensable (on a stand-alone basis), non-transferable, worldwide, limited license to reproduce the Wiley Materials for the purpose specified in the licensing process. This license, **and any CONTENT (PDF or image file) purchased as part of your order**, is for a one-time use only and limited to any maximum distribution number specified in the license. The first instance of republication or reuse granted by this license must be completed within two years of the date of the grant of this license (although copies prepared before the end date may be distributed thereafter). The Wiley Materials shall not be used in any other manner or for any other purpose, beyond what is granted in the license. Permission is granted subject to an appropriate acknowledgement given to the author, title of the material/book/journal and the publisher. You shall also duplicate the copyright notice that appears in the Wiley publication in your use of the Wiley Material. Permission is also granted on the understanding that nowhere in the text is a previously published source acknowledged for all or part of this Wiley Material. Any third party content is expressly excluded from this permission.
- With respect to the Wiley Materials, all rights are reserved. Except as expressly granted by the terms of the license, no part of the Wiley Materials may be copied, modified, adapted (except for minor reformatting required by the new Publication), translated, reproduced, transferred or distributed, in any form or by any means, and no derivative works may be made based on the Wiley Materials without the prior permission of the respective copyright owner. **For STM Signatory Publishers clearing permission under the terms of the [STM Permissions Guidelines](#) only, the terms of the license are extended to include subsequent editions and for editions in other languages, provided such editions are for the work as a whole in situ and does not involve the separate exploitation of the permitted figures or extracts**, You may not alter, remove or suppress in any manner any copyright, trademark or other notices displayed by the Wiley Materials. You may not license, rent, sell, loan, lease, pledge, offer as security, transfer or assign the Wiley Materials on a stand-alone basis, or any of the rights granted to you hereunder to any other person.
- The Wiley Materials and all of the intellectual property rights therein shall at all times remain the exclusive property of John Wiley & Sons Inc, the Wiley Companies, or their respective licensors, and your interest therein is only that of having possession of and the right to reproduce the Wiley Materials pursuant to Section 2 herein during the continuance of this Agreement. You agree that you own no right, title or interest in or to the Wiley Materials or any of the intellectual property rights therein. You shall have no rights hereunder other than the license as provided for above in Section 2. No right, license or interest to any trademark, trade name, service mark or other branding ("Marks") of WILEY or its licensors is granted hereunder, and you agree that you shall not assert any such right, license or interest with respect thereto
- NEITHER WILEY NOR ITS LICENSORS MAKES ANY WARRANTY OR REPRESENTATION OF ANY KIND TO YOU OR ANY THIRD PARTY, EXPRESS, IMPLIED OR STATUTORY, WITH RESPECT TO THE MATERIALS OR THE ACCURACY OF ANY INFORMATION CONTAINED IN THE MATERIALS, INCLUDING, WITHOUT LIMITATION, ANY IMPLIED WARRANTY OF MERCHANTABILITY, ACCURACY, SATISFACTORY QUALITY, FITNESS FOR A PARTICULAR PURPOSE, USABILITY,

5/9/2021

RightsLink Printable License

INTEGRATION OR NON-INFRINGEMENT AND ALL SUCH WARRANTIES ARE HEREBY EXCLUDED BY WILEY AND ITS LICENSORS AND WAIVED BY YOU.

- WILEY shall have the right to terminate this Agreement immediately upon breach of this Agreement by you.
- You shall indemnify, defend and hold harmless WILEY, its Licensors and their respective directors, officers, agents and employees, from and against any actual or threatened claims, demands, causes of action or proceedings arising from any breach of this Agreement by you.
- IN NO EVENT SHALL WILEY OR ITS LICENSORS BE LIABLE TO YOU OR ANY OTHER PARTY OR ANY OTHER PERSON OR ENTITY FOR ANY SPECIAL, CONSEQUENTIAL, INCIDENTAL, INDIRECT, EXEMPLARY OR PUNITIVE DAMAGES, HOWEVER CAUSED, ARISING OUT OF OR IN CONNECTION WITH THE DOWNLOADING, PROVISIONING, VIEWING OR USE OF THE MATERIALS REGARDLESS OF THE FORM OF ACTION, WHETHER FOR BREACH OF CONTRACT, BREACH OF WARRANTY, TORT, NEGLIGENCE, INFRINGEMENT OR OTHERWISE (INCLUDING, WITHOUT LIMITATION, DAMAGES BASED ON LOSS OF PROFITS, DATA, FILES, USE, BUSINESS OPPORTUNITY OR CLAIMS OF THIRD PARTIES), AND WHETHER OR NOT THE PARTY HAS BEEN ADVISED OF THE POSSIBILITY OF SUCH DAMAGES. THIS LIMITATION SHALL APPLY NOTWITHSTANDING ANY FAILURE OF ESSENTIAL PURPOSE OF ANY LIMITED REMEDY PROVIDED HEREIN.
- Should any provision of this Agreement be held by a court of competent jurisdiction to be illegal, invalid, or unenforceable, that provision shall be deemed amended to achieve as nearly as possible the same economic effect as the original provision, and the legality, validity and enforceability of the remaining provisions of this Agreement shall not be affected or impaired thereby.
- The failure of either party to enforce any term or condition of this Agreement shall not constitute a waiver of either party's right to enforce each and every term and condition of this Agreement. No breach under this agreement shall be deemed waived or excused by either party unless such waiver or consent is in writing signed by the party granting such waiver or consent. The waiver by or consent of a party to a breach of any provision of this Agreement shall not operate or be construed as a waiver of or consent to any other or subsequent breach by such other party.
- This Agreement may not be assigned (including by operation of law or otherwise) by you without WILEY's prior written consent.
- Any fee required for this permission shall be non-refundable after thirty (30) days from receipt by the CCC.
- These terms and conditions together with CCC's Billing and Payment terms and conditions (which are incorporated herein) form the entire agreement between you and WILEY concerning this licensing transaction and (in the absence of fraud) supersedes all prior agreements and representations of the parties, oral or written. This Agreement may not be amended except in writing signed by both parties. This Agreement shall be binding upon and inure to the benefit of the parties' successors, legal representatives, and authorized assigns.
- In the event of any conflict between your obligations established by these terms and conditions and those established by CCC's Billing and Payment terms and conditions,

these terms and conditions shall prevail.

- WILEY expressly reserves all rights not specifically granted in the combination of (i) the license details provided by you and accepted in the course of this licensing transaction, (ii) these terms and conditions and (iii) CCC's Billing and Payment terms and conditions.
- This Agreement will be void if the Type of Use, Format, Circulation, or Requestor Type was misrepresented during the licensing process.
- This Agreement shall be governed by and construed in accordance with the laws of the State of New York, USA, without regards to such state's conflict of law rules. Any legal action, suit or proceeding arising out of or relating to these Terms and Conditions or the breach thereof shall be instituted in a court of competent jurisdiction in New York County in the State of New York in the United States of America and each party hereby consents and submits to the personal jurisdiction of such court, waives any objection to venue in such court and consents to service of process by registered or certified mail, return receipt requested, at the last known address of such party.

## WILEY OPEN ACCESS TERMS AND CONDITIONS

Wiley Publishes Open Access Articles in fully Open Access Journals and in Subscription journals offering Online Open. Although most of the fully Open Access journals publish open access articles under the terms of the Creative Commons Attribution (CC BY) License only, the subscription journals and a few of the Open Access Journals offer a choice of Creative Commons Licenses. The license type is clearly identified on the article.

### The Creative Commons Attribution License

The [Creative Commons Attribution License \(CC-BY\)](#) allows users to copy, distribute and transmit an article, adapt the article and make commercial use of the article. The CC-BY license permits commercial and non-

### Creative Commons Attribution Non-Commercial License

The [Creative Commons Attribution Non-Commercial \(CC-BY-NC\) License](#) permits use, distribution and reproduction in any medium, provided the original work is properly cited and is not used for commercial purposes.(see below)

### Creative Commons Attribution-Non-Commercial-NoDerivs License

The [Creative Commons Attribution Non-Commercial-NoDerivs License \(CC-BY-NC-ND\)](#) permits use, distribution and reproduction in any medium, provided the original work is properly cited, is not used for commercial purposes and no modifications or adaptations are made. (see below)

### Use by commercial "for-profit" organizations

Use of Wiley Open Access articles for commercial, promotional, or marketing purposes requires further explicit permission from Wiley and will be subject to a fee.

Further details can be found on Wiley Online Library  
<http://olabout.wiley.com/WileyCDA/Section/id-410895.html>

### Other Terms and Conditions:

5/9/2021

RightsLink Printable License

**v1.10 Last updated September 2015**

**Questions? [customercare@copyright.com](mailto:customercare@copyright.com) or +1-855-239-3415 (toll free in the US) or +1-978-646-2777.**

